UNIVERSITY OF SOUTHAMPTON

Automated High Voltage Cable Joint Inspection using X-ray Techniques

by

Adrian P. Robinson

A thesis submitted for the
degree of Doctor of Philosophy

in the
Faculty of Engineering, Science and Mathematics
School of Electronics and Computer Science

March 2006

UNIVERSITY OF SOUTHAMPTON

ABSTRACT

FACULTY OF ENGINEERING, SCIENCE AND MATHEMATICS
SCHOOL OF ELECTRONICS AND COMPUTER SCIENCE

Doctor of Philosophy

Automated High Voltage Cable Joint Inspection using X-ray Techniques

by Adrian P. Robinson

Non-destructive testing methods for high voltage joints cables include dimensional checks and insulation system contamination evaluations that are generally performed using conventional x-ray technology. This thesis investigates the feasibility of converting from photographic x-ray imaging and manual inspection to a digital image capture with automated inspection. To do this a new inspection facility was constructed that replaces the photographic film with an x-ray CCD camera coupled with a microfocus x-ray source, enclosed in an irradiation chamber. The images produced from the new facility have to be photometrically corrected to removed the noise in the image associated with the CCD array/scintillating screen. The interfaces between each component of the insulation system can be found using novel feature extraction techniques on the differentiated cable joint image. From this detection the size of each component can be calculated. Once the dimensions of the joint are known, the defect free insulation system data can be removed from the image to allow the insulation contamination evaluation to be completed. This is achieved using statistical analysis of pixel intensity distributions of regions of the image. The results of this cable joint defect inspection can then be used along with the data from the dimensional checks to generate a virtual 3D cable joint. The analysis of the dimensional and contamination investigations along with the virtual cable joint can then be used to determine if the cable joint is fit for service.

The new facility and associated digital inspection demonstrates that it is possible to convert from a manual analogue system to an automated digital process. This conversion improves flexibility of the cable joint inspection process, because with the use of an x-ray CCD camera, there is no need for a dark room, no chemical waste produced, and a reduced operator knowledge and skill requirement. The images produced can also be inspected digitally which removes the possibility of interpretation and human errors related to manual inspection. The results of the digital inspection produce a more thorough analysis of the cable joint along with a tangible virtual cable joint. This simplifies the comprehension of the manufacturing quality of the cable joint. The results can also be catalogued, stored and distributed more easily. The conversion to a digital system, therefore, improves the quality assurance for cable joint manufacture.

Contents

List of Figures

List of Tables

Acknowledgements

This PhD would not have been undertaken if it had not been for the guidance of Dr Paul Lewin during my undergraduate studies. Since then Paul has 'unwrapped the chocolate' which has brought this PhD to fruition. My thanks must also go to our late colleague Professor Tony Davies who helped form the foundations of this work; he is sadly missed. The construction of the new x-ray inspection facility would not have been to the same standards had it not been for the help of Neil Palmer, Brian Rogers, Mike Smith and Steve Harrision. Their help has been invaluable. It is a shame that Roland Caldecutt is not still with us, because, like he said, "It would have been an honour to work with him." I would like to thank Alex Forrester, not only for the many hours of cycling but also for his input into this work. My gratitude is extended to National Grid Transco and EPSRC for their financial support of this work. Finally, I would like to thank two people that have made this whole experience rich and exciting, in more ways than can be or should be described in an acknowledgements of a PhD thesis, namely Graeme 'Les' Williams and David Swaffield.

Nomenclature

U_0	Nominal power-frequency voltage between a conductor and earth
δ	Dielectric loss angle
Z	Acoustic impedance
ρ	Material density
c	Velocity of sound within a material
B_0	Ultrasound magnetic field
f	Larmor frequency
γ	Gyromagnetic constant
f_f	Fill factor
A_p	Pixel area
A_c	Pixel collection area
d_r	Dynamic range
S_p	CCD array peak signal
S_n	CCD array readout noise
I	Raw image
I_d	Dark image
I_{ff}	Flat field image
$b(x, y)$	Precharge value of a pixel at (x, y)
$d(x, y, t, T)$	Dark current of a pixel at (x, y)
t	Exposure time
T	CCD array temperature
$r(x, y)$	Response to x-rays of a pixel at (x, y)
β	Flat field image mean
m	Image width
n	Image height
Z	Atomic number
d	Image magnification
w	Target to window spacing
l	Window to CCD camera face plate distance
x	CCD camera face to cable joint centre distance
s	CCD camera face to image plane distance
S	The wire separation

M^+	Forward diagonal Roberts operator template
M^-	Backward diagonal Roberts operator template
M_x	Horizontal 3 x 3 differential template
M_y	Vertical 3 x 3 differential template
C/CS	Conductor to conductor shield interface
CS/I	Conductor shield to insulation interface
I/IS	Insulation to insulation shield interface
IS/A	Insulation shield to air interface
I'	The differentiated image
$P_{(x,y)}$	The pixel intensity of a pixel located at (x,y)
$\mathbb{N}$	Natural Integers
$\bar{P}_{(x,y)}$	The mean of the pixels surrounding $P_{(x,y)}$
$\sigma^2_{P(x,y)}$	The variance of the pixels surrounding $P_{(x,y)}$

To Debs, a better wife I could not hope to find.

Chapter 1

Introduction

The first a.c. power cables were constructed in the 1880's using either gutta-percha, rubber, or vulcanised bitumen as the insulating material [1]. In 1914 Ferranti developed a 10 kV power cable that used paper to insulate the conductor. The voltage ratings of cables were increased further by Hochstadler in 1914 by the addition of conductor screening. This allowed the distribution voltage to be increased to 33 kV. The maximum transmissible voltage was then further increased in 1923 by Dr Emanueli of Pirelli who impregnated the papers, used to insulate the conductor, with oil. This increased the distribution voltage to 66 kV. Shortly after its discovery by Waldo Semon in 1926, plasticised PVC was used to insulate cables. The next major advance in cable insulation systems saw the use of extruded polymeric insulating materials in 1940. By 1953 General Electric had established the application of chemical cross linking, six years later, cross linked polyethylene (XLPE) was commercialized in Japan [2]. Currently, the two most widely used methods of insulating high voltage cables are fluid filled paper insulation (formally oil impregnated paper insulation however, the fluid used now is synthetic) and extruded polymeric insulation. The most commonly used polymeric materials are thermoplastic polyethylene (PE), cross linked polyethylene (XLPE) and ethylene propylene rubber (EPR) [3]. PVC is not used for high voltage cables because its maximum operating temperature is only 65°C; it is brittle at low temperatures and therefore cannot be laid in cold weather; and its dielectric losses are high. This restricts its use to lower voltages up to 1 kV [3].

1.1 Modern Cable Manufacturing

There are advantages and disadvantages in using either fluid filled or extruded polymeric cable insulating systems. The advantage of using a polymeric insulation, compared to fluid filled paper insulation, is that polymeric insulation does not have the problems associated with containing the insulating fluid. This reduces the complications related to installation and maintenance of these cables [4, 5]. The disadvantage of using polymeric insulation is the operating electrical stresses for polymeric insulation are lower than oil impregnated paper insulation cables. This currently limits the use of EPR and XLPE to 500 kV cables and EPR to 150 kV cables [3]. The benefits of using polymeric insulation means that most new cable installations between 36 kV and 500 kV are now insulated with an extruded polymeric insulation, with XLPE being used in the majority of these cable systems [1, 6, 7]. XLPE is more widely used because it can insulate cables with a higher operating voltage compared with EPR; it has a higher working temperature, 90°C, compared with PE, 70°C, which has a significant effect on the relative current ratings; XLPE has a dielectric loss angle (δ) of 0.001 compared with 0.0023 for paper; and XLPE has a relative permittivity of 2.3 compared with 3.4 for fluid filled paper insulation [1, 8]. As XLPE insulation is by far the most widely used polymeric insulating material, this research has concentrated mainly on the development of inspection techniques for these cables, however most of the designs, theories and details described apply equally to cables with PE or EPR insulation.

1.1.1 Cable Construction

The conductors used in high voltage cables are generally constructed from either stranded aluminium or copper wire. A stranded design is used in order to reduce the resistive losses in the conductor that are caused by the skin effect. The strands or wires used to form the conductor are compacted into a tight bundle, ranging from 150 mm^2 – 3000 mm^2. Cables with a cross-sectional area less than 1000 mm^2 are generally a compacted circular design, whereas above 1000 mm^2 a four or five segment Milliken type conductor is generally used. Both of these types of conductor design produce a circular cross-section, however due to the stranded nature, the profile of the conductor surface is not smooth. If such a conductor was energised, the electrical flux emanating from it would be non-uniform. If this conductor was then insulated without a conductor

screen, the insulation would be subjected to localised high electrical stresses, reducing the voltage rating of the cable. To improve the uniformity of the electrical stress that the insulation is subjected to, a conductor screen can be applied between the conductor and the insulation. For a polymeric insulated cable, this screen is a layer of semiconducting polymer. The polymer can be extruded onto the cable ensuring that the interstices between the stands of wire are completely filled, creating a circular envelope around the conductor, which can reduce the maximum electric stress imposed on the insulation by between 10% and 15% [1]. This screen has to be completely mechanically bonded to the conductor and the insulation in order to minimize the risk of delamination that may occur due to the thermal variations that an insulation system is subjected to when in service. A delamination is undesirable because partial discharge can occur in the gap that forms. The profile of the semiconducting screen also has to be smooth in order to minimize any local high electrical stresses. The smoothness of the semiconducting screen is most critical with higher voltage rated cables because the electrical stress differential between the conductor and the cable earth is greater. The nominal thickness of the conductor screen is typically between 0.4 mm and 2.0 mm.

Extruded on top of the conductor screen is the XLPE insulation. This must be applied so that there is:

- an absence of voids or cavities (gas or vacuums trapped in the insulation),
- a low concentration of inclusions or contamination (mainly metallic or carbonised materials),
- the smoothest interfaces between the conductor screen and the insulation to minimize local electrical stresses,
- no significant reduction in its thickness, and
- good circularity and concentricity to minimize stress variations.

If any of these defects are introduced into the insulation it can cause the cable to fail prematurely due to breakdown of the insulation. The required thickness of XLPE for high cable insulation is not internationally standardised, however the general relationship between cable voltage rating and insulation thickness is shown in Table 1.1.

Voltage (kV)	Insulation Thickness (mm)	Maximum Stress (MV/m)
66	12	3 – 6
132	18 – 22	5 – 8
275	22 – 32	8 – 10
400	25 – 32	13 – 14

TABLE 1.1: Relationship between cable voltage and insulation thickness [1].

The last layer of the insulation system is the insulation screen. This is generally constructed from the same semiconducting polymers used in the conductor screen. The main function of this screen is ensure that the electric field is confined to the polymeric insulation. This screen also has to be fully bonded to the insulation to minimize the risk of delamination/partial discharge sites. Both the conductor and insulation screens also have to be constructed to the same defect tolerances as the insulation. The general construction of these three insulation system components of a high voltage polymeric cable is shown in Figure 1.1

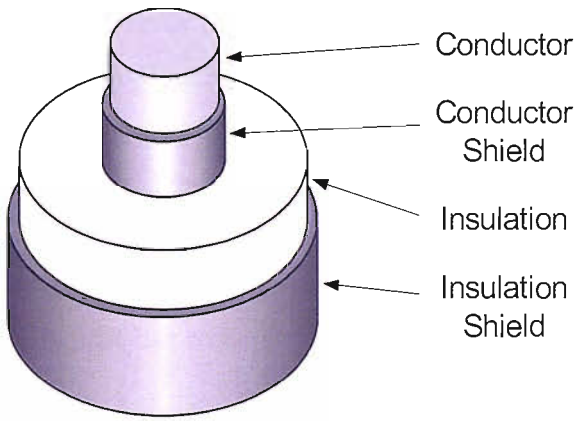

FIGURE 1.1: General construction of a high voltage cable with extruded insulation.

1.1.2 Manufacturing Quality Assurance

To successfully produce an XLPE insulated cable, it is essential to ensure that any raw material extruded onto the conductor has the lowest levels of contamination. To ensure this, the insulation and screening compounds are filtered and stored in a fully enclosed storage system before being transported to the extruder. The cable is then drawn through a triple extrusion die box where the semiconducting conductor screen, the insulation and the semiconducting insulation screen are applied. The cable then has to be heated to above 200°C to trigger the cross-linking process. After which the cable

is then allowed to slowly cool back to ambient temperature. The extrusion, heating and cooling process can last several days and are performed in a pressurized environment to ensure that the volatile by-products of the cross-linking process do not form voids, but remain dissolved in the insulation.

This entire process is an automated procedure, however, due to logistical constraints, cables can only be produced in finite lengths. The production length of a cable is determined by the type of cable being manufactured. In general, the higher the rating of the cable the shorter the production length because of the increased insulation system volume. For cable lengths longer than the manufacturing length, two or more cables have to be joined together. The process of joining two cables lengths together is not an automated procedure due to its complexity. The process involves electrically joining the conductors, followed by the application of the conductor screen, insulation, and insulation screen over the conductor joint. For submarine cables, the aim of the jointing process is to produce a joint with electrical, mechanical and physical properties that are similar to the cable lengths either side of the joint, so that the jointed cable can be wound onto a large turntable for storage and subsequent laying. To achieve this 'seamless' joint the screens and insulation are applied by hand lapping semi-conducting and insulating polymer tapes around the joint. Despite the ability to monitor this joint lapping process with in-process visual examination, defects are more likely to be introduced into the insulation system during the jointing procedure compared with the extrusion process, and so the quality of the joint has to be determined with post-process testing.

There are two groups of tests used to ensure that the conductor and insulation system of a cable can perform to the level stated in a cable specification. These are factory and acceptance tests. The factory tests are performed on the individual lengths of cable, where as the acceptance tests are performed on the new cable network after installation. The factory tests are used to evaluate the electrical and mechanical properties of the cable. The tests are performed on either the whole cable length or on samples taken from each cable length. It is also necessary to to ensure that the cable joints have been manufactured to the same standards as the cable lengths either side of it. For this reason each joint also undergoes a range of tests, however it is not possible to take samples from the cable joints. For this reason the cable joints have to be tested using non-destructive testing (NDT) techniques in order to determine the manufacturing quality of their insulation system.

1.2 Project Aims and Objectives

The Tony Davis High Voltage Laboratory at the University of Southampton currently has a method of inspecting cable joints using conventional photographic film plate x-ray imaging techniques. With this system it is possible to produce images of the internal structure of the cable joint. These images can then be used for dimensional checks and defect detection. The process employed to inspect the joints however is labour intensive, produces significant chemical waste, and requires specialist knowledge and skills. The aim of this research was to design and construct a new cable joint test facility that requires less specialist knowledge and skills to operate, that is less labour intensive and does not produce chemical waste, while still retaining the ability to detect any defects introduced into the joint.

The factory tests performed on each cable length are described in Chapter 2. The cable joints in the new cable network also has to comply with the specifications of these tests. The factory tests that are non-destructive are electrical resistance measurements of the conductor, partial discharge testing, and withstand voltage tests. As these tests are non-destructive they can also be performed on a cable joint. The sample tests used to ascertain the manufacturing quality of the cable include, dimensional measurements and contamination estimation of the insulation system components. These tests can also be determined using non-destructive techniques. The viable methods of determining the dimensions and contamination of the insulation system are ultrasound, magnetic inspection methods, far-infrared laser inspection, and radiography. The most appropriate method of inspection appears to be radiography as it can produce good quality images of the internal structure of the cable joint. The current x-ray inspection method at Southampton uses photographic film and manual inspection. There are problems associated with both of these aspects of the system. These problems can be removed by converting the inspection to digital system. The different types of digital x-ray capture are described in Chapter 2 with evidence to support the use of CCD array technology.

In order to convert to a digital system, a new inspection facility was constructed. Chapter 3 describes the construction of the new facility. In order to produce an x-ray image of a cable joint, an x-ray source, an imaging system and positional hardware are required. The factors affecting the suitability of an x-rays source for cable inspection include the tube voltage and current, its focal spot size, and the exposure geometry. The current

source is a 50 kV 1.0 mA macrofocus source that has a large focal spot size. This source has to be used in a pseudo-parallel geometry. The main problem with this arrangement is that the exposure geometry is a compromise between exposure time and need for a large separation between the source and the cable joint. For the new inspection facility, this source has been replaced with a 100 kV 100 µmA source with a 5 µm focal spot size. This new source is used in a pseudo-radial set up and as a result is able to produce better quality images. The original system uses photographic film to capture the x-ray images, however there are processing and inspection problems associated with this method. The photographic film can be replaced with a CCD array, providing that the capture and readout method can produce a sharp, good contrast image with a low noise content. The choice of source and x-ray CCD camera are discussed in Chapter 3 along with the required positional hardware required to safely inspect a cable joint.

The images produced by the x-ray CCD camera are digital images. Chapter 4 describes the characteristics of a digital x-ray image along with a comparison of photographic and CCD array images. A digital image consists of rows and columns of pixels. Each pixel is a data point that contains a measure of the x-ray flux that has captured by the CCD camera. The characteristics of a digital x-ray image of a cable joint is determined by the exposure setting of the x-ray source. Chapter 4 describes the method of choosing the correct exposure setting in order to optimise the image content and quality. The image produced, however, also contains pixel specific noise. This noise comprises of precharge, dark current and pixel response variations. These three noises can be removed from the image using photometric correction. In order to determine the relative quality of the photometrically corrected image and a photographic x-ray image, three test pieces were imaged using both imaging methods. The results of this comparison showed that CCD array images were significantly better than the photographic film image. The main disadvantage to using a CCD array to capture the images is the field of view of the array. The images captured by the CCD array are significantly smaller than those captured on the film plates. To produce a larger field of view, the images can be montaged. The final sections of this chapter describe the alignment of the x-ray source, CCD camera, and the positional hardware required before the images could be montaged successfully.

The montaged images generated have to be inspected in order to determine the dimensions and the contamination levels of the insulation system components. Chapter 5 describes the detection of the interfaces between each insulation component. The size

of each component can then be determined by the distance between the interfaces. The standard methods of detecting edges in an image can be used to determine the locations of the interfaces in the image, however, the results using these methods are either incomplete detections or images with high levels of noise. The results are significantly improved if the interfaces in the image are found by locating known characteristics within the image relating to each interface. To implement this method of detection, the image is first differentiated and then the differentiated image is inspected for known differentiated pixel intensity relationships, namely inflexions and troughs. Once these structures have been found, the size of the components can be calculated. The accuracy of this method of component dimension determination is then assessed by imaging a section of cable joint in order to determine the size of each component. The section of cable joint was then sliced into segments and the components measured. The results of this analysis are discussed at the end of Chapter 5.

After the size of each component has been determined, it is necessary to assess the levels of contamination within the insulation system of the joint. The processes used are described in Chapter 6. The main contaminates are inclusions and voids. The detection of these structures within the insulation system cannot be undertaken with standard edge detection techniques due to the fact that the difference in the image between a defect and the surrounding insulation can be very small. This means that any defect within the insulation system has to be found using feature extraction techniques. An inclusion will tend to produce a defined group of pixels that have pixel intensities that are significantly less than defect-free insulation. Inclusions can therefore be found by locating groups of pixels with a reduced pixel intensity. Voids, however, produce regions of the image that have pixels with increased intensities. The edges of these defects are generally not as well defined as an inclusion. For this reason, voids have to be found using the variance of the distributions of pixels that contain the void. Both of these detection processes can be significantly improved by removing any pixel data in the image relating to defect-free insulation. This can be achieved by creating an artificial defect-free image. This image can then be subtracted from the original image to produce an image containing only the defects. The size and number of defects can then be determined by inspecting this defect image using the techniques described.

The final section of the inspection process is to produce a three dimensional (3D) image of the cable joint that shows the relative size and locations of the different components

of the insulation system, along with the location of any defects. Chapter 7 details how the montaged images are arranged in three dimensional space. The locations of interfaces can then be used to generate a 3D representation of each component. These components can then be combined together to produce a virtual cable joint. Into this virtual cable joint can be added any of the defects found within the insulation system. This 3D tool can then be used to contextualize the dimensional measurements and contamination levels of the insulation system components. It is this 3D image combined with the statistical analysis of the components and defects within the insulation system that represent the result of the proposed digital inspection system. Finally, Chapter 8 contains the conclusions from this work along with suggestions of areas that require further investigation.

Chapter 2

Testing of Polymeric High Voltage Cables

The commercial use of polymeric cables, that is cables insulated with either crosslinked polyethylene (XLPE) or ethylene propylene rubber (EPR), dates back to the middle of the 20th century [5]. Since then, standards of manufacture and a range of cable tests have been developed to ensure that the performance and reliability of polymeric cable systems, and industrial acceptance of them, matches or exceeds that of oil impregnated paper insulated cables, which have had a good service history spanning more than 100 years [9]. This chapter is concerned with the testing methods used to evaluate the manufacturing quality of extruded polymeric cables.

2.1 Testing Methods

When a new high voltage cable design is produced, regardless of the type of insulation system, tests are undertaken to ensure that the cable and its associated accessories, such as joints, stop joints, branching units and terminations, can demonstrate satisfactory performance characteristics to meet the intended application. These tests, known as type tests, are designed to evaluate the current and long term mechanical and electrical properties of the cable and its accessories, and to ensure that the new cable design can deliver electrical power in the manner stated in the specification for the new cable. The details of the tests used for evaluating power cables with extruded insulation and their

accessories can be found in [10–12]. These type tests are such that, once they have been undertaken on a length of cable, there is no need to retest any further production lengths of the same cable design, unless changes are made in the cable material, design, or method of manufacture which might change the performance characteristics of the cable.

Once a new cable design has successfully undergone the full range of type tests, production lengths can be manufactured for commercial applications. Each length of cable produced, however, still has to be electrically and mechanically tested during and after production to determine its manufacturing quality and to predict its performance characteristics. The range of tests available can be categorised into two groups, factory and acceptance tests [13]. Factory tests are performed on each length of cable and its accessories directly after production. They are designed to ensure that each cable length has achieved a minimum level of electrical and mechanical performance, as stated in the specification for the cable. After the cable lengths have passed these tests they can be joined together to produce the full cable length that will be installed into the transmission and distribution network. Before the new cable is energised, however, a full range of electrical tests have to be performed on the complete cable circuit to ensure that the new installation meets the specification of the new delivery network. This research has concentrated on the range of factory tests that can be used to test extruded polymeric insulated cable cable lengths and more specifically the joints between these cable lengths. The following sections describe procedures and methods used to test cables with extruded insulation. The details of the tests are based on [10–12].

2.1.1 Factory Tests

Factory tests are performed on each length of cable and its accessories after manufacture and before the component is installed into the power delivery network. They are carried out before the delivery network is installed, to ensure that individual components of the power delivery network are fit for service and will not fail prematurely during the estimated working lifetime of the network. The tests used for this purpose are:

- electrical resistance measurements of the conductor,
- partial discharge tests,

- voltage tests,
- dimensional checks, and
- sample tests.

2.1.1.1 Electrical Resistance Measurements of the Conductor

The conductors of power cables are manufactured from strands of either copper or aluminium/alumninium alloy. Copper was initially used because it can easily be rolled and drawn to wire, it has a very low resistance (1.724×10^{-8} Ωm at 20°C) and mechanical strength. Aluminium started to be used as a conductor when the cost of copper rose in the 1950's. Aluminium has a third the density of copper, however this advantage is offset by the fact that the resistance of aluminium is 2.803×10^{-8} Ωm at 20°C [1]. The maximum level of resistance that the conductor is allowed to have is determined by the power rating of the cable. Higher rated power cables must present a lower resistance per metre than lower rated power cables. This is achieved by incorporating more strands into the conductor to produce a larger cross sectional diameter for higher rated cables. The level of conductor resistance is therefore directly related to the cross sectional area of the cable. Due to the reduced conductivity of aluminium, the cross-sectional area of these conductors have to be increased by a factor of 1.6 compared with copper [1]. If defects have been introduced into the conductor during manufacture, this could affect the conductivity of the conductor. To test the manufacturing quality and performance of the conductor, the d.c. resistance can be measured following the methods described in Appendix A, Section A.1 in accordance with [14].

2.1.1.2 Partial Discharge Testing

Partial discharge (PD) tests are performed to determine if the cable's insulation system contains any defects, such as voids or inclusions within the insulation or defective areas of the semi-conducting sheaths. To detect such a defect in the insulation system the cable has to be energized. If the electrical stress is great enough, then PD can occur at the defect site. This causes an electrical transient to be produced, which sets up travelling waves that propagate to both ends of the cable. If a PD detector is located at one end of the cable then this travelling wave can be detected. If a wave is detected

then it is assumed that there is a defect present in the cable's insulation system. The size of the defect determines the magnitude of the PD detected: a larger defect will produce a large PD signal [15–17]. The PD signal is a measure of the charge detected by the PD transducer, and is given in pC [13]. The partial discharge test methods used to determine the defect status of the cable are detailed in Appendix A, Section A.2.

2.1.1.3 Withstand Voltage Tests

This test is performed to check if the cable will be able to tolerate the commercial-frequency overvoltage, which might be applied to the cable during operation. The test is made at ambient temperature using an alternating voltage at power frequency. The voltage is raised slowly to 2.5 U_0 and then held for 30 mins. For the cable to withstand this test voltage no breakdown in the insulation should occur.

2.1.1.4 Dimensional Checks

In order for the cable to perform in accordance with the specification for that cable, each component of the insulation system must be manufactured to within the tolerances stated in the cable's insulation specification. If any component has been manufactured such that it does not comply with the specification, it can have a detrimental effect on the performance of the insulation system during the working lifetime of the cable and/or adversely affect the working lifetime of the cable. For this reason a sample of each length of cable has to be taken from one end of the cable length and a measurements taken of the thickness of the insulation, semiconducting screens, metallic sheath and the oversheath. The details of the measurements taken and the compliance criteria are shown in Appendix A, Section A.3.

2.1.1.5 Sample Tests

The four tests outlined above are performed on each production length of cable; more in-depth sample tests are also undertaken in addition to these tests. The frequency at which the samples are taken from manufactured lengths of cable as shown in Table 2.1. Each sample is then subjected to the following tests:

Cable Length		Number of samples
Above (km)	Up to and Including (km)	
2	10	1
10	20	2
20	40	3
40	60	4
etc.	etc.	etc

TABLE 2.1: Number of samples required for sample testing of cables

- resistivity tests on the semiconducting screens,
- hot set test for XLPE insulation,
- shrinkage test for XLPE insulation,
- cross-linking by product concentration,
- insulation contamination examination, and
- measurement of capacitance.

Resistivity tests on the semiconducting screens. The semiconducting screens have to be partially insulating and partially conductive in order to smooth the electrical field generated by the conductor. This is achieved by doping a suitable polymer with carbon black [3]. The amount of carbon black added and homogeneity of the mixture determines the resistivity of the material. The methods used to determine if the semiconducting screens have been manufactured so that they will smooth the electric field are detailed in Appendix A, Section A.4.

Hot set test for XLPE insulation. Polyethylene is a partially crystalline polymer, which means it can be used to form stable shapes below its crystalline melting point. Above this temperature however it softens and melts, restricting the operating temperature of the cable to 70°C. This maximum operating temperature can be increased to 90°C by cross-linking the polymer chains after the extrusion process [3]. The tests uses to determine if adequate cross-linking of the polyethylene chains has taken place are described in Appendix A, Section A.5.

Shrinkage test for XLPE insulation. To reduce the risk of in-service cable failures, the insulation must not significantly shrink. If the insulation shrinks significantly during the operating lifetime of the cable, this can result in mechanical stresses that could lead to a service failure. This test is used to evaluate the the amount of shrinkage that might occur in the insulation during the operational lifetime of the cable, the details of which can be found in Appendix A, Section A.6.

Cross-linking by product concentration. Polyethylene is normally cross-linked by adding peroxide to the polyethylene and then heating it to at least 180°C. This causes the peroxide to decompose into its radicals which attack the polyethylene polymer chains, causing cross-linking [3]. A second measure of the amount of cross-linking can therefore be made by heating samples of the insulation to a temperature just below 180°C. At this temperature the cross-linked polyethylene is unaffected, however the unlinked polyethylene is evaporated, causing a change in weight of the sample. This change in weight can therefore be used to determine if sufficient cross-linking has taken place (Appendix A, Section A.7).

Insulation contamination examination. This test is used to estimate the size and concentration of voids and inclusions in the insulation. To perform the test, five 3000 mm^3 cross-sectional slices of insulation are taken from the sample and examined using a $\times 50$ magnification transmission microscope. The five largest defects per slice are then recorded. To be considered defect free the quality of the XLPE material and the extrusion process should be such that:

- there should be no voids greater than 75 μm in diameter and there should be less than 20 voids measuring 50 μm in diameter recorded from all five samples;
- there should be no inclusions larger than 150 μm in any dimension and the number of inclusions measuring 50 – 150 μm should not exceed 10 from all five samples.

Measurement of capacitance. To ensure that the power losses in the cable the are kept low, the manufacturer of the cable will specify a nominal value of capacitance for the cable. The details of the test used to ensure that the cable complies with the manufacturer's specification are shown in Appendix A, Section A.8.

2.2 Testing High Voltage Cable Joints

Once each cable length has passed the factory tests they can be jointed together. For submarine cables the cable joint has to be electrically and mechanically identical to the cable lengths either side of the joint. To do this the conductor screen, insulation and insulation screen are pencilled down to expose the conductor. The conductors are then electrically and mechanically joined. Then the insulation system is reapplied between the two pencil cones. This arrangement can be seen in Figure 2.1. This joint then has to be tested to ensure that it also meets the level of electrical and mechanical performance as stated in the specification of the cable. Ideally each joint would be tested using the same range of factory tests used to evaluate the parent cable either side of the joint, however it is not possible to complete all these tests on a joint. Conductor resistivity, partial discharge and voltage withstand tests can be performed on the cable, because these tests are non-destructive, and provide a base-line level of quality assurance for the joint. Dimensional checks and sample tests, however, require sections to be cut from the cable for testing, therefore, these tests cannot be performed on the joints. It is possible however to carry out dimensional checks and defect detection using NDT techniques. The main theory behind NDT inspection of joints is to produce an image of the internal structure of the joint that can be used to perform dimensional checks and to determine the concentration of voids and inclusions in the joint. This NDT inspection can then be used, in addition to the applicable factory tests, in order to evaluate the quality of the joint. The methods that can be used to NDT the internal structure of a cable joint include ultrasound, magnetic methods, far-infrared inspection, and radiography. The theory, application, advantages and disadvantages of all these methods are detailed below.

2.2.1 Ultrasound

Ultrasonic sound wave, or ultrasound, detection has been used since 1940 for locating corona on high voltage insulators in air and partial discharge detection in oil-immersed transformers and gas insulated apparatus [18]. Acoustic imaging, initially used for medical purposes, however, was only developed in the 1970s. The principles and equipment used for medical application is also applicable to industrial inspection [19, 20]. Ultrasound is high-frequency sound waves with a frequency greater than 20 kHz, but typically

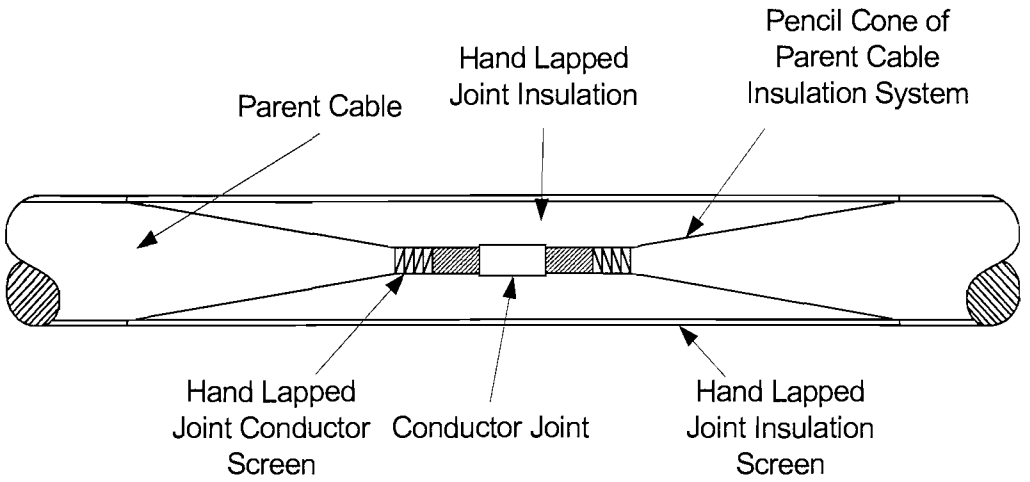

FIGURE 2.1: Joint schematic.

the range used for inspection of polymers and composites is 0.5 to 20 MHz [21]. When ultrasound travels though any medium it is attenuated. In an ideal material the ultrasound waves would be attenuated solely by the spreading of the wave, away from the source of the ultrasound wave, decreasing inversely with the distance from the source. Natural materials, however, attenuate the sound wave even further, known as the material specific attenuation. This is caused by absorption and scattering of the sound wave. Absorption by the material is caused by the conversion of the ultrasound wave into heat within the material itself, due to the natural resistance to vibration within the material. It is this part of the material specific attenuation that causes greater attenuation of higher frequency waves [22]. The scattering results from the fact that materials are not strictly homogeneous, causing slight changes in the density of the material, and so the acoustic impedance, Z of the material is not constant [21]. Acoustic impedance is given by:

$$Z = \rho c \tag{2.1}$$

where ρ is the density of the medium and c is the specific velocity of sound in that material.

If the homogeneity of the material changes dramatically, such as boundary between two different materials, resulting in a large difference in Z across the boundary, an acoustic mismatch occurs, causing some of the wave to be reflected back against the original direction of travel of the sound wave. The greater the acoustic mismatch, the more the interface reflects the sound wave. If the individual components of a composite material

are considered to be relatively homogenous, then the speed of the incident and reflected ultrasonic wave through the individual components can be considered uniform. This means that the time taken for an ultrasound to travel through a material, be reflected and travel back to the site of sound generation can be used to determine the distance between the generation location and the material interface. If a probe, therefore, can generate pulses of sound in the ultrasonic frequency range and can also detect any reflected echoes, then the relative location of the material interfaces in a test object can be determined [19, 21].

Using ultrasound in this way, to measure acoustic mismatch locations, is essentially a range-measuring system. It is known as A- (or Amplitude) scanning, and is based on the submarine detection system, Sonar (Sound Navigation and Ranging), developed during World War I [22]. A short pulse of ultrasound is directed through the cable sample. The boundaries of the insulation screen, the insulation, the conductor screen and the conductor reflect back echoes of this pulse, as well as the boundaries of any defects. The time, t, taken between the transmission of the pulse and reception of the echo has to then be measured, normally with an oscilloscope. The relative locations of the interfaces can then be calculated from the relative time delay of the received echoes. To convert the time delay signals into a spatial measurement the velocity, c, of ultrasound has to be determined. If the velocity of the ultrasound is known then the distance, d, from the transmitter can be calculated using the following formula:

$$d = \frac{ct}{2} \tag{2.2}$$

The factor of 2 is required since the pulse has to travel to the interface and then back to the receiver. Equation 2.2 is a simplification, however, as c is not a constant through the whole of the cable sample, rather it changes at each interface, therefore, Equation 2.2 should read

$$d = \sum_{i=1}^{n} \frac{c_i t_i}{2} \tag{2.3}$$

where n is the total number of different materials that the transmitted and subsequently reflected ultrasound passes through.

To determine the value of c for the conductor, conductor screen, insulation and insulation screen a defect free section of cable with known geometry has to be imaged. The reflected echoes can then be used, along with the known dimensions, d, for each component to determine the individual values of c. With this procedure it is therefore possible to determine the relative locations of material interfaces within a cable joint. Detection of voids and inclusions also uses the acoustic mismatch at the boundary between the insulation/screen and the inclusion or void. The level of acoustic mismatch is similar with both voids and inclusions, which results in similar detection rates of both types of defect [20].

The general system arrangement for performing A-scans is shown in Figure 2.2. The rate generator simultaneously activates the ultrasound transmitter and the time-base generator. This causes the transmitter to generate a short pulse of ultrasound, normally by stimulating a piezoelectric transducer, and starts the time-base generator timing the delay between the initial pulse and any reflected pulses. The received echo is detected using the transducer to convert the sound wave back into an electric signal. This signal can then either be viewed on the oscilloscope or stored digitally for further processing. Due to attenuation of the ultrasound pulses in the cable, echoes from deeper interfaces tend to be very weak. These weaker signals are, therefore, amplified using the time-gain amplifier. By using a time-gain amplifier, the signal related to a deeper conductor screen/insulation interface, point 7, in Figure 2.2 is amplified more than the signal related to the upper conductor screen/insulation, point 2. Signal 1, the initial sound pulse, is also included as a point of reference for the subsequent echoes. The signals from a single pulse can therefore be used for a point location inspection of a cable. To generate an image of the full cable joint, the transducer probe has to be scanned along the length of the cable and 180° around the cable. The transducer also has to be kept in contact with the cable, preferably with an acoustic coupling medium to improve the transmission and detection of the ultrasound wave. Each point location scan can then be used to generate a three-dimensional, 3D, image using standard tomographical techniques.

The resolution of images generated from such a scan therefore depends on three factors; axial and lateral resolution of the ultrasound wave and the positional resolution of the translational movement of the transducer. Axial resolution describes the ability of the ultrasound wave to detect two objects directly inline with the line of travel of the sound

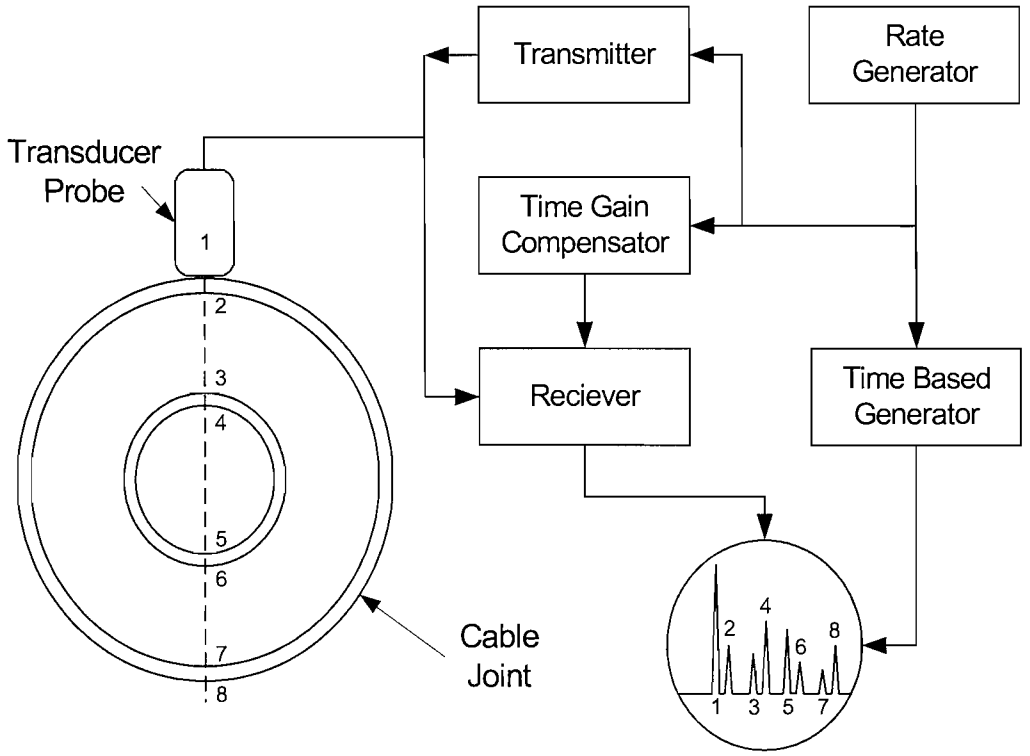

FIGURE 2.2: Schematic diagram of ultrasound generation and detection.

wave at different distances from the transducer, as shown in Figure 2.3. This resolution is determined by the pulse duration: the shorter the pulse the better the axial resolution. Shorter pulses, however, have less sound to be reflected and so the signal to noise ratio of the system is reduced with a shorter pulse. Lateral resolution describes the differentiable distance at right angles to the wave travel. Lateral resolution is determined by the frequency of the ultrasound. Higher frequencies will generate better lateral resolution due to their smaller wavelengths, however, as mentioned above, higher frequency waves tend to be absorbed more readily by a material. The choice of ultrasound frequency is therefore a trade off between penetration capability and spatial resolution [20, 21]. The translational resolution of the transducer probe determines the distance between each point location scan and the accuracy of the distance between these locations. The spatial resolution of the system therefore determines the accuracy of the tomography, and the number of point location scans determines the level of detail of the resulting 3D image.

XLPE has a high acoustic impedance, this means that it is difficult to penetrate it even with low frequency ultrasound. The thickness of the insulation that can be imaged is restricted to approximately 15 mm and the long wavelength required results in a

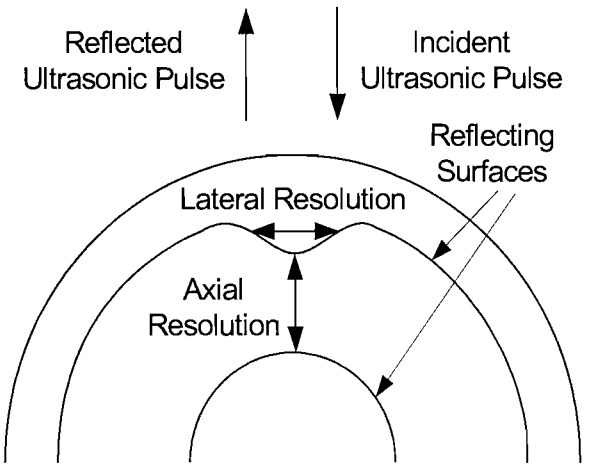

FIGURE 2.3: Axial and lateral resolution of ultrasound.

minimum spatial resolution of approximately 20 μm. Using ultrasound, it is also only possible to detect voids and inclusions 0.5 mm – 1 mm in diameter at a maximum depth of 15 mm [23].

2.2.2 Magnetic Methods

The nuclei in most atoms are not stationary; they spin about a central axis through the atom. This means that the nucleus of most atoms can be considered as magnetic dipoles because of the spinning positive charge, due to the presence of protons in the nucleus. If these nuclei are placed in a magnetic field then the axis of spin of the nuclei tend to align either parallel or anti-parallel to the field depending on the energy state of the nucleus. The lower energy state corresponds to parallel alignment, and in equilibrium, more of the protons are found in this state. The exact alignment of the axes of spin of the nuclei however is not perfectly inline with the applied external magnetic field, B_0, instead they precess about the direction of B_0, similar to a spinning top in a gravitational field [24]. The radial frequency of this precessing is called the Larmor frequency, f, defined as:

$$f = \frac{\gamma B_0}{2\pi} \qquad (Hz) \qquad (2.4)$$

where γ is the nucleus specific gyromagnetic ratio.

From Equation 2.4 it can be seen that f is dependent on the nucleus and on the strength of the magnetic field B_0. The amplitude of the precess is also dictated by the strength of B_0. The stronger the magnetic field used, the smaller the amplitude of the precess of

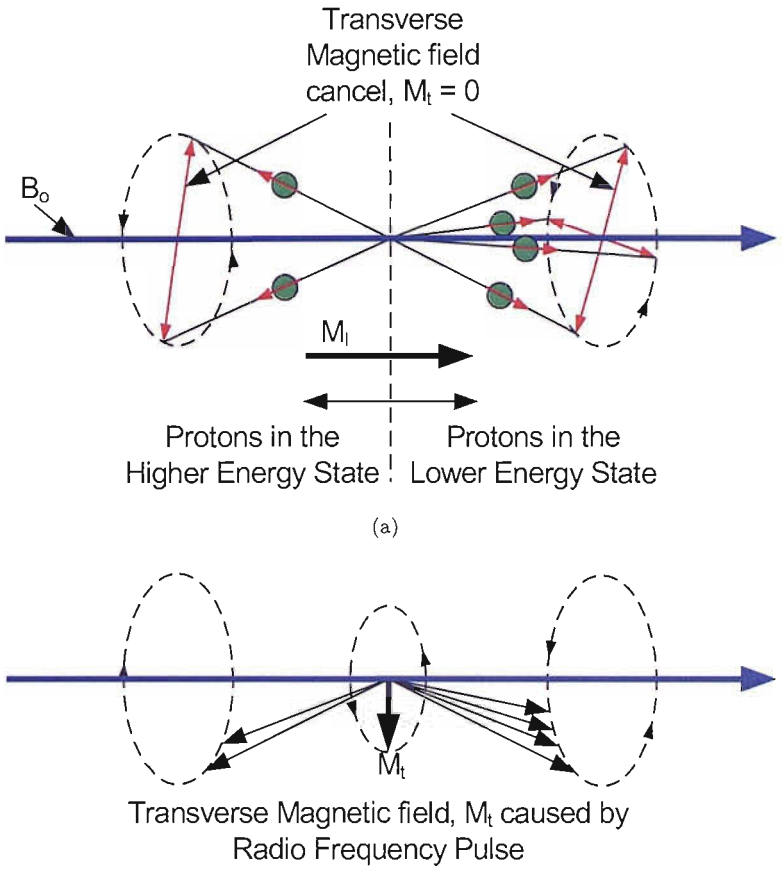

FIGURE 2.4: Transverse and longitudinal magnetic fields due to spinning protons: a) no rf pulse, random phase, and b) rf pulse, in phase.

each nucleus. The phase of the precess of each atom in the magnetic field, however, is random, which means that the resultant magnetic field, M, of the precessing atoms is in line with B_0, i.e. M_I shown in Figure 2.4. By applying a second externally applied force to the atoms with the frequency f, it is possible to force the atoms to precess in phase with the external force and with each other. With the in-phase precessing of the atoms, a transverse field is set up, M_t, with frequency f. In this state the protons of the nuclei are maintained at a higher energy level compared to the energy level of the protons before the application of the second external force. When this second external force is removed the protons release this extra energy and the precessing of the atoms gradually relaxes back to a random state. The energy released also has the same frequency f. This energy can therefore be detected using an inductance coil [25, 26]. It is these characteristics of atoms that is used to image materials using magnetic fields. The process is nuclear magnetic resonance (NMR) imaging [27].

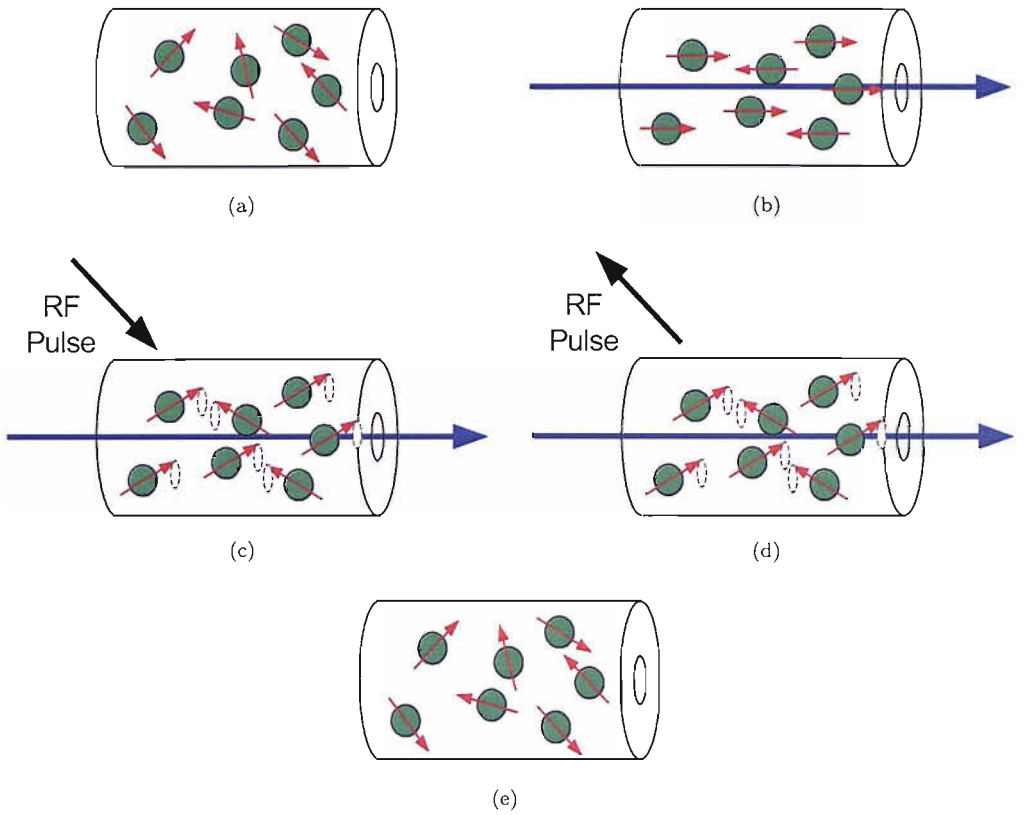

FIGURE 2.5: NMR procedure: a) cable at rest, b) application of B_0, c) application of rf pulse, d) rf pulse emitted by cable, and e) removal of B_0 cable returns back to rest configuration.

The nucleus of hydrogen atoms consists of a single proton. This makes hydrogen the most sensitive stable NMR nucleus and hydrogen is also abundant in organic compounds [24]. For these reasons, hydrogen is the atom normally interrogated during NMR imaging. The constant $\gamma/2\pi$ has a value of 42.57 MHzT^{-1} for hydrogen, which means that with a magnetic field of 1 or 2 T, the Larmor frequency is within the radio frequency range. This means that if hydrogen is used to image a test object, the second external force applied to the test object, while in the magnetic field B_0, can be a radio frequency, rf, signal. The whole process therefore has no adverse health risks. The process of producing a NMR signal in a cable joint can be seen in Figure 2.5.

Initially the hydrogen protons spin randomly. Once the magnetic field B_0, is applied the protons align either parallel or anti-parallel to the magnetic field. A rf signal is applied to the cable joint and the hydrogen protons precess in phase. The radio signal is removed and the protons relax back to the random phase precessing by emitting a radio frequency magnetic signal with frequency f. This signal is then detected using an

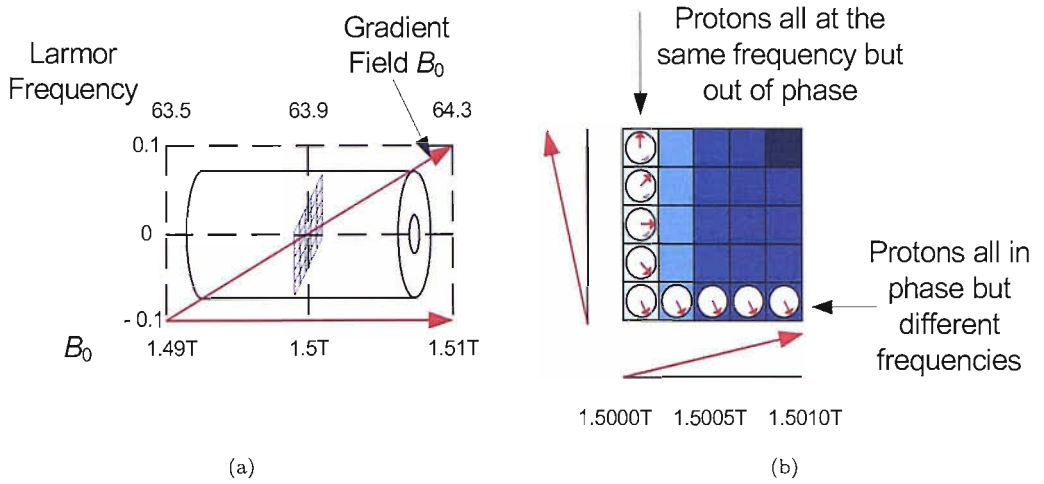

FIGURE 2.6: NMR signal localisation: (a) Plane localisation, and (b) Pixel localisation.

inductance coil. The magnetic field, B_0 is then removed and the protons relax back to a random spin orientation.

With this arrangement however all the hydrogen protons will be excited by the same radio frequency and as a result the signal detected by the inductance coil will be the sum of all the hydrogen atoms relaxing back to an out of phase precess. To image a cable, the signal detected has to be localised. First, a plane of interest is set up. This is achieved by varying the magnetic field strength along the length of the cable joint, which means that the B_0 varies along the length of the cable and hence the Larmor frequency f varies along the length of the cable joint. Different radio frequencies are then used to excite the hydrogen protons along the length of the cable, in effect slicing the cable into small sections. These sections then have to be divided up into sub-areas in order to generate an image of that slice. Each sub-area then forms a pixel in the final image of the slice. To do this the slice is split into columns by applying a separate second magnetic gradient along the slice in the x-direction. This gradient therefore sections the slice in the same manner as the gradient of B_0 sections the cable into slices. To divide the y-axis a third magnetic gradient is set up. This gradient alters the phase of the precess of the protons. With these three separate magnetic fields it is therefore possible to generate a specific frequency and phase signal for discrete sections of the cable joint, as shown in Figure 2.6. These signals can then be detected by the inductance coil and then decomposed into an image using Fourier transforms [22, 28].

The intensity of the signal from each pixel is determined by the proton density within

that section; the more hydrogen protons there are the bigger the signal. The resolution of the images is determined by the uniformity of the gradient of the magnetic fields, the size of the gradient along each axis and the bandwidth of the radio frequency applied. The more uniform the gradient of the magnetic fields, the better the probability of localising a signal to a specific point in the cable sample. The larger the gradient of the magnetic fields, the greater the change in f, which means each slice and pixel become more defined. The bandwidth of the radio frequency also affects the localisation of the detected signal. The smaller the bandwidth, the better the localisation.

Using this inspection technology it is possible to NDT a cable joint with clear distinct images. The systems however are generally relatively large in order to house the magnetic coils, hence they are not generally portable. These systems are also very expensive, costing approximately £2 million. The absolute spatial resolution of the system is limited by the signal to noise ratio, because increasing the resolution by increasing the magnetic field gradients and reducing the bandwidth of the radio frequency pulse decreases the signal-to-noise ratio of the images [29]. It is possible to produce a system with a spatial resolution of 4 µm, however commercially available systems tend to only have a spatial resolution around 50 µm [30].

2.2.3 Far-Infrared Laser Inspection

Visual inspection is a simple tool that can be used to inspect the outer surface of a joint for defects. The process can also be automated by detecting the light reflected from the surface of the joint, converting it into a digital signal and then processing the signal using standard image processing techniques [31]. With this process it is only possible to inspect the application of the joint insulation and screen tapes as they are applied, because the carbon filled screens and insulation tapes are opaque and block deeper inspection. Visual methods are therefore normally restricted to in-process inspection of the joint manufacture.

The depth of view can be increased using far-infrared (FIR) lasers. The process is similar to visual inspection, however instead of a conventional light source being used to illuminate the joint, a laser with a wavelength in the order of 120 μm can be used [6, 32]. FIR lasers can penetrate further into a material because of their longer wavelength, however

they cannot be detected using standard visual detectors, instead low temperature germanium photodetectors are used. To inspect a cable joint the FIR beam is directed into the cable joint. If no defects are present, the laser beam penetrates the insulation without scattering. The presence of a defect, however, can scatter the beam. If, therefore, the photodetector detects a scattered laser beam, it can be assumed that the section of cable joint that the beam is focused on contains defects. The size and location of the defect can be estimated by the amount of scatter of the beam. If there is little scattering of the beam, i.e. the main signal collected by the photodetector is unscattered, then the defect is presumed to be small in diameter; a larger defect scattering more of the laser beam. The spread of the scatter, i.e. the distance of the scatter away from the center of initial beam indicates the location of the defect. The greater the deflection away from the center of the main beam the closer the defect is to the front side of the cable. If the beam is scanned along the length of the cable, and fully around the cable then the size and location of defects can be ascertained [33]. A 3D image of the cable's insulation and defect content can then be generated from this data.

The resolution of the system is determined by the wavelength of the laser. The minimum definable feature is therefore equal to the wavelength of the laser. This means that the smallest resolvable defect with this inspection method is 120 μm. At present the maximum power level of this type of FIR laser is 300 mW, which gives the laser enough penetration power to inspect insulation thicknesses up to 50 mm [33]. The laser however cannot penetrate the carbon filled screens or the central conductor. This means that no information about the screens or the central conductor can be collected. It also means that inspection can only occur before the outer insulation screen is applied. In effect this method of inspection can only provide defect information contained within the joint insulation, and no information about the dimensions and geometry of the cable joint. Other problems associated with this technique are high levels of noise, which are produced due to surface roughness. If the surface of the insulation is not smooth it can cause scattering of the laser beam, which can significantly affect the detection rate of defects within the insulation. This type of system is better suited to online inspection of the extrusion of the insulation [34, 35].

2.2.4 Radiography

X-rays are short wavelength electromagnetic radiation, with wavelengths in the region of 10^{-13} - 10^{-9} m. They display the same properties that are common to all types of electromagnetic waves, including, travelling in straight lines and the potential capability of being polarised. X-rays are also able to penetrate the majority of materials, and the refractive indices of all materials are very close to unity for x-rays, so very little bending occurs when they pass from one material to another. The penetration power of x-rays depends on the density of the material being irradiated and the energy of the wave. Dense materials are able to absorb more radiation than less dense materials, i.e. dense materials have a greater stopping power, which means they tend to be opaque in terms of x-ray radiation [22, 36]. This material specific radiological density means that x-rays can be used to image the internal structure of composite material.

X-rays can be produced when high energy electrons are decelerated, or by the transition of electrons in the inner orbits of atoms. This can be achieved by accelerating a focused beam of electrons into a dense metallic target, such as tungsten, copper or molybdenum. When the electrons hit this target they tend to impact on the nuclei of the metallic target causing the electrons to be rapidly decelerated, some electrons can even cause the displacement of the high energy inner orbital electrons of the metallic atoms of the target. Both of these processes cause energy to be released by the electrons. Almost all of the energy released is in the form of heat energy, however approximately 1% is released as x-ray radiation [37].

In most modern x-ray sources the high energy electrons are supplied by thermionic emission in a heated cathodic filament. The amount of electrons emitted from the cathode is determined by the filament temperature: the filament temperature is controlled by varying a current through the filament. The electrons emitted from the cathode are then accelerated towards a heavy anodic metal target by a high potential difference set up between the cathode and the anodic target. The magnitude of the potential difference between the cathode and the anode determines the extent to which the electrons are accelerated. The high voltage supply can either be an ac or dc supply, however, electrons are only emitted from the cathode when the anode is positive in relation to the cathode. In an ac supply, therefore x-rays are only generated during the positive half cycle, in a

dc supply, x-rays are continually emitted [38]. The general system arrangement is shown in Figure 2.7.

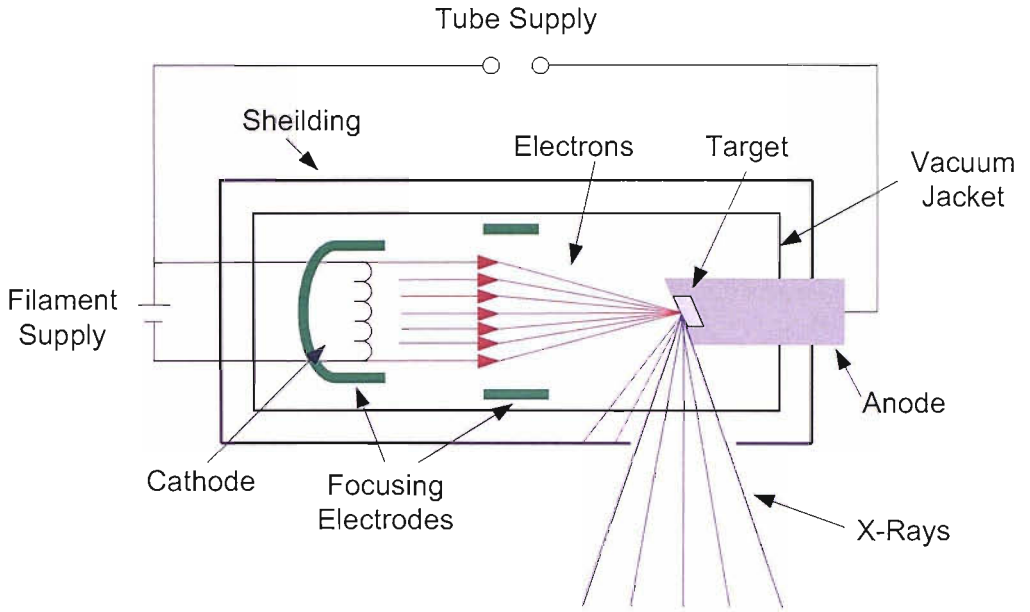

FIGURE 2.7: Schematic diagram of an x-ray source.

It is, therefore, possible, with a source that has independent control of the filament current and the tube voltage, to control the number of electrons produced and the speed with which they they impact the target. By increasing the number of electrons produced, the number of electrons that are decelerated by the target is increased. This means that the number of sites where x-rays are produced is increased, hence, by increasing the filament current, the flux density of x-ray beam produced is increased. By increasing the speed at which these electrons impact with the target, the amount of energy released when the electrons are decelerated is increased. This has the effect of increasing the energy of the x-rays produced, and by increasing the energy of the x-rays, the penetration power of the x-rays is increased. With a source that has independent control of the filament current and tube voltage it is, therefore, possible to control the flux density of the x-ray beam produced and penetration power of this beam. The flux density of the x-rays determines exposure time required to image the test object, because if more x-rays are passing through the test piece in a given time period, then the integration time required to generate an image is reduced. The penetration power of the x-rays determines which materials can be imaged. A source that can produce x-rays with a greater the penetration power will be able to image more radiologically dense materials or thicker sections of less radiologically dense materials. The ability to control the tube

voltage and filament current, makes it possible to irradiate a test object in order to image its internal structure.

X-rays can be detected by a range of techniques, but the conventional method uses photographic film. Most x-ray specific photographic film plates consists of a tri-acetate or polyester film base which is coated with an emulsion consisting of gelatine and silver halide crystals, such as silver bromide and silver chloride. Due to the very low solubility of silver halides, the photographic emulsion is not a true emulsion; it is a dispersion of silver halide lattice crystals. When x-rays strike a silver halide crystal, energy is released which frees an electron from the bromide ion. The bromide ion is then released from the lattice of the crystal as bromine and is absorbed by the gelatine. The free electron is then attracted to the positive silver ions, which are neutralised to form silver atoms. If enough silver atoms form at a single point then a latent image is created. The amount of silver halide grains being reduced to silver is proportional to the exposure time and the intensity of the radiation [39, 40].

The latent image is then developed using chemical agents that supply electrons to the latent image, thus attracting and neutralising more silver ions in order to produce a visible image. A fixer is then used that converts any unexposed silver halide to soluble salts. These salts can then be washed out of the emulsion before allowing the plate to dry [36, 41]. The result is an x-ray negative of the internal structure of the cable joint. A schematic diagram of the process is shown in Figure 2.8.

The quality of the image produced is governed by the silver halide molecules in the emulsion. The smaller the silver halide grains the finer the image produced, however the exposure time increases because there are more silver halide grain to reduce. The larger the silver halide grains are the coarser the image, however the exposure demands are

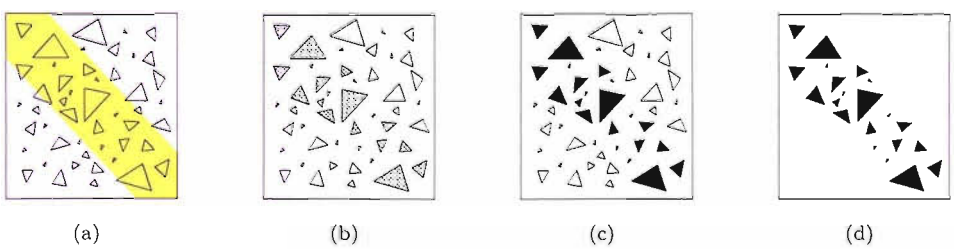

FIGURE 2.8: X-ray photographic plate theory: (a) exposure: light incidence shown as a yellow strip, (b) development: developed crystals shown as shaded triangles, (c) fixing: fixed crystals shown as black triangles, and (d) washing: non-fixed crystals removed.

less. With the correct choice of film, it is therefore possible to produce a fine resolution negative image of the internal structure of cable joint.

2.3 Evidence to Support the use of X-rays in the NDT Cable Joint Inspection

All of the four NDT techniques described above can be used to inspect cable joints. The two functions that the inspection procedure must be able to perform is dimensional checks and to be able to evaluate the size and number of defects. Ultrasound, NMR and radiological inspection can all perform full dimensional checks, however, FIR methods can only perform dimensional checks on the insulation and not semiconducting screens, therefore this methods is not suitable for complete joint inspection. NMR imaging of cables can produce high contrast, high resolution images that can used for both dimensional checks and defect detection, however these systems are not portable and have excessive cost. This type of system therefore does not present a cost effective method of cable joint inspection. The two remaining viable systems are therefore ultrasonic and radiological imaging. Both of these methods of inspection are accepted by the cable industry as suitable methods of NDT inspection, the main difference between the two systems, however, is the level of resolution that can be achieved by each system and the safety aspect of each system. As mentioned above ultrasound is able to resolve voids and defects as small as 0.5 mm to 1 mm in XLPE up to a depth of 15 mm [23]. X-ray radiology however can penetrate insulation thicknesses in excess of 100 mm and voids in the region of 200 µm can be resolved. There are, however, health and safety issues relating to human exposure to x-rays. Adverse health effects range from mild effects, such as skin reddening due to radiation poisoning, to serious effects, such as cancer and ultimately death. These adverse health effects are determined by the amount of radiation absorbed by the body, the route of exposure, and the length of time a person is exposed. The radiation exposure is cumulative and consequences of exposure may not be seen for many years. For this reason it is necessary to implement safety precautions and procedures to ensure that no individual is exposed to significant amounts of radiation. For this reason the x-rays generated by the x-ray source have to be contained within a predetermined volume. This can be achieved using two methods. The first method uses the fact that the x-ray flux decreases following an inverse square law. This means that if

a wide restriction area is imposed around the x-ray source while x-rays are being generated the risk of dangerous exposure is minimized. The second method of confinement is to manufacture an irradiation chamber to ensure that the x-rays are contained within a smaller volume. The material used to construct this irradiation chamber must therefore have a high x-ray stopping power. The most appropriate material for this application is lead. The thickness of lead sheeting required to absorb all the x-rays produced is determined by the penetration power of the x-ray source, i.e. available tube voltage. The greater the penetration power of the x-rays produced, the greater the thickness of the lead required. With these precautions it is therefore possible to minimize the health and safety risks. There are however no related health and safety issues relating to the use of ultrasound, ultrasound systems are generally less expensive compared to x-ray systems, and are also generally more portable. Despite the disadvantages due to the the health and safety issue relating to the use of x-rays, however, the increased spatial resolution makes radiological imaging the chosen NDT technique for this work.

2.4 Current Inspection Procedure

Currently the Tony Davies High Voltage Laboratory has the facilities to NDT cable joints utilising conventional x-ray and photographic film technologies. This process is approved by the cable industry and is used for quality assurance of joints. The inspection takes place on site, where the cable joint is manufactured, which can be either in the factory or on a cable laying ship. The process uses a Kevex E5014S-MF high stability x-ray tube to 'back light' the cable joint. The attenuated flux is then detected using a AGFA Structurix D7 photographic film plate. The general system arrangement is shown in Figure 2.9. This plate is then fixed and developed in a dark room to produce an x-ray plate negative. Finally, the plate is then inspected by trained operatives. This inspection consists of scanning the plate by eye using a x10 magnifier. The joint is then either passed or failed depending on the type and number of defects found.

With this system, it is possible to produce clear images of the cable conductor, conductor screen, insulation, and insulation screen and identify inclusions in the insulation as small as 50 μm and voids as small as 200 μm. The health and safety aspects relating to the use of x-rays have been addressed by the use of interlocked 3 mm thick lead

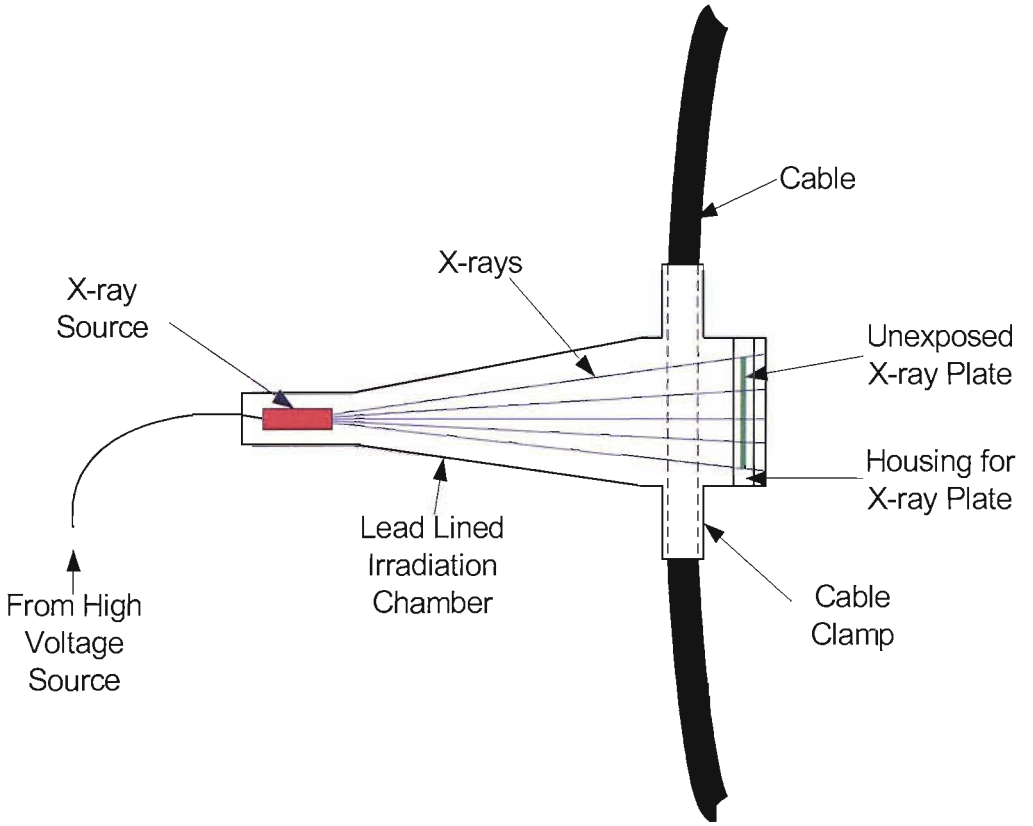

FIGURE 2.9: Current inspection system setup.

screening. This level of screen ensures that the inspection system complies with recommendations detailed in [42]. The inspection process, however, is labour intensive time consuming, requires a dark room for processing, uses specialist knowledge, produces significant chemical waste, can be subject to interpretation and other human errors, is inflexible, and it is difficult to catalogue the inspection results.

For example, the inspection time, using the current procedure, to inspect a 90 kV XLPE cable joint takes approximately two and a half hours. This type of cable has a nominal total diameter of 55 mm, a nominal conductor diameter of 21 mm, and an insulation thickness of 15 mm with a total joint length of 450 mm. To image all of this cable joint requires 12 different exposures. 12 exposures are required because:

- The length of the joint is longer than 296 mm, (the length of a photographic plate) and so each joint has to be inspected in two halves, left and right
- The central conductor of the cable is opaque and so masks the central section of the cable's insulation. To overcome this problem, the joint is inspected at three

angles, 0°, 60°, and 120°. By inspecting the joint at these three angles, the majority of the joint's insulation can be irradiated and inspected without the x-rays being occluded by the central conductor.

- Cables are cylindrical, therefore by inspecting the cable from the side the amount of insulation interacting with the x-rays at the top and bottom of the cable is less than the amount in the centre of the cable. This means that the amount of radiation required to penetrate the insulation screen is less than the radiation required to penetrate the conductor screen, i.e. the radiation required to penetrate the conductor screen would overexpose the photographic plate in the region storing information about the insulation screen, therefore any information about the insulation screen is lost. This means that each exposure angle requires two exposures, one to inspect the conductor screen, and one to inspect the insulation screen.

The conductor screen exposure requires a tube voltage of 45 kV and a tube current of 0.7 mA, with an exposure time of approximately five minutes, where as the insulation screen only requires 30 kV and 0.7 mA for two minutes. The total time of exposure is therefore approximately 42 minutes. It is possible to fit two exposures per plate, however this still requires that 6 plates are developed. Each plate can take up to ten minutes to be developed and dried ready for inspection. This means that up to an hour is required for developing the plates for one joint. The final process of inspection requires each plate to be scrutinised by two trained inspectors. This process can take up to 30 minutes per plate depending on the defects found in the joint. With the additional time factors due to setting each exposure and the logistics of the whole process, each joint can therefore take up to four and half hours to inspect.

In addition to these time demands the production of the x-ray negative requires that a dark room is set up where all light is excluded. This adds to the time required to inspect a joint and reduces the number of places where the inspection can be performed. The dark room is required for developing and fixing the photographic plate because any stray light absorbed by the film's silver halide during processing will compromise the image produced. The process of fixing and developing the photographic plates in this dark room also requires a skilled technician and specialist developing equipment. After the plates have been fixed, the developing and fixing agents are not recyclable, so once used

become chemical waste. Prolonged exposure to these chemicals can also cause breathing and skin problems [43].

The inspection of the developed plate also requires trained operatives to examine the image. This part of the process can introduce interpretation errors and other human errors related to manual inspection, such as fatigue. Once a plate has been inspected, any defects detected are logged and the plate is then stored. It is difficult to store this data because only hard copies of the x-ray plate are available, and so these have to be catalogued and then stored in a protective sleeve.

2.5 Improving the process

The current inspection process can inspect high voltage cable joints. The accuracy, repeatability, resolution, ease of use, and flexibility of the system however can be enhanced by improving the type of x-ray source and sensor used to produce the NDT image of the joint and the method of inspection.

2.5.1 X-ray Source Type

To produce clear images it is desirable to generate either parallel or radial x-ray rays. Parallel rays will produce an image with no penumbral regions and no magnification of the test object's image, however radial x-rays, from a point source, will also produce images with clear edges and this type of beam can be used to magnify the test object's image, see Figure 2.10. The type of beam, radial or parallel, is determined by the focal spot of the x-ray source.

The focal spot is the cross-sectional area of the target where the majority the electrons impact the target. The electrons emitted from the cathode do not naturally produce an electron beam focused on the target, because the electrons leave the cathode in every direction. The electric field set up between the cathode and the anode does accelerate the electrons in the general direction of the target but it does not focus the electron beam onto the target. To focus the electrons onto the target, electrodes are positioned near the cathode. The amount of focussing is determined by the shape, size, relative

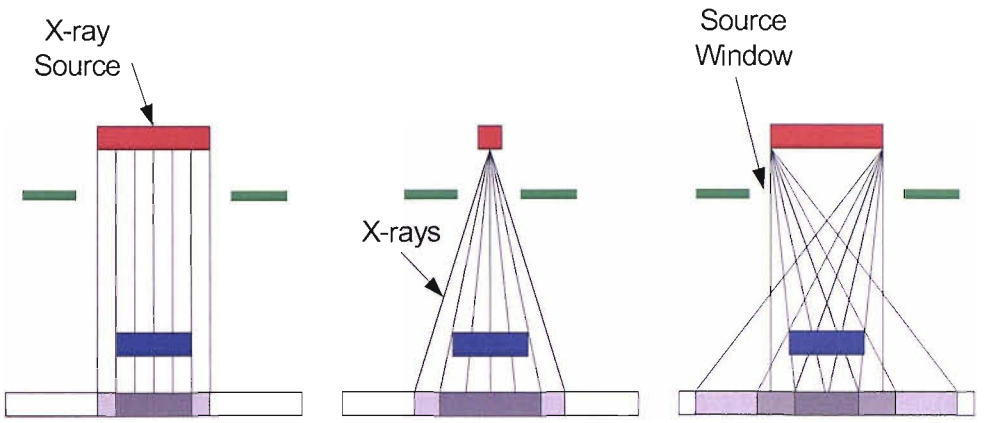

FIGURE 2.10: Diagram of the effects on image clarity due to the type of x-ray beam produced: (a) parallel rays no penumbral regions no magnification, (b) radial rays no penumbral regions but magnification, and (c) nature of the rays found in most sources.

potential and relative positions of these electrodes in relation to the cathode and the anode.

The size of the focal spot generated determines how the x-ray source can be used. X-rays are only produced at the locations of the interactions between the electrons and the target. To produce a parallel beam of rays a large focal spot size is required located at an infinite distance away from the test object. To create a radial source would require a focal spot size with an infinitely small cross-sectional area. In reality, it is impossible to produce either configuration. This means that the nature of the beam produced is somewhere in between these two extremes.

It is possible to improve the image quality of a source by either tending to produce parallel or radial rays. To produce a pseudo-parallel source the test object is placed at a significant distance from the source, where the rays tend towards being parallel. By reducing the size of the focal spot, a pseudo-radial x-ray source is produced (Figure 2.11). Due to the geometry of the sources, however, pseudo radial sources produce a beam that is a closer approximation to a radial beam than the approximation made by a pseudo parallel source of a parallel beam. X-ray sources that can be used in a pseudo-parallel setup are called high stability tubes or macrofocus tubes. These tubes have a focal spot size greater than 50 µm in diameter. X-ray sources that are used in a pseudo-radial setup are called microfocus sources. These tubes have a focal spot size less than 50 µm in diameter [44–46].

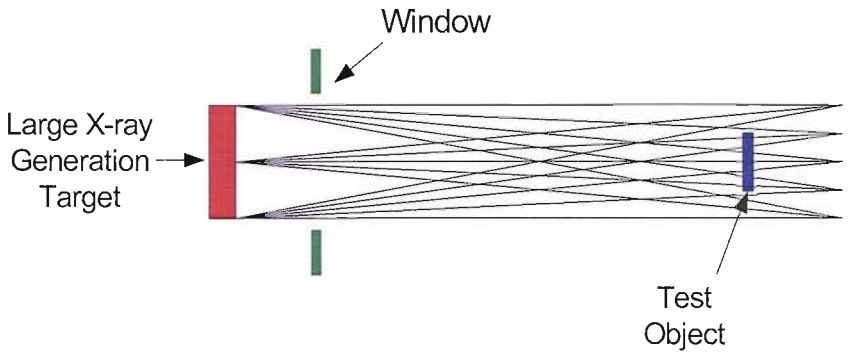

(a)

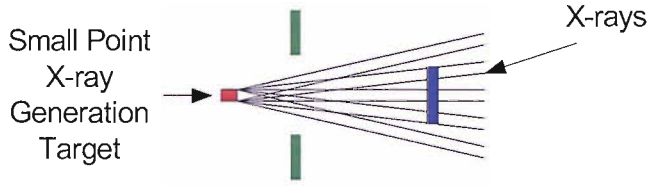

(b)

FIGURE 2.11: Source geometry: (a) Pseudo parallel beam created by placing the test object a significant distance from the source where the x-rays tend to be less radial and more parallel, and (b) Pseudo radial beam created by reducing the size of the focal spot.

The current x-ray source is a high stability tube used in the pseudo-parallel setup. This means that the images produced by this system tend to have less defined edges due to the penumbral nature of the source; this reduces the resolution of the system. This can be improved by changing to a microfocus source used in the pseudo-radial arrangement.

2.5.2 X-ray Imaging Sensor

Most of the problems associated with the photographic plate method described in Section 2.4 can be removed or reduced if the plate is replaced with a digital sensor [47]. With a digital sensor, it is possible to automate the capture and processing of the x-ray inspection information, which reduces the required skill base, production of waste and the possibility of human error. There are two groups of technologies concerned with digital capture of x-ray images, indirect and direct capture [48, 49].

2.5.2.1 Indirect Digital Capture

Indirect capture has intermediate steps between x-ray generation and the digital image acquisition. The intermediate steps are generally the conversion of x-rays into light and then light into a digital signal [48, 49]. The three indirect methods are screen/film systems, storage phosphor/computed radiography, and scintillating screens with CCD arrays.

Screen film systems. X-rays possess most of the characteristics of visible light. This includes the ability to reduce photographic film. The process is similar to black and white photography. Photographic film consists of silver halide grains in gelatine. When the silver halide is exposed to radiation, it is reduced to metallic silver. The duration and intensity of the irradiation determines the percentage of the silver halide molecules that are reduced to metallic silver. This feature of photographic film is used to produce a negative image plate of the object being irradiated.

To convert an x-ray plate into a digital format a film digitiser is used. Film digitisers function in a similar way to paper-based scanners, except the light source is used in transmission rather than reflection, i.e. the sensor detects light that passes through the plate and does not detect the light that is absorbed or reflected by the plate. The general set up for a digitiser is a light source and a sensor separated by the film plate. The light is directed at the film plate. The density of reduced silver halide on the plate determines the amount of light that passes through the plate. The transmitted light is then converted into an electrical signal [50, 51].

Storage phosphor systems/computed radiography. Storage phosphor or computed radiography systems use a rare earth phosphor screen that stores a latent image by trapping electrons when irradiated with x-rays. Irradiation causes electrons in the storage phosphor to become excited. The extra energy that these electrons hold forms the image. This image can be read by scanning the screen with a laser. If the excited electrons are stimulated with an appropriate wavelength laser, the electrons release the extra stored energy in the form of visible light. This light is then detected with a photomultiplier tube, and an image produced [52, 53].

Scintillating screens and CCD arrays. There are a range of crystals that fluoresce when irradiated with x-rays. These crystals can, therefore, be used to produce scintillating screens that convert x-rays into light. There are many different commercially available screens, all with different properties. The most appropriate screen is dependent on the application, however for x-ray imaging gadolinium oxysulphide or caesium iodide crystals are generally used. A CCD camera can then convert light produced into a digital image. To ensure that the light is converted efficiently the CCD camera used has to be tuned to detect the fluorescence produced the screen. The combination of an appropriate screen and a tuned CCD camera can therefore be used to convert x-rays into a digital image [49, 54, 55].

2.5.2.2 Direct Digital Capture

Direct conversion detectors reduce the number of stages required to produce an image to one single process [56, 57]. The reduced number of stages generally helps to produce a higher intrinsic spatial resolution and sharper images because there is less opportunity to introduce noise [58, 59]. The three direct methods are flat panel direct detector arrays, hybrid solid state semiconductor detectors, and gas detectors [50]

Flat panel direct detector arrays. This modality uses the organic compounds of silicon, germanium, or selenium as the sensor and a matrix of amorphous silicon thin film transistors as the readout electronics. Under a bias voltage, applied across the detector structure, incident x-rays directly generate electron hole pairs in the organic compound layer. These charges can be guided to the surface of this layer and are collected by individual storage capacitors associated with each detector element for readout by customized electronics within the array. The signals produced can then be converted to a digital image [48, 49, 60, 61].

Hybrid solid-state semiconductor detectors. A second method of direct capture that is currently emerging uses the non-organic compounds of cadmium telluride (CT) or cadmium zinc telluride (CZT). The theory behind these detectors is similar to that of flat panel devices. The sensor converts the x-rays directly into electrical charge, which

is then collected using readout electronics to produce an image. The benefits of using CZT/CT are that CZT/CT have:

- higher attenuation coefficients than organic compounds and so they stop the majority of x-rays, negating the need for protection of the associated electronics
- improved linearity, providing fast, easy to interpret images
- high stability which allows the detector to work at room temperature with good signal to noise characteristics [49, 56, 57, 62].

Gas detectors. Gas proportional detectors consist of a small diameter anode wire enclosed in a gas volume. These detectors are used to count single photon events. When the x-rays interact with the gas, a small proportion of the gas atoms are ionised. The electrons evolved are attracted to the positive anode wire. As these electrons approach the anode wire, they are accelerated by a high electric field set-up between the anode and the cathode, producing a cascade of electrons that result in a relatively large electrical pulse. This pulse is then amplified by a low noise preamplifier to produce a usable signal [63]. This is the simplest form of a gas detector. It is limited, however to producing single point location x-ray flux intensities, and therefore can only generate a one-dimensional signal. The commonest form of this type of detector is the Geiger Muller counter [64].

To overcome the one dimensional limitations of gas proportional detectors, multiwire and microstrip proportional chambers have been developed. These detectors are position sensitive and can produce two dimensional signals. Multiwire chambers use a grid of fine wires spaced approximately 2 mm apart as the anode plane in a gas proportional chamber. Microstrip detectors use the photolithographic process to etch ultra fine conducting strips into an insulating or partially insulating glass substrate to produce the anode plane. The strips are etched onto the glass in an anode-cathode pattern [65]. The spatial resolution can be as good as 30 μm. Recently, gas electron multiplying detectors have been developed that have improved spatial resolution and lower operating voltages [66–68].

2.5.2.3 Comparison of X-ray Imaging Systems

All of the six technologies outlined above could be implemented in a digital cable inspection system, however the suitability of each modality varies considerably. The main disadvantage of using a screen film system is that two conversions are required. The first conversion from x-rays to a photographic plate does not introduce significant noise, however it is slow and time consuming [40]. The second process, digitising the film, is quicker but can introduce noise due to the scattering of light between the light source and the detector, which can reduce the probability of detecting defects [50]. A further disadvantage with this type of system is the need for a bespoke system because commercially available film digitisers are designed for the medical market where the requirement for a spatial resolution is less stringent. This system would also still suffer from the disadvantages outlined in section 2.4.

Storage phosphor systems would decrease exposure and development times, remove the need for a dark room, and reduce the amount of chemical waste. The commercially available systems, however, are designed for medical applications and so only have maximum spatial resolutions of 100 µm, which is inadequate for this application and considering the cost of the upgrade to a storage phosphor system is approximately £80 000, this system does not present a cost effective improvement.

CCDs and scintillating screens can have very high spatial resolutions (as small as 5 µm), are completely portable, are relatively cheap, and there are systems designed specifically for NDT. Another benefit of using this system is that it uses established techniques that industry accepts as a good alternative to film [61, 69, 70]. The disadvantage of using this type of system is that the conversion of x-rays into light can introduce noise because of lateral spread of light in the scintillating screen, however this is becoming less of an issue with the production of thinner scintillating screens and the development of microcolumnar screens [71].

The images produced by flat panel direct detector arrays are very sharp and have high contrast, producing very clear images [49, 50]. Once again, the market for which they are intended is the medical market, and so the maximum spatial resolution is 50 µm. The organic flat panel direct detector arrays also would not withstand the environment of a portable system because of the potential damage caused by vibration, and they also currently cost more than £100 000 [58, 59]. Even though they can produce good

quality images, the price and fragility of these systems makes them unsuitable for this application.

Hybrid solid-state devices are cheaper than flat panel direct detectors at around £50 000 for a small detector array measuring 5 x 5 mm. The pixel size, however of the detectors is typically 50 µm, which would not be fine enough for this application. Another disadvantage of this system is the size of the field of view, typically only 240 x 240 pixels (12 mm x 12 mm), which would make imaging a relatively large joint a time consuming process because the detector would have to scan many times along the joint [49, 56, 57, 62].

Gas detectors are a developing technology. The spatial resolution of this type of sensor can be as little as 5 μm [49, 63–65]. At present, however, there are no commercially available systems therefore there is limited information available relating to this approach.

In conclusion the resolution of storage phosphor systems, flat panel direct detector arrays, and hybrid solid state devices are too coarse for stringent inspection. Storage phosphor systems, flat panel direct detector arrays and hybrid solid-state devices are considerably more expensive compared with the other available systems. No gas detector systems are commercially available. Screen film systems still suffer from the problems associated with film processing and would require a bespoke scanner with a high spatial resolution. Of the above systems, therefore, only scintillating screens and CCD arrays provide a functional, cost effective, and viable method of digitising the inspection process. Replacing the current film detection method with a scintillating screen and CCD array will therefore reduce the labour intensity of the process, remove the need for a dark room, reduce the amount of chemical waste, and improve the flexibility of the system, especially the cataloguing of the inspection results.

2.5.3 Inspection Procedure

The current inspection procedure uses manual inspection to detect defect in the photographic plate. This requires specialist operator skills and can be subject to interpretation errors, such as fatigue. The process is also not completely repeatable. With the conversion to a scintillating screen and CCD array, the image produced can still be inspected in the same manner as a photographic plate, however because the image is digital it can also be examined using a range of digital image processing techniques. This then

removes the need for specialist operator skill, any human interpretation error and ideally makes the process 100% repeatable.

2.6 Summary

Factory tests are required to evaluate the quality of each production length of cable. The tests used however are not all applicable to joint inspection. To perform dimensional and defect investigation on a cable joint ultrasound, NMR imaging, FIR laser inspection, and radiography can be used. Despite the health and safety issues relating to the use of x-ray, this technology provides the most appropriate method of joint inspection. The University of Southampton currently has an inspection facility that uses x-rays to image cable joints. This facility uses photographic plates to generate the x-ray image. There are, however, improvements that can be made to the current system. A microfocus source could be implemented to improve the image quality. The problems associated with the use of photographic plates including production, inspection and storage of the plate can be removed or reduced by converting the inspection procedure into a digital process. The most suitable digital detector available for cable inspection is a scintillating screen coupled to a CCD array. The inspection procedure can also be improved by converting from the current manual system to a digital image processing system. The following chapters describe the implementation and assessment of these changes.

Chapter 3

The Development of the Cable Joint X-ray Inspection Facility

In order to implement a high voltage cable joint inspection system using x-rays, a source is required that can produce high energy rays capable of penetrating the cable joint. The source also has to produce sufficient flux in order to image the joint over a reasonable time period. The attenuated x-rays then have to be detected and converted into an image. During the irradiation period the source, detector and the cable joint cannot be allowed to move in relation to each other, i.e. the geometry of the source, cable joint and sensor must be fixed, otherwise the resulting image will be blurred. The system must also allow full inspection of the cable joint. This means the system must be able to index along the cable joint in order to inspect the full length of the joint, and also be able to take images of the joint from a range of angles so that all the insulation can be irradiated without being obscured by the central conductor. Due to the health and safety risks related to the use of x-rays, this process has to be undertaken such that there is no risk of irradiating any personnel. For these reasons the hardware related to x-ray inspection can be divided into four groups, the x-ray source, the imaging detector, the irradiation chamber, and positional hardware.

3.1 X-ray Source Hardware

The main requirement of the x-ray source is to produce a good quality, reproducible x-ray image of the whole length of the cable joint within a reasonable time scale. The following sections describe the theory behind these requirements.

3.1.1 Image Production

In order to produce a good quality image of the internal structure of a cable joint, an x-ray source is required that can generate x-ray beams that have sufficient penetration power to irradiate the cable joint. To generate this beam, the filament must be heated in order to thermionically emit electrons. These electrons then have to be accelerated towards the target using a high voltage source (as shown previously in Figure 2.7). The filament and target have to be housed in a vacuum in order to allow the electrons to be accelerated unhindered towards the target. Without this vacuum the electrons would simply collide with the atoms of any gas present and would therefore be scattered. The acceleration of the electrons is determined by the potential difference between the filament and the target. By increasing the potential difference between the filament and the target, the electrons impact onto the target with greater speed. This means that the impact releases more energy. This has two effects, firstly more heat is generated, moreover the energy of the x-ray beam produced is increased, and as a consequence the penetration power of the x-ray beam is increased. X-ray beams produced by a source with a higher tube voltage will, therefore, have a greater penetration capability than an x-ray beam produced with a lower tube voltage. X-ray sources with higher maximum tube voltage can therefore image a wider range of cable joint types and diameters, compared to an x-ray source with a lower maximum tube voltage.

The timescale in which this image is produced, however, is related to amount of x-ray beams, or flux, that can be produced to irradiate the cable joint. The greater the flux density through the cable joint, the shorter the exposure time becomes. The flux density through the cable joint is determined by the amount of flux the source can produce and the percentage of this flux that is directed towards the cable joint. The amount of flux the source can produce is determined by the amount of electrons generated at the cathode, the ability to focus these electrons onto the target, and the capacity to dissipate

the heat generated by these electrons colliding with the target. In general, a source with a small focal spot size will be able produce less flux than a source with a large focal spot size. This is because it is difficult to focus large amounts of electrons on to a small focal spot due to the negative charges repelling each other. The focal spot size also determines the ease with which the heat, generated during the production of x-ray, is removed from the target. With a small focal spot size, all the heat produced by the impact of the electrons is generated in a very small area of the target. This makes it difficult to efficiently remove this heat, which also limits the amount of x-ray flux that can be produced. This means that macrofocus x-ray tubes can generally produce more x-ray flux compared with a microfocus source. The amount of flux passing through the cable joint, however, is also determined by the relative geometry of the source and the cable joint. Macrofocus tubes are generally used in a pseudo-parallel configuration. This means that the x-ray tube and cable joint have to be positioned at a significant distance apart, which means that the amount of flux that actually passes through the cable joint is reduced because x-ray flux decreases following the inverse square law. With a microfocus tube, however, the cable joint and x-ray source can be positioned closer together, which means that more of the x-ray flux produced will pass through the cable joint. In general, however, to image a cable with relatively similar exposure times, macrofocus x-ray tubes have a higher filament current than microfocus x-ray tubes.

To irradiate the whole length of the cable joint, the x-ray source must produce a beam with a sufficiently large field of view. The field of view of the x-ray beam is determined by the shape of the x-ray flux. To prevent stray radiation leaving an x-ray source, it is generally shielded with lead. A window in this shielding however is required to allow the useful x-rays to leave the source. The relative location of this window to the target, and the focal spot size of the target determines the shape of the x-ray flux generated. This characteristic of the x-ray beam is called the x-ray cone, and it is measured in terms of the angle of the cone (Figure 3.1). A sources with larger x-ray cone angle will, therefore have larger field of view. The contrast of the image however is improved with a narrow flux as a narrower beam will contain less scatter. The contrast of the image is defined in Section 3.1.2.2. For this reason the x-ray source should have a cone angle that is large enough to produce a good field of view, but not too large as to impair the image contrast.

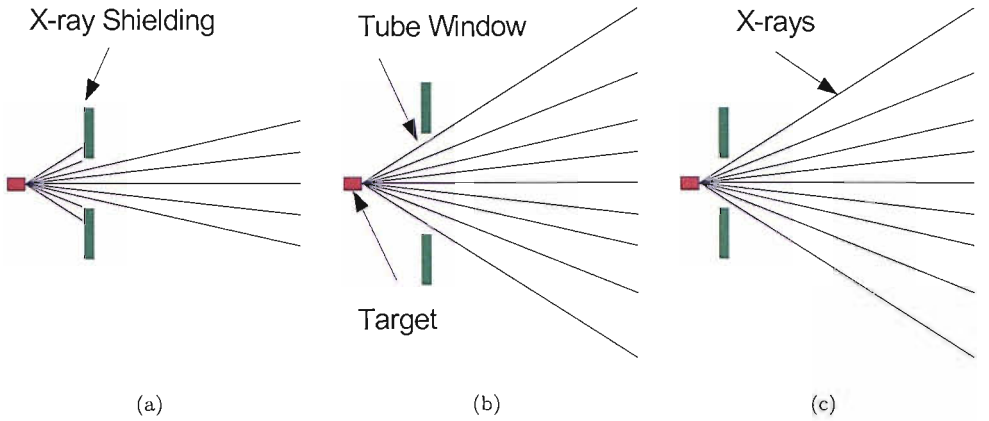

FIGURE 3.1: The effect on the x-ray cone angle of the target and tube window geometries: (a) Small window further from the target, (b) Larger window further from the target, and (c) Small window closer to the target.

3.1.2 Image Quality

The factors that affect the image quality produced by the source are definition and contrast. The definition refers to sharpness of the image, and is determined by the irradiation geometry, the focal spot size of the source and the radiographic energy produced. Contrast is the density difference between areas of the image, and is also dependent on radiographic energy and the amount of radiation scatter in the x-ray beam [72].

3.1.2.1 Image Definition

The definition of the image is improved by ensuring that the irradiation geometry is appropriate for the focal spot size of the source and that the radiographic energy bandwidth of x-ray beams produced is small. The irradiation geometry refers to how the x-ray beam is utilised, i.e. a pseudo-parallel or pseudo-radial geometry. To produce an image with good sharpness, either a parallel or radial x-ray source is desirable, however, as mentioned in Section 2.5.1, it is impossible to produce a purely parallel or purely radial source due to the nature of the production of x-rays. For this reason either a pseudo-parallel or pseudo-radial configuration is used. In general the x-ray sources with a large focal spot size are used in the pseudo-parallel setup, while x-ray sources with small focal spot sizes are used in the pseudo-radial setup. The main problem, however, with using a macrofocus source in the pseudo-parallel setup is that the beam quality, i.e. the approximation to a parallel beam, improves as the distance from the source increases.

This means that the best possible image would be produced by placing the cable joint and x-ray source at a considerable distance apart. With this arrangement, however, the amount of x-ray flux that would pass through the cable joint would be reduced, and so the exposure time would be very long. This means that the pseudo-parallel geometry is a compromise between image quality and exposure time, which means that the image quality is compromised. With the advances in the reduction of the focal spot sizes of microfocus sources, however, a good approximation to a radial source can be made [73]. This means that using a microfocus source in a pseudo-radial geometry, the cable joint can be placed significantly closer to the x-ray source without compromising image quality. A microfocus source will therefore produce a better quality image compared with a macrofocus source [72].

The second factor that affects image sharpness is the radiographic energy of the x-rays used to irradiate the cable joint. Ideally the source should produce x-rays with the same penetration power. In reality however the x-ray beam produced contains a range of x-ray energies due to the stochastic nature of the electron excitation in the x-ray tube. This means that the cable joint is irradiated with a nonuniform beam, which reduces the sharpness of the image. To improve the image sharpness, high pass filters can be added to remove the lower energy x-rays. These filters are generally beryllium or aluminium plates that are placed close to the tube target in order to absorb any low energy x-rays, while allowing the higher energy rays to pass through.

3.1.2.2 Image Contrast

The better the contrast of the image the easier it becomes to discern material interfaces and defects within the cable joint. The contrast of the image is determined by the radiographic energy and radiation scatter of the x-ray beam. The range of radiographic energy produced reduces contrast in the same manner that it reduces sharpness, therefore the use of low pass filters also improves the contrast of the image as well as its sharpness. Radiation scatter is produced when x-rays reflect off a surface. Ideally all the x-rays used to image the cable joint should travel in a straight line from the source to the cable joint, in either a parallel or radial manner, to produce an image without penumbral regions. The x-rays produced, leave the target at any angle, however, only the x-rays travelling in the direction of the test object are useful. If the 'non-useful' x-rays are

allowed to scatter they will, therefore, not be travelling in a parallel or radial manner and so introduce noise into the image, reducing the contrast of the image (Figure 3.2). To reduce the amount of scatter the source can be shielded with lead to absorb, rather than reflect, any stray x-rays, however a window is required in this shielding to allow the useful x-rays to leave the tube. This window in the shielding is normally made of beryllium or aluminium in order to implement the high pass filter described in Section 3.1.2.1.

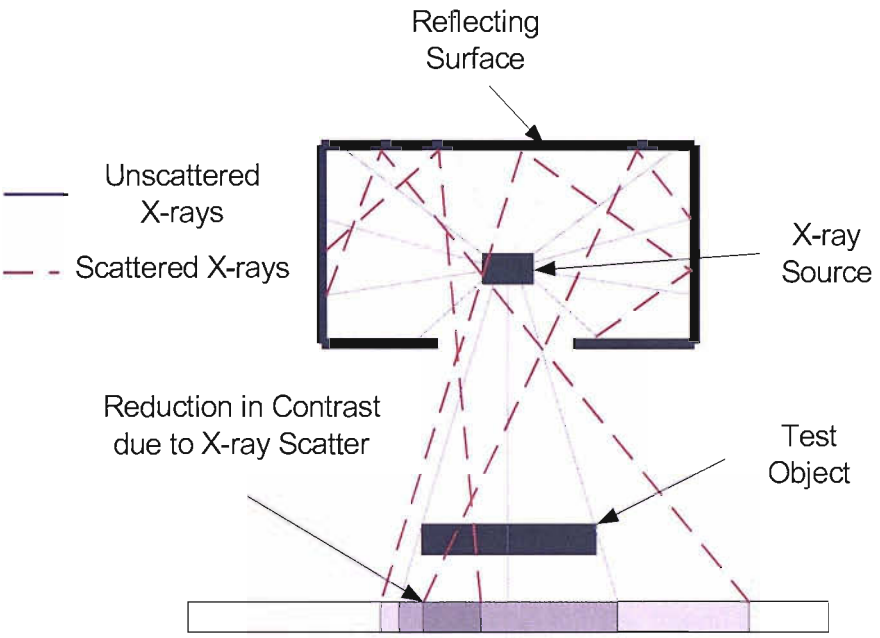

FIGURE 3.2: The effect of x-ray scatter on image contrast.

3.1.3 Factors that Affect the Suitability of an X-ray Source to Cable Joint Inspection

The ideal x-ray source for cable joint inspection must be able to produce x-rays that can penetrate the cable joint. The maximum tube voltage of the source must therefore be at least 50 kV in order to have the same penetration power as the original source. The amount of flux that the source can produce must be sufficient so that the exposure time is short. It is difficult to quantify this requirement due to many factors that affect exposure time. The penetration power and flux density must also be controllable, therefore the source must have accurate independent controls for the tube voltage and tube current. The focal spot of the source should be a small as possible, so that a pseudo-radial configuration can be utilised in order to produce images with high spatial

resolution. The source must have a high pass aluminium or beryllium filtering window in order to reduce the bandwidth of the x-ray flux and be shielded in order to reduce x-ray scatter to improve the contrast of the images produced. The source must also be able to maintain a vacuum around the filament and the target. The vacuum envelope can be achieved with a sealed-off tube or with a tube fitted with a vacuum pump. With a sealed tube there is no need for a vacuum pump and its accessories, however if the tube fails, i.e. the burning out of the filament, then a sealed tube cannot be repaired easily. Tubes where the vacuum is maintained with a vacuum pump, however, are demountable and so maintenance is possible.

3.2 X-ray Imaging Hardware

The main function of the imaging hardware is to convert the x-ray image of the cable joint into a useable format. For a sensor to be able to produce an image, it must have a field of view that can detect the local flux density of the x-rays across the whole of the cable joint and then be able to represent these flux densities in an analogue or digital image format. The quality of the image produced is determined by the definition and contrast of the image. Definition is determined by the lateral spread of the x-ray energy in the system and the resolution of the imaging system. The lateral spread is caused by the energy of the x-ray beam being scattered in the sensor. This reduces the sharpness of the image, therefore, ideally there should be no lateral spread of energy in the sensor. The resolution of the imaging system determines the level of detail that the imaging system can produce, therefore a high resolution is desirable. The contrast of the system is determined by the sensitivity and response of the sensor to x-ray radiation, and the dynamic range of the system. With a sensor that has a high sensitivity to x-ray radiation the contrast is improved because small variations in the x-ray flux are discernable. The response of the sensor determines how these small variations are represented. Ideally the sensor should have a linear response to x-rays so that contrast between two flux densities is similar across the whole density range. The dynamic range determines the range of x-ray flux densities that can be uniquely detected by the imaging system. The greater the dynamic range, the greater the contrast across the whole range of x-ray flux densities.

3.2.1 The Imaging Hardware Systems

The two imaging hardware systems used in this research are photographic film and a scintillating screen optically coupled to a CCD array. The following sections describe the theory of these two imaging systems.

3.2.1.1 Photographic Film Imaging

The conventional method of converting the x-ray image is to use a photographic plate. The process involved in converting the image is described in Section 2.2.4. The x-ray image is converted into a latent image that is then developed and fixed in order to produce a monochrome photographic image of the cable joint. The field of view of the photographic film is determined by the size of the area of the silver halide emulsion. The larger this area is, the larger the field of view. The lateral spread of x-ray energies and resolution of the photographic film are determined by the grain size and emulsion thickness. Sharper images are created by thinner films with small silver halide grains (Figure 3.3). The disadvantage of using a finer grain size, is that the exposure time required to generate the image is increased due to the increased energy required to reduce more silver halide grains. For this reason, finer grain films are generally used for imaging low-density composite materials, electronic components, and castings of light metals and alloys. These films are not suitable for imaging more radiologically dense materials such as welds and casting of dense metals, concrete and dense composite materials because a long exposure times would be required to produce an image. For these applications larger grained films are used [74]. The spatial resolutions of these large grained films however are generally of the order of microns [75]. There are also problems associated with reducing the thickness of the film because photographic film is relatively insensitive to x-ray radiation, therefore to improve the contrast of the image a thicker film is required. The rate of reduction of silver halide grains caused by the incidence of x-rays is also not a linear process, which results in poor contrast at low flux and energy level. The dynamic range of the film is limited which also impairs the contrast [76].

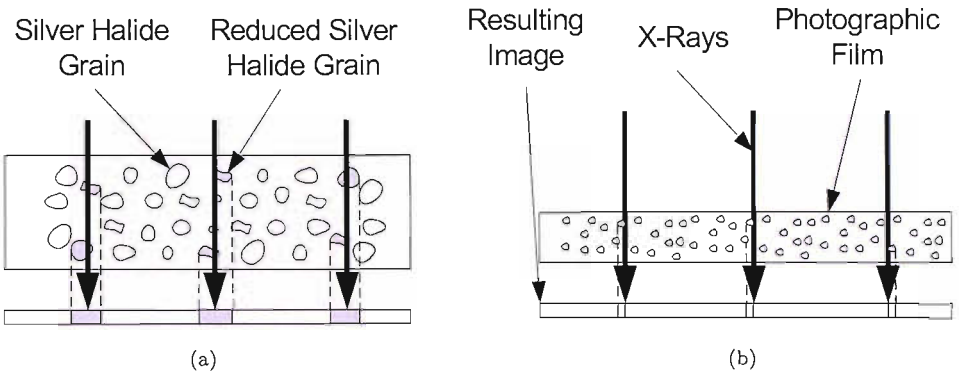

FIGURE 3.3: The lateral spread of x-ray energy and resolution of photographic film: (a) Thick film, large grain sizes resulting in a reduced image sharpness, and (b) Thin film, small grain resulting in a improved image sharpness.

3.2.1.2 Scintillating Screen and CCD Array Imaging

When an x-ray photon interacts with a material, it can leave a number of electrons in elevated energy states. This extra electron energy then tends to decay, emitting photons of ultra violet or visible light. The amount of light produced at each of the scintillation centre is proportional to x-ray energy absorbed. If this process occurs rapidly after the initial irradiation of the material, the material is transparent to the light photons produced and the frequency of light produced can be detected by a CCD array then the material can be used to make a scintillating screen [77, 78].

A CCD array is a collection of metal-oxide-semiconductor (MOS) capacitors. Each capacitor is a picture element, or pixel. When a capacitor is exposed to light, electron-hole pairs are generated. The electrons are then attracted to the surface under the gate; where they remain whilst the gate voltage is positive, see Figure 3.4. The amount of charge trapped under the gate is proportional to the amount of light flux falling on the surface of that capacitor during the exposure time. There is a limit to how much charge can be stored. When this limited is reached, if more light falls on the capacitor no extra charge is generated. This saturation point is known as the full well capacity.

After the exposure period, the charge under each gate must be read out. This requires that the charge under each gate be transferred to a readout register and converted into a digital signal. The charge is transferred by shunting the packets of charge from one pixel to the next. This is achieved by using three gates, instead of one gate, for each pixel. This means that charge can be passed between gates by altering the individual gate

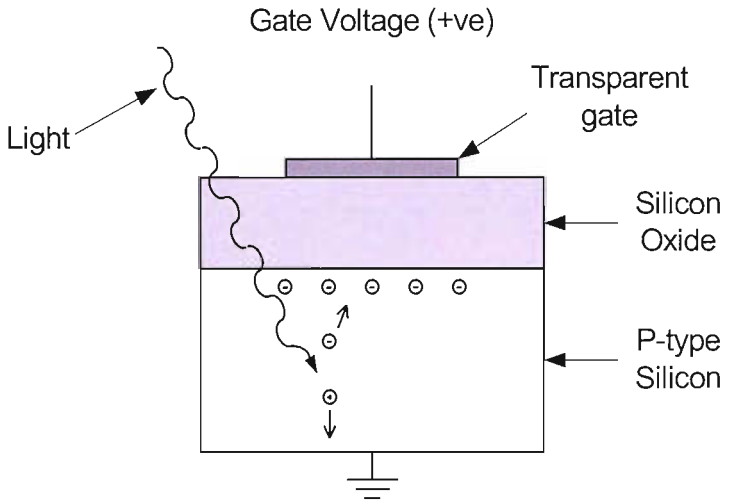

FIGURE 3.4: Schematic diagram of a MOS capacitor pixel.

voltages. A single right shift of charge is shown in Figure 3.5. This readout sequence can be performed using two different approaches, interline scan, where the charge is dumped into a second set of light shielded capacitors, and full frame read out, where the charge is moved into a separate array for readout (Figure 3.6). Interline scan is generally quicker but the spatial resolution is decreased due to the shielded capacitors, however this method is generally less noisy. Full frame is generally slower, however the spatial resolution is increased, but more noise can be generated [54].

Once the charge under each gate has been transferred to the readout register it must be converted into a digital signal. This is achieved by passing the charge to an analogue to digital converter. In the converter, the charge is converted into a quantised digital voltage. The range of useful voltage values is determined by the full-well capacity of the individual capacitors and the bit depth of the analogue to digital converter.

The final stage of the image generation is the conversion of the voltage values into a digital image. To do this, each voltage value is read into a computer. The voltage value is then converted into a greyscale value and stored in an 'm' x 'n' array. This image can then be displayed on a computer monitor.

The field of view of this type of imaging system is determined by the number and size of the individual pixels and the optical coupling method between the CCD array and the scintillating screen. A large field of view can be achieved with a large number of large pixels. The resolution of the system however is improved with smaller pixels but

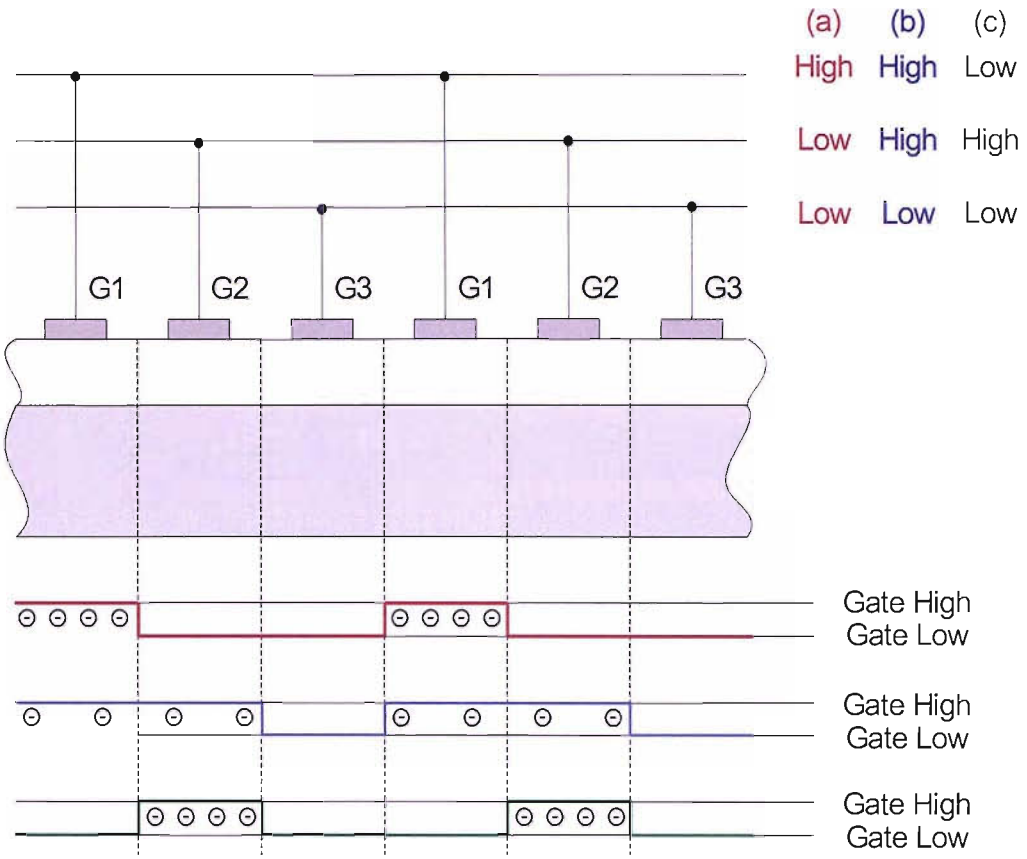

FIGURE 3.5: CCD array of MOS capacitors.

the number capacitors in the array is limited by the manufacturing process. The field of view can be increased by using a reducing coupling between the scintillating screen and the CCD array, however the effect of the coupling is to artificially increase the pixel size, which therefore reduces the resolution of the system.

The lateral spread of x-ray energy can occur in the scintillator and the CCD array. The energy conversion at the scintillation centres of x-ray photons into light energy can trigger adjacent scintillation centres to also emit light, causing an avalanche effect in the scintillator. This causes the lateral spread of light in the scintillator (Figure 3.7) [48]. This can be reduced by making the scintillator thinner or by producing a columnated scintillator. Lateral spread in the CCD is caused by 'leakage' of the electrons under each gate. This can happen either during read out due to charge not being transferred fully, or by overspill when the full well capacity is reached, known as digital bloom. The CCD therefore should have a high full well capacity and low readout noise characteristics.

The imaging resolution is determined by the lateral spread of light in the scintillator and

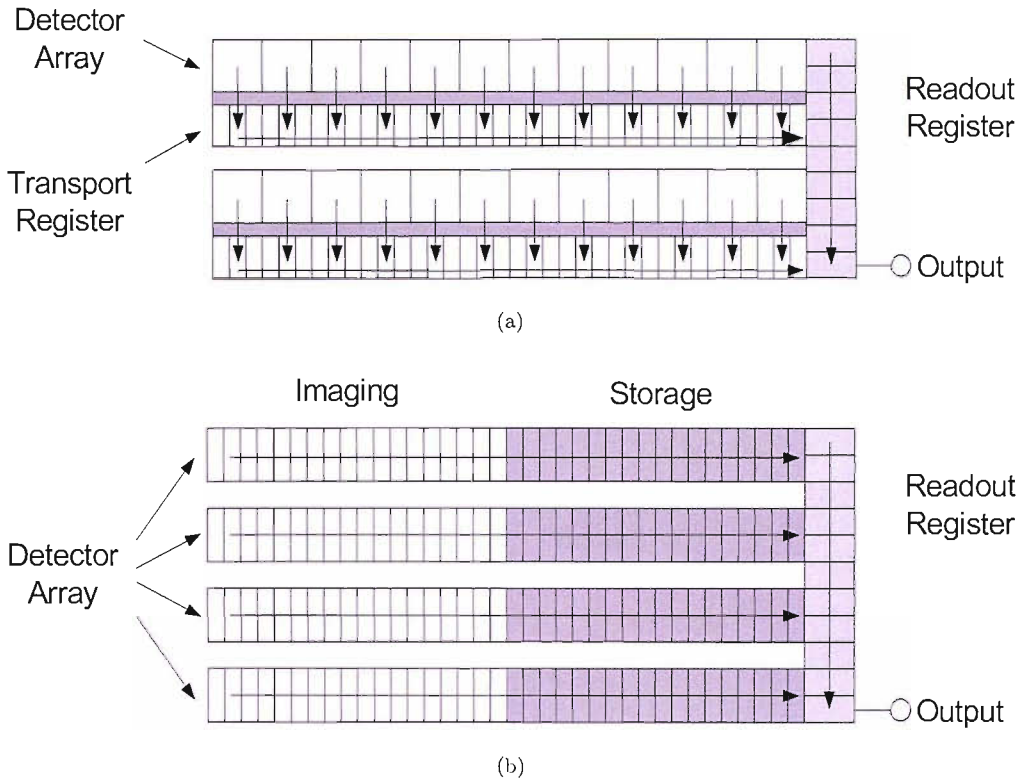

FIGURE 3.6: Schematic diagram of the main readout methods: (a) interline, and (b) full frame.

the spatial resolution of the CCD array. The lateral spread of light is generally better in a columnated scintillator, this means that the spatial resolution of the scintillator is determined by the size of the columns in the scintillator. The spatial resolution of a CCD array is determined by the size of the capacitors. Ideally, therefore, for the scintillator and CCD array to be matched the column size of the scintillator and the pixel size of the CCD array should be the same, and each column should be located above a pixel [71].

The sensitivity of the system is determined by the ability of the scintillator to convert the x-rays into light and the ability of the CCD array to convert the light into an electronic charge. Most CCD arrays are designed to detect wavelengths 200-1000 nm, and the majority of x-ray scintillators are designed to emit green light (520-580 nm). This means that, if a scintillator is optically coupled to a CCD array then an image will be created when the scintillator is irradiated with x-rays. The efficiency of the image production however is determined by the amount of light produced by the scintillator and ability of the CCD array to convert green light wavelengths [79, 80]. As with film, the sensitivity of the scintillator is improved by increasing its thickness, however this

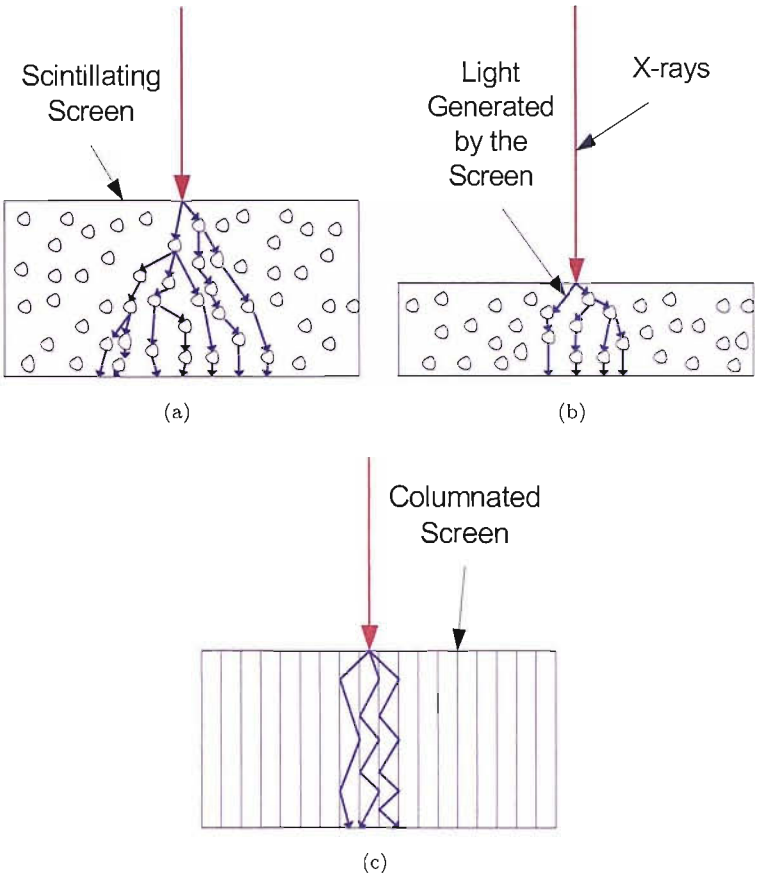

FIGURE 3.7: The lateral spread of x-ray energy in a scintillating screen: (a) thick screen, (b) thin screen, and (c) columnated screen.

decreases its spatial resolution. The scintillator therefore has to be sufficiently thick to improve the sensitivity of the screen but not too thick as to reduce its resolution [81, 82]. A second factor that affects the sensitivity of the system is the fill factor of the CCD array. Fill factor is the ratio of charge collection area compared with the physical size of the pixel. Ideally the fill factor would be 100%, however this is unlikely to occur in practice due to the construction of the individual pixels. In general, pixels are square, however the region of charge collection associated with that pixel is round and therefore only the light flux falling over the charge collection area is detected (Figure 3.8). This means that not all the light falling on the CCD array is detected. Fill factor, f_f is therefore defined as:

$$f_f = \frac{A_p}{A_c} \tag{3.1}$$

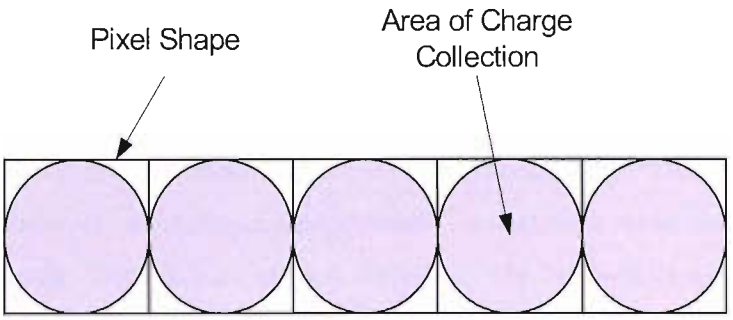

FIGURE 3.8: Fill factor.

where A_p is the pixel area and A_c is the collection area.

The problems associated with a decreased fill factor become less with smaller pixel sizes, because, even though the same percentage of the sensor will not detect X rays, the areas of non detection are dispersed more finely across the field of view, minimizing the possibility of not detecting a small defect.

The limiting factors of the dynamic range of this type of imaging system are the dynamic range of the CCD array and the number of quantization levels in the analogue to digital converter. Dynamic, d_r range for a CCD array is defined as the peak signal, S_p, to noise ratio, S_n.

$$d_r = \frac{S_p}{S_n} \tag{3.2}$$

A wide dynamic range means that the detector has a large signal to noise ratio, which makes the detection of difficult to find defects, such as small voids or partially occluded defects, easier because the difference in signal between the defect and defect-free insulation becomes more significant. In terms of a CCD array the signal to noise ratio is defined as the number of electrons a pixel can contain compared to the electronic noise generated during readout.

The contrast of this type of imaging system is aided by the linear nature of the conversion of x-rays into light and the conversion of light into electronic charge [47, 83]. This makes imaging complex geometries much easier because the contrast of the image is enhanced. The greyscale range of an image is the number of distinct tones of grey each pixel can hold. With a wider greyscale range the image can display greater detail, for example a black and white image has only two levels of grey, white and black. This means

that below a certain pixel charge, the image pixel will be black and above this charge, the image pixel will be white. With this type of image, fine detail and texture of the test object is lost. This can be improved by quantising the pixel charge with a finely divided greyscale range, such as a 8-, 12- or 16-bit greyscale range. Each greyscale value however, must have its own range of charge values, so that each value of charge has only one greyscale value. For a 12-bit camera, therefore, the full well capacity must be at least 2^{12}, or 4096, otherwise the signal becomes over quantised. It is beneficial, however, to have more than one electron per quantisation level otherwise noise becomes more significant than the signal and will distort the actual quantisation level [84].

3.2.2 Factors that Affect the Suitability of Film and CCD Camera to Cable Joint Inspection

Film is categorised by the size of the emulsion area and its grain size. The area of photographic film emulsion must be as large as possible, ideally so that only a single film is required to image the full length of the joint, i.e. the height of the film for a 90 kV cable joint would have to be at least 60 mm and the width greater than 450 mm. If more than one film is required, then two or more films can simply be overlapped in order to image the full length. A film with a relatively large grain size should be used in order to reduce the exposure time required to produce the image.

Scintillating screen and CCD arrays cameras are categorised by the field of view, the scintillator, the full well capacity, the pixel size, the fill factor, the readout noise and greyscale digitization. The field of view of most x-ray specific cameras is between 13.3 x 13.3 mm and 47.2 x 31.0 mm. The scintillators used are either columnated caesium iodide or gadolinium oxysulphide, however the choice of scintillator is dependent on the CCD array. The full well capacity of the CCD arrays range between 13300 to 100 000 electrons per pixel and is dependent on the manufacturing method and construction of the array. The pixel sizes of these arrays vary between 6.45 µm and 13.5 µm. Most CCD arrays have a fill factor above 75%. The readout noise varies between 3 and 13 e rms, producing dynamic ranges between 2250:1 and 33 333:1. All the cameras have at least a 12 bit greyscale. The specification of all the available x-ray scintillating screen and CCD array cameras are detailed in Appendix B. The main factors that determine suitability

of a camera to the inspection of cable joints is that it must have a small pixel size, a relatively large field of view and a good dynamic range.

3.3 The Irradiation Chamber

X-rays must be contained within a predetermined volume that has no human access. As described in Section 2.3 this can be achieved by either imposing a wide restriction area around the x-ray source while x-rays are being generated or by confining the x-rays within a smaller volume using radiation shields. The first method of protection is unfeasible for cable joint inspection because the joints are imaged on site, either at the cable factory, within a joint inspection bay or on board a cable laying ship, which can make it difficult to maintain an exclusion zone. The use of radiation shielding to create a smaller irradiation volume, or irradiation chamber, is a more suitable option for cable joint inspection. To implement this shielding, a radiologically dense material must be used to surround the source, the imaging hardware and the cable joint. In general, lead is used for this purpose due to its radiological density, structural properties, and relatively low cost. Lead can therefore be used to line a rigid enclosure in order to produce an irradiation chamber. The required lead thickness is dependent on the maximum available tube voltage. The greater the maximum tube voltage of the source, the greater the maximum penetration power of the x-rays produced, and the thicker lead shielding that is required. The main problem with using a lead lined irradiation chamber is that because the cable joint has to be enclosed within this chamber, and either side of the joint will be lengths of cable, a method of maintaining the radiation shield while allowing the joint to pass through the irradiation chamber is required. This can be achieved by extending the radiation shield along the cable, on either side of the joint.

3.4 The Positional Hardware

The positional hardware must maintain the geometry of the source, imaging hardware and the cable joint; prevent the cable joint moving during an exposure to prevent motion blur; and provide sufficient degrees of freedom to allow the whole cable joint to be imaged. The source and imaging hardware have to be attached to the rigid frame of

the irradiation chamber. The relative locations of the source and imaging hardware are determined by the type of source configuration used, i.e. pseudo-parallel or pseudo-radial. The cable joint then has to be aligned between the source and the imaging hardware, then it has to be clamped into this position in order to prevent motion blur. The final function of positional hardware is to enable complete imaging of the cable joint. If photographic film or the CCD imaging array is not large enough to capture the full length of the cable, then the source and imaging hardware has to be able to index along the cable. It is easier to index the source and imaging hardware rather than the cable joint, due to the indeterminate lengths of cable either side of the joint. To inspect all the insulation around the cable joint the source and imaging hardware must also be able to rotate around the axis of the cable to image the insulation from a range of angles. Once again it is easier to rotate the source and imaging hardware, rather than the cable joint.

3.5 Implementation of the Hardware: The Original Inspection Facility

The original test facility was built in 1995, and was initially designed to inspect sub-sea fibre optic telephone cable joints. The facility was later modified by replacing the original x-ray source so that polymeric cable joints could be inspected. The following sections describe this facility. Figure 3.9 shows photographs of this system.

3.5.1 The Original Source

At the time of construction of the original inspection system, only high stability x-ray sources were available. The most appropriate source for the system at the time was a Kevex E5014S-MF high stability tube. This source has a maximum tube voltage of 50 kV. Tubes with higher maximum tube voltages were available at the time, however, the extra capacity of these sources was not required because the existing facility was limited to inspecting cable joints with an overall diameter less than 102 mm, and it was found that 50 kV was sufficient to penetrate all XLPE and EPR cables and joints of this diameter. The cable diameter limitation is caused by the cable clamp design and because the system was initially developed for a fibre optic cable joint of 102 mm

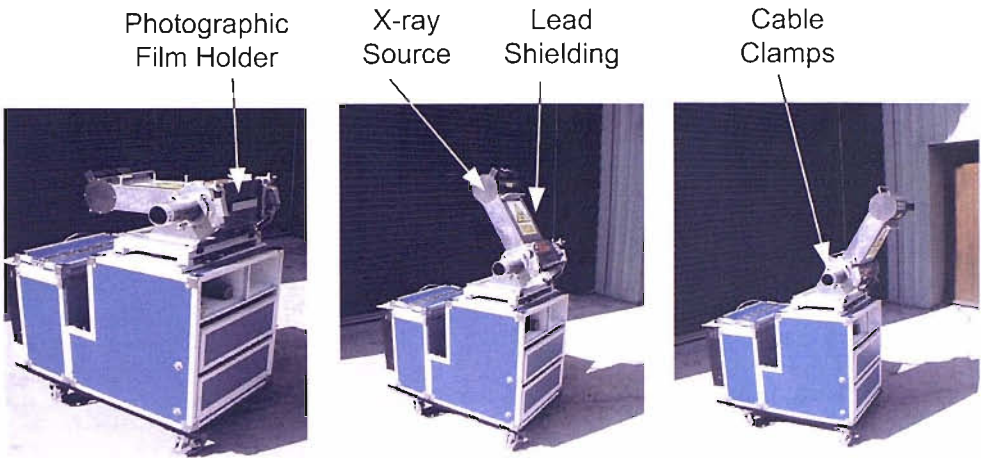

FIGURE 3.9: The original inspection facility with the source and film holder rotated at three angles: (a) 0°, (b) 60°, and (c) 120°.

(Section 3.5.3). The maximum filament current of the tube is 1.0 mA d.c. therefore x-rays are produced continuously while the source is energised. Using this x-ray source, the maximum exposure time for a 90 kV cable joint is approximately 5 minutes. The high stability nature of the tube is due to a focal spot size of 200 x 400 µm. The focal spot is produced on a tungsten target. To produce distinct images using this tube, the source has to be used in a pseudo-parallel set up. The vacuum in the tube is maintained by a sealed glass envelope tube. To prevent stray unwanted x-rays from exiting the tube, the envelope is encased in 1.6 mm steel covered in 2 mm lead sheets. To allow the x-rays to leave the tube a 13 x 8 mm window of 0.5 mm aluminium is used. The window is located at 10.6 mm from the tungsten target. This geometry produces an x-ray cone with a nominal cone angle of 30°.

The operation of this source is controlled by three analogue dials that determine the tube voltage, filament current and exposure time. The dials have a relatively course tuning effect and there is no fine-tuning ability. To improve the accuracy of the exposure setting, two analogue meters are used that indicate the instantaneous voltage and current levels of the tube (Figure 3.10). The tube voltage meter has a scale with 5 kV divisions. With this meter it was possible to control the tube voltage to within ± 2.5 kV. The filament current meter has a scale with 0.1 mA divisions. With this meter it was possible to control the filament current to within ± 50 µA. The exposure duration timer however does not have a time-based scale and has to be set by timing the exposure duration and

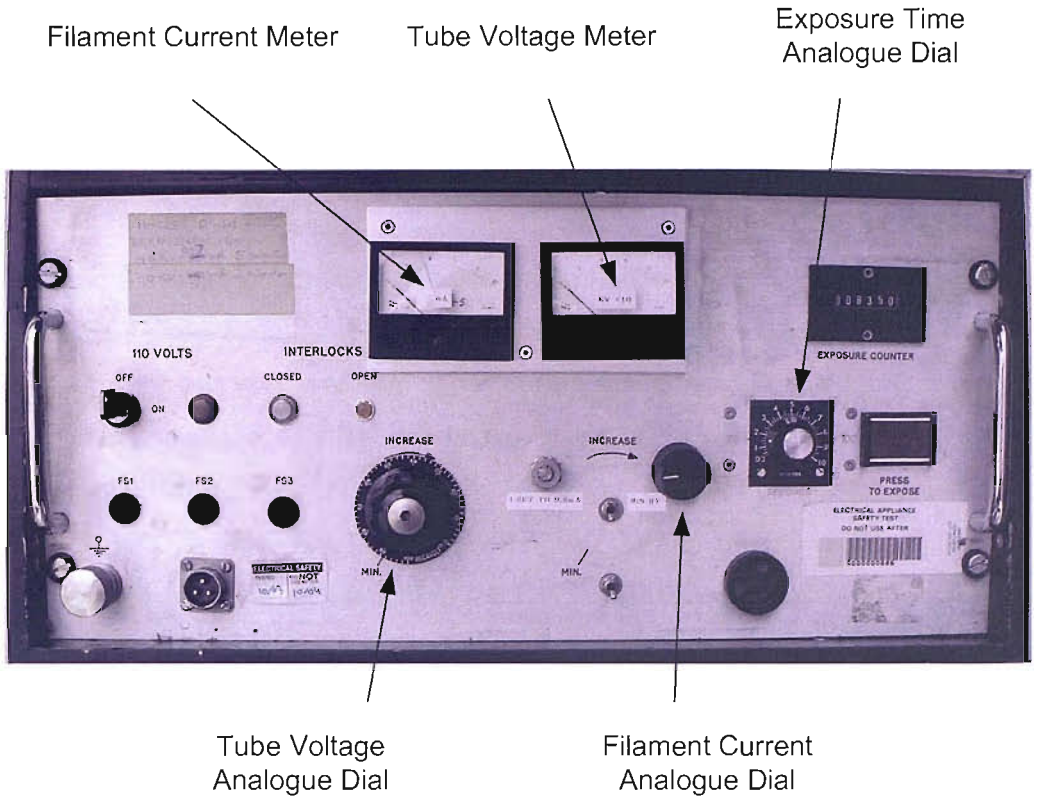

FIGURE 3.10: The control panel of the original inspection facility.

then increasing or decreasing the duration using the control dial. With this system it was possible to control the exposure time to within ± 0.5 seconds.

3.5.2 Photographic Film Imaging

The film chosen to image cable joints was a AGFA Structurix D7 photographic film plate. This type of film categorised as a ISO 11669-1 T3 film, which means it has relatively large grains that produce a film that has high x-ray sensitivity and good contrast [74]. The film is designed to reduced the exposure time required to image radiologically dense objects while trying to maintain a reasonable level of image quality. It is suitable for inspecting welds, castings and composite material. Other films can be used for imaging cable joints, however, these either have silver halide grains that are smaller and therefore the exposure times required are too long, or the grains are too big and so the image definition is reduced. The largest emulsion array size of this film is 298 mm x 234 mm. It is therefore not possible to image the whole of the cable joint length with one film.

This means that at least two exposures are required to image full length of the cable joint.

3.5.3 The Irradiation Chamber and Positional Hardware

The original irradiation chamber was designed to allow the imaging of a whole length of a 102 mm diameter fibre optic joint using two exposures. These images could then be captured on two widths of film. In order to optimise the use of the film the system was therefore designed to allow two images to be taken per film, using the film in a portrait orientation. This is achieved by restricting the field of view of the source to 225 x 125 mm, corresponding to just less than half the film emulsion area. The image is then captured by clamping one half of the film into the irradiation chamber. A second image can then be captured using the other half of the of the film. In order to capture images of that size using the 30° cone angle of the Kevex tube, the photographic film would have to be positioned at least 420 mm from the target with the cable resting against the film. The system, however, was not originally designed with this Kevex tube as the x-ray source. The original source had a cone angle of 30.5°, therefore the target to plate distance is set at 410 mm (Figure 3.11). This results in no image being captured close to the corners of the 225 x 125 mm field of view, however this reduction of image area does not impinge on the production of 225 mm long image of a 102 mm diameter cable.

The back wall of the irradiation chamber can be hinged open to load the cable joint into the irradiation chamber and consequently, prevent it from moving during the exposure period. The joint can then be loaded into the irradiation chamber from above. To hold the joint in position, split cable bushings have to be manufactured that have an outer diameter of 102 mm and and internal diameter to match the external diameter of the joint. The back wall of the chamber can then be closed and clamped shut; clamping the cable in a fixed position. Incorporated into the cable bushings are cable radiation shield that extends along the cable to maintain the radiation protection (Figure 3.12).

With this system it is possible to image 225 mm of the cable joint, however, to image the full length of the cable joint, two exposures are required. To do this the left-hand side of the joint is imaged and then the camera repositioned towards the right-hand side of the joint and a second image taken, ensuring that there is a significant overlap in order

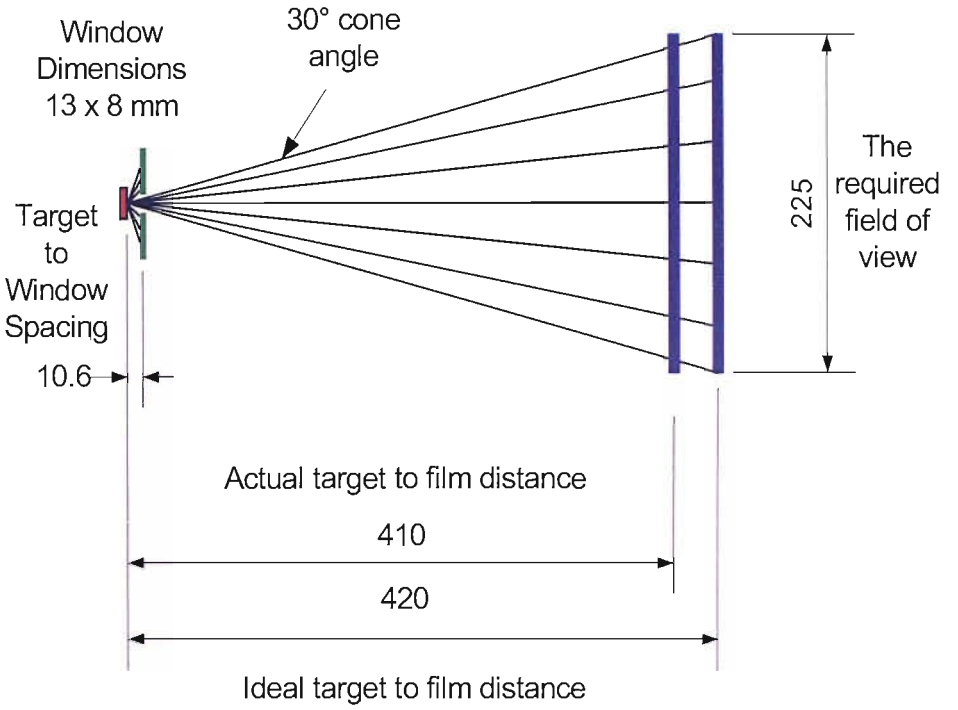

FIGURE 3.11: The target to film geometry of the original inspection facility.

to marry the two images together after development. To inspect all of the cable joint insulation, the x-ray source and film can rotated around the central axis of the cable joint, and locked in place at 15° intervals, allowing images to be taken over a range of angles from 0° to 165°.

To contain the x-rays within the irradiation chamber the source, film and cable joint were encased by 1.6 mm of steel plate and 2 mm of lead sheet. To ensure that the source cannot be energised while the hinged back wall of the chamber is open, seven microswitches are fitted in strategic locations. The switches are located so that all seven contacts are only made when the cable is clamped in position and the back wall of the chamber is shut. If any of these microswitches are open then the power to the x-ray tube is cut. The second safety measure implemented in this system is a pre-warning buzzer sounds for three seconds before the x-rays are produced, and while x-rays are being produced an indent with the words "X-RAYS ON" is lit to warn the operator and any other person close by that there is a radiation source energised.

This system is portable to allow it to be used on site. This is achieved by mounting the source, the source control panel, source power supply, and irradiation chamber on castors. To use the inspection facility on site, all that is required is a 240 V 13 A supply.

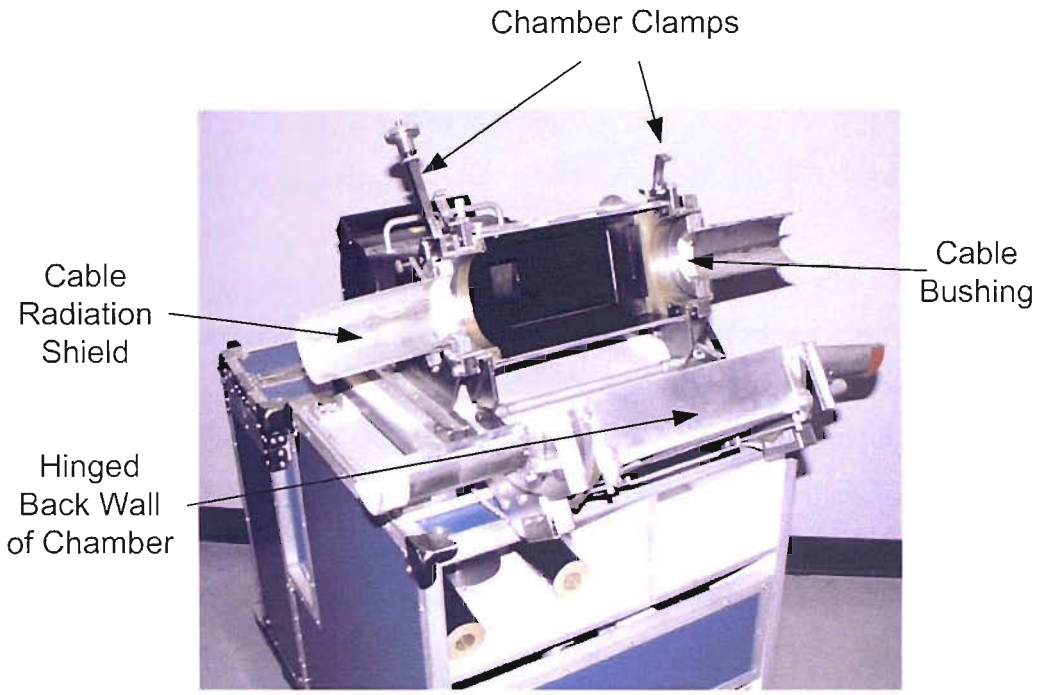

FIGURE 3.12: The cable clamps.

3.5.4 Limitations of Original Facility

It is possible to generate film-based images of the complete internal structure of a high voltage cable joint, using a portable system that does not subject the operator to any significant health and safety risk. The disadvantages of this approach are that a macro-focus tube is used which reduces the image definition of the images produced; the images are produced using film which is inflexible in terms of its inspection and post processing enhancement; the control of the exposure setting is not very accurate and therefore the system suffers from a lack of repeatability; and finally the source is a sealed x-ray tube which means that maintenance on the tube cannot be performed. If the tube fails, the complete tube has to be replaced which is expensive.

3.6 Implementation of the Hardware: The New Inspection Facility

To overcome the limitations of the original test facility, a new system has been designed. The new facility uses a microfocus x-ray tube and a scintillating screen coupled to a CCD

camera to digitally generate images of the cable joint. The following sections describe the hardware used.

3.6.1 The Microfocus Source

The microfocus source used to improve the definition of the images was a X-Tek 100 kV open tube Xi x-ray source. This source is capable of producing x-rays using a tube voltage between 25 – 100 kV, with a maximum d.c. filament current between 0 and 0.2 mA. The focal spot size of this source is a 5 µm, created on a tungsten target. The target is positioned 6 mm behind a round 0.5 mm thick aluminium window. The diameter of this window is 2.6 mm, which produces a 25° cone angle. This tube is demountable allowing modular replacement of damaged components. To maintain the vacuum in the envelope a 80 ls^{-1} turbo-molecular pump backed by a two stage rotary vane pump is used. The new source is shown in Figure 3.13.

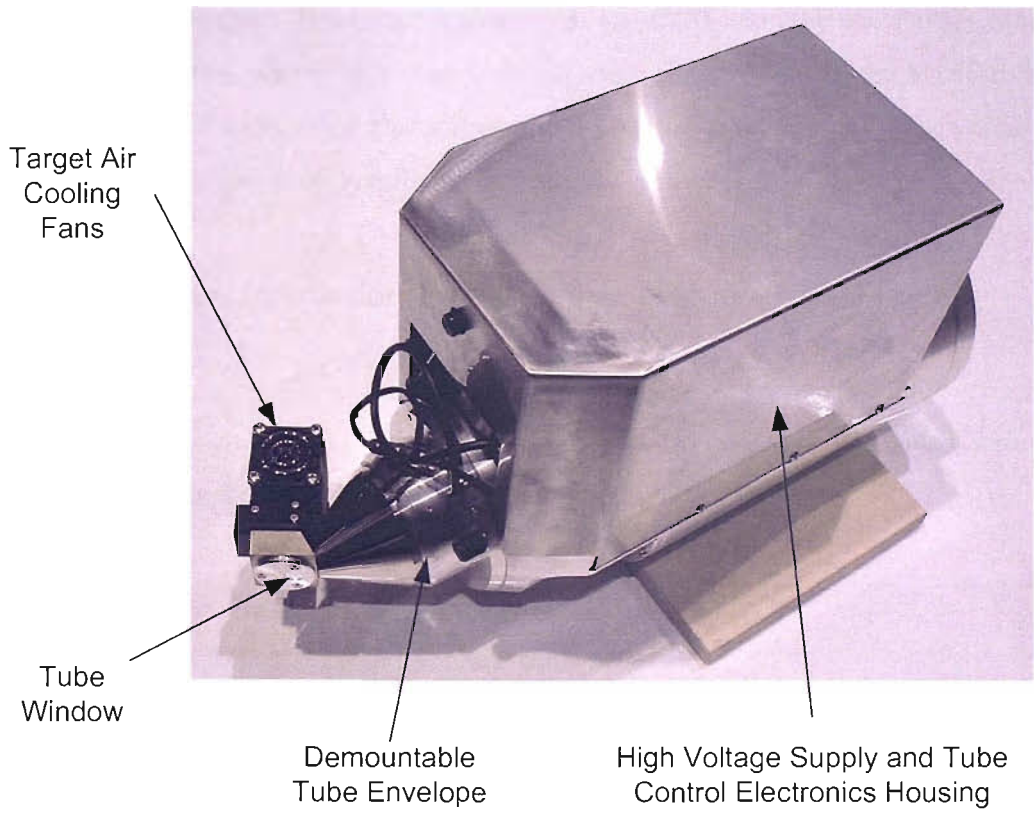

FIGURE 3.13: The X-Tex microfocus source.

The source is controlled using a PCI slot Xodiac control card and iXS control software. This enables computer control of the tube voltage, filament current and exposure time.

With this digital control, the problems of accuracy and repeatability associated with the original source are removed.

3.6.2 The CCD X-ray Camera

The scintillating screen and CCD array camera used to replace film as the imaging hardware is a Marconi CCD42-40 CCD array coupled to a gadolinium oxysulphide scintillating fibre screen using a 1:1 image taper. The CCD array comprises of 2048 x 2048 13.5 μm pixels, producing a field of view of 27.6 x 27.6mm. The full well capacity of each pixel is 100 000 electrons and the readout noise is 3 electrons rms. This produces a dynamic range of 33 333:1. The images produced have a 12 bit greyscale digitization. The camera is manufactured by XCAM limited and is shown in Figure 3.14. In order to reduce the dark noise inherent in the CCD chip, the array is chilled to -25°C using a Peltier cooler. The temperature is controlled using a Wavelength Electronics LFI-3751 temperature controller. The heat removed from the CCD array by the Peltier cooler is removed from the camera by a closed circuit water chiller. The camera is controlled using xcDiplay software. With this software it is possible to set the integration time of the image capture and pixel binning configuration.

3.6.3 The New Irradiation Chamber and Positional Hardware

In order to asses the validity of converting from the original inspection facility to a micro-focus/digital inspection facility an intermediate irradiation chamber was manufactured followed by a completely new irradiation chamber.

3.6.3.1 The Intermediate Irradiation Chamber

In order to verify that a CCD camera would produce images comparable to the images generated using photographic film, the original irradiation chamber was modified to incorporate the XCAM x-ray CCD camera. The modification involved removing the existing sprung loaded back plate of the original irradiation chamber and replacing it with a new back plate. The new back plate was identical in design to the old back plate, however, a circular aperture was made in the plate to ensure that the imaging surface of the x-ray CCD camera was inside the irradiation chamber. A camera housing was

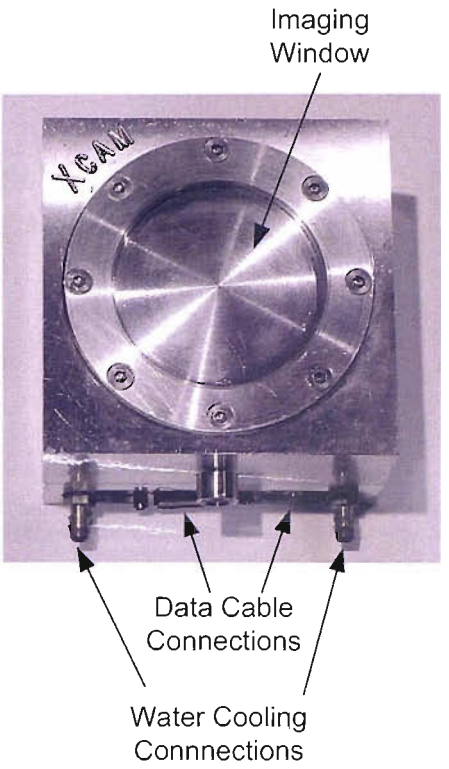

FIGURE 3.14: The X-Cam x-ray scintillating screen and CCD array camera.

then incorporated on to the back surface of the plate see Figure 3.15. With the camera located in the camera housing, it was therefore possible to generate camera-based images of cable joints using the procedure detailed in Section 3.5.3. Due to the similar designs of the original and modified back plates, it is also possible to generate film based images of the same test piece by inserting a photographic into the irradiation chamber, making it possible to compare the images generated using both film and digital x-ray imaging hardware.

3.6.3.2 The New Irradiation Chamber

A new chamber was designed because the old irradiation chamber was incompatible with the X-Tex microfocus source, therefore the new chamber was designed to house the new source and the x-ray CCD camera in order to verify that the conversion to a digital inspection system is possible and that the new digital inspection process is comparable or better than the original analogue inspection process. For this reason the irradiation chamber was designed to only take cable joint samples to make the construction of the irradiation chamber simpler.

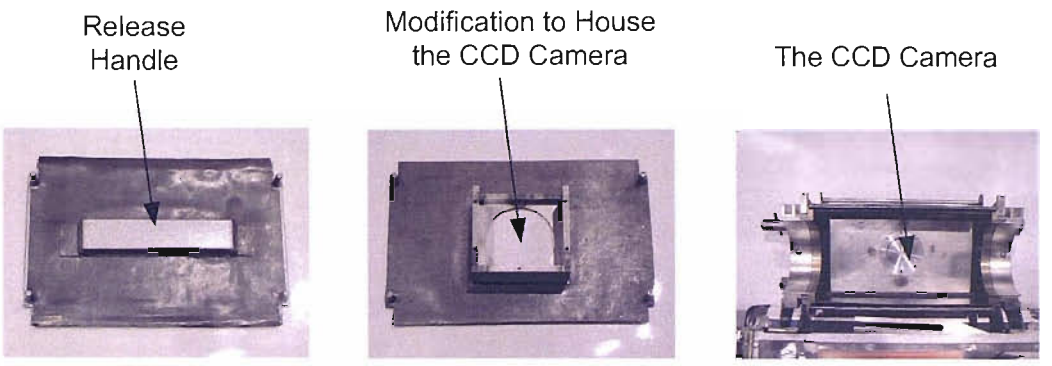

(a) (b) (c)

FIGURE 3.15: The intermediated chamber: (a) original irradiation back plate (rear view), (b) modified irradiation back plate (rear view), and (c) X-ray camera mounted on the modified back plate (front view).

The new irradiation chamber was designed to be a large cabinet with two hinged doors in the top of the cabinet. The cabinet was made to be 1.5 m long by 0.875 m wide by 0.5 m high to create a large irradiation chamber to house the source, sample and camera, but with sufficient space to allow easy access and maintenance. The framework for the cabinet was made out of sheets of 12 mm thick plywood, except the base which was 25 mm thick, strengthened by 33 x 33 mm timber lathes. The inside of the cabinet was then lined with 6 mm thick lead, with double skinned lead around the timber lathes. The hinged lids were constructed using the same technique as the cabinet, however, 40 mm 'L' steel angle was used to further strengthen the two lids. At each end of the cabinet is a lead labyrinth to enable the services for the x-ray source and camera to enter the cabinet. The cabinet is then mounted on a square section steel frame to prevent twisting of the cabinet. Under the steel frame are four nylon casters, so that the cabinet is moveable. Figure 3.16 shows the new irradiation chamber and the associated design drawings can be found in Appendix C.

In order to prevent x-rays from being produced when either cabinet door is open, two microswitches are positioned under each door. The contacts of these four switches can only be made when both doors are fully closed. To ensure that there is no microswitch malfunction, a polling procedure is used to check each switch can be opened and closed. There are also indicator LED's that display the status of each switch. This interlock system is integrated into the x-ray source control software, therefore if either door is opened while x-rays are being produced, the power to the source is cut. The pre-warning buzzer has been replaced with pre-warning LEDS, however the pre-warning duration is

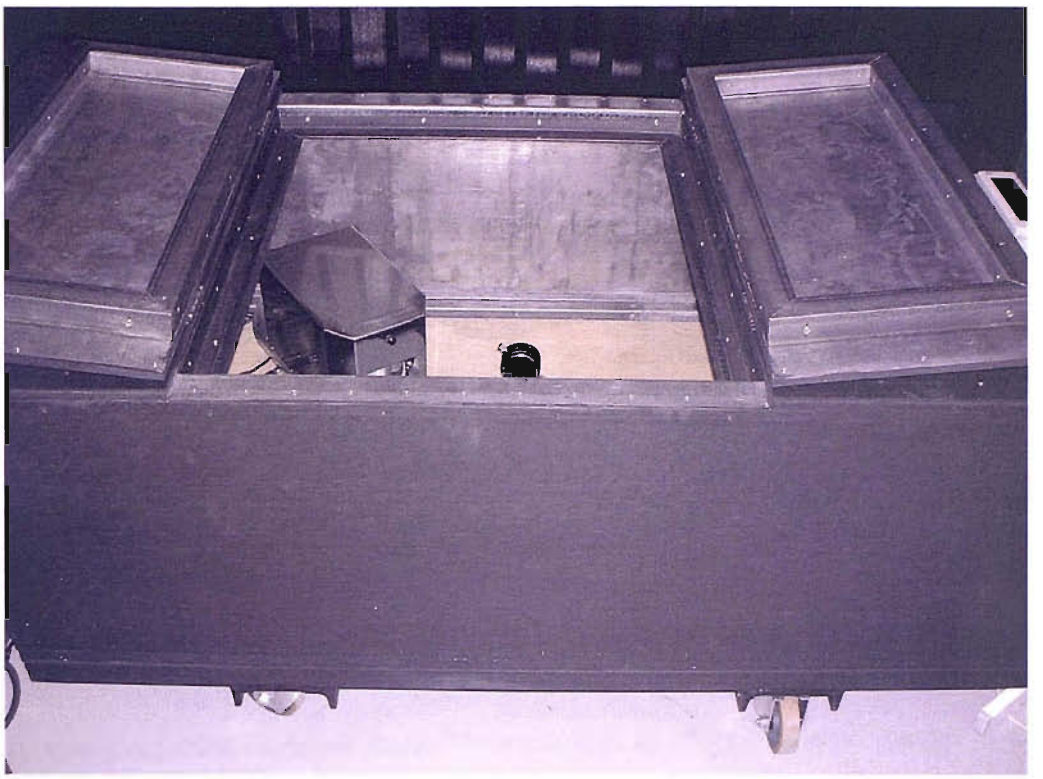

FIGURE 3.16: The new irradiation chamber.

user defined. There is also an "X-RAYS ON" indent which is illuminated when the source is energised. The details of this are shown in Appendix D.

To mount the cable joint sample in the cabinet, a translational and rotational positional stage was manufactured so that the cable could be indexed past the x-ray source and camera. This was achieved by attaching one end of the cable joint sample to a Melles Griot 30 mm diameter polarizer holder, allowing the sample to be rotated manually 360° with a 1° resolution. The other end of the cable being supported by a length of brass studding. The polarizer holder and brass studding are both held in line by two custom made mounts and a length of optical bench track. The optical bench track is then mounted on an Edmund Optics 305.8 mm rack and pinion translational stage. This stage is capable of producing 200 mm of linear movement using the coarse adjustment pinion. With this cable mount, it is therefore possible to index the cable sample, with up to 200 mm of travel, and rotate it by 360° in single degree increments. The cable mount is shown in Figure 3.17. The geometric positioning of the source, CCD x-ray camera and the cable joint mount are such that the source back lights the cable joint in a similar design to the original chamber. The exact details of the position of each

component is discussed in Chapter 4.

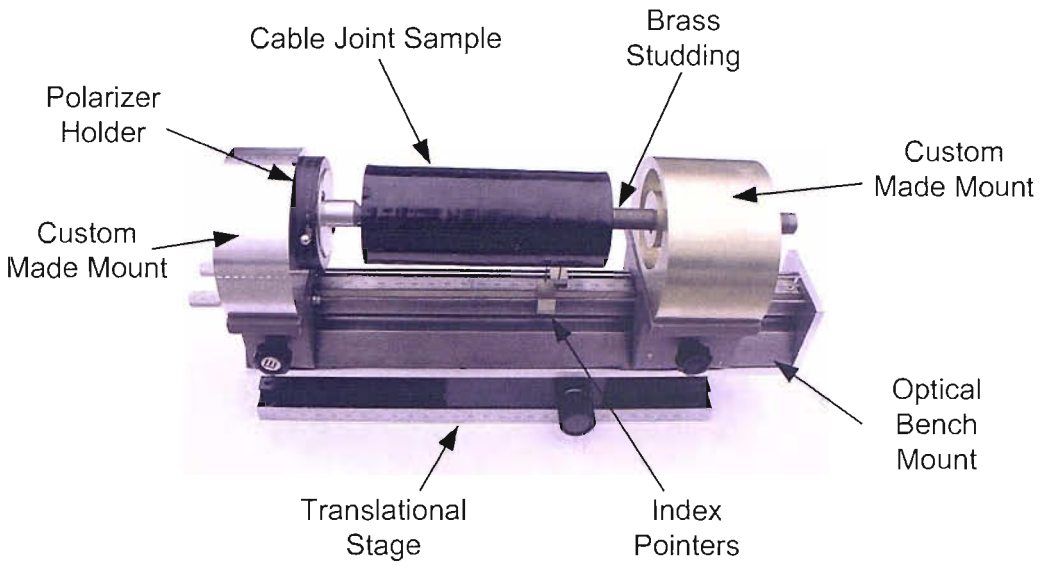

FIGURE 3.17: The cable mount.

With this irradiation chamber design, it is possible to generate digital images of the internal structure of a high voltage cable joint that can be inspected using digital image processing algorithms, without subjecting the operator to any significant health and safety risk.

3.7 Summary

To produce an image of the internal structure of a cable joint, an x-ray beam is required that has sufficient penetration power and flux density to irradiate the joint. For this research, the attenuated x-ray flux is then captured using either photographic film or a scintillating screen optically coupled to a CCD array. The quality of the images produced is determined by the definition and contrast of the source, the film, the scintillating screen and the CCD array. The original facility used by the University of Southampton for high voltage cable joint inspection used a macrofocus x-ray source and photographic film. This method of imaging however suffers from a reduced image definition, because of the large focal spot size of the source, and a lack of flexibility in terms of post-processing and image inspection due to the use of photographic film. A new facility has been designed that uses a microfocus source and a CCD x-ray camera. This new system can be used

to produce digital images of the cable joint. These images can then be enhanced and inspected using digital imaging processing techniques.

Chapter 4

Production of Digital X-ray Images

The hardware described in Chapter 3 can be used to generate x-ray images of cable joints. These images can then be used to determine the manufacturing quality of the joints. The original inspection system used photographic plates to image the joints, however the new system is designed to image the joints using a CCD camera. This chapter describes the images produced using this camera; the digital methods that can be used to improve the signal to noise ratio of these images; the exposure setting required to produce the images; a comparison between the images generated by the camera and images captured by photographic film plates; and the methods used to image the whole of a cable joint using the camera.

4.1 The Properties of Digital Images

A digital image is a two dimensional array of data points, known as picture elements, more commonly known as pixels. For cable x-ray images, each pixel intensity value is proportional to the x-ray flux energy of the corresponding point in the attenuated cable x-ray image. The XCAM x-ray camera generates digital images using 2048 x 2048 pixels, thus producing arrays with 4,194,304 pixels. Each pixel in this array has a 12-bit digitization, therefore the pixel intensity value for each pixel requires two bytes of storage space. This results in a monochrome image that is 8.65 MB in size. It is possible to

represent the image using a range of different display techniques including a simple array of numbers, a monochrome image, a surface plot of the image intensities, or a pseudo-colour image. The image in the Figure 4.1 is a simple 10 x 10 pixel image of the letter 'A.' From Figure 4.1(a) the individual pixel intensities can be easily obtained. With 100 pixels, however, it is difficult to discern the global image content. In the pixelated image in Figure 4.1(b) the letter 'A' is clearly defined, but the distinction between the background of the image and the 'legs' of the letter 'A' is difficult to determine. This is due to the fact that the eye is only able to discern 32 levels of grey between white and black [85]. The extent of the legs of the letter 'A' and the relative values of each pixel is most obvious in the surface plot in Figure 4.1(c), however, determining what the individual mesh heights actual represents is less obvious. The final method of displaying a monochrome image is a pseudo-colour image. In a pseudo-colour plot the greyscale range is converted into a colour map, where the each greyscale value is mapped to a distinct colour. The advantage of using this representation is that the eye is no longer limited by only 32 levels of greyscale, however the colour map used is arbitrary, and so the interpretation of colour changes in the image can be difficult.

4.2 Characteristics of Digital X-ray Images of High Voltage Cable Joints

The 4.2 million pixels of the CCD camera represent a field of view measuring 27.6 x 27.6 mm. This means that it should be possible to image the thickness of insulation of most cables in the 66 – 275 kV voltage range using only one exposure, as these cables generally have a maximum electrical stress of 8-10 MV/m, therefore requiring an insulation thickness of 22-32 mm (Table 1.1). To image higher rated cables, with thicker insulation, two exposures are required. For this reason this work only concentrates on the 66 – 275 kV cable joints with insulation thicknesses less than 27.6 mm. The field of view of the CCD camera, however, still means that only the upper or lower section of insulation can be imaged in a single exposure (Figure 4.2).

The general content of an x-ray image of either the upper or lower insulation thickness is the same. The image is a shadowgraph of the cable joint, i.e. it is similar to generating an image of a translucent object on a blank screen by back lighting the object. This

0	0	0	0	10	10	0	0	0	0
0	0	0	9	9	9	9	0	0	0
0	0	8	8	8	8	8	8	0	0
0	7	7	7	0	0	7	7	7	0
6	6	6	6	6	6	6	6	6	6
5	5	5	5	5	5	5	5	5	5
4	4	0	0	0	0	0	0	4	4
3	3	0	0	0	0	0	0	3	3
2	2	0	0	0	0	0	0	2	2
1	1	0	0	0	0	0	0	1	1

(a)

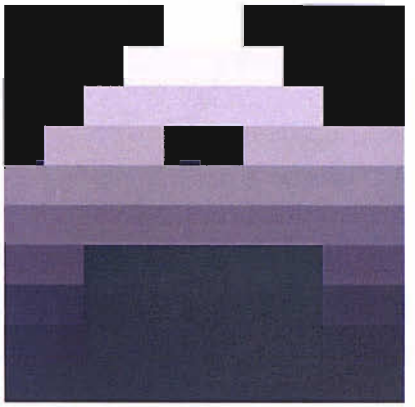

(b)

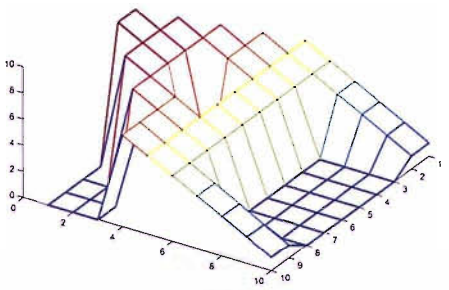

(c)

(d)

FIGURE 4.1: Four common methods of representing an image (a) numerical array, (b) monochrome image, (c) surface plot, and (d) pseudo-colour.

means that a two-dimensional image is generated with regions corresponding to the conductor, conductor shield, insulation, insulation shield and the air gap above/below the cable. Figure 4.3 is four representations of an x-ray image of the upper section of insulation from a 90 kV EPR submarine cable joint. In the monochrome image it is possible to see the air gap at the top of the image (the brightest region). Below this is a slightly darker grey region running across the image. This is the insulation shield. The only other feature discernable in the image is the interface between the insulation shield and the insulation, this is due to the limited greyscale resolution of the eye. To be able to see the conductor and conductor shield the pixel intensities have to be uniformly increased, in effect brightening the image (Figure 4.3(b)). In this brighter image the conductor is clearly visible, and the conductor shield can also be seen, however the air gap, insulation shield and the top section of the insulation have been lost due to saturation. The surface plot, Figure 4.3(c), displays effectively the relative pixel

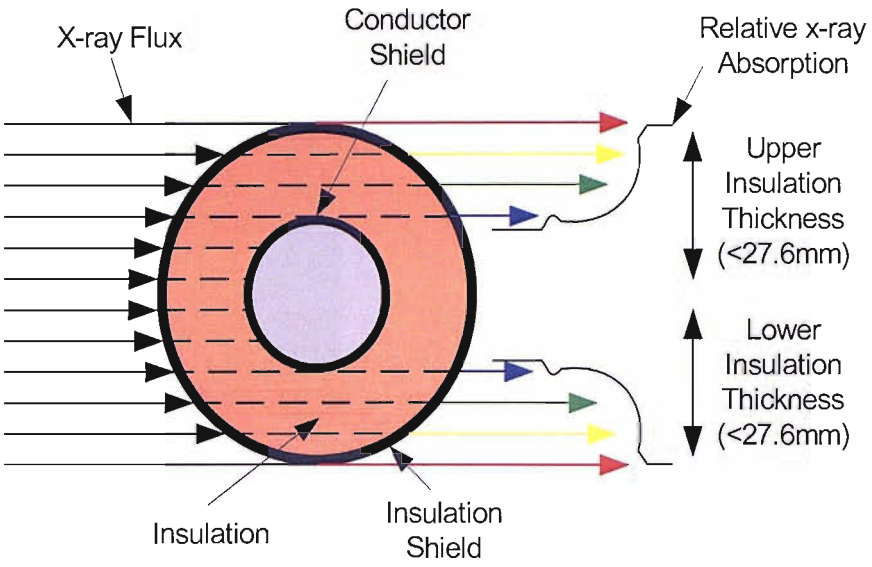

FIGURE 4.2: The attenuation of x-ray flux caused when imaging a cable joint

intensities from the air gap (red), to the conductor (dark blue) in one single image. From this image it is possible to assess the amount of attenuation of the x-ray flux caused by each component of the insulation system. The pseudo-colour image does offer greater contrast across the image compared to the monochrome image, however determining the exact locations of the material interfaces is difficult, especially the interface between the conductor shield and the insulation. A number array representation has not been added to the figure because it too difficult to comprehend the global content of the image from the 4.2 million individual data points.

The regions in Figure 4.3 are generated by the amount of attenuation of the x-ray flux. The conductor, conductor shield, insulation, insulation shield and the air gap absorb x-rays to different extents. The relative attenuation is best visualized using Figure 4.3(c). The radiological density of the aluminium/copper conductor is large enough that the conductor will absorb all the x-rays. This results in the low signal value at the base of the 'ramp.' Conversely, the radiological density of air is low, which results in very little x-ray absorption in the air gap, therefore the signal value at the top of the ramp is relatively large. The radiological densities of the insulation and the semiconducting material of the insulation and conductor shields fall between these two extremes, with the insulation being radiologically more dense than the shields. The attenuation of x-rays by these components is therefore determined by the radiological density of the material, but also the thickness of the material that the x-ray flux has to pass through. The x-rays passing

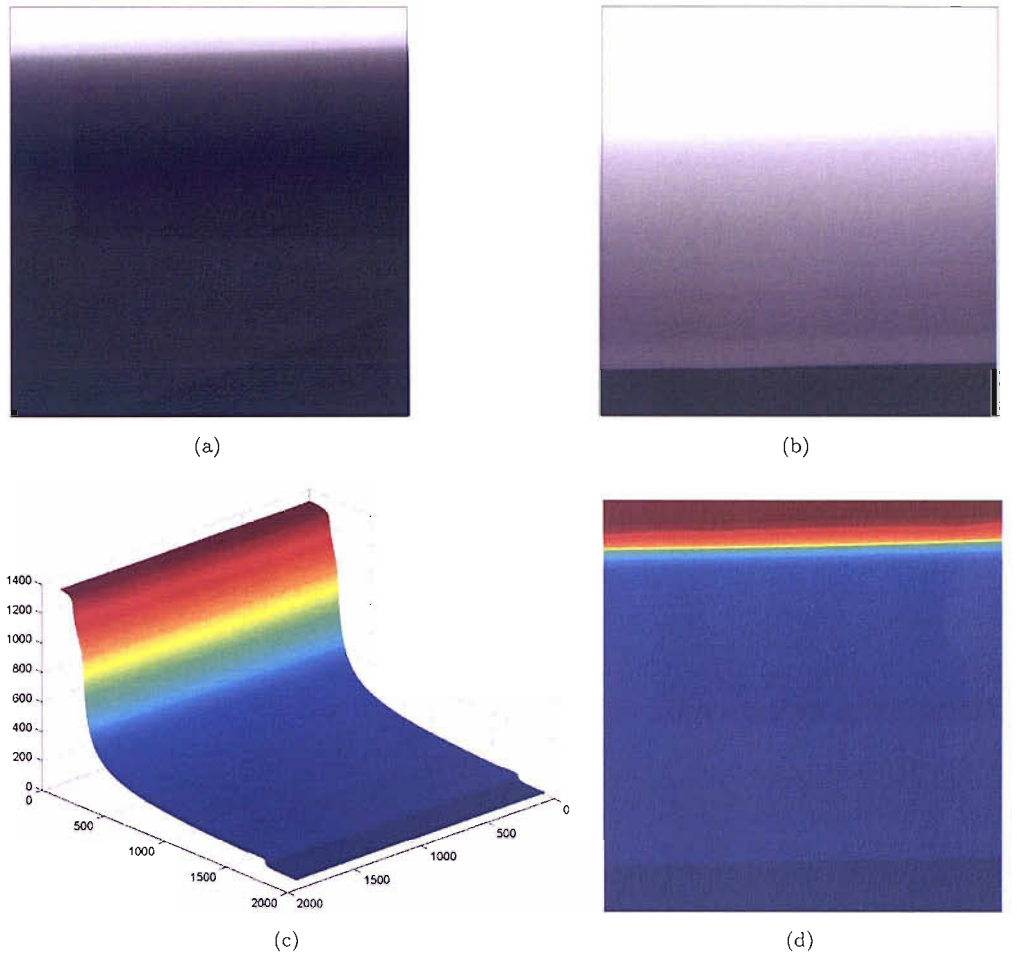

FIGURE 4.3: Representations of a cable joint image (a) monochrome Image, (b) increased brightness monochrome image, (c) surface plot, and (d) pseudo-colour.

through the insulation close to the conductor have to pass through more insulation than the x-rays passing through the insulation close to the insulation shield (Figure 4.2). This results in a greater attenuation of x-rays close to the conductor compared to the attenuation close to the insulation shield, even though the radiological density of the insulation does not change. This causes the ramp shape in Figure 4.3(c). The conductor and insulation shield, however, have a lower radiological density compared to the insulation and therefore the attenuation of the x-rays caused by these components is reduced compared to the attenuation of insulation. This causes subtle changes in the ramp profile, however these are not apparent in the figure. The theory behind the imaging of the radiological density mismatches between different components of the insulation system also applies to the imaging of inclusions and voids. The relative radiological density of the defect causes either greater or less attenuation of the x-rays

flux compared to the material the defect is located in. This will then manifest itself as either a darker or lighter area in the image.

It is these radiological properties of the material interfaces and defects that are used to fulfill the inspection requirements as described in Chapter 2, Section 2.2, namely dimensional checks and defect detection. The inspection methods used to extract this information from the digital x-ray cable joint images produced are detailed in Chapters 5 and 6. However, before any post processing inspection of the images is performed in order to determine the manufacturing quality of the cable joint, the images can be pre-processed in order to remove any noise associated with the image capture.

4.3 The Raw X-ray Image Content

The raw image captured by the CCD camera contains more than just information relating to the attenuation of the x-ray flux caused by the cable joint. Unwanted noise is generated by the 'dark' response of the CCD array and the variation in response of the CCD camera across the image [86].

4.3.1 Dark Image

The dark image produced by a CCD array comprises of two noise signals, a precharge signal and dark current. The precharge signal is artificially introduced into the array to ensure no negative pixel values are generated. This noise is uniform across the whole of the array and is independent of exposure time and array temperature. Dark current, however, is caused because electrons are thermionically generated in each of the pixel capacitors. This process is not uniform; rather it is pixel dependent. Its influence on the final image can be reduced because:

- Under identical temperature conditions, each pixel will generate the same number of electrons per unit time with a narrow statistical dispersion and therefore it is a relatively reproducible phenomenon.
- The generated electric charge is proportional to the integration time.

- The dark current is dependent on the CCD array temperature. Reducing the CCD array temperature therefore reduces the amount of current. Each time the CCD array temperature is reduced by 6°C, the current is reduced by a factor of two [87].

Figure 4.4 is a dark image produced using the XCAM CCD array with a 100 second exposure at 20°C (The image was taken at 20°C in order to increase the dark current content within the image). The speckled appearance of this image is caused by the pixels generating thermal electrons. This means that all the images produced of the cable joint contain useful information about the joint and thermal electrons. The majority of this noise can be removed by generating an image containing just dark current information. This image can then be subtracted from the cable joint image. To generate this dark current image, several images must be taken with identical thermal and exposure time conditions as used to image the cable joint, except with no x-rays being produced. The images produced with these exposure settings will therefore only contain the dark current and offset signals. A single dark current image can then be generated by calculating the average pixel intensity values for each pixel from the dark images generated. Then this image can be subtracted from the cable joint image [88].

FIGURE 4.4: The dark image obtained with a 100 sec exposure at 20 °C.

Despite being able to subtract the dark current from the cable image, it is still necessary to reduce the amount of thermal electrons produced because an image generated with a high CCD array temperature or long exposure time could become saturated due to a large dark current, resulting in no cable joint data captured. To limit the generation of

thermal electrons, the CCD array can be cooled. With the XCAM CCD array this is achieved using a Peltier cooler. The heat removed by the cooler is then removed by a closed circuit water cooling system. With this system is therefore possible to cool the CCD array to -40°C. For the purpose of dark current suppression it would be advisable to cool the CCD array to the minimum temperature of -40°C, however a bi-product of chilling the array is that the scintillator is chilled too, which slows the rate at which the scintillator converts the x-ray energy into light energy. As a result of this, the time delay between the cessation of x-ray production and arrest of scintillation is increased. If a second image is taken quickly after the initial image, some of the data from the first image is captured in the second image; an effect called 'image ghosting.' The cooling temperature is therefore a compromise between dark current suppression and image ghosting prevention. It was found that the optimum temperature for cooling the CCD array was -25°C as the dark current was significantly reduced, however no ghosting appeared. A temperature of -25°C was chosen by imaging the cable joint, then immediately after this image was taken, a second image was captured using the same exposure settings, except the x-ray source was not energized. After a period of five minutes a third image was taken using the same exposure settings as the second image. This image was then subtracted from the second image (the image captured immediately after the x-rays were turned off). A mesh plot was then generated of this subtraction. If a residual image was captured in the second image, then this would be apparent in the mesh plot generated. If no residual image was detected, the CCD array was cooled further and new images were taken. This process was repeated until a residual image was detected. It was found that below -27°C ghosting started to appear in the image. To ensure that no ghosting was introduced, the slightly higher temperature of -25°C was chosen to image the cable joint.

A second benefit of subtracting the dark image from the cable image is that all CCD arrays will have some defective pixels due to the manufacturing process. Defective pixels are pixels whose gain differs significantly from the array's average. These can either be 'hot pixels' that saturate very quickly or 'dead pixels' that stay black regardless of the light they receive. If these defective pixels are not removed from the cable joint image, they can be misinterpreted as defects in the cable joint, because, as described in Section 4.2, voids and inclusions also manifest themselves as pixels with intensities significantly different to the local pixel average. The defective pixels, if not corrected, will therefore

limit the minimum detectable size of a void or defect. By subtracting the dark image from the cable joint the value stored by a hot pixel is reduced to the local pixel average. Subtracting the dark image, however does not correct the dead pixels, this is achieved by using the methods described in Section 4.3.3.

4.3.2 Camera Response

The response of the CCD camera to exposure to x-ray radiation is not uniform across the imaging area due to optical transmission irregularities in the scintillating fibre screen and variations in the response of the different MOS capacitors in the CCD array. To minimize the lateral spread of information in the scintillating screen, gadolinium oxysulphide fibres are grown in order to decrease the lateral spread of light as described in Section 3.2.1.2. These fibers are then grouped together in small hexagonal bundles. These hexagonal bundles are then pieced together to produce the scintillating screen. Ideally, each fibre should have the same cross-sectional area as a pixel, i.e. 13.5 x 13.5 μm. In addition to this, each fibre should be positioned exactly over a pixel. With this arrangement the scintillator and CCD array would be perfectly coupled. In general however the fibres cannot be grown and positioned with this level of accuracy, and so each fibre is not perfectly coupled with a pixel. This means that an interface between two or more fibres can be located over a pixel, and as light is not channeled along these interfaces, the light received by the pixel is reduced. Light also is not transmitted in the gaps between each hexagonal bundle. This means that the pixels directly under a bundle gap are exposed to a reduced light flux compared to the pixels either side of the gap. These two effects result in a non-uniform illumination of the CCD array [89]. Figure 4.5 displays a 200 x 200 pixel section of a uniform exposure image, i.e. the CCD camera has been uniformly exposed to x-rays, without a test object. The hexagonal bundle boundaries can easily be seen along with the graininess caused by the fibre-pixel coupling. In this image some dark pixels can also be seen. These are dead pixels as described in the preceding section.

The second factor affecting the response of the CCD camera is the small variations in the response across the CCD array. Each pixel is a discrete capacitor, however, due to the manufacturing methods used to make the array, the materials used, and the size of each pixel, there are small microscopic variations between pixels [88]. The effect on the

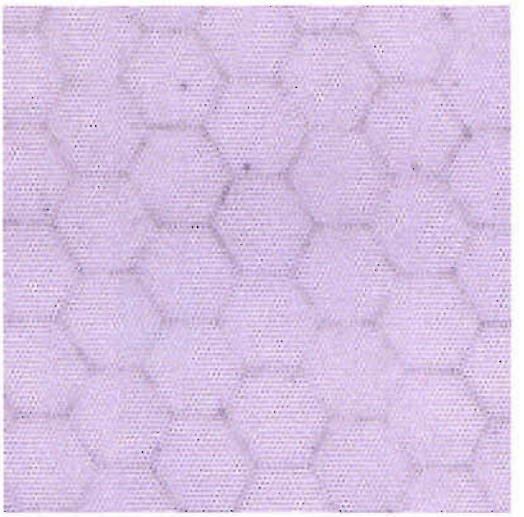

FIGURE 4.5: A 200 x 200 section of a uniform exposure image, that shows the effect on the image of the gadolinium oxysulphide fibre bundles of the scintillating screen.

image of these variations is much less significant than the scintillator effect, however, to produce a true image of the cable joint, these variations in pixel response have to be removed.

4.3.3 Photometric Correction of Images

The contributions to the raw pixel intensity, $I(x, y)$, of the above CCD camera characteristics can be defined by three fundamental parameters [88, 90]:

- $b(x, y)$ – the precharge value of pixel.
- $d(x, y, t, T)$ – the dark current due to the accumulated thermal loads during the exposure. The value of $d(x, y, t, T)$ is dependent on the exposure time t and CCD array temperature T.
- $r(x, y)$ – the response of the CCD camera.

The relationship of three parameters to $I(x, y)$ is displayed in Figure 4.6.

From this figure it is possible to see that the pixel intensity value relating to the attenuated x-ray flux that impinges on the pixel, $i(x, y)$, is related to $I(x, y)$ by [91]:

$$I(x, y) = b(x, y) + d(x, y, t, T) + r(x, y)i(x, y) \tag{4.1}$$

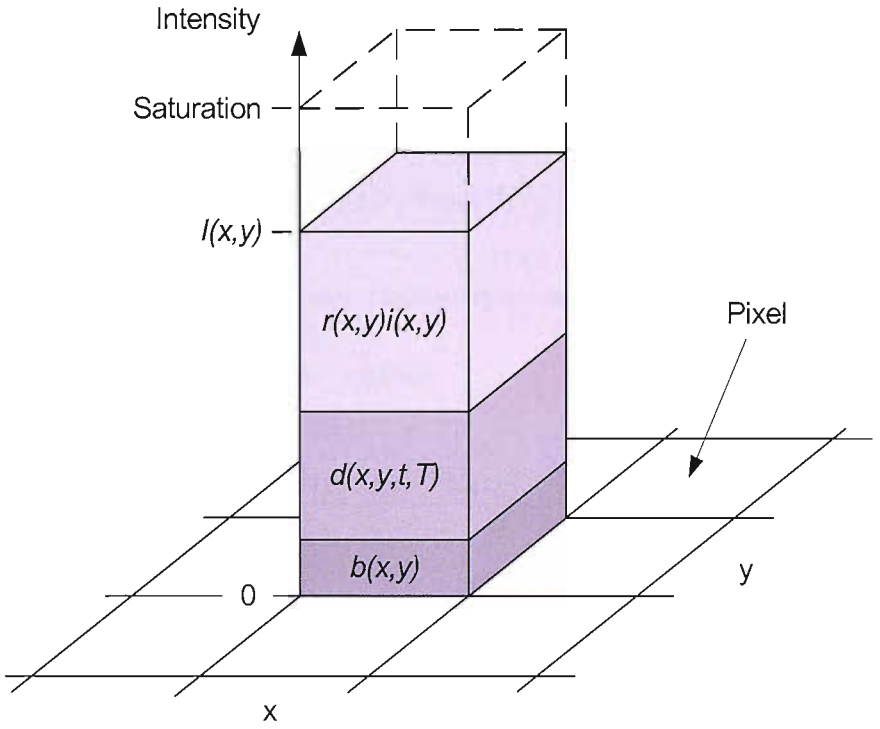

FIGURE 4.6: The different contributions to $I(x, y)$ of the raw x-ray image

In order to extract only the pixel intensity value relating to the attenuated x-ray flux, Equation 4.1 can be rearranged to

$$i(x, y) = \frac{I(x, y) - [b(x, y) + d(x, y, t, T)]}{r(x, y)} \tag{4.2}$$

The variables $b(x, y)$, $d(x, y, t, T)$, and $r(x, y)i(x, y)$ can be obtained from calibration images. $d(x, y, t, T)$ can be obtained by capturing an image with no x-rays being produced with an integration time the same as the raw cable image exposure time and the CCD chilled to the same temperature, namely -25 °C. This dark image, I_d, will also contain the offset, $b(x, y)$, therefore:

$$I_d(x, y) = b(x, y) + d(x, y, t, T) \tag{4.3}$$

To obtain the response of the individual pixels a flat field image can be obtained. A flat field image, I_{ff}, is obtained by irradiating the scintillating screen with a uniform x-ray flux. This is produced by irradiating the camera with no test object between

the x-ray source and the CCD camera. This will produce an image with the following characteristics:

$$I_{ff}(x,y) = b(x,y) + d(x,y,t,T) + r(x,y) \times \beta \tag{4.4}$$

where the β is the uniform x-ray flux impinging across the scintillating screen.

Equation 4.4 can be rearranged to produce:

$$r(x,y) = \frac{I_{ff}(x,y) - [b(x,y) + d(x,y,t,T)]}{\beta} \tag{4.5}$$

If Equation 4.3 is substituted into Equation 4.5, then the pixel response for the pixel located at (x,y) becomes:

$$r(x,y) = \frac{I_{ff}(x,y) - I_d(x,y)}{\beta} \tag{4.6}$$

Equation 4.3 and Equation 4.6 can then be substituted into Equation 4.2 to produce:

$$i(x,y) = \frac{I(x,y) - I_d(x,y)}{I_{ff}(x,y) - I_d(x,y)} \times \beta \tag{4.7}$$

To determine the value of β, the average pixel response caused by exposing the CCD array to a uniform x-ray flux must be calculated. This is achieved by subtracting the dark image from the flat field image to produce an image of the pixel responses. Then the average pixel value of this image can be calculated. This means that:

$$\beta = \frac{1}{m \times n} \sum_{x=1}^{m} \sum_{y=1}^{n} I_{ff}(x,y) - I_d(x,y) \tag{4.8}$$

where m and n are the dimensions of the image. For images from the XCAM CCD array m and n are both equal to 2048. Using this value of β also maintains the dynamic range of the raw image because it normalises the denominator in Equation 4.7 [88].

This process of extracting the x-ray flux attenuation data from the image is photometric correction. In practical terms this is achieved by capturing the required image of the

cable joint with the predetermined tube voltage, tube current, and exposure time. Then a dark image is taken with no tube voltage or current, using the same exposure time setting as the first image. After this, an image is taken with the cable joint removed from the exposure chamber. The same exposure time as the first two images is used for this image in order to maintain the same dark noise. The tube voltage and current, however, are set such that a uniform image can be captured without saturating any pixels, while allowing sufficient x-ray flux to impinge on the scintillating screen in order to obtain a good estimate of the individual pixel responses for the exposure time and temperature settings. The dark image is then subtracted from the cable and flat field images. The mean value for the flat field image, with the dark noise subtracted, is then obtained. After this the cable image is divided by the dark noise subtracted flat field image and the result multiplied by the mean of the flat field. The final process is to smooth the dead pixels. The division of the cable joint image by the flat field image corrects the dead pixel greyscale level so that the new pixel value is approximately the same as the local pixel intensity average, however this approximation can be improved, without affecting the surround pixels by further averaging. This is achieved by inspecting the flat field image for any pixel that has a greyscale value that is less than the mean value of the pixels of the whole flat field image minus three standard deviations of the distribution of all the pixels in the image. It can be assumed that these pixels are dead because the flat field image is illuminated by a uniform x-ray flux. The location of any pixel falling in this greyscale value band can then used to smooth the dead pixels in the cable joint image, by taking the mean of the local pixels surrounding the dead pixel in the cable image, and then replacing the dead pixel value by the calculated mean value.

4.3.3.1 Number of Exposures Required for Photometric Correction

In order to perform photometric correction of a x-ray image a good quality dark image, flat field image and raw cable joint image is required. The random nature of the thermal content of the dark image means that one single dark image will not necessarily be true representation of the thermal noise generated in subsequent cable joint exposures. To improve the representation, more than one dark image is required. These dark images are then combined into on single image by calculating an average of each pixel value for each specific image coordinate, from all the dark images generated. This average value for each pixel location is then used to generate a better representation of the

dark image. The central point indicator chosen to generate this image was the median. The median value was used rather than the mean or the mode, as it is resistant to individual pixel extremes unlike the mean, and is less computationally expensive than a mode estimator [92]. Ideally the number of images taken to generate the average dark image should be very large, because as the number of images tends to infinity, the effect of random variations in the individual images becomes less significant. To produce an infinitely large number of dark images, however, is not feasible due to the time constraints of capturing the images, and the memory requirements needed to store the images on a computer. From testing it was found that there were no significant changes in the medians calculated after seven images. Above seven images the median was not completely stable, however it would only vary by plus or minus one greyscale value. This represents approximately 0.4% error for a dark image taken at -25°C which has an average pixel greyscale of 250 points. Each dark image produced for subsequent photometric correction, was generated from the median average of seven dark images.

Due to the large signal produced and the repeatability of the imaging process, the flat field and cable joint images do not suffer from the same random fluctuations associated with the dark image. From testing, a good representation of both the flat field and cable image can be generated by a single image, however to ensure that that no errors are introduced into the inspection process three images of the flat field and cable joint were taken for all the images of cable joints and flat fields. These three images were then averaged in a similar manner to the dark image.

The effect of photometric correction of a cable joint image using the averaged image of seven dark images, and the average of three flat field and cable joint images can be seen in Figure 4.7. From this figure, it is apparent that the removal of the offset, dark current and camera response noise components from the raw image signal improves the clarity of the image produced, which in turn, improves the definition of the material interfaces. The increased definition is most noticeably seen in Figure 4.7(d) where the definition of the conductor shield is much more obvious in the photometrically corrected image compared to the raw data image.

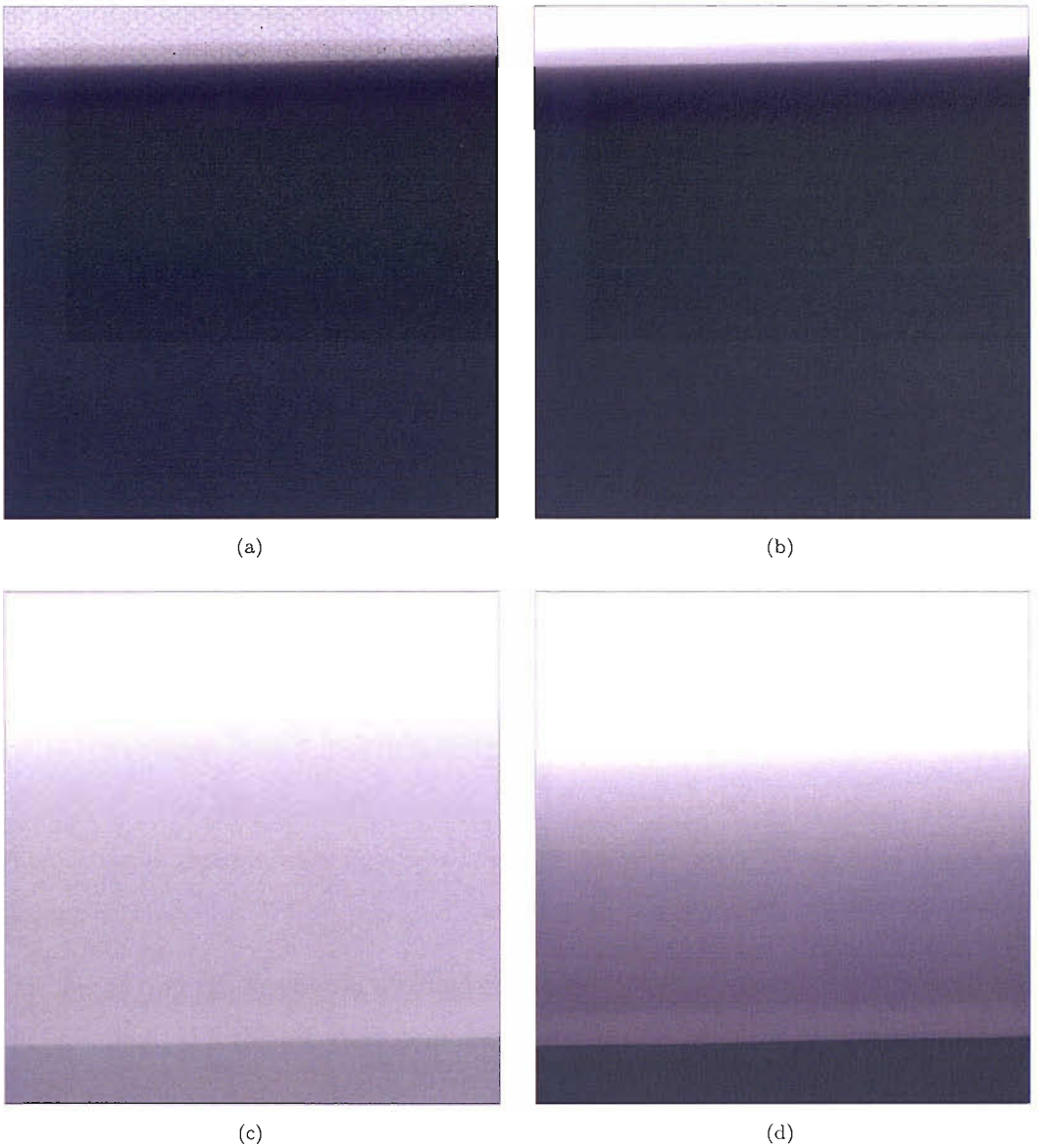

FIGURE 4.7: The effect of photometric correction of an x-ray image (a) raw image, (b) photometric corrected image, (c) increased brightness raw image, and (d) increased brightness photometric corrected image.

4.4 Generation of the X-ray Images

The techniques described above improve the quality of image of the cable joint generated by the CCD camera. These measures increase the chances of finding the material interfaces and any defects in the cable joint. The actual value stored by each pixel in the image, however, is determined by the cable component materials and dimensions, the x-ray energy generated by the source, the integration time of the exposure, and the conversion of the charge generated by each pixel into a voltage in the readout register.

4.4.1 The Material Properties of the Cable Joint Components

Section 4.2 states that in order for an image to be captured by the CCD array, the components within the cable joint must attenuate the x-ray flux. The amount of attenuation of the x-ray flux is determined by the radiological density of the material, its thickness, and the energy of the x-ray flux. The relationship between these variables is shown in the exponential attenuation law in Equation 4.10 [93].

$$I = I_O \times \exp^{\left[-\left(\frac{\mu}{\rho}\right)x\right]} \tag{4.9}$$

where I is the energy of the attenuated x-rays emerging from the material, I_O is the energy of the x-ray flux impinging on the material, $\frac{\mu}{\rho}$ mass attenuation coefficient, and x is the mass thickness defined as:

$$x = \rho t \tag{4.10}$$

where ρ is the material density and t is the thickness of material that the x-rays pass through.

This means that the amount of attenuation caused by each component in the cable joint can be estimated if the the x-ray source energy, the density of the each component, the thickness of each component and the mass attenuation coefficient for each material is known. The x-ray source energy is determined by the tube voltage and its units are MeV. The density of each material can be determined by weighing a known volume of a sample of the material. The density must then be calculated using the units g cm^{-3}. The thickness of the material can be determined by measuring the estimated pathway that the x-ray flux will take through the material in cm. The mass attenuation coefficient of the material can then be found in the look up tables in [93]. The tables contain the mass attenuation coefficients for all of the elements Z = {1,2,3... ...92}, and for 48 compounds and mixtures of radiological interest. For compounds and mixtures that are not listed in these tables, the values of their mass attenuation coefficient can be obtained by combining the mass attenuation coefficient values for each element according to their proportion by weight. With this information it is possible to estimate the attenuation caused by each material, in order to determine if the cable joint can be imaged. The

same results, however, can be achieved experimentally by x-raying the cable samples over a range of x-ray source tube voltages and currents.

4.4.2 The Effects of X-ray Source Voltage, X-ray Source Current, and Exposure Time on the Image Produced

Changing the x-ray source voltage, x-ray source current and the exposure time all affect the exposure conditions. As described in Section 2.2.4, increasing the x-ray source voltage increases the penetration power of the x-ray beam. A threshold voltage therefore exists that has to be exceeded in order to penetrate the whole of the cable joint. Changing the x-ray source current and exposure time affects the amount of x-ray flux that passes through the cable joint. If too little flux passes through the cable joint then the image will be too faint; if too much flux passes through the cable joint then the image becomes saturated. Figure 4.8 displays eight line plots of the pixel intensities of column of pixels from images of the 90 kV cable joint imaged in Figure 4.3. All the images generated for Figure 4.8 had a constant x-ray source current of 100 μA, however the x-ray source voltage and exposure time were varied. The current was set at 100 μA because the maximum power of the x-ray source is 10 W, therefore the maximum current available at 100 kV is 100 μA. The individual plots show the effect of increasing the voltage for a given exposure time. In all the plots it can be seen that increasing the x-ray source voltage increases the penetration power of the x-ray beam produced. This is characterised by the increased pixel intensity of the higher voltages compared to the lower voltages. Increasing the exposure time increases the amount of x-ray energy detected by the CCD camera, however if the voltage is below the threshold voltage there is little increase in the amount of energy detected. This is depicted by the plots of the 40 kV exposures. In the 20 second exposure the peak intensity (in the air gap above the cable) is approximately 400 greyscale levels; in the 90 second exposure this has increased to around 1000 greyscale levels; however the line plot to the right of 500 pixels (going into the cable) remains unchanged by the increased exposure time. Conversely, for the higher voltages, increasing the exposure time increases the amount of energy detected by the CCD camera across the whole image. In Figures 4.8(f) – 4.8(h) the increased exposure time has meant that 100 kV images are saturated at the air gap and insulation shield, and by Figure 4.8(h) even the 90 kV image has some saturation.

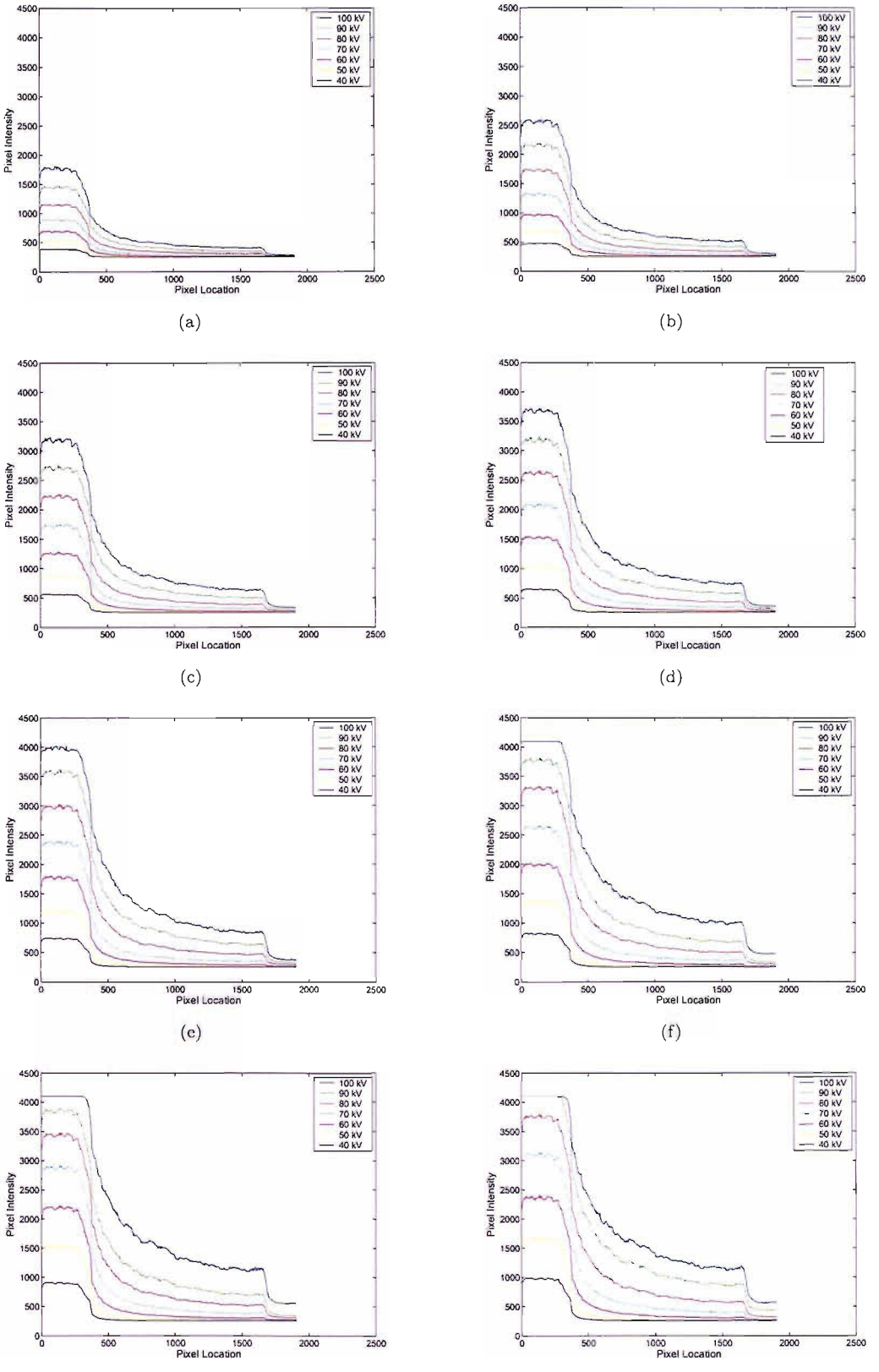

FIGURE 4.8: The effect of time and voltage on the image produced (a) 20 sec, (b) 30 sec, (c) 40 sec, (d) 50 sec, (e) 60 sec, (f) 70 sec, (g) 80 sec, and (h) 90 sec.

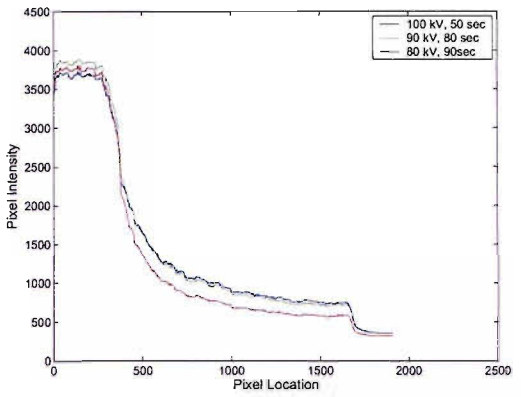

FIGURE 4.9: Three suitable exposure conditions to image a 90 kV EPR submarine cable joint.

With reference to Figure 4.8 it is possible to select the best exposure condition for the cable imaged. For this 90 kV cable either the 50 sec 100 kV, 80 sec 90 kV, or the 90 sec 80 kV exposure can be used because it is possible to see the conductor (the flat section to the right of 1600) and the insulation shield, and air gaps are not saturated. It would seem that with an increased exposure time both 60 kV and 70 kV setting could be used, however this would increased exposure time which would place additional time penalties on the inspection process. The 40 kV and 50 kV are not suitable exposure setting because even with a long exposure time they are unable to penetrate the cable joint insulation near to the conductor and conductor shield. Figure 4.9 displays the line plots of the three suitable exposures. From this plot it can be seen that the 100 kV exposure utilises the smallest proportion of the greyscale range from the edge of the conductor to the air gap above the cable. The 90 kV image uses more of the greyscale range, however the 80 kV image utilises the most of the range. This means that the contrast between the air gap and the edge of the conductor will be greater in the 80 kV image compared to the other two images.

The full range of greyscale levels have not been utilised with the 80 kV, 100 µA, 90 sec exposure, because the maximum value of the plot is around 3750 greyscale levels, 346 greyscale values less than saturation. To improve this greyscale utilisation, the amount of flux passing through the cable can be increased. This can be achieved by either increasing the x-ray source current or increasing the exposure time (Figure 4.10). Increasing the time or current both have the same effect: increasing the maximum pixel value up to saturation point. The advantage of increasing the current is that the exposure time is not increased, however the increased electron flux in the source makes focusing the

electrons more difficult, and so there is a slight increase in the focal spot size. This has the effect of reducing the sharpness of the image. For this reason a 10 second increase of the exposure time will produce a better image than a 25 µA increase in the current.

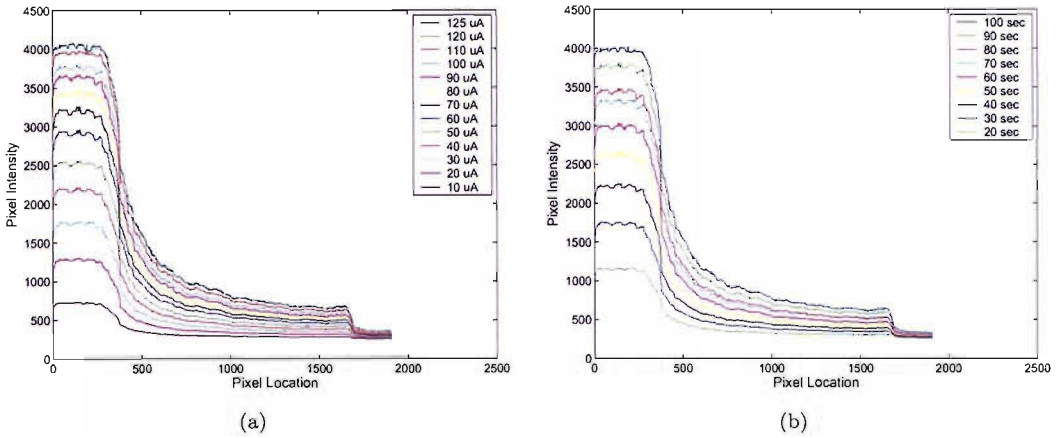

FIGURE 4.10: The effect of (a) current, and (b) exposure time on the image produced.

In order to image a 90 kV EPR submarine cable joint, the optimum x-ray source voltage, x-ray source current and exposure time is 80 kV, 100 µA for 100 second. These exposure settings are specific to this type of cable joint only. Other cable joints with either a smaller thickness of EPR insulation or a different insulation material such as XLPE will require different exposure settings. These exposure settings can be found using the same approach as detailed here.

4.4.3 Other Imaging Variables

To improve the signal to noise ratio of the images, resulting in improved detection of material interfaces and any defects that are present in the cable joint, it is possible to use a technique called binning. For standard x-ray capture the number of pixels in the image is the same as the number of capacitors in the CCD array, therefore the elementary site of the CCD array could be termed a pixel, however is not strictly correct. The elementary site of the CCD array should really be termed a photosensor. This distinction is required to explain the theory of binning. The technique of binning consists of adding the electrical charges contained in several photosensors; all of these photosensors are considered to be a single image pixel. Using the XCAM CCD x-ray camera it is possible to bin over either a 2 x 2 or a 4 x 4 groupings of adjacent photosensors. The addition of the charge occurs in the readout register of the CCD array. The advantage of this

technique is that the signal to noise ratio of each pixel is increased due to the reduction in number of pixels being read out. For a 2 x 2 setting, the contents of 4 photosensors are read as one packet of electrons. This means instead of four packets of electrons being read out individually, with the possibility of introducing readout noise each time, only one packet is read out, reducing the chance of readout noise being introduced by a quarter. The signal to noise ratio is therefore multiplied by a factor of 4 using 2 x 2 binning. The second advantage of binning is shorter exposure times can be used to generate an image because the photosensor area is multiplied by a factor of N^2 for a N x N binning, which means that the exposure time required to achieve the same pixel intensity value in the N x N binned pixel can be reduced by a factor of N^2 compared to the unbinned pixel. A second time benefit from binning occurs in the readout time of the CCD array. As there are fewer pixels to read, the time required to read this pixels is reduced correspondingly. The drawback to binning is the lowering of the resolution of the array. The disadvantage of this reduction in resolution, however, can be outweighed by the increased accuracy in detecting material interfaces and defects in the cable joint.

A second method of reducing the exposure time required to image a cable joint is to increase the charge to voltage amplification of CCD camera. The charge trapped under each pixel after the x-rays have stopped being produced is amplified into a voltage in the readout register. The XCAM camera has four gain settings for this process. The relative gains are such that the each gain setting increases the pixel charge by approximately twice the amount of the setting below. Increasing the gain, therefore, increases the greyscale values of each pixel, reducing the time required to generate the image. The main problem with using the gain to increase the signal produced, consequently reducing the exposure time, is that not only is the signal increased but the noise in the image is also increased. This means that an image generated on the lowest gain setting that fully utilises the 12-bit greyscale range will have a better signal to noise ratio compared with an image that fully utilises greyscale range generated on the highest gain setting.

4.5 Comparison of Photographic and CCD Array Images

The techniques described above can be used to optimise sharpness, resolution and contrast in the images of a cable joint generated by the CCD camera, while maintaining a short exposure time. In order to ascertain if these techniques produce comparable or

improved images of a cable joint compared to the original inspection procedure using photographic film, images of three test pieces were generated using both film and the CCD camera. The test pieces used were an image quality indicator (IQI), a penetrometer and a cable joint sample.

The IQI consists of seven steel wires of known thickness mounted in a translucent plastic envelope. The wire thicknesses used were 200, 160, 125, 100, 80, 63, and 50 µm. The wires were equally spaced at approximately 5 mm intervals (Figure 4.11). The purpose of using the IQI was to determine whether both imaging technologies could detect a steel wire 50 µm in diameter and to ascertain the relative quality of the images generated.

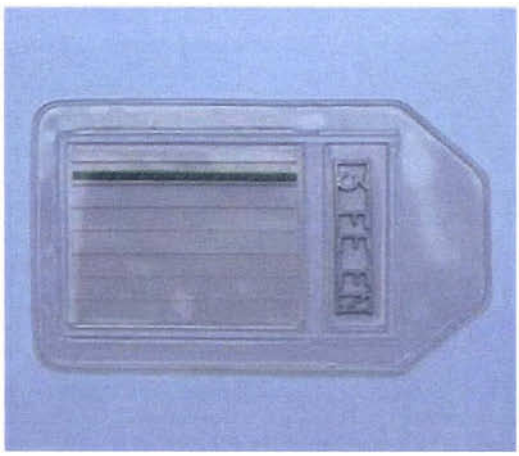

FIGURE 4.11: Photograph of IQI.

The penetrometer consisted of a moulded piece of polyethylene (Figure 4.12). The mould used to create the penetrometer was designed to create different thicknesses of polyethylene with a surface flaw introduced into each stage thickness. The flaws generated are 4 mm diameter cylindrical surface voids with a depth equivalent to 5% of the thickness of the particular stage of the penetrometer where the defect is located. This test piece was used to determine the ability of both imaging methods to detect known void defects.

The cable joint sample consisted of a hand lapped joint section of a 90 kV cable. Three holes were then drilled into the insulation and the semiconductive sheaths so that a wire could be inserted into each hole cable. The wires used extended from the central conductor to the outer semiconducting sheath. The thicknesses of these wires were 690, 230, 150 µm. This test piece was used to investigate how both imaging techniques performed when inspecting a cable with known defects (Figure 4.13).

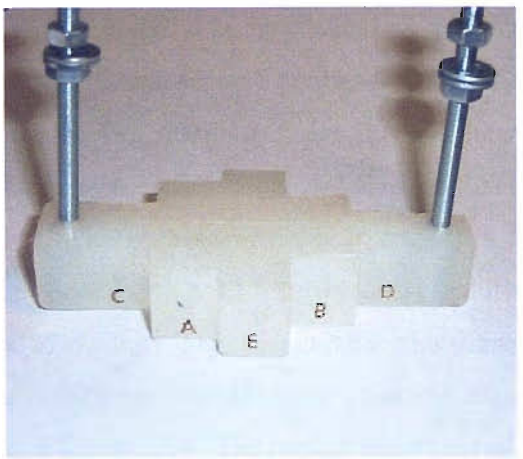

FIGURE 4.12: Photograph of Penetrometer.

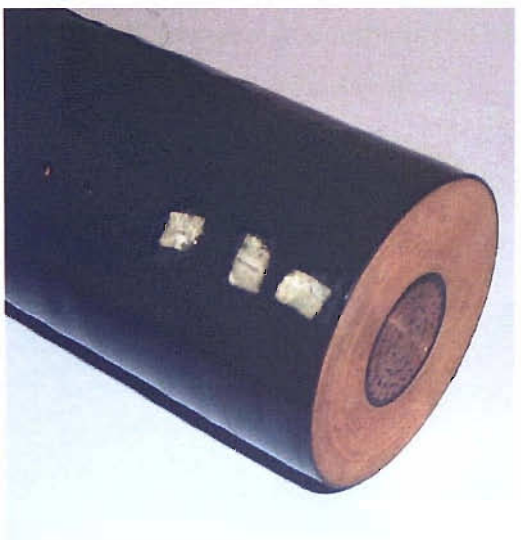

FIGURE 4.13: Photograph of Cable Sample.

In order to generate the two sets of images the test pieces were irradiated using the Kevex high stability x-ray tube and the intermediate irradiation chamber described in Section 3.6.3.1. The source exposure setting used to generate the images are shown in Table 4.1

Test Object	Sensor Type	Tube Voltage (kV ±2.5 kV)	Tube Current (mA ±50μA)	Exposure Time (sec ±0.5 sec)
IQI	Film	45	0.7	30
IQI	Camera	45	0.7	15
Pentrometer	Film	30	0.7	120
Pentrometer	Camera	30	0.7	85
Cable	Film	45	0.7	300
Cable	Camera	45	0.7	100

TABLE 4.1: Exposure setting for the generation of the test piece images.

This produced six images, three digital images and three photographic plates. In order to compare these images the film images were digitised. To do this, 35 mm^2 sections were cut out of each photographic film plate after the film had been irradiated, developed and finally fixed. To digitise these film sections, a Nikon LS-200 35 mm^2 high-resolution negative scanner was used. This scanner was able to scan each film section at a spatial resolution of 13.5 µm per pixel, with a 12 bit greyscale resolution. These images were then cropped to 27.6 x 27.6 mm. This meant that the digital images produced by scanning sections of the film plates were identical in specification to the digital images produced using the x-ray CCD camera. The images generated are shown in Figures 4.14 – 4.16.

Figure 4.14 shows the film and camera generated images of the IQI. The four wires shown are the smallest four wires, with diameters from 100 down to 50 µm. Both images of the IQI appear to be relatively similar. The thickness of and the spacing between the wires are comparable, but the background illumination is darker in the camera generated image. This is due to the exposure settings used to generate each image.

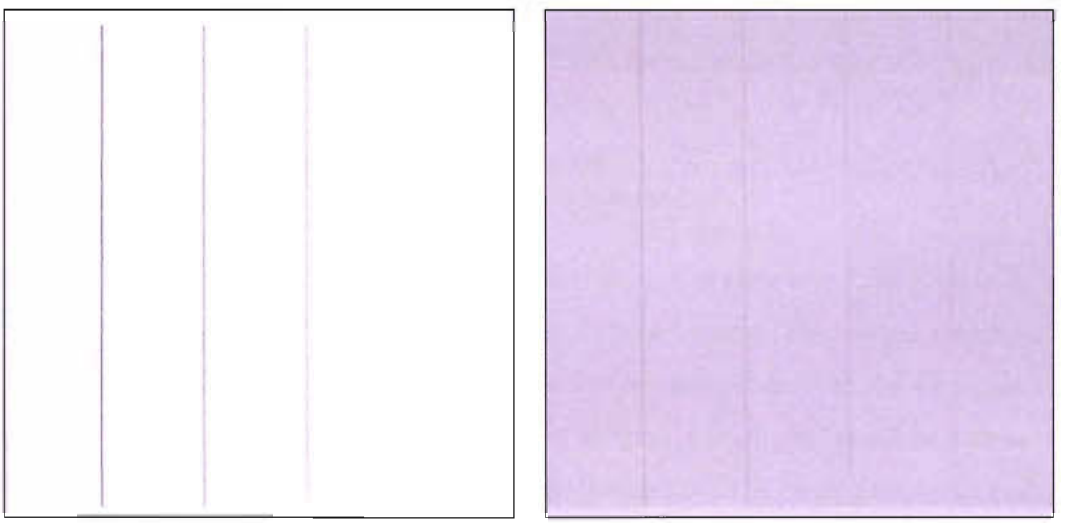

(a) (b)

FIGURE 4.14: X-ray images of the IQI (a) Film generated image, and (b) Camera generated image

Figure 4.15 shows the camera and film generated images of the penetrometer. The two stages shown are the thickest and third thickest stages with depths of 42 and 22 mm respectively. Both images have the letters 'E' and 'B' clearly depicted. These letters are the brass identification lettering on each stage. The letter 'E' is the identification letter

on the thicker of the two stages. Above the letter identification of each of these stages is the known cylindrical surface flaw. The 'double edge' effect that can be seen in both images was caused because the alignment of the penetrometer was not perpendicular to the x-ray flux. The penetrometer images also display a difference in background illumination, with the camera generated image being darker again. The film image also has noticeable digital bloom around the letter identifications, introduced when the film was digitised.

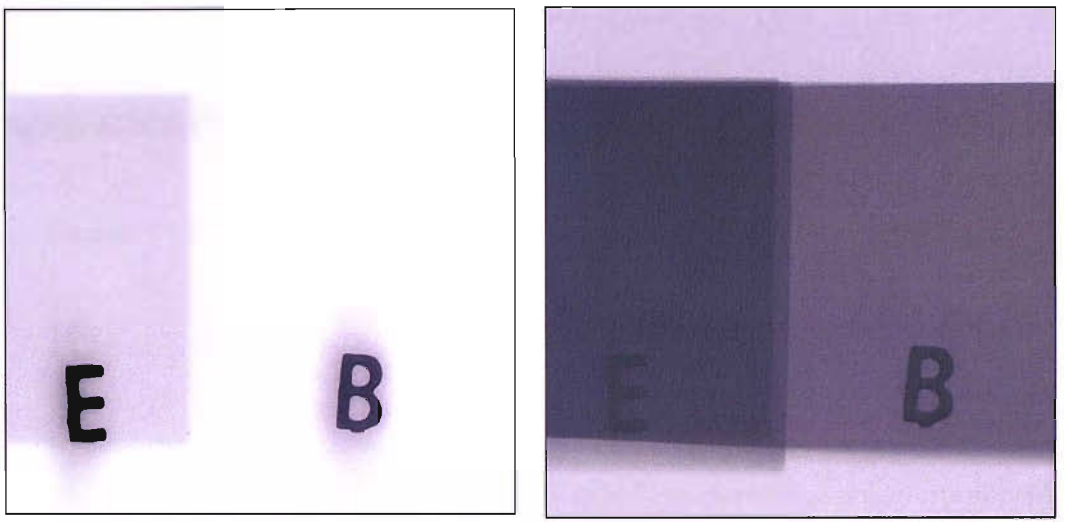

(a) (b)

FIGURE 4.15: X-ray images of the Penetrometer (a) Film generated image, and (b) Camera generated image

Figure 4.16 shows the camera and film generated images of the cable joint sample. It is possible to see sections of the two largest wires in both images. The central portions of the wires can be seen in the film image, however, the external ends of the wires can be seen in the camera image. Due to the exposure settings, the insulation shield and some of the insulation has been over exposed in both images, but the overexposure is greater in the film based image. The reason for over exposing the outer insulation and insulation shield in the film generated image is due to the non-linear response of the film making it difficult to see the insulation shield and the conductor shield in one single image, as described in Chapter 2, Section 2.4. The background illumination of these two images also follows the trend shown in the other two pairs of images. Unfortunately, during the production of the 35 mm slide of film based image, the film was scratched, as seen in the lower portion of this image. The thicker wire in this image is less straight than the camera image, due to the wire being reinserted before exposure.

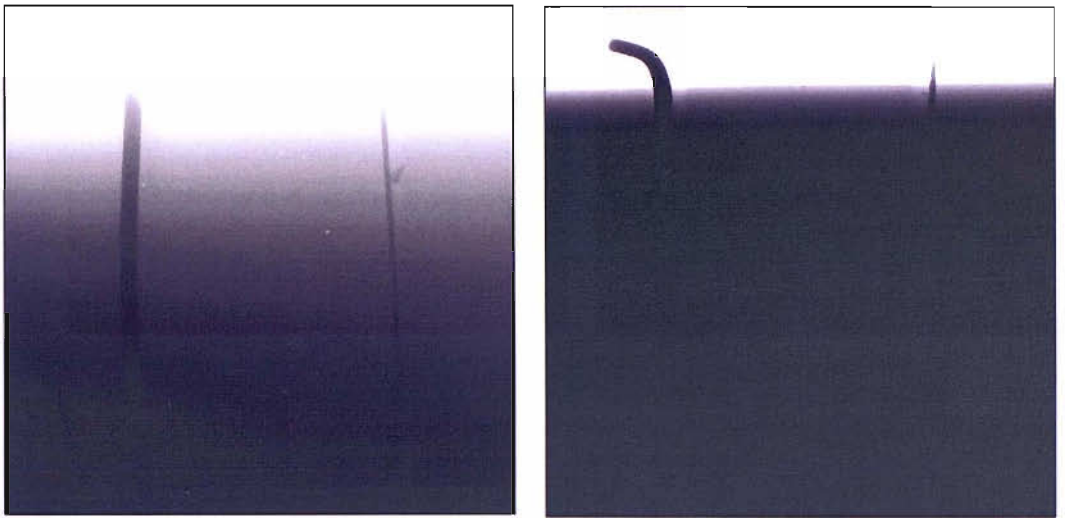

(a) (b)

FIGURE 4.16: X-ray images of the cable joint sample (a) Film generated image, and (b) Camera generated image

4.5.1 Analysis of the Initial Results

To compare the quality of these film and camera based images, and the ability to detect defects, the images were processed using a statistical image processing algorithm based on theories that are described in Chapter 6. These algorithms were used to improve the contrast between the different components in the cable and to highlight the defects in the images. The images produced as a result of processing the images in this way are shown in Figures 4.17 – 4.19

Figure 4.17 shows the processed images of the IQI. All of the four wires can be seen in both images, therefore proving that both imaging systems can detect steel wires 50 µm in diameter. The clarity of the camera images, however, is much greater than the film images. The decreased clarity in the film image is caused by digital blooming generated during the digitisation process. The background of the camera image is also more uniform compared to the background in the film image.

Figure 4.18 shows the processed images of the penetrometer. Both of the images show the 'E' and 'B' letter identifications, however the letter clarity is better in the camera generated image. The reduced clarity of the identification letters in the film image is caused by the digital blooming that has been introduced during the digitisation of the film. The edges of the penetrometer are more defined in the camera image and both the

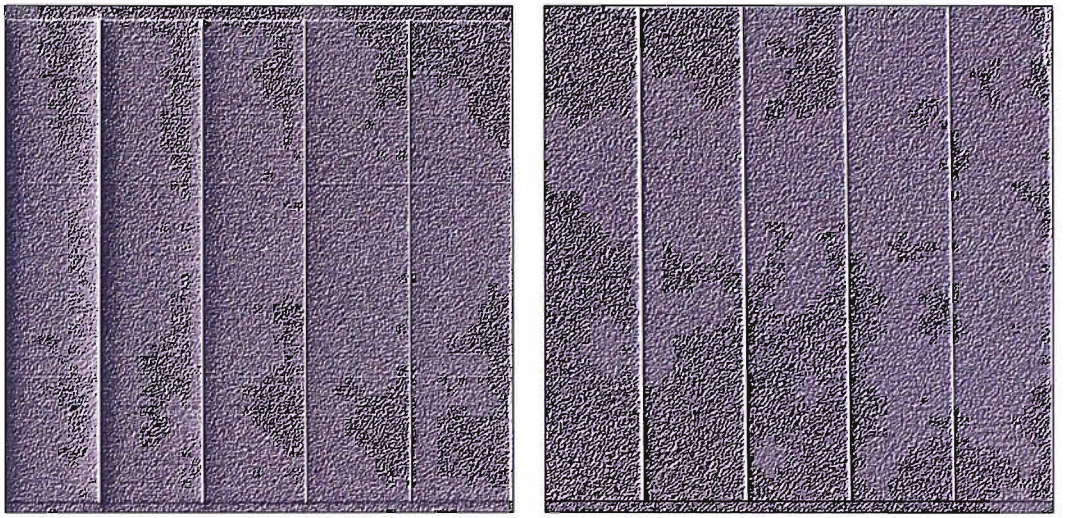

(a) (b)

FIGURE 4.17: Processed images of the IQI (a) Film generated image, and (b) Camera generated image

known voids are also only detected in the camera image. Both defects have not been detected in the film image due to the non-linear response of film to x-rays [94]. From this test piece it appears that the known defects are detected better using the camera to generate the images.

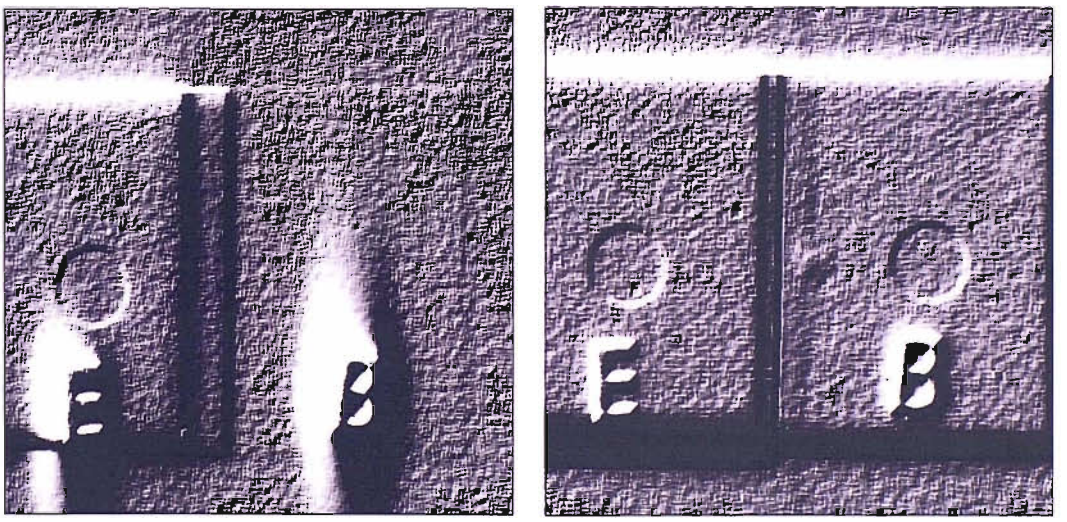

(a) (b)

FIGURE 4.18: Processed images of the penetrometer (a) Film generated image, and (b) Camera generated image

Figure 4.19 shows the images of the cable joint sample. In both the camera and film images it is possible to see the central conductor, the two wires extending completely

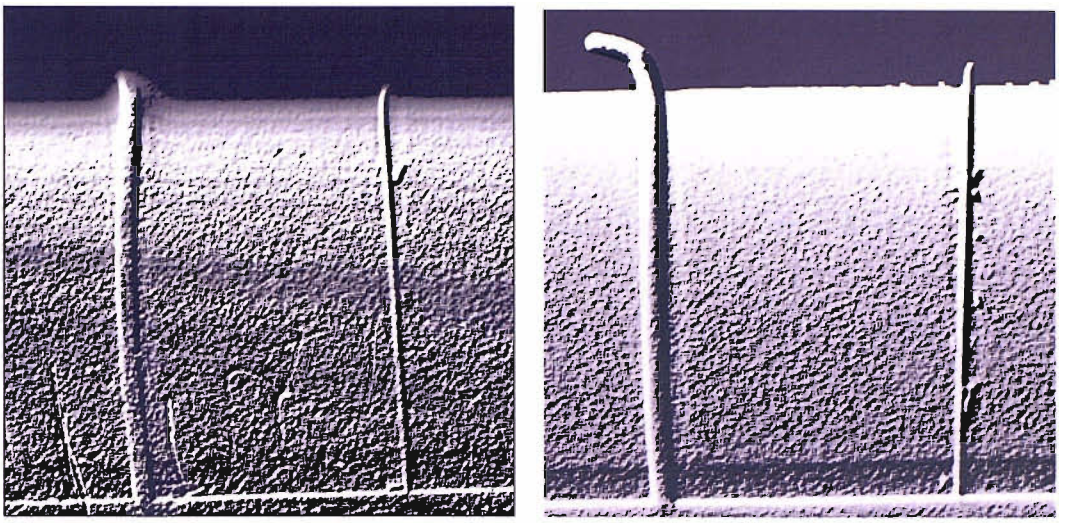

(a) (b)

FIGURE 4.19: Processed images of the cable joint sample (a) Film generated image, and (b) Camera generated image

through the conductor shield to the central conductor. Due to the exposure settings, all of the wires have been overexposed except for the larger wire in the camera image. The clarity of the camera image is better than the film image, due to the increased contrast between the wires and the cable and between the different components of the cable joint. In the camera generated images the conductor shield is clearly defined, whereas it is barely visible in the film image. The drilling holes are also more discernable in the camera image. In this image the drilling swarf generated during the manufacture of the holes is clearly visible; this swarf is not readily seen in the film image. The wires in the camera image are also better defined. From these two images it is possible to conclude that the camera generated images produce clearer images, with a greater information content, of the cable joint sample, compared to the digitized film generated images.

From the test images it can be seen that digital images generated using the camera are significantly better than the digital images generated using film techniques and a digital scanner because the amount and clarity of information in the camera images exceeds the information obtained from the film images. This conclusion has also been reached by other researchers, for example, Turner et al [95]. The main disadvantage in using camera generated images is that the field of view is relatively small in comparison to the size of a photographic plate. To build an image of the whole of the cable joint sample, therefore requires multiple images of the joint to be captured at a range of angles along the entire length of the joint in order to completely monitor the insulation system as

described in Chapter 2, Section 2.4. This method of imaging the whole length of the cable joint is similar to the original inspection system, however due to the use of a digital sensor, the images produced can be combined to produce one single image of the cable joint sample. In order to combine the individual images into a single image, the images of the cable joint sample taken at the same angle have to be first spliced together, i.e. the images taken along the length of the cable joint at 0° are spliced together. This splicing of the images produces one single image of the entire length of the insulation system of the cable joint sample at that given imaging angle. This process then has to be repeated for all the imaging angles to produce a set of full length images of the cable joint sample. These images can be combined into one single image if the centre of the rotation of the cable joint sample, in relation to the spliced images, is known. This is achieved by arranging the full-length images in 3D polar coordinate space, using the centre of rotation as the reference point for all the images. The 3D image produced will therefore geometrically relate the information in each of the individual images and allow complete visualisation of the internal structure of the cable joint. This chapter describes how the imaging hardware was aligned in order to produce 3D images of the cable joint samples, the affect on the individual images caused by the position of the imaging hardware components, and the method by which the individual images are montaged to produce the full-length images of the cable joint. The inspection of these images and production of the final 3D image is detailed in Chapters 5 – 7.

4.6 Positioning and Alignment of the X-ray Imaging Hardware

Using the microfocus source and digital x-ray camera in order to capture images along the entire length of a cable joint sample, and at a range of angles, the sample has to be clamped into the cable joint sample mount described in Chapter 3, Section 3.6.3.2. With this mount, the cable sample can be indexed along the axis of travel of the translational stage and rotated about the axis between the conical tips of polarizer and the brass studding in the custom made brass mount (Figure 4.20). The montaging and 3D image production process can only be achieved using the cable joint sample mount, if location of the axis of rotation of the cable joint sample, the plane translational axis of the

translational stage, the plane containing the CCD array of the CCD camera, and the point source of the x-ray source are known.

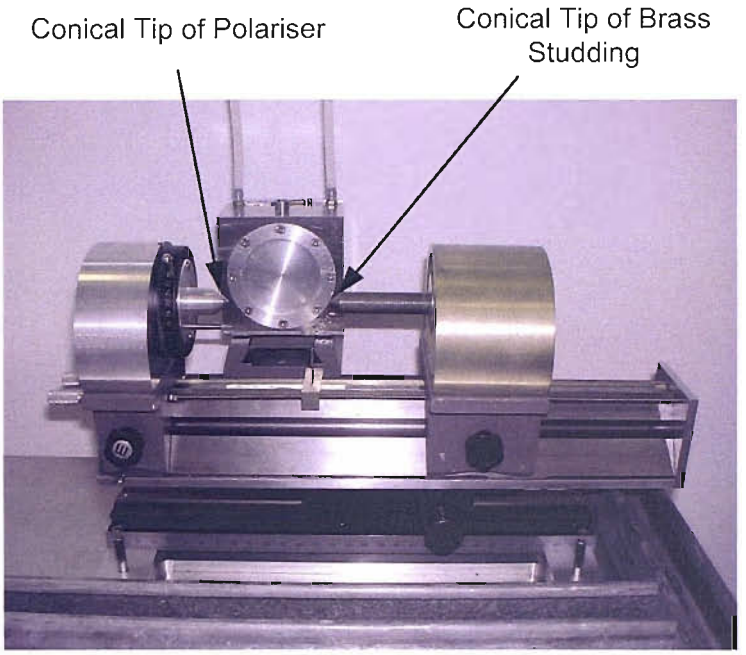

FIGURE 4.20: The cable mount showing the axis of rotation of the cable joint sample

4.6.1 CCD Array, Translation Stage and Axis of Rotation Alignment

The main components of the cable mount are the cable mount translational stage and its associated fixings; the cable mount optical rail and its associated fixings; the polarizer and its associated fixings; and the custom made brass mount. The main components of the camera mount are the camera optical rail and its associated fixings and the camera translational stage. All of these components were arranged on a 6 mm thick aluminium base plate. In order to ensure that this main base plate was flat, two steel 'U' sections were fixed along the longer sides of the plate and then cross struts were added (Figure 4.21). This arrangement meant that the cable mount, CCD camera and x-ray source were mounted on a known flat plane. This was essential in order to be able to determine the relative locations of each component in 3D space.

To ensure that the cable mount translational stage would move the centre of rotation between the polarizer and brass studding in an axis parallel to the plane of the CCD array, a known datum was set on the 6 mm aluminium plate. Each component was then added to the system and aligned to the known datum. The datum used was the track

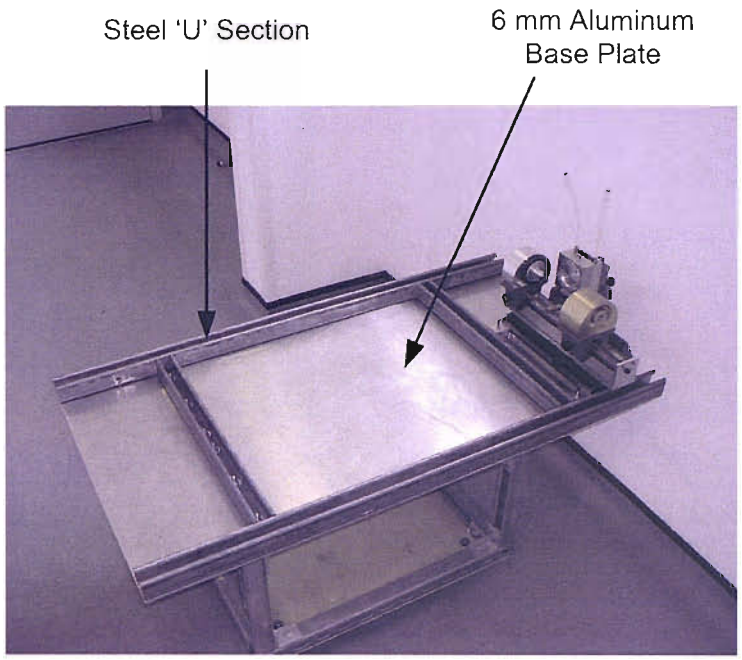

FIGURE 4.21: The aluminium base plate and steel 'U' sections. The base plate is supported on a small trolley for photographic purposes

of the cable mount translational stage, that was attached to the main aluminium base plate via two aluminium plates. The lower of these two plates is rigidly fixed to the main base plate and has four aluminium pillars attached perpendicularly to its upper surface. The upper plate is rigidly fixed to the base of the translational stage track, and has four holes through which the pillars of the lower plate can pass through (Figure 4.22). This allows the track to be raised and lowered, parallel to the main base plate. This translational freedom was required in order to position the cable joint sample at the correct height for the insulation system to be imaged. With this arrangement, when the four pillars of the lower plate are located in the holes in the upper aluminium plate, the translational stage track is located in a plane parallel to the main aluminium base plate. The track of the translational stage therefore could be used as the datum to which the remaining components of the cable and camera mounts could be aligned.

The second component to be added to the system was the camera optical rail. To provided a degree of translational freedom for the camera and cable mount, optical rails were used with optical rail mounts. Optical rails were used to allow the camera to be moved along the rail without having to re-align the system. The camera optical rail is attached to the main aluminium base plate by two aluminium raising blocks. These blocks are required to elevate the camera so that the CCD array is at a suitable height

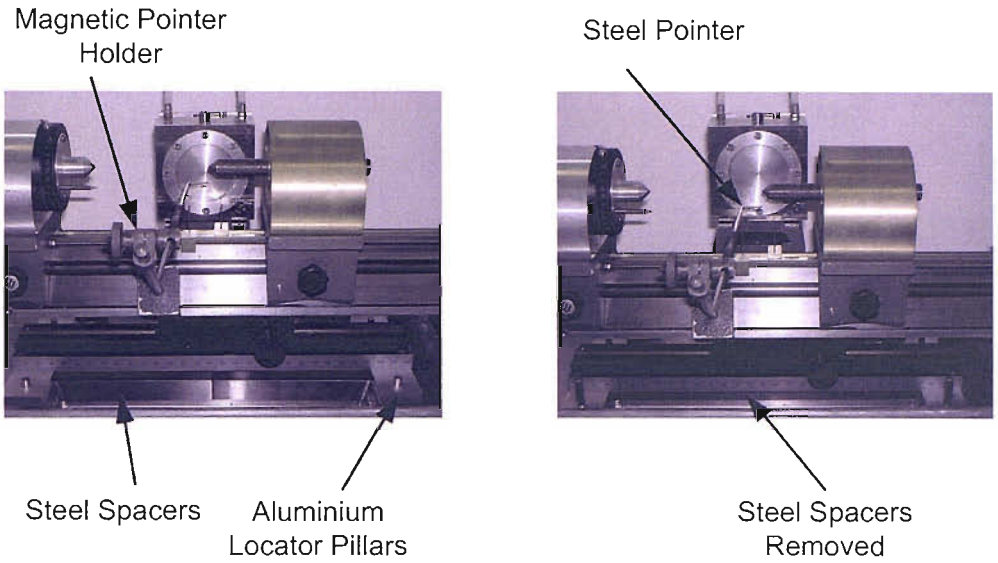

FIGURE 4.22: (a) The translational stage elevated by two 18 mm steel spacers, and (b) the translation stage in the lowered position.

in order to image the cable joint sample. These two blocks are rigidly fixed to the base of the optical rail, however, the fixings used to attach the blocks to the aluminium plate provide a small amount of rotational freedom for the optical rail. This is achieved by using a single bolt to hold each block to the 6 mm aluminium base plate. The righthand block (viewed from the position of the x-ray source) also has a set of adjustment screws. These screws are housed in a 'n' shaped block of aluminium attached to the right hand optical rail mounting block. Inside the 'n' of the adjustment block is a second block of aluminium attached to the 6 mm aluminium base plate (Figure 4.23). By tightening the front screw, of the adjustment mechanism, and releasing the back screw (again looking from the position of the x-ray source), the righthand optical rail block is rotated away from the cable mount translational stage track, and vice versa. The camera mount optical rail and the cable mount translational stage track were therefore aligned using these adjustment screws. To increase the accuracy of the alignment process two laser levels were used. Both laser levels consisted of a straight edge in parallel with a laser light line. The laser lines produced were used to extend the axis of both optical rail and the translational stage track, by clamping the straight edges of the laser levels to the translational stage track and the optical rail. The light beam produced was projected onto two parallel white surfaces separated by 20 m. The closer of the two surfaces was 1 m from the centre of the translational stage track. This closer surface could

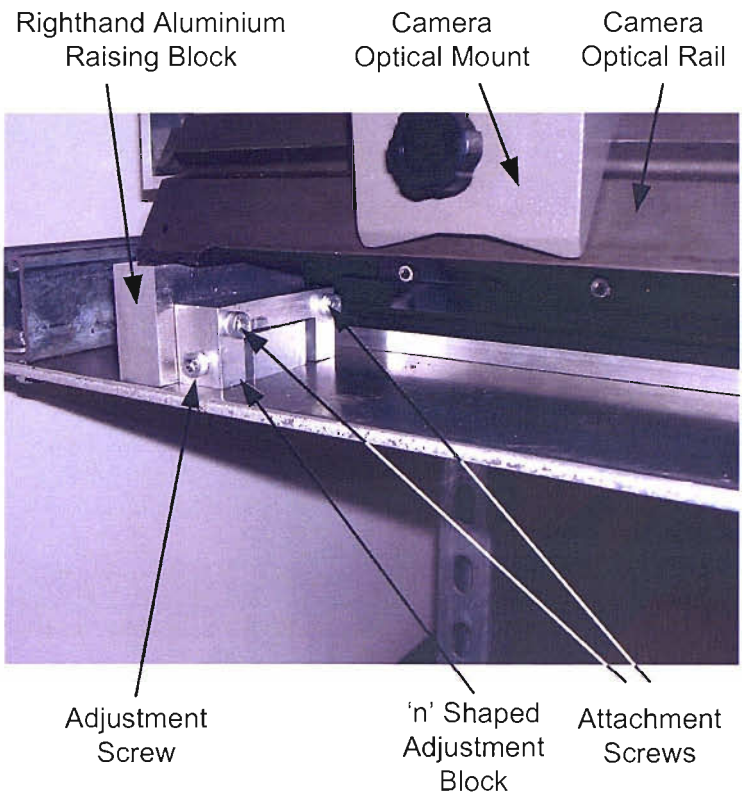

FIGURE 4.23: The camera optical rail mounts and adjustment

rotate to enable the laser lines to be projected onto the rear surface. If the two beams were parallel, and hence the translational stage track and camera optical rail also being parallel, the distance between the points where the beams hit the the two white surfaces would be the same. To measure the distance between these two lines a digital vernier was used. Using this system it was possible to measure the separation between the beams to within 100 µm. This means that the alignment of the components was within 0.000603°. To achieve this level of alignment, the angle between the camera optical rail and the translational stage track was adjusted, using the camera optical rail adjustment screws, until the two components were parallel.

The next component added to the system was the cable mount optical rail. This was aligned to the camera mount optical rail using the laser line method described above. The alignment adjustment of the cable mount optical rail was also achieved using a similar system of adjustment screws as used for the camera optical rail (Figure 4.24).

The final component to be added to the system was the camera translational stage. This translational stage was also mounted on optical rail mount (Figure 4.25). It was

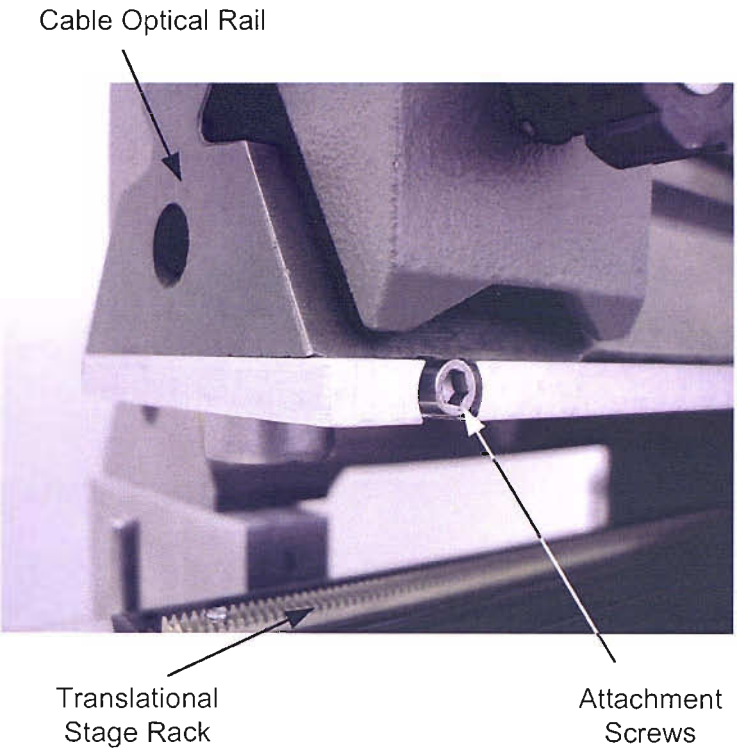

FIGURE 4.24: The cable optical rail mounts and adjustment

therefore only necessary to align the translational stage, which was achieved using the small amount of float offered by the fixings between the translational stage and the optical rail mount. Once this had been aligned, the camera was then mounted onto it. The alignment of the front face was then verified using the laser levels. The polarizer and brass cable mount were then mounted onto the cable mount optical rail. The polarizer and brass cable mount were also mounted on optical rail mounts. The alignment of these components with their optical rail mounts was set during manufacture. This alignment process therefore ensured that the cable joint sample could be indexed past the CCD array with the centre of rotation of the cable joint sample parallel to the plane containing the CCD array of the camera.

4.6.2 CCD Array and X-ray Source Alignment

As well as aligning the camera and the cable mount, it was also necessary to align the camera with the x-ray source. It was not possible to align these two components using the method described in the section above because the source of the x-ray flux is a point rather than a axis. The main requirement of the x-ray source was to ensure that the

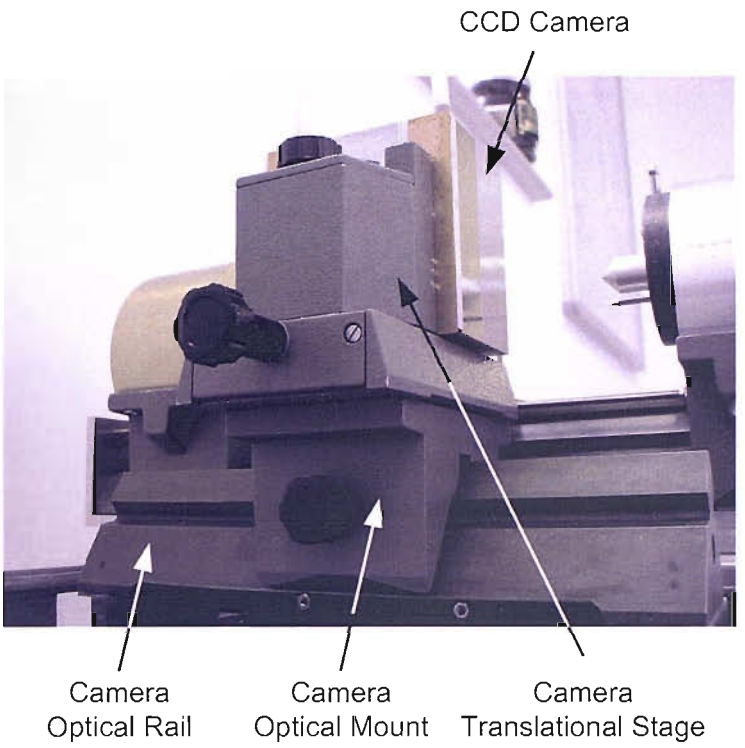

FIGURE 4.25: The camera translational stage

central line of the x-ray flux produced from the point source was directed at the centre of the CCD array at a perpendicular angle. If the source was not aligned in this manner the images produced would be affected by the non-uniform irradiation of the cable joint samples caused by the misalignment.

To align the x-ray source and the CCD array, a mandrel was manufactured. The mandrel was made from a length of brass bar. Into this bar were cut twelve 2 mm wide, 5 mm deep grooves. Each end of the bar was machined flat with a conical hole that allowed the mandrel to be held by the polarizer and the brass studding of the cable mount (Figure 4.26). To align the source and the CCD array, the mandrel was imaged to produce an image similar to the image in Figure 4.27. Due to the conical nature of the x-ray flux produced by the source, only the central section of the x-ray flux would impinge on the mandrel at right angles. Either side of the central section of the flux the beam would impinge at slightly smaller angles, resulting in some of the x-ray flux passing the sides of the castellations of the mandrel. This manifests itself in the image as a castellation with slightly bowed edges. This means than the centre of the x-ray flux can be found by imaging the mandrel to find the the castellation with parallel edges. The process of locating the castellation in the image with parallel edges was improved

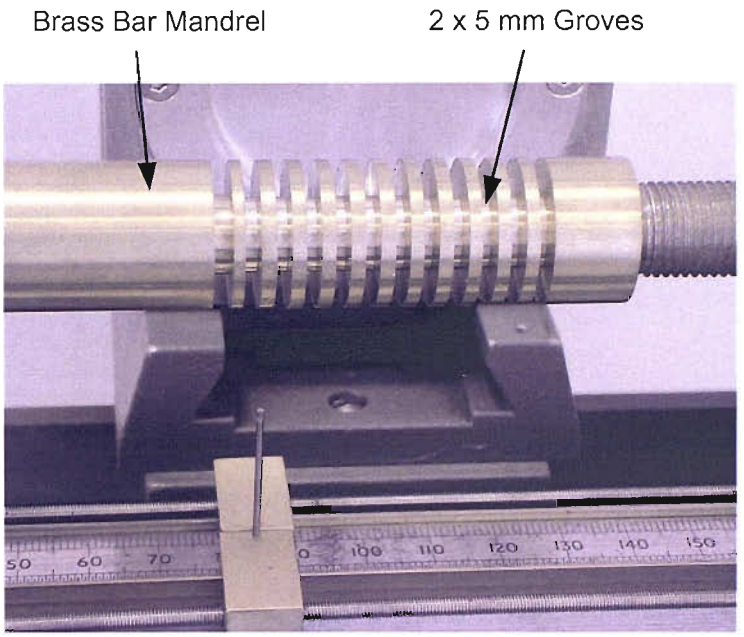

FIGURE 4.26: The alignment mandrel

by finding the edges of the mandrel using a Canny edge filter [96]. The basic operation of this filter is to detect any significant changes in pixel intensity that are associated with the step changes that occur at the boundaries of the structure within an image. This is achieved by first smoothing the image with a Gaussian filter [85]. The smoothed pixel intensities are then differentiated to find the gradient of the image. This gradient image is then thresholded. Any gradient greater than the threshold is then deemed to be an edge, and the associated edge pixels are plotted on a binary image. This edge detection operator is described in more depth in Chapter 5, Section 5.1.1. The edges could then be plotted onto the image as white lines. These white lines could then be used to find the castellation with parallel edges (Figure 4.27(a)). If this castellation is then positioned in the centre of the image, by moving the source, then the x-ray flux can be assumed to be in the centre of the CCD array. This process had to be performed for both the vertical and horizontal axes of the CCD array by imaging the mandrel horizontally and adjusting the source position, followed by imaging the mandrel in the vertical position and adjusting the height of the source. Once these two processes had been performed, the source was mounted onto aluminium plate with nylon pillars. The pillars were manufactured to ensure that the source would maintain the correct elevation above the 6 mm aluminium base plate regardless of it position on the base plate.

To ensure that the x-ray flux was at 90° to the CCD array, as well as centralised, the

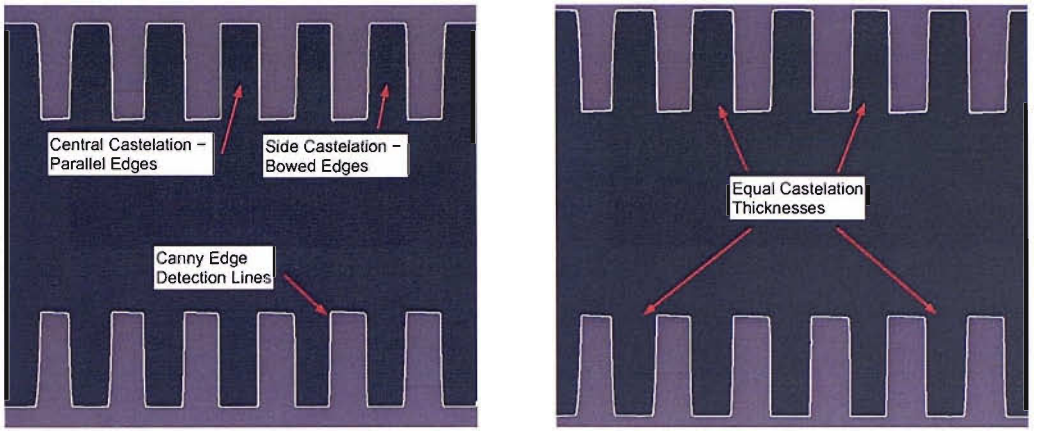

(a) (b)

FIGURE 4.27: (a) Centralisation, and (b) skew alignment of the x-ray flux using the mandrel.

widths of the castellations can be used. If the x-ray flux is at 90° to the CCD array, the two castellations either side of the central castellation should be the same width. The next two outer castellations should also be the same width, and so on (Figure 4.27(b)). The size of the castellation could be measured using the Canny edge filtered data. Using the upper edge of the mandrel, the thickness of each castellation can be calculated by counting the number of pixels between the start of the upward deflection of the castellation and the end of the downward deflection. This process can also be used to measure the thicknesses of the castellations of the lower half of the image. The thickness of the respective upper and lower castellations, however, should be identical. In order to improve the accuracy of this process, the camera was retracted to the back of its translational stage in order to increase the magnification of the mandrel. For the vertical and horizontal alignment however it was beneficial in reduce the size of the castellations by reducing the magnification of the mandrel, in order to ensure that the centre of the 'straight edged' castellation was located in the centre of the image.

The final use of the mandrel was to check the horizontal alignment of the axis of rotation of the cable mount in relation to the CCD array. To do this the mandrel was clamped into the cable mount, imaged and the edges detected using the Canny edge detection method. The flats of the upper and lower outer surface of the bar were then located, and the average height of these two sets of flats calculated. A horizontal line was then drawn across the row of the image relating to the average height of both flats. The translational stage could then be shimmed at the relevant end in order to make the

lines of the flats parallel to the horizontal line. Figure 4.28, displays the result of this alignment process. From the figure, it can be seen that the mandrel is horizontal to the x-axis of the CCD array.

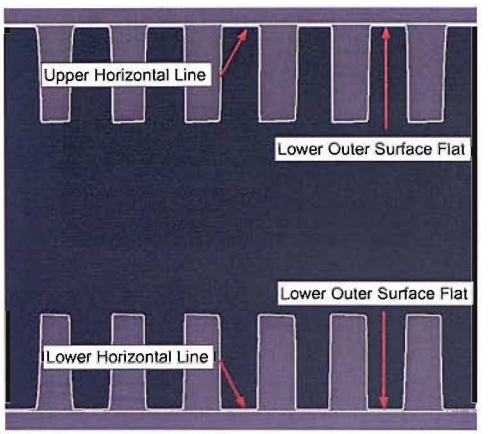

FIGURE 4.28: Horizontal alignment using the mandrel

4.7 Magnification Effect of the Source Positioning

The alignment of the x-ray imaging hardware ensures that the individual images of the cable joint sample can be montaged into a full length image of the insulation system of the cable joint sample. To ensure that these full length images can be used for dimensional checks on the thickness of the components of the cable joint sample and to determine the size of any defects in the cable joint, the magnification introduced into the image by the hardware positioning has to be determined.

The X-Tek source has a focal spot size of 5 µm with a cone angle of 25°. This means that the size of the x-ray beam increases proportionally with distance from the source. If the x-ray source was positioned and then aligned close to the cable joint sample mount, then more x-rays will pass through the cable joint sample compared to the amount of x-rays that would pass through the sample should the source be located further from the mount. This means that less flux is required to image the joint sample if the source is placed close to the sample mount. Secondly, because x-ray power decreases following the $1/r^2$ relationship, the penetration power of the source can also be reduced. The main disadvantage of placing the x-ray source close to the sample mount is that due to the cylindrical shape of the cable joint and the flat imaging surface of the CCD array, the image generated is magnified. Figure 4.29 shows that even if the CCD array is placed

directly behind the cable joint, there is still a degree of magnification introduced into the image, however as the distance between the source and the cable joint increases, this magnification is reduced. Magnification of the cable is not detrimental to the image quality, in fact the spatial resolution is increased due to this magnification, however, the CCD camera has a field of view that is only 27.6 x 27.6 mm. This is a relatively small field of view compared to the size of the cable joint, and therefore any magnification increases the number of images required to inspect the whole cable joint, as described in Chapter 3, Section 3.4. In order to reduce the amount of magnification in the image, it was therefore necessary to place the source as far from the cable joint sample as possible, however as the distance increases the penetration power and flux density of the x-ray beam decreases. The source, therefore, had to be placed at a distance that was a compromise between reduced magnification and maintenance of the penetration power and flux density.

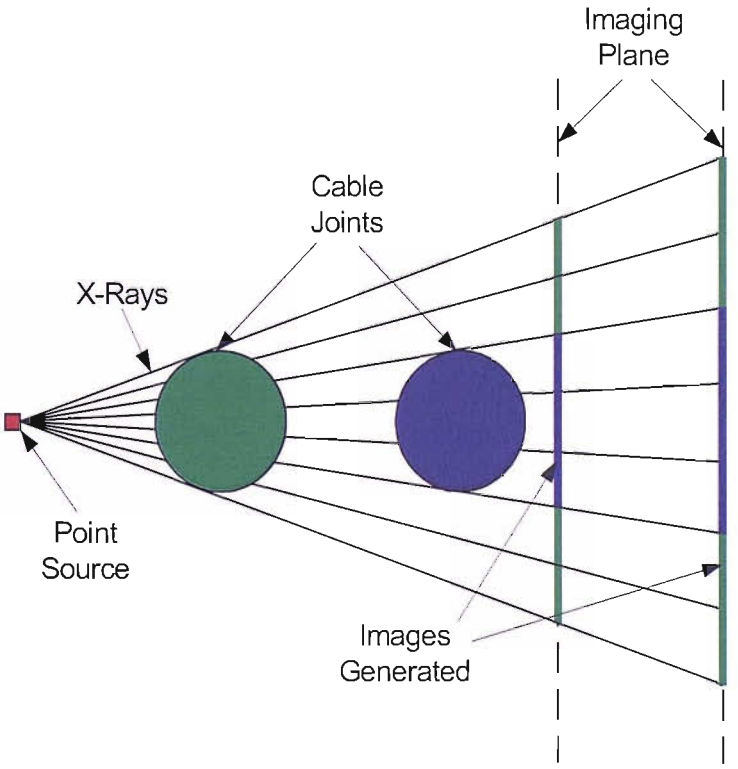

FIGURE 4.29: The magnification due to the geometry of the source, cable joint and imaging sensor

In order to determine the optimum position of the x-ray source, in relation to the CCD array, the amount of magnification introduced into the image, caused by varying the separation between the source and the CCD array, and between cable joint sample

axis of rotation and CCD array, had to be calculated. This was achieved by initially maintaining a fixed distance between the axis of rotation of the cable joint sample and the CCD array while varying the separation between the CCD array and the x-ray source. With the height of the source fixed, the source could then be retracted away from the CCD camera along the perpendicular axis determined in Section 4.6.2. This meant that the magnification introduced could be calculated. Figure 4.30 shows the relative locations of x-ray source, cable sample and the CCD camera, where w is the target to window spacing, l is the window to CCD camera face plate distance, x is the distance between the CCD camera face and the centre of the cable joint, and s is the distance behind the CCD camera face plate that the image is generated in the scintillating screen. The magnification, d, can then be determined using the theory of similar triangles using the equation:

$$d = \frac{w + l + s}{w + l - x} \tag{4.11}$$

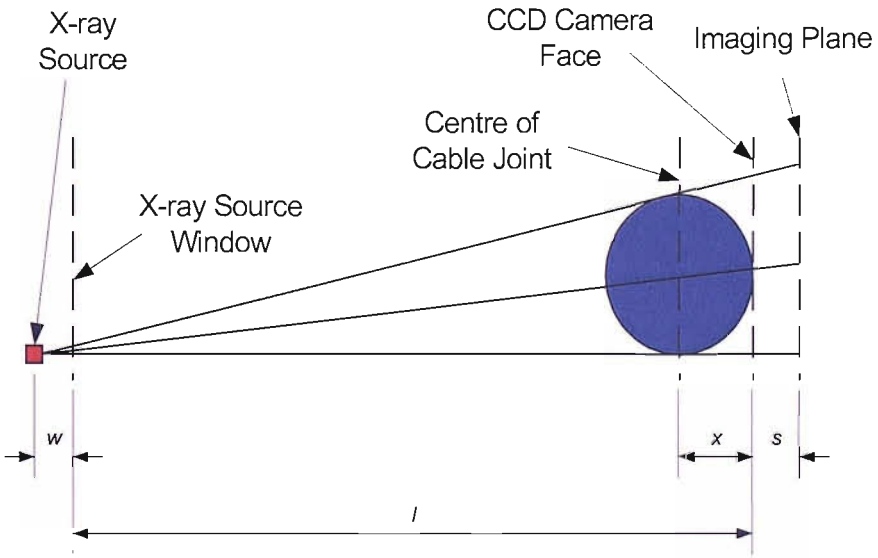

FIGURE 4.30: X-ray source, cable joint and CCD camera geometry

It is possible to measure l and x as these measurements are easily accessible, w is stated by X-Tex to be 6 mm, however the exact value of s was not stated by XCAM and so is unknown. In order to calculate s and confirm that w is 6 mm, a set of images were taken of using the IQI described in Section 4.5. The IQI was used instead of using a cable joint sample because the size and spacings of the wires are known, the thickness of the envelope is such that the IQI can be considered to be planar, whereas

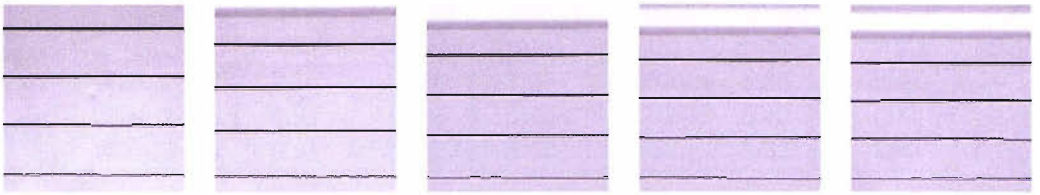

(a) (b) (c) (d) (e)

FIGURE 4.31: Images of the IQI with the source located at (a) 143 mm, (b) 200 mm, (c) 300 mm, (d) 400 mm, and (e) 500 mm.

the dimensions of the components of a cable joint are not as easily defined. The IQI was positioned so that it would lie in the same plane of the central vertical plane of a cable joint sample when mounted on the translational stage. The height of the IQI was set so that the four largest wires could be seen. The IQI was then imaged by irradiating it for 20 seconds at 50 kV and 100 µA with the source located at 143, 200, 300, 400, and 500 mm from the CCD camera face plate with a measuring of tolerance of ± 1 mm. The reason for choosing 143 mm was that the source could not be positioned closer to the CCD camera face plate with the cable mount in place. The distance between the plane containing the IQI and the plane containing the face plate of the CCD array was set at 35 mm, as this represents the middle of the range of travel of the translational stage of the CCD camera. The location of CCD camera was determined using a digital vernier that allowed a positional accuracy of 100 µm. In order to perform photometric correction on the images produced, the IQI was imaged three times at each position, three flat field images were generated using the same exposure setting and placing the source at 300 mm, and seven background images were taken. The images were then photometrically corrected and can be seen in Figure 4.31. In all five images, the four wires can be seen, however as the distance between the x-ray source and the CCD camera increases, the distance, in the image, between the wires decreases, due to the decreased magnification. The decreased magnification in Figure 4.31(e) causes an increase in the field of view of the image, such that the edge of the wire envelope can be seen (the bright band in the image).

From the IQI images it was possible to calculate the average spacing between each wire by counting the number of pixels between each wire for every column of the image; the median average was then calculated for each separation and then multiplied by 0.0135, to get a measurement in millimetres. The separations calculated are shown in Table 4.2, where wire 1 is the top wire in the image and wire 4 is the bottom image in the image.

Figure	4.31(a) (mm)	4.31(b) (mm)	4.31(c) (mm)	4.31(d) (mm)	4.31(e) (mm)	Spacing (mm)
Wire 1 – 2	7.10	6.40	5.91	5.67	5.54	5.00
Wire 2 – 3	6.94	6.25	5.76	5.53	5.40	4.90
Wire 3 – 4	6.81	6.14	5.67	5.44	5.32	4.80

TABLE 4.2: The calculated spacings between each IQI wire for the images in Figure 4.31 and the measured spacings between the wires in the IQI (Calculated separations to within ±1 pixel and measured spacing to within ±50 μm)

In order to calculate the magnification introduced into each image, the spacing between each wire in the actual IQI is required. The stated separation, from the manufacturer, was 5 mm, however if that was the case, the separations measured in each individual image would have been the same. This is not the case because the calculated spacings are different between each wire. This is due to the fact that the wire spacing vary slightly in the IQI. To measure the actual spacings between the wires, a x8 magnifying eye glass was used. Incorporated into this eye glass was a graticule scale that would allow measurements to be taken with a resolution of 0.05 mm. Each spacing was measured at three separate points to within the nearest 100 μm, and the average of the three results used. The measured spacings are shown in the last column of Table 4.2. From the measurements detailed in Table 4.2, the magnification of each image was calculated as shown in Table 4.3

Figure	4.31(a) (d_1)	4.31(b) (d_2)	4.31(c) (d_3)	4.31(d) (d_4)	4.31(e) (d_5)
Magnification	1.420	1.280	1.179	1.131	1.107

TABLE 4.3: Image Magnification

These values of magnification, d, can then be using to generate the following equations from Equation 4.11:

$$\frac{w + 143 + s}{w + 143 - 35} = 1.420 \tag{4.12}$$

$$\frac{w + 200 + s}{w + 200 - 35} = 1.280 \tag{4.13}$$

$$\frac{w + 300 + s}{w + 300 - 35} = 1.179 \tag{4.14}$$

$$\frac{w + 400 + s}{w + 400 - 35} = 1.131 \tag{4.15}$$

$$\frac{w + 500 + s}{w + 500 - 35} = 1.107 \tag{4.16}$$

As stated by X-Tex, w is equal to 6.00 mm. When substituted into the Equation 4.12 – 4.16, this gives s an average value of 13.6 mm. These values were then substituted back into Equations 4.12 – 4.16 in order to compare the results of calculating the magnification using Equation 4.11 and the magnification calculated from the IQI measurements. The results are shown in Table 4.4.

	Image Generated Magnification	Geometry Generated Magnification
d_1	1.420	1.427
d_2	1.280	1.285
d_3	1.179	1.180
d_4	1.131	1.131
d_5	1.107	1.103

TABLE 4.4: Comparison of image based magnification calculations and geometrical calculation of the the magnification for all five images

From the table it can be assumed that the image is generated at 13.6 mm behind the face of the CCD camera face plate, and that the magnification of the system is governed by Equation 4.11. The magnifications generated using the IQI were measured using a planar test piece, however, the cable sample will not all lie in a single plane. This means that a defect nearer the front of the cable joint sample, looking at the cable joint sample from a position behind the x-ray source, will be magnified more than a defect located at the back of the cable joint. This does not pose a significant problem because the interfaces imaged will lie in the same plane as the IQI, and measurements of the size of any defect can be taken from the image where the defect is closest to the central plane. The image in which this occurs can be found by choosing the image where the defect is furthest from the conductor.

The location of the x-ray source in relation to the CCD camera, therefore, determines the magnification introduced into the image. Figure 4.32 shows the relationship between x-ray location and magnification generated using Equation 4.11. The plot contains seven lines in order to depict the magnification of the cable with the CCD camera in seven

locations within the 30 mm travel of the camera stage, i.e. x varies from 20 mm to 50 mm. From Figure 4.32 it can be seen that ideally the source should be located at least 600 mm from the CCD camera, however, from tests, locating the source around this distance significantly reduces the penetration power and flux density of the x-ray beam that reaches the cable sample. This results in increased exposure times. For this reason the source was placed at 405.5 mm as the magnification range with this geometry is 6.9 – 14.0 % which results in a pixel size range from 12.63 – 11.8 µm, respectively.

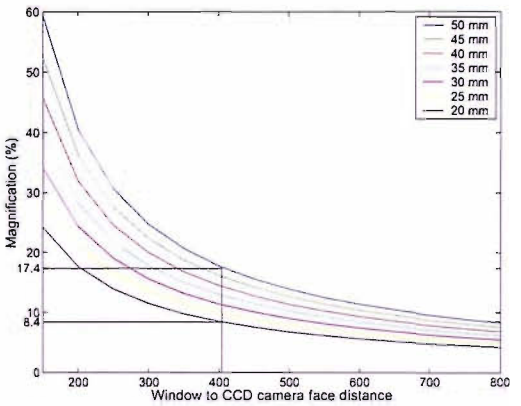

FIGURE 4.32: The relationship between magnification and x-ray source to CCD camera distance.

4.8 The Montaging Process

With the camera and cable mount aligned, the camera and source aligned and the geometric separation between the source and the CCD array set, the cable sample can be indexed past the camera such that the height of a interface or defect will remain constant in the image regardless of the translational stage position. The height of the interface or defect can also be determined because the magnification in the image is known. This means that if the cable sample is imaged and then indexed left past the camera, such that the right hand edge of the cable sample, imaged in the first exposure, is visible in the second image, the two images can be spliced together at the point of the right hand edge of the first image. This process can then be repeated along the whole length of the cable joint sample to generate an image of the whole of the length of the cable joint sample that can be inspected to determine the thickness of the insulation system components and the size of any defects present.

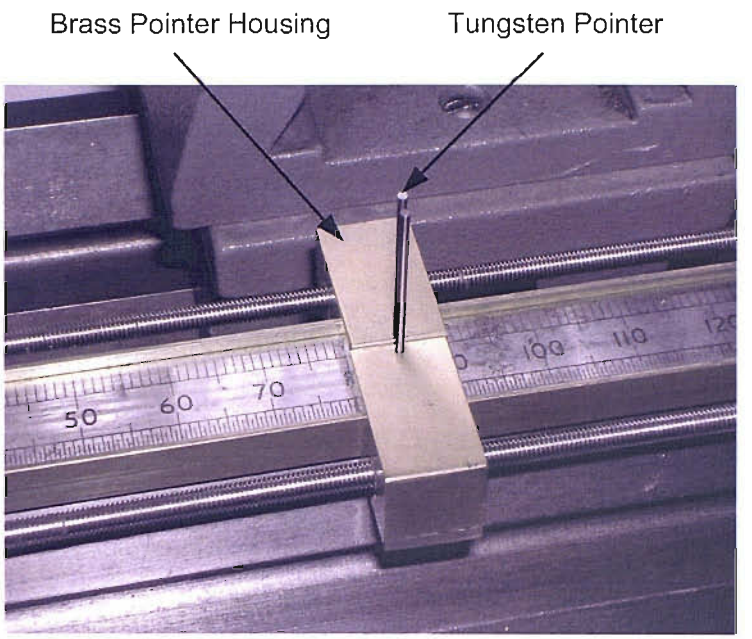

FIGURE 4.33: The indexing pointers

In order to automate the splicing procedure two pointers, mounted on top of the cable mount optical rail, were used to mark known points in the image (Figure 4.33). Both pointers are made from tungsten needles, and cut to length such that the pointer is visible in the image, but does not interfere with the cable joint sample. The pointers are also able to move independently of each other. This means that if an image is taken with one of these pointers in the right hand corner of the image and then the cable joint sample is indexed left past the CCD camera and a second image is taken with the pointer in the image, the two images can be spliced at the column that bisects the pointer in both images. Two pointers have been used so that more than two images can be spliced by alternating the splice between pointers, i.e. in the previous example the second pointer would have been located in the lower right hand corner of the second image so that a third image could be taken, and so on. To ensure that the pointers do not move between images the position of the pointers is determined by the studding that passes through the bass pointer housing. By rotating this studding the pointer housing and pointer can be moved along the length of the cable mount optical rail.

In order to image the whole of the cable joint sample, the translational stage has to be positioned so that the one end of the cable joint sample can be imaged. The pointers then have to be moved into position so that there is a pointer in the lower corners of the image (Figure 4.34(a)). This distance is then measured using the steel rule in the

pointer rail. An image of the cable joint sample is then taken. The cable then has to be indexed past the camera so that there is one a pointer is still visible. The other pointer is then moved along the rail so that it is then visible in the opposite corner of the image. The cable joint sample is then imaged again (Figure 4.34(b)). This process is repeated until the other end of the cable joint sample is reached. When the end of the sample is reached the cable can be rotated and the indexing procedure repeated. In order to produce a detailed 3D image of the cable using the techniques described in the following chapters, it would be desirable to image the cable joint at at 1° increments, however this is impractical due to the time and memory demands this level of inspection would introduce into the inspection procedure. For this reason the angular separation between images is a compromise between time and memory constraints and inspection detail. From testing it was found the detail of the 3D image of a cable joint sample was not significantly improved by decreasing the angle of inspection below 45°, however with an angular separation larger than 45° the image produced was less valuable in terms of inspection power. For this reason the indexing and imaging process had to be completed using eight inspection angles, separated by 45°. Once all the images of the cable joint sample had been captured in this way, they were to be spliced together. To do this, the edges of the pointers are found in each image using the Canny edge detection method. The vertical edges of the pointers can then be found by searching the edge image for vertical lines. The centerline of the pointer can then be determined by finding the column that is located half way between the vertical edges of the pointer. When both pointer centrelines have been found, the cable joint sample image can be cropped to remove any image data lying outside of these centerlines. Once all the images, for a given imaging angle, have been cropped in this way, they can be butted together in sequence to produce an image of the cable insulation system for that imaging angle. Figure 4.34(c) shows the effect of the montaging process applied to the images in Figure 4.34(a) and 4.34(b). From Figure 4.34(c), it can be seen that the insulation shield semiconducting layer and outer edge of the insulation are continuous either side of the splicing location. Figure 4.34(d) shows that this is also the case for the outer edge of the conductor, conductor shield semiconducting layer and the inner edge of the insulation, therefore the montaging process has been optimised by the alignment of the imaging hardware and by the use of the tungsten indexing pointers.

This cropping and butting together of the image therefore produces eight long images of

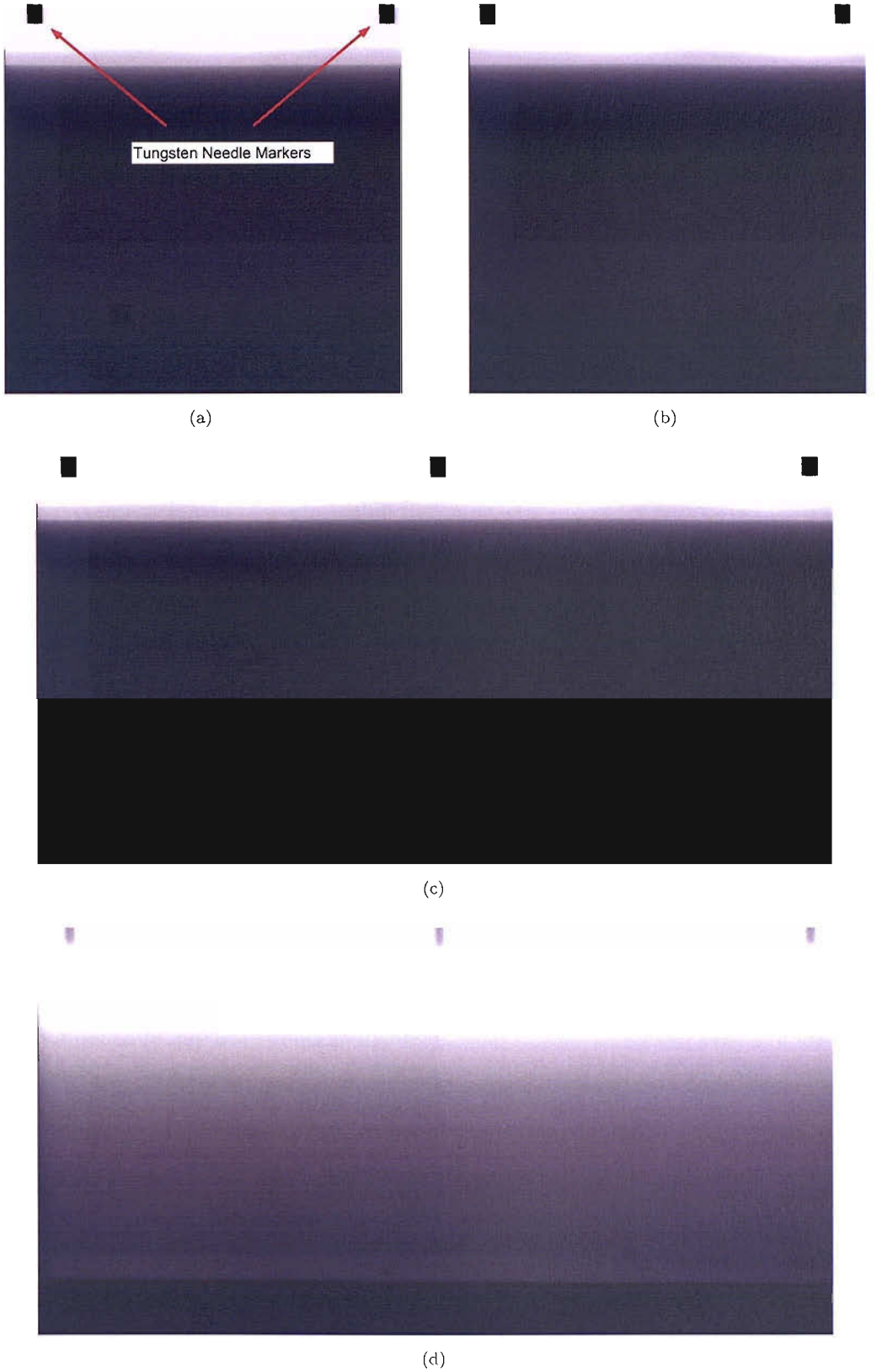

FIGURE 4.34: The montaging process (a) left-hand image, (b) the right-hand image (c) the montaged image, and (d) the montaged image with increased brightness.

the cable joint sample. These images then have to be inspected to obtain the dimensions of the components of the cable joint sample and to determine defect status of the cable joint. The results of these inspections can then be used to generate a three dimensional image of the cable joint.

4.9 Summary

Digital images consist of geographically arranged numerical values. These can be represented using a range of techniques, of which the most appropriate methods for cable images are monochrome, pseudo-colour and mesh plots. These three representations can be used to display the differences in radiological densities and material thicknesses of the different components and defects within the cable joint. In order to improve detection of the material interfaces and any defects present, it is possible to pre-process the image using photometric correction techniques. These techniques can be used to reduce the noise generated by the manufacturing method and image capture of the CCD camera. The content of the image however is mainly determined by the the exposure settings used to image the cable joint. To compare the photometrically corrected images produced using using the optimum exposure setting with images generated by photographic film, three test pieces were imaged using both imaging technologies. The three test pieces were used to compare sharpness and contrast. For all three test pieces the images generated by the CCD camera were significantly better than the film generated images, however the images produced by the camera have a field of view significantly less than the image captured using photographic film plates. To inspect a cable joint using the camera, it is therefore necessary to capture sets of individual images along the length of the cable joint at a range of angles. These sets of images can then be spliced together to produce a single image for the given angle of inspection. In order to be able to perform the splicing procedure, the imaging hardware components have to be accurately aligned. Once they are aligned, it possible to combine adjacent images by simply cropping the images at the correct point and then butting the images together. In order to determine the correct point at which to crop the images, a system of pointers are used to mark the splicing points of the images. With this system the images can be digitally cropped to produce a single image of the insulation system of the cable joint sample. The dimensions of the features in this image are determined by the magnification introduced into

the image due to the separation between the x-ray source and the CCD array, and the axis of rotation of the cable joint sample and the CCD array. This magnification can be easily determined, and so the full length images of the cable joint sample can be used to determine the size of the components of the insulation system and estimate the size of any defects in the cable joint.

Chapter 5

Insulation System Component Interface Detection

The eight full length images produced using the techniques outlined in Chapter 4 are digital equivalents of the x-ray photographic film plates used in the original inspection system. These images still have to be inspected to check the dimensions of the insulation system components and to detect defects in the cable joint as described in Section 2.2. This chapter describes a novel method used to digitally measure the dimensions of the insulation system components.

The conductor shield, insulation, and insulation shield are designed so that if the components are manufactured within the specified dimensional range for that particular cable, each component is expected to function reliably for the predicted lifetime of the cable system. Should any of the dimensions of these components be outside their specified tolerance, this will have an effect on the working lifetime of the cable joint, and consequently on the expected lifetime of the cable transmission system.

The function of the conductor semiconducting shield is to ensure that the conductor presents a smooth surface to the insulation. If this layer is too thin, its field-evening properties are reduced and as a result will subject regions of the insulation to relatively high electrical stresses. Should the thickness of the inner semiconducting layer become very thin, then it will eventually take on the same profile as the conductor; exacerbating problems with the high electrical stress. The overall diameter of the factory installed cable joint insulation system is designed to be the same as the parent cable to ensure

that it can be easily coiled onto a storage or laying turntable. For this reason, if the conductor shield becomes too thick, then extra volume of semiconducting material in the screen replaces insulation material. This means that the remaining insulation in this region will be subjected to a higher electrical stress than it was originally designed to withstand under normal working conditions. If the insulation is too thin then, as mentioned, it will have an increased electrical stress gradient across its thickness. If the insulation is too thick then either one of the other components will subsequently be thinner or the overall diameter of the cable will be affected, neither of which, in quality control terms, are permissible. The final component of the insulation system is the outer insulation shield. This screen is used to confine the electrical field to within the insulation system. Should this screen be too thin, then it will allow the electric field to leave the insulation system, and as a result the surrounding conductive components of the cable system may be raised from a ground state. If the insulation shield is too thick then it will, once again, either reduce the thickness of other components, or will make the overall diameter of the cable larger [1]. These components therefore, need to be imaged and measured to ensure that they are within the specified design tolerances. In order to measure the thickness of the conductor shield, insulation and insulation shield, these structures first have to be located in the cable joint image.

5.1 Edge Detection

The cable joint component interfaces, as described in Chapter 4, Section 4.2, are created by the juncture of two materials with different radiological densities. The abrupt changes in density of the materials, across the interface, manifest themselves in an x-ray image as rapid changes in pixel intensity. This change in contrast means that the edges of each of the cable joint components can be found by locating rapid changes in intensity in the image. In order to detect these changes, the image can be differentiated [85].

5.1.1 First-Order Edge Detection

The gradient of a continuous two dimensional (2D) function can be defined as:

$$G[f(x,y)] = \begin{bmatrix} \lim\limits_{\delta x \to 0} & \dfrac{f(x+\delta x, y) - f(x,y)}{\delta x} \\ \lim\limits_{\delta y \to 0} & \dfrac{f(x, y+\delta y) - f(x,y)}{\delta y} \end{bmatrix} \tag{5.1}$$

$$= \begin{bmatrix} \dfrac{\partial f}{\partial x} \\ \dfrac{\partial f}{\partial x} \end{bmatrix} \tag{5.2}$$

An image, however, is constructed of discrete pixels and so is not a continuous function. For this reason δx and δy in Equation 5.2 are equal to 1, therefore:

$$G[f(x,y)] = \begin{bmatrix} f(x+1,y) - f(x,y) \\ f(x,y+1) - f(x,y) \end{bmatrix} \tag{5.3}$$

This can be represented by the convolution masks:

$$G_x = [-1, 1] \tag{5.4}$$

$$G_y = \begin{bmatrix} -1 \\ 1 \end{bmatrix} \tag{5.5}$$

To differentiate an image, therefore, the convolution masks G_x and G_y can be passed over the image. Figure 5.1(a) displays an edge between a dark region and a lighter region. To demonstrate the effect of using the horizontal operator in Equation 5.5 the pixel intensities of the pixels between A and A′ are shown in Figure 5.1(b). The horizontal operator has then been convolved with these pixels, and the results are shown in Figure 5.1(c). From this figure, it can be seen that the edge is located at the maximum point of the trace. This means that to find any vertical edges, the horizontal operator can be convolved with the image and any local maxima found. This could then be repeated for the vertical operator to find any horizontal edges, however, this would generate two edge images. To overcome this, the horizontal operator can be passed over

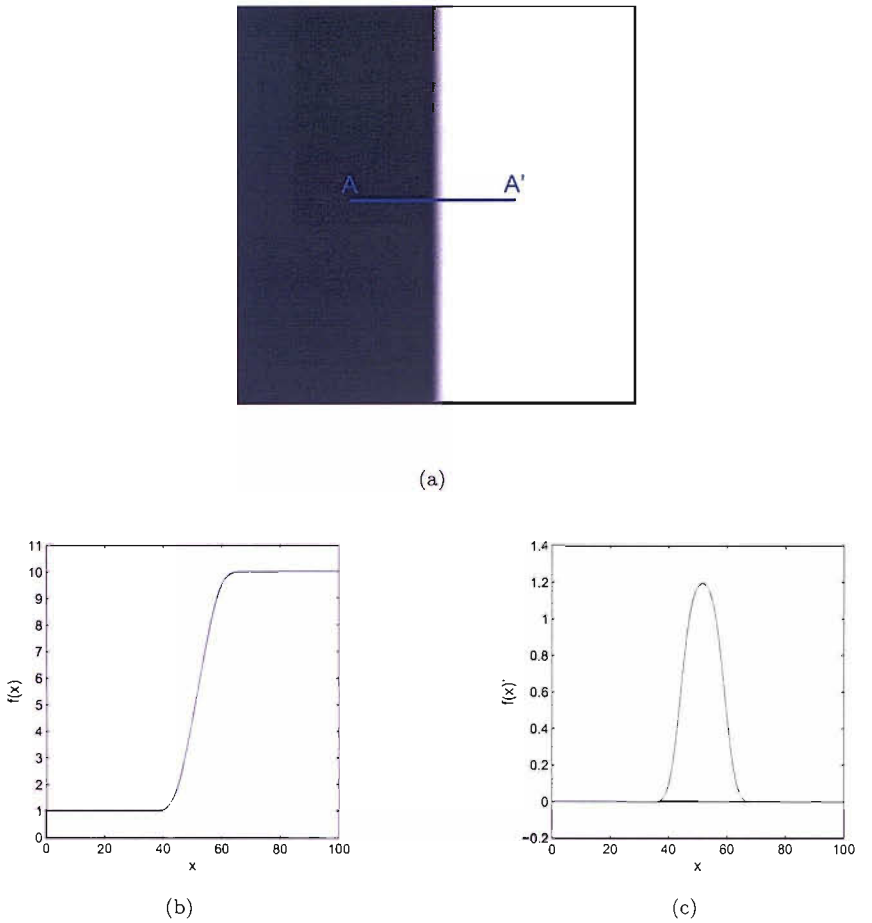

FIGURE 5.1: First-order differentiation of an edge (a) edge image, (b) pixel intensity plot of line A–A′, and (c) first-order differentiation of (b).

the image, followed by the vertical operator. Then these images can be combined using vector addition to produce an edge magnitude image and an edge direction image. The magnitude image can then be inspected for local maxima, to produce an edge image.

The simplest method of finding the local maxima is by thresholding. This is achieved by setting a threshold value; any edge magnitudes above this value are then deemed to be an edge, and any value below this value are considered not to be associated with an edge. This method of finding the edge pixels, however, can produce an image with edge lines that are more than one pixel wide, because multiple pixels around the edge location could be above the threshold level. In order to thin the number of pixels deemed to be an edge, non-maximal suppression can be used. Essentially non-maximal suppression locates any pixel that can be associated with a peak in the differentiated image. To achieve this, the edge direction information, calculated when the two edge operator images are added,

can be used. The direction calculated indicates the direction of a possible edge through that pixel. If a pixel is located on the ridge of an edge, the gradient in a normal direction either side of this pixel will be less than the gradient at the pixel. If the gradient on either side of the pixel is greater, then this pixel is not located on the ridge of the edge and so the pixel is set to zero. Non-maximal suppression therefore filters out any pixel that is not located on the ridge of an edge. This non-maximal suppressed image can then be thresholded to produce an edge image with single pixel width edges.

5.1.1.1 The Roberts Edge Detection Operator

The simplest edge detection method is the Roberts operator. This operator uses two templates which differentiate pixel values in a diagonal manner. The two templates shown in Figure 5.2 are called M^+ and M^- [85].

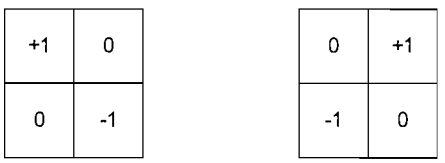

FIGURE 5.2: Templates for Roberts operator (a) M^+, and (b) M^-.

In order to implement the edge detection, both templates are passed over the image, the edge magnitude image is then non-maximally suppressed, followed by thresholding. The threshold value is then set such that the trade off between filtering out any noise in the edge image and full detection of any edges is optimised. Decreasing the threshold value increases the number of pixels deemed to be edge pixels, however the system then becomes more susceptible to noise. Increasing the threshold value reduces the amount of noise in the edge images, but reduces the probability of detecting an edge [97]. The two images in Figure 5.3 show the effect of applying the Roberts operator to a cable joint image, using two different threshold values. The cable joint image used is the same as the image in Figure 4.1(b), however to improve visualisation of the edge detection process using the Roberts operator, the cable joint image was 8 x 8 computer binned. To produce Figure 5.3(a) a threshold value of 10 was used, i.e. if the calculated edge value at an individual pixel was greater than 10 then this pixel was noted in the final image. Figure 5.3(b) was produced using a threshold value of 110. From Figure 5.3(a) it can

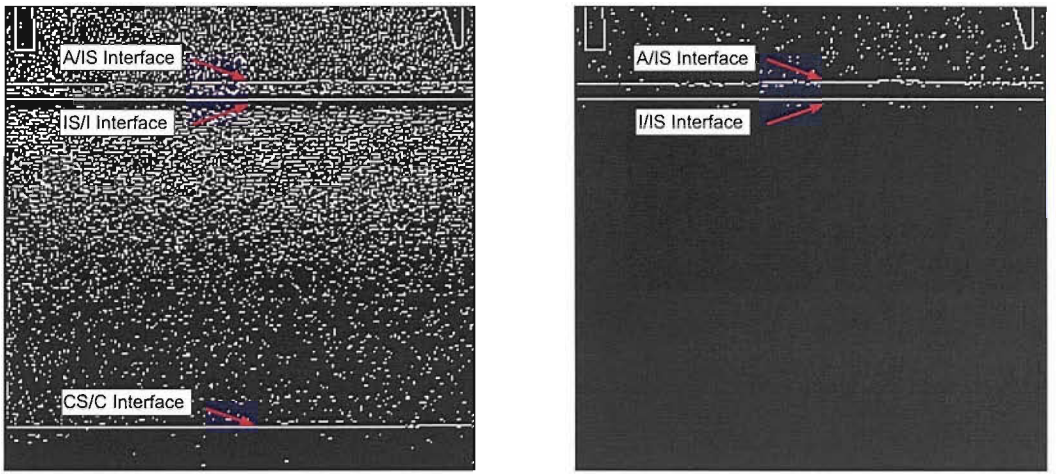

(a) (b)

FIGURE 5.3: Roberts edge detector operator applied to the cable joint image (a) low threshold, and (b) high threshold.

be seen that with the lower threshold value the air/insulation shield (A/IS), insulation shield/insulation (IS/I), and conductor shield/conductor (CS/C) interfaces have been found, however the noise in the image has almost obscured the upper two interfaces. Figure 5.3(b) shows that increasing the threshold value does reduce the amount of noise in the image however the CS/C interface is no longer detected.

5.1.1.2 The Prewitt Edge Detection Operator

It is apparent from Figure 5.3, that the Roberts edge detection method is not suitable for interface detection due to the noise levels in the image and the inability to detect the IS/I interface. The Prewitt operator is an improvement on the Roberts method [85]. Instead of diagonal differentiation, the templates used for this edge detection method differentiate vertically and horizontally, M_x and M_y, respectively (Figure 5.4).

+1	0	-1
+1	0	-1
+1	0	-1

(a)

+1	+1	+1
0	0	0
-1	-1	-1

(b)

FIGURE 5.4: Templates for Prewitt operator (a) M_x, and (b) M_y.

Both of these templates have to be passed over the image, vector added and thresholded in a similar way to the Roberts templates. Figure 5.5 displays the effect of using the Prewitt edge detection technique, using the same thresholding values that were used to generate the Roberts processed image in Figure 5.3. From Figure 5.5(a) it can be seen that with the lower threshold value the A/IS, IS/I and CS/C interfaces are all detected and that it is also possible to vaguely see the insulation/conductor shield (I/CS) interface, however the image still contains large quantities of noise. Figure 5.5(a) shows that this noise can be reduced by increasing the threshold value, however the CS/C and I/CS interfaces are not detected.

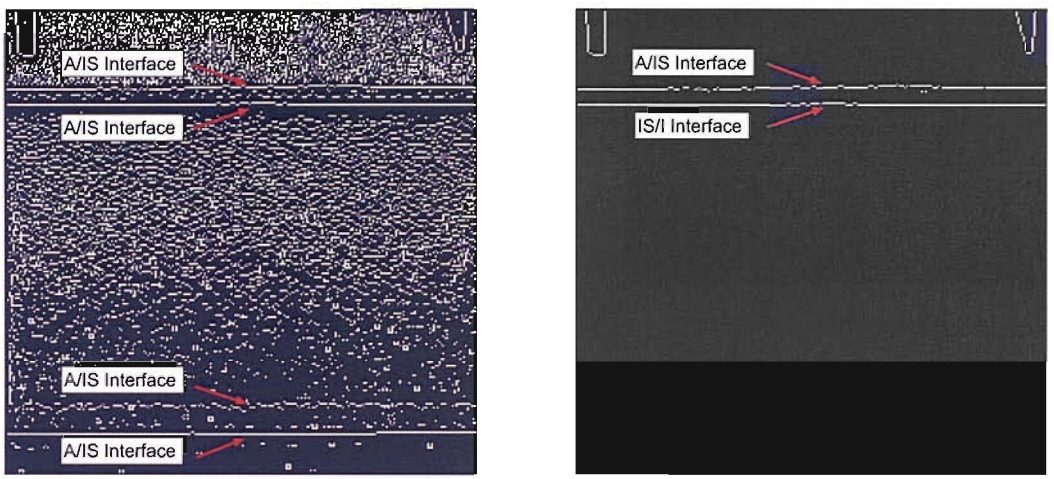

(a) (b)

FIGURE 5.5: Prewitt edge detector operator applied to the cable joint image (a) low threshold, and (b) high threshold.

5.1.1.3 The Sobel Edge Detection Operator

From the results shown in Figure 5.5 it can be assumed that the Prewitt operator is not suitable for interface detection in x-ray cable joint images due to the noise levels and detection power. The Prewitt operator can be improved by weighting the central pixels for both templates. In the Sobel operator, the central weighting is doubled (Figure 5.6) [98]. These two templates are passed over the image in the same way as the Prewitt templates. The two images in Figure 5.7 were generated using the same threshold values as used in the previous two edge detection methods. The two images in the figure show slight improvements on the Prewitt method, however there is still high levels of noise in Figure 5.7(a), and 5.7(b) does not contain any conductor shield data.

+1	0	-1
+2	0	-2
+1	0	-1

(a)

+1	+2	+1
0	0	0
-1	-2	-1

(b)

FIGURE 5.6: Templates for Sobel operator (a) M_x, and (b) M_y.

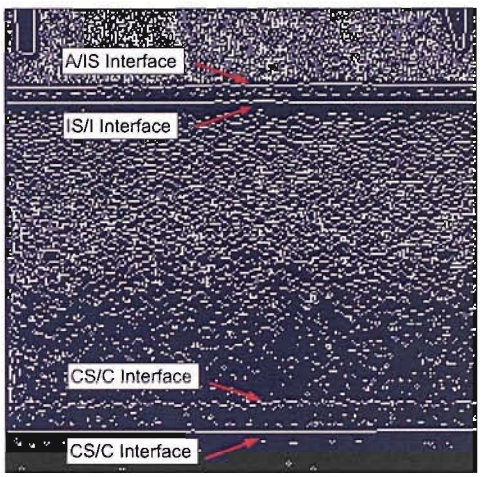

(a)

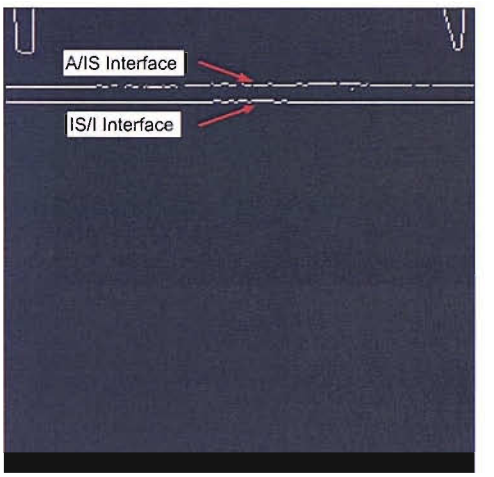

(b)

FIGURE 5.7: Sobel edge detector operator applied to the cable joint image (a) low threshold, and (b) high threshold.

The Roberts, Prewitt, and Sobel edge detection methods all differentiate the raw image data. This means that if the image is noisy, the noise in the image is differentiated. This noise can present itself in the image as rapid changes in pixel intensity. This means that if there is significant noise in the image, it will reduce the possibility of correctly detecting the edges in the image. Figure 5.8(a) shows a noisy version of the edge image in Figure 5.1(a). The green trace in Figure 5.8(b) shows the pixel intensities, between the points A and A′, from the noisy image. In this plot it can be seen that the noise in the image is significant but the underlying trend (the blue trace) is not obscured. The effect of differentiating this noise however, is a differentiated plot with many peaks (red trace in Figure 5.8(c)). These peaks would then pass through the non-maximal suppression as local maxima, therefore could be falsely detected as edges after thresholding. It is possible, however, to remove this noise using a smoothing filter. The Gaussian averaging operator is considered to be optimal for image smoothing [85]. The Gaussian function

at pixel location g at co-ordinates x,y is defined by:

$$g(x,y) = e^{-\left(\frac{x^2+y^2}{2\sigma^2}\right)} \tag{5.6}$$

Equation 5.8 can be used to generate a Gaussian template which can be convolved with the image because it is a linear, shift invariant filter [99]. The size of the filter window is determined by the value of σ, because the Gaussian function tends to zero at more than 3 standard deviations from the mean. This means that the Gaussian operator can be approximated by a filter of local extent, therefore as σ increases so does the size of the template generated. A larger value of σ will remove more of the high frequency noise, however this tends to blur the edges within the image. The value of σ is therefore a compromise between noise reduction and edge definition. To demonstrate the effect of using a Gaussian smoothing operator, the noisy trace in Figure 5.8(b) has been Gaussian smoothed to produce Figure 5.8(d). This smoothed trace was then differentiated to produce the green trace in Figure 5.8(e). From this figure, it can be seen that smoothing the image has reduced the influence of the noise on the differentiated plot.

5.1.1.4 The Canny Edge Detection Operator

The Canny operator utilises this Gaussian smoothing to improve the edge detection process. This is achieved by first smoothing the image, followed by calculating the gradients in the smoothed image. After this the edge data is subjected to non-maximal suppression and finally thresholded, however the hysteresis thresholding is used in the Canny operator. To implement this, the image is scanned for a pixel that has a value greater than the upper threshold limit. This pixel is called a 'seed' pixel. Once this has been found the surrounding pixels are scanned to see if any of these pixels have a value greater than the lower limit. If any of the pixels fit this criteria, then the pixels surrounding this new pixel are scanned. This is repeated until no pixels are found that have a value above the lower threshold limit. Then a new seed pixel is sought. In this way the ridges and troughs in the image are found [31, 85].

Figure 5.9 displays the results of detecting edges using the Canny method. Unlike the previous three edge detection methods, the Canny method has three variables: the upper

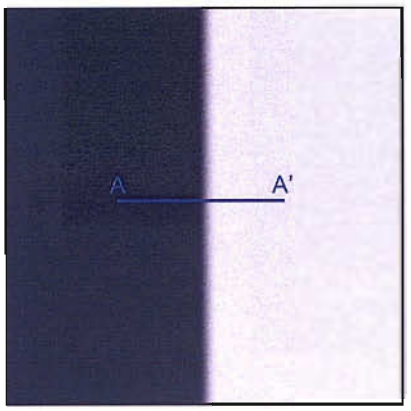

(a)

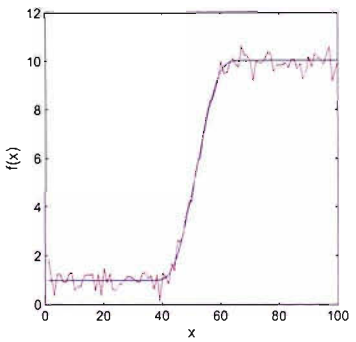

(b)

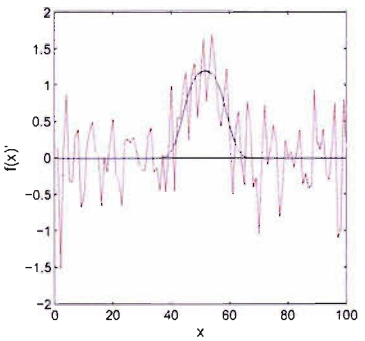

(c)

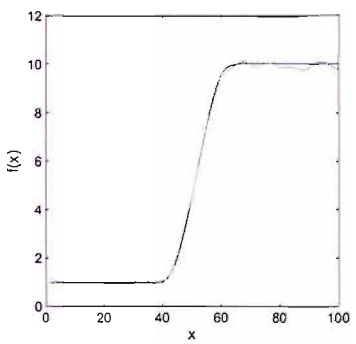

(d)

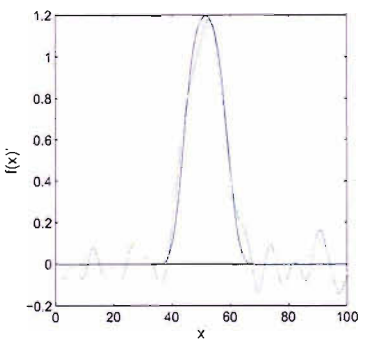

(e)

FIGURE 5.8: Edge detection in a noisy image (a) noisy edge image, (b) pixel intensity plot of line A–A′ (red trace – actual image, blue trace – noise-free image), (c) first-order differentiation of both traces in (b), (d) Gaussian smoothed intensity plot of noisy image (green trace) and noise-free intensity plot (green trace), and (e) first-order differentiation of both traces in (d).

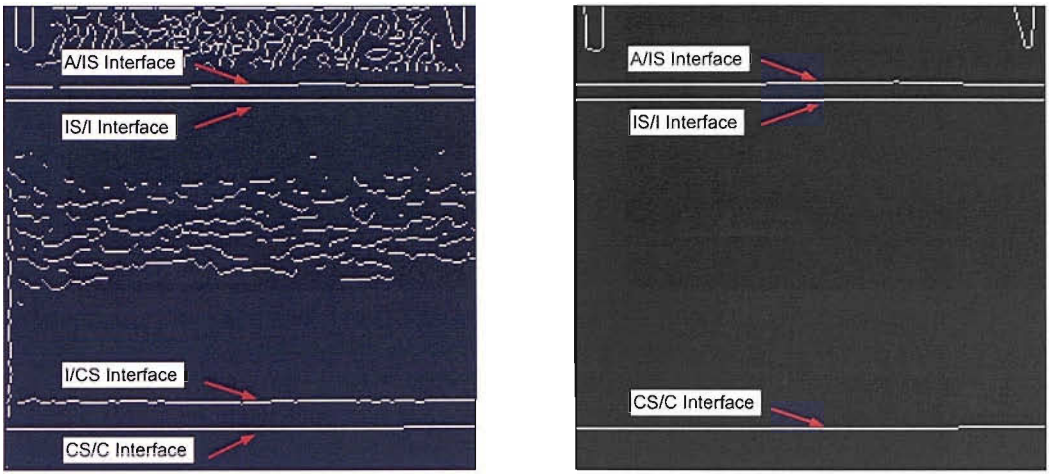

(a) (b)

FIGURE 5.9: Canny edge detector operator applied to the cable joint image (a) low threshold upper limit and large σ, and (b) higher upper threshold limit and decreased σ.

and lower threshold limits and the σ value of the Gaussian smoothing template. These three values have to be optimised in order to detect the edges in the image. In order to detect all four interfaces with the least amount of noise, the optimum value of σ was found to be 1.5, and the corresponding upper and lower threshold values were set at 0.009 and 0.001 respectively. These variable values were used to produce Figure 5.9(a). In this figure, all four interfaces have been found, but there is still some noise in the insulation region and the air gap, however this level of noise is considerably less than the the image produced using the Roberts, Prewitt or Sobel methods of edge detection. The noise level has been reduced in Figure 5.9(b), which was produced using a σ value of 1 and an upper and lower threshold values of 0.09 and 0.06 respectively. The smaller σ value results in less smoothing of the image, which has resulted in the loss of the I/CS interface, however the noise has been reduced by the increased threshold levels.

The main problem with first-order differentiation edge detection methods is the thresholding process. The threshold levels used in each method are image specific and have to be found by either operator experience, experimentally, automatically by considering the edge data, or empirically [85]. If the threshold value is set too high then not all the edges are detected; if the threshold value is set too low, any noise in the image is detected and considered to be an edge. It should also be noted that by changing any of the threshold values used in the first-order edge detection methods, the operators detect

the interfaces in slightly different positions, for example the A/IS interface detected in Figures 5.9(a) and 5.9(b).

5.1.2 Second-Order Edge Detection

The first-order detection techniques are based on the fact that edges can be found in an image by locating in the differentiated image the points of maximum gradient change, i.e. local maxima. At the local maxima, however, the gradient is constant, leading up to the maxima the gradient is positive, and beyond the maxima the gradient is negative (Figure 5.10(b)). If the rate of change of the image gradient is calculated using second-order differentiation, the rate of change at the peak of the first-order derivative will be zero, before the peak the rate of change will be positive, and after the peak the rate of change will be negative(Figure 5.10(c)). This means that edges can be found by locating the zero-crossing point of the second derivative of the image.

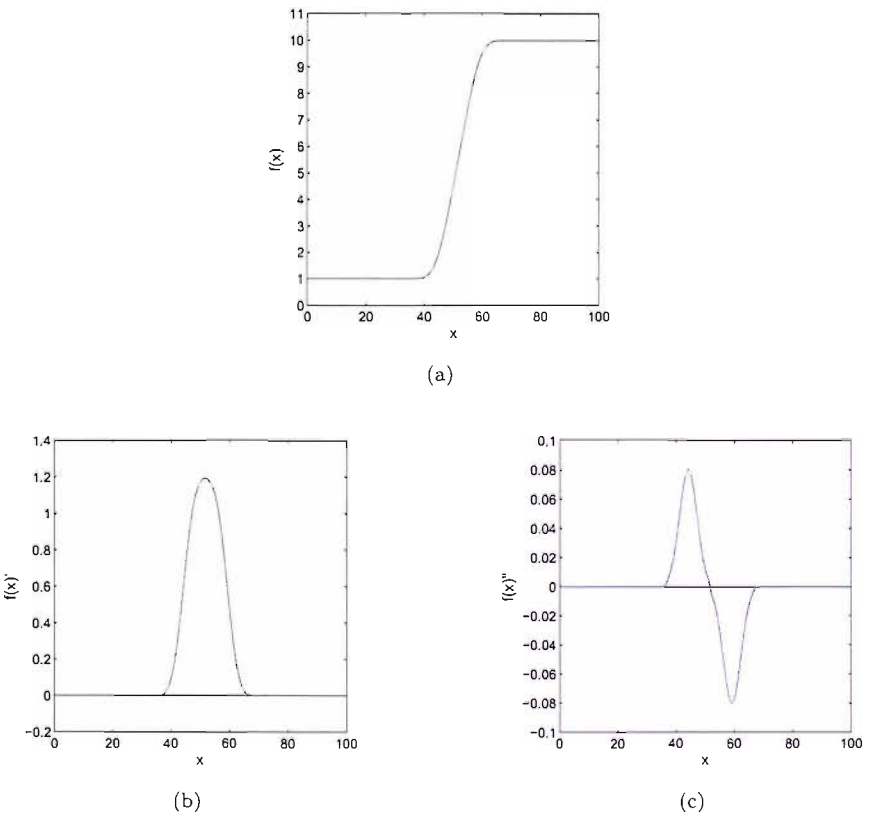

(a) (b) (c)

FIGURE 5.10: Second-order differentiation of an edge (a) pixel intensity plot of line A–A′ from the edge image in Figure 5.1(a), (b) first-order differentiation of (b), and (c) second-order differentiation of (b).

A good approximation to a second-order differentiation is the difference between two adjacent first-order differentiations [85]:

$$\begin{aligned} f''(x,y) &\cong f'(x,y) - f(x-1,y) \\ &\cong f(x,y) - f(x+1,y) - (f(x-1,y) - f(x,y)) \\ &\cong -f(x-1,y) + 2f(x,y) - f(x+1,y) \end{aligned} \tag{5.7}$$

This produces the horizontal second-order template:

-1	2	-1

FIGURE 5.11: Horizontal second-order template

Similarly a vertical second-order template can be produced, which when combined with the horizontal template produces the Laplacian second order template (Figure 5.12).

0	-1	0
-1	4	-1
0	-1	0

FIGURE 5.12: The Laplacian template

This template has to therefore be passed over the image, however, this method of edge detection does not contain any smoothing, and so is susceptible to noise in the image, more so than the first-order differentiators as the Laplacian is differentiation of a high order. As with the Canny operator, the optimum smoothing operator that can be used to smooth the image is the Gaussian smoothing operator. The Marr-Hildreth operator combines the Laplacian operator with the Gaussian smoothing operator to produce a Laplacian of Gaussian operator. This operator is generated by twice differentiating the Gaussian function in Equation 5.8 to produce:

$$g(x,y)'' = \frac{1}{\sigma^2}\left(\frac{x^2+y^2}{\sigma^2} - 2\right) e^{-\left(\frac{x^2+y^2}{2\sigma^2}\right)} \tag{5.8}$$

The Laplacian of Gaussian operator therefore uses second order differentiation combined with image smoothing. The image produced by passing this operator over the original image can then be inspected for any zero-crossing points. This is achieved by piecewise bilinear interpolation [100]. Essentially this method of zero crossing finds the pixel closest to the interpolated zero crossing point. The simplest method of implementing this is to use a 3 x 3 template split into quadrants, each containing the central pixel. The average of the four pixels in each quadrant can then be calculated. If the average calculated for any quadrant differs in sign compared with any of the other quadrants, then a zero crossing can be attributed to the central pixel of the 3 x 3 matrix [85]. A more sophisticated implementation of zero-crossing detection can be found in [100].

The implementation of the Laplacian of Gaussian for image edge detection is non-trivial. From Equation 5.8 it can be seen that the Laplacian of Gaussian has an infinite extent, however for practical reasons, a finite sampled function is required. This means that the function has to be truncated, which can introduce errors in the zero-crossing detection [100]. The error can be reduced by increasing the size of the function, however increasing the size of the function imposes extra computational costs. The size of the function is therefore a trade off between the required accuracy and the computational demands. Once the size of the function has been chosen, the error introduced by the truncation of the function can be reduced by the use of a bias correction in order to restore zero mean property of the function [101]. The choice of σ is also important, because if the value chosen is too small, then it will not be possible to describe the function using the unitary sampling interval. If σ is too large, then the function will not be adequately represented by the truncated window. A robust implementation of the function therefore requires a suitable mask size, the introduction of bias correction, and the choice of a value of σ that will allow the function to perform as intended.

Figure 5.13 shows the effect of processing the cable joint image with this second-order edge detection operator using a σ value of 2.0. The result is relatively noise free, however the I/CS interface is not present and there seems to be a third interface that has been falsely detected in the insulation shield region. The main advantage of this method however is no thresholds have to be set for detection and there is reduced computational cost as a result.

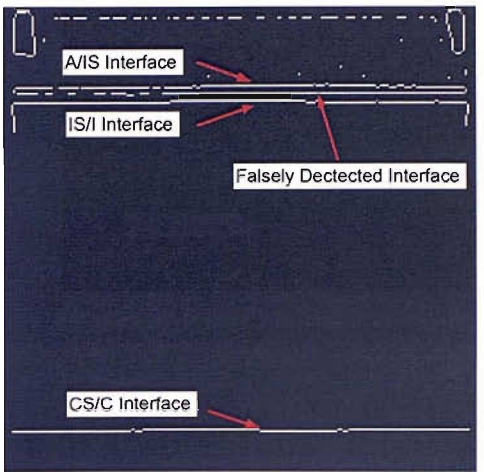

FIGURE 5.13: The Laplacian-of-Gaussian edge detector operator applied to the cable joint image

5.2 Detection of Cable Joint Interfaces based on Cable Joint Interface Morphology

From initial studies and comparisons, the most appropriate standard edge detection technique is the Canny operator as it is able to detect all four interfaces with an acceptable level of noise. This method of edge detection is still not suitable for detecting the insulation component interfaces in a cable joint x-ray image because the image still contains significant levels of noise and also requires a threshold value to be set, which is image specific and has an effect on the detected location of the interface. There are automatic thresholding methods that will choose a threshold level that is somewhere between the threshold values used to create the images in Figure 5.9. The images produced using automatic threshold level setting still have high levels of noise or incomplete interface detection.

To overcome the noise and detection problems associated with standard edge detection methods, an operator has been developed that utilizes feature extraction. Owing to the similar geometry of all polymeric high voltage cables, the general characteristics of the x-ray image produced are constant from image to image, only varying in scale between different cables. This means that the material interfaces in the x-ray image have the same basic characteristics from cable to cable. The interfaces can therefore be found by searching for known features in the image. This is achieved by determining

a mathematical definition for the features of each interface. The image can then be scanned for all four of these mathematical definitions.

A good representation for visualising the material interfaces in order to determine the mathematical definition for each interface is the mesh plot (Figure 4.3(c)). With this representation the absolute pixel greyscale intensity value can be easily discerned, and the global changes in intensity can also visualised relatively accurately. The general profile of the mesh plot for a cable joint image is a ramp. For an individual pre-spliced image, this ramp is constructed from 2045 individual line plots, each plot representing a column of pixels in the image. Figure 5.14 displays one of these line plots.

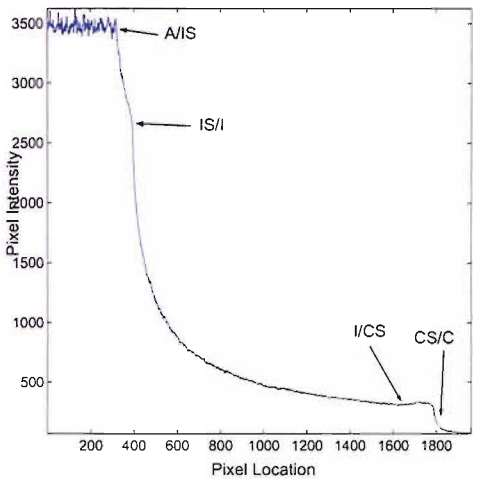

FIGURE 5.14: Line plot of a column of pixels from a cable joint image.

In this plot the air gap above the cable joint is represented by the noisy near-horizontal line from pixel location 0 to approximately 320. To the right of the air gap is the insulation shield. This manifests itself in the plot as the curve from approximately 3500 to 2800 greyscale levels and between the pixel locations 320 and 380. This sudden decrease is due to the relative increase in absorption of the x-ray flux by the semiconducting material of the insulation shield compared to the absorption by the air. The curved nature of the slope is caused by the non-linear increase in semiconductor thickness that the x-rays have to pass through (Figure 4.2). To the right of the insulation shield is the insulation. The insulation is radiologically more dense than the semiconducting material used in the insulation shield. This increased density causes the profile of the ramp decreases even more rapidly. The shape of the profile is also curved due to the non-linear increase in insulation thickness. The insulation ramp extends from around pixel location 380 to 1650 after which there is a slight inflection in the ramp shape caused by

the conductor shield. The small inflection is caused by the reduced insulation thickness (being replaced by semiconducting material) that the x-ray flux has to pass through, resulting in a reduced absorption of the flux. The last feature of the plot profile is the interface between the conductor shield and conductor. The copper of the conductor causes almost complete attenuation of the x-ray flux, producing the horizontal region to the right of pixel location 1800. The interface between the conductor and the conductor shield therefore lies between the small inflection and the horizontal section.

These features are common to each column in the image and can be used to locate the material interfaces. Each interface, however, is difficult to define mathematically using the raw image data in Figure 5.14 due to the complexity of the ramp shape. From the visual description of the ramp above, each interface is defined by the relative changes in the ramp shape. For this reason, it is easier to define the interfaces by differentiating the image. The features of this differentiated image can then be used to define and locate the material interfaces [102].

5.2.1 Differentiation

From the above analysis of first- and second-order edge detection operators, it appears that first-order differentiation produces images with a higher noise content, however, there is no false detection of edges, as is the case with second-order techniques. For this reason, first-order differentiation was used as the basic operator. To reduce the computational demands of the differentiation process, it is possible to only differentiate vertically down the image and still detect the interfaces, because the interfaces can be seen in each column of the image, therefore there is no need to differentiate horizontally. In order to suppress the noise in the x-ray image, smoothing has been introduced by obtaining the average gradient of the image at each pixel rather than just the instantaneous gradient between pixels. To do this, the gradient between the pixel under investigation and the past five pixels is calculated along with the gradient between the pixel under investigation and the future five pixels. Then the mean of these ten gradients is calculated. This mean gradient then becomes the differentiated value, I', for the pixel under investigation, i.e.

$$I'_{(x,y)} = \frac{1}{10} \sum_{i=-5}^{5} \frac{I_{(x,y)} - I_{(x,y+i)}}{|i|} \tag{5.9}$$

The template for this operation is shown in Figure 5.15; it can be seen that the template is heavily weighted in favour of the pixels closest to the the pixel under investigation, therefore even though the differential is smoothed across ten pixels it is a very good approximation to the 'true' instantaneous gradient.

	0.2
	0.25
	0.333
	0.5
	1
1/10 x	0
	-1
	-0.5
	-0.333
	-0.25
	-0.2

FIGURE 5.15: The differentiation template

5.2.2 The Features of the Differentiated Image

The result of passing this template over the image is a new differentiated image that clearly displays the A/IS, IS/I and CS/C interfaces as dark lines (Figure 5.16(a)). The I/CS interface, however, is not so apparent, but this does not affect the detection of this interface . The profile of a column of pixels from this differentiated image can be seen in the line plot in Figure 5.16(b). From this plot it can be seen that the pixel values in the differentiated image can take negative values. In order to produce Figure 5.16(a) the pixel values all had to be positive. This was achieved by introducing a positive offset to ensure that the minimum value of the image data is equal to 1. Despite its noisy appearance of the image data, the mathematical characteristics of each interfaces can be defined relatively simply from this plot. The four points of interest are shown in Figure 5.16(b) as P1 to P4, these correspond to the regions where the interfaces are located.

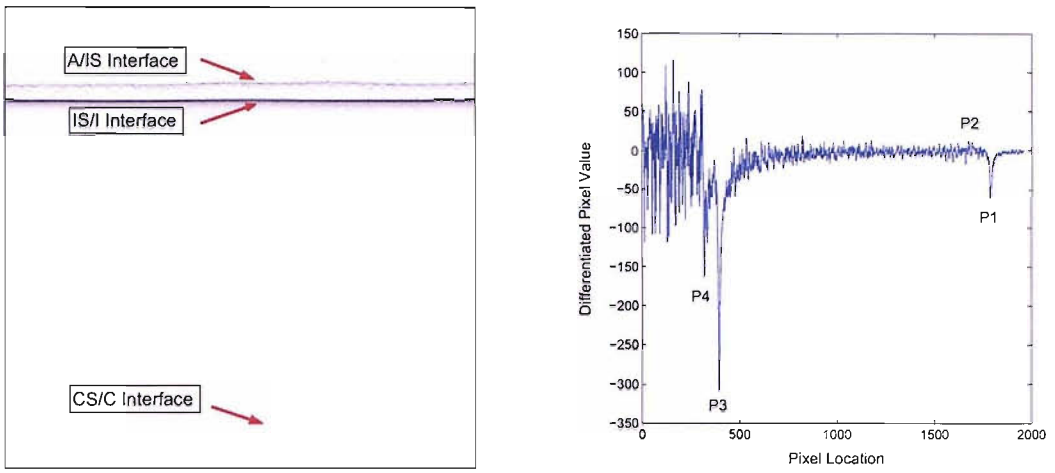

(a) (b)

FIGURE 5.16: (a) The effect of passing the template over the cable image in Figure 4.1(b), and (b) a line plot of a column from the differential image

5.2.2.1 Conductor Shield Interface/Conductor (P1)

The CS/C interface is highlighted in Figure 5.16(a) as the horizontal line near the bottom of the image. This line is darker than the surrounding pixels, therefore will present itself as a negative-going spike in the line plot. This spike is located at around pixel value 1785 (Figure 5.16(b)). From Figure 5.17(a), it can be seen that location (P1) of the CS/C interface is the local minima for that region of the image, therefore, to locate the CS/C interface in the differentiated image, the local minimum of this region has to be found. Due to the hardware geometry and the cable mount, the conductor and conductor shield will always be located in the lower half of the x-ray image. The CS/C interface will therefore always be found to the right of pixel location 1000 and the right hand end of the differentiated line plot for every column of the image, and as P1 is still the local minimum for this region of the plot, the interface is found by simply scanning the lower half of the image for the minimum value of each column in the differentiated image. The location of this point in each column can then be transposed to the original image in order to highlight the material interface. Figure 5.17(b) shows a section of the original image with the CS/C interface marked by a white line. This image has been brightened in a similar manner to Figure 4.3(b), in order to improve the visualisation of the interface. From Figure 5.17(b), it can be seen that this method of locating this interface is accurate, does not suffer from the 'salt and pepper' noise of standard edge detection techniques, and requires no thresholding.

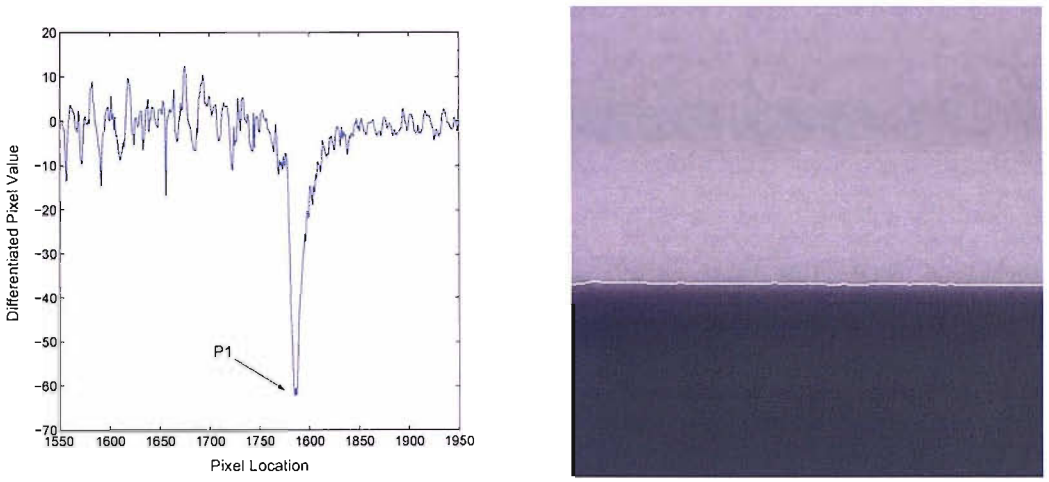

(a) (b)

FIGURE 5.17: (a) The differential line plot of the conductor region, and (b) the image showing the detection of the CS/C interface

5.2.2.2 Insulation Interface/Conductor Shield(P2)

Of the four interfaces, the I/CS interface is the most difficult to locate. This is evident in all the standard methods of edge detection, and also in Figure 4.3(b) where the edge of the conductor shield is less well defined compared to the conductor. The edge of the conductor shield is defined in Figure 5.14 as the change from a negative going ramp to positive going inflexion, in other words a positive change in gradient. When differentiated this feature will present itself as local maxima. The blue trace in Figure 5.18(a) displays the differentiated plot of the image. The trace is very noisy, with a large number of peaks and troughs. In order to determine the location (P2) of the I/CS interface, the plot can be improved by smoothing the original image using a median filter. This smoothed image can then be differentiated in the same way as described in Section 5.11. The median filter is used once again because, unlike linear smoothing operators, the median will preserve monotonic structures (regions of constant intensity), step edges and ramps in the image, while at the same time removing impulsive noise, such as the noise in the blue trace in Figure 5.18(a)[103]. As such, the median filter will smooth the image without the blurring that a linear filter would introduce. From testing the optimum window size for this median filtering was found to be 31 x 31 pixels. The size of the filter window is a trade off between smoothing and removal/attenuation of image features. If the window is too small the smoothing effect is reduced; if the window is too large then image features can be removed, because the filter will remove any structure

that is less than half the width/height of the filter window [104]. This means that any structure in the cable joint image that is less than 16 pixels ($\approx$ 200 µm) in either direction is attenuated/removed. For this reason, the noise content in the conductor shield region is reduced without removing the conductor shield structure from the image, because the conductor shield should be in the region 0.8 – 1.5 mm thick. The red trace in the Figure 5.18(a) displays the smoothed image differentiated plot. This smoothing has reduced the noise content in order to extract the underlying trend of the data. From this red trace it is therefore possible to determine the point of the local maxima, P2. This point can be located by searching for a local maximum close to the CS/C interface. To reduce the time required to detect P2, it is possible to reduce the region of the original image that is smoothed by only smoothing the region of the image above the average location of the CS/C interface. The height of this region was set to be twice the thickness of the expected conductor shield thickness. For the 90 kV cable joint sample used to generate the images in Chapter 4, the larger of the two end thickness measurements of the conductor shield was approximately 1.5 mm. The height of the region of smoothing was therefore set at 3 mm, or 250 pixels. For a full cable joint where the ends cannot be measured, the stated specification for the cable joint has to be used to calculate the height of the smoothed region. By only smoothing a small section of the image, the processing speed is improved in two ways: the area of smoothing is reduced and the region of the local maximum search is reduced as a result. Once the image has been smoothed, differentiated and then P2 located, the I/CS interface can be transposed back onto the original cable image in a similar manner to P1. Figure 5.18(b) is a section of image with the I/CS interface highlighted. From this image it is possible to see a single line running parallel to the conductor edge. This line is also free from salt and pepper noise and requires no threshold value.

5.2.2.3 Insulation Shield Interface/Insulation (P3)

The IS/I interface is depicted in Figure 5.16(a) as the darkest of the three lines running horizontally across the image. This means that P3 is located at the global minimum for each column, which, owing to the exposure geometry, should be found in the upper half of the image. P3 is therefore located in a similar manner to P1, except this time the minima is located in the upper half of the image, and is a global minimum, rather than just a local minima. Figure 5.19 shows the location of P3 and the effect of transposing

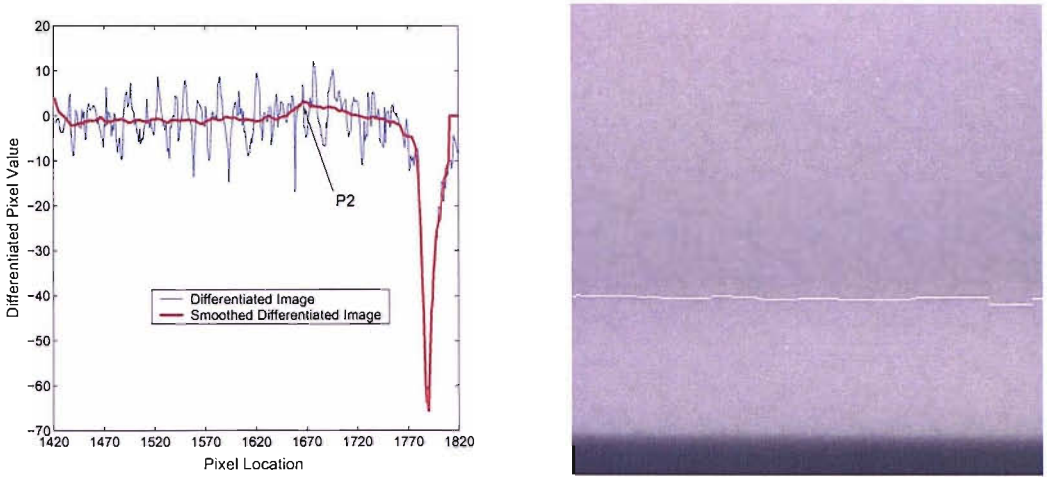

(a) (b)

FIGURE 5.18: (a) The differential line plot of the conductor shield region, and (b) the image showing the detection of the I/CS interface

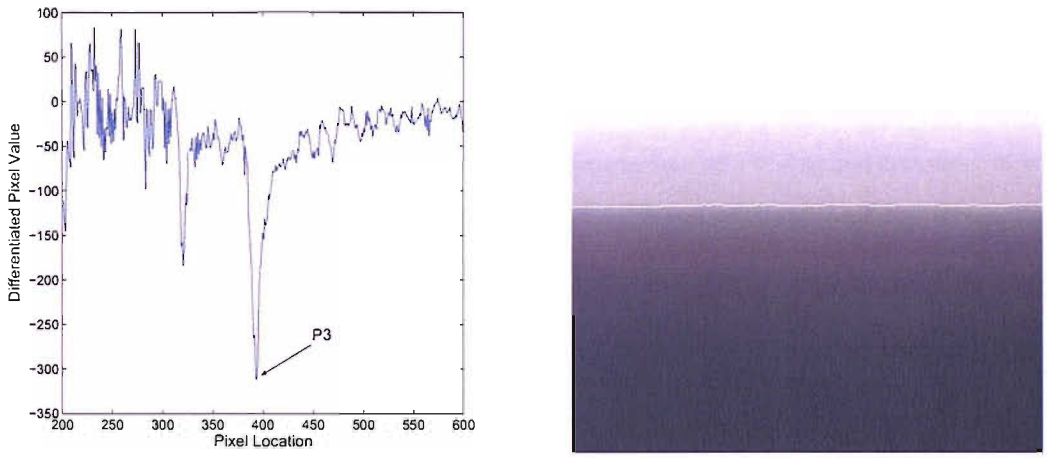

(a) (b)

FIGURE 5.19: (a) The differential line plot of the upper insulation region, and (b) the image showing the detection of the IS/I interface

its location back onto the original image. From the figure it can be seen that the IS/I interface has been found successfully.

5.2.2.4 Air Interface/Insulation Shield (P4)

The A/IS interface in Figure 5.16(a) is shown as a line that is lighter than the IS/I interface. The line is also less defined compared to the IS/I line. This means that the location of the A/IS interface is at second largest local minima after P3 in the upper

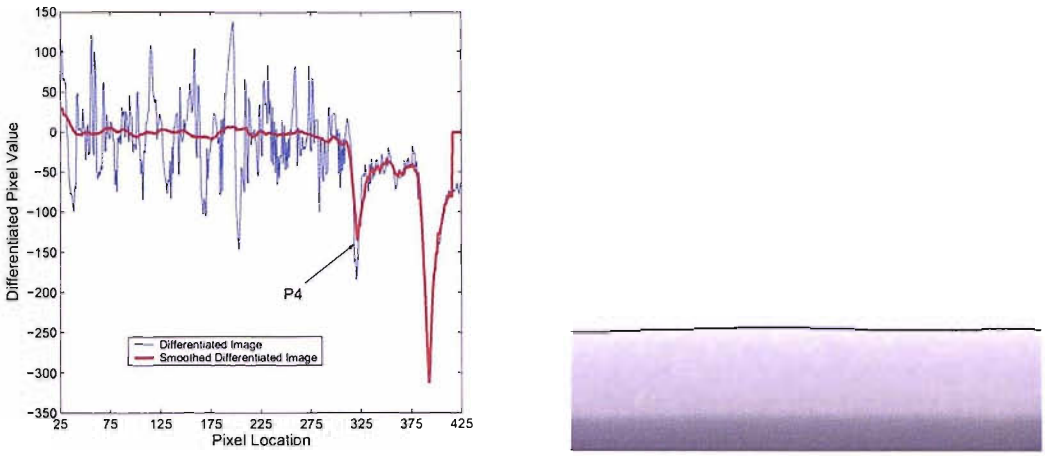

FIGURE 5.20: (a) The differential line plot of the insulation shield region, and (b) the image showing the detection of the A/IS interface

section of the image. To find the second largest local minima in a data set is more difficult than simply finding the minimum value of that data set, because P4 is not the second smallest data point, rather it is the second largest negative spike. To find this point, each pixel in the column-wise image data has to be checked to see if it is a local minima. This is achieved by setting a spatial bandwidth to half the size of the expected thickness of the insulation shield. Each pixel then becomes the central pixel of this bandwidth. If this central pixel is the data point in the bandwidth with the most negative value, this pixel has to be a local minima. The bandwidth is set at half the thickness of the insulation shield so that the data points of the negative spike of the IS/I shield do not become grouped with the data points of the negative spike of the A/IS interface and as a result produce a false local negative close to P3. To improve the detection of P4, the image is smoothed in a similar manner to the image data used to detect P2, once again using a 31 x 31 median filter. This is necessary to ensure that the noise in the data between P4 and P3 does not affect the interface detection. The speed of the process of smoothing and interface detection are also improved by restricting the inspection process to an area twice the expected thickness of the insulation shield, in a similar manner to the process used to locate P2. Figure 5.20 shows the line plot and subsequent interface image relating to the detection of the A/IS interface. From this image it can be seen that the A/IS interface has also been located successfully.

5.3 Insulation Component Thickness Determination

The four methods of interface detection described above can therefore be used to determine the location of the edges in the image that relate to insulation system component interfaces in the cable joint sample. The output from the procedure is a four row matrix with the same number of columns as the image inspected. The first row of the matrix is the location of the A/IS interface and the fourth row is the CS/C interface, the middle two rows correspond to the IS/I and I/CS interfaces respectively. This means each column of the image has four interface locations stored in the four row matrix. The rows of this matrix can be used to produce four continuous interface lines that, unlike the standard edge detection methods, are free from the salt and pepper noise and do not require thresholding values to determine the edge location. In order to verify that these lines correspond to the actual locates of the interfaces, they can then be superimposed onto the original image. From Figures 5.17 – 5.20 it can be seen that all four interfaces appear to have been found correctly, however, this method of verification is limited by the ability of the human eye to decern greyscale differences. To improve the reliability of the verification process, it is possible to compare the actual thicknesses of the insulation components of the cable joint sample with calculated component thickness generated from the interface location data.

Each column of the four row interface data matrices contains the location of the interfaces for the corresponding the columns of the cable joint sample image. Each location interface is the distance, in pixels, between the bottom edge of the image and the interface. The thickness of each component can therefore be determined by subtracting the pixel location value of its lower interface from the pixel location value of its upper interface. To convert this pixel separation value into a physical measurement, it must be multiplied by the size of the pixels (13.5 μm) and then divided by the magnification factor, d, determined from Equation 4.11. For the conductor shield (CS) the equation used for a single column of the image would be:

$$\mathrm{CS(j)} = (\mathrm{I/CS(j)} - \mathrm{CS/C(j)}) \times \frac{13.5 \times 10^{-6}}{\mathrm{d}} \tag{5.10}$$

where I/CS is the conductor shield to insulation interface line data point in the array, CS/C is the conductor to conductor shield interface line data point in the array, and j

is column under investigation.

This component thickness calculation can be used to find the thickness of the insulation shield, insulation, and the conductor shield for each column of the image. This means that the thickness of each component can be measured with a sample interval equal to the size of a pixel. From this data a mean, minimum, and, maximum thickness for each component can be calculated, along with a standard deviation for each component. The thicknesses generated can therefore be compared with measured thicknesses from the actual cable joint sample. The following section details the method used to undertake this verification process.

5.3.1 Calculated Insulation System Component Thickness Verification

In order to verify that the component thicknesses generated using the edge detection algorithms described above are accurate, a 55 mm section of a 90 kV cable joint sample was used as a test case. This sample consists of central conductor insulated with hand lapped semiconducting and EPR tapes. The sample was also used to generated the images in Chapter 4. The section of cable joint used is shown in Figure 5.21(a). The upper circular face in the image is the left-hand end of the cable joint sample. The EPR insulation appears as the orange portion of the cable joint insulation, while the black rings and outer surface relate to the semiconducting screens.

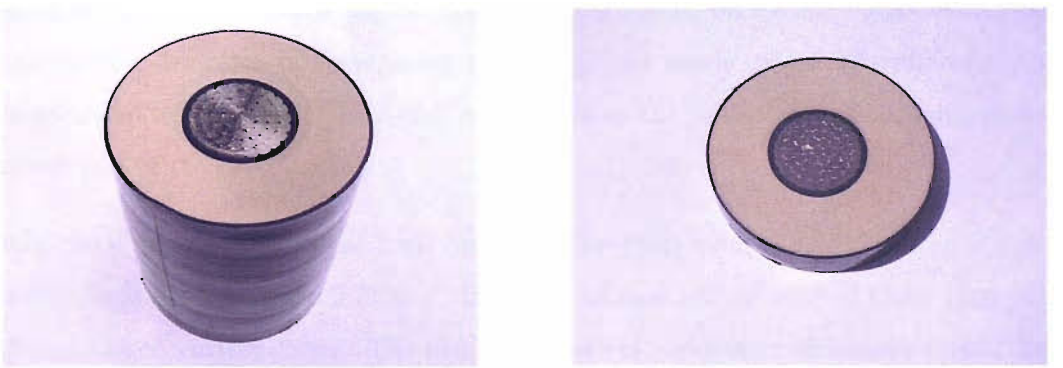

(a) (b)

FIGURE 5.21: The cable joint sample used to verify the insulation component thickness calculations. (a) the full sample, and (b) a slice of the cable sample

The sample was imaged following the process described in Chapter 4, Section 4.8. To image the full length of the joint sample, it was indexed past the camera to produce

three images per image angle. Each set of three images were then montaged together to produce eight full length images of the cable joint. Figure 5.22(a) shows the montaged image for the 0° inspection angle. This image was produced in the same manner as the image in Figure 4.34(c). The eight full length images were then processed to find the interfaces in the image. Figure 5.22(b) is a plot of the four row matrix produced. The 'y' axis label has been omitted from this plot to improve the comparison of the superimposition of the interface line onto Figure 5.22(a). The data in the four row matrix in Figure 5.22(b) was then superimposed onto Figure 5.22(a). Figure 5.23(a) displays the detected interface lines. The lines have been thickened in this image from a single pixel width to 10 pixels in order to improve the visibility of the lines in the Figure. To verify that the lower two interface lines correspond to the appropriate interfaces, Figure 5.23(a) has been brightened to produce Figure 5.23(b) in order to highlight the conductor and conductor shield.

From Figure 5.23 it appears that the interface lines detected correspond to the interfaces in the image. This process was then repeated for all eight inspection angles. The thickness of the components between the interface lines on all eight images were then calculated. The magnification factor for the geometry used to image the cable joint was 1.1057. This results in pixels that are equivalent to 12.21 x 12.21 μm. Table 5.1 contains the results of this calculation. The values in this table have a tolerance of ± 1 pixel width and then have been rounded to the nearest 10 μm. Included in the table are mean, minimum, and maximum thicknesses of the insulation system components, plus the standard deviation of these measurements for the whole cable. The dimensions in the columns 'left end' and 'right end' correspond to the thicknesses of the components at each end of the cable sample.

Once these measurements had been obtained, the cable sample was dissected into six equally sized slices (Figure 5.21(b)). The approximate size of each of these slices was 8.5 mm due to cutting losses. The insulation system component thicknesses were then measured at 0°, 45°, 90°, 135°, 180°, 225°, 270°, and 315°, using the x8 magnifying eye glass described in Section 4.7. The eye glass graticule made it possible to take measurements with a resolution of 0.05 mm. Table 5.2 contains the results of this measurement process.

In order to verify the accuracy of the measurements taken, the conductor was also

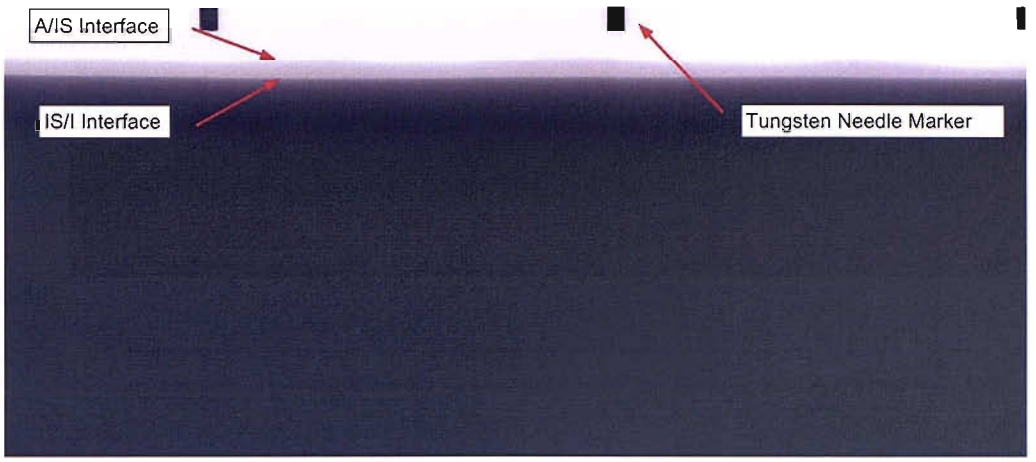

(a)

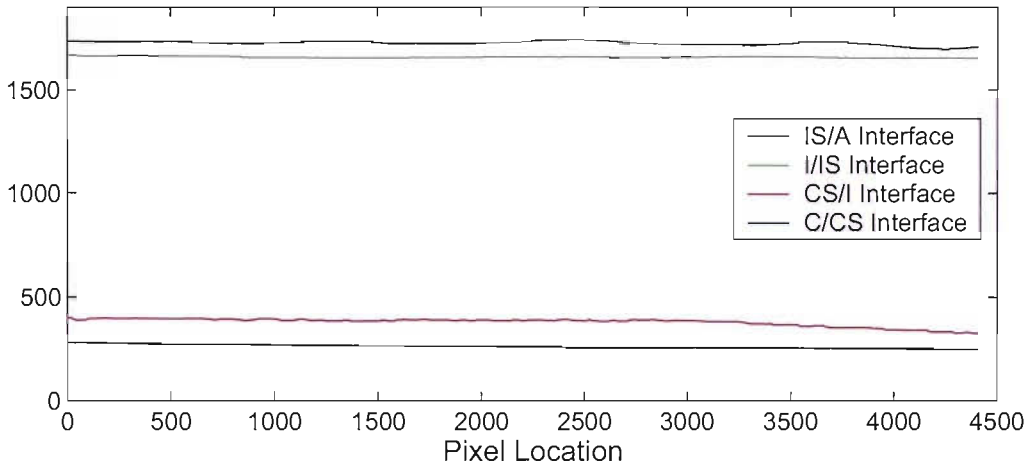

(b)

FIGURE 5.22: (a) Cable joint image, and (b) a plot of the interface lines.

measured at 0°, 45°, 90°, and 135°. The sum of the insulation system components at opposing angles plus the corresponding conductor thickness could then compared with the outside diameter of the cable joint sample, i.e. the component thickness of the 0° and 180° measurements plus the conductor thickness at 0° should equal the outside diameter of the cable in that plane. The total diameter of the cable was measured using a vernier with a tolerance of ±50 µm. This approach was used to ensure that minimal measurement error was introduced into the process.

To verify the calculated component thicknesses generated using the edge detection method, the calculated thickness of the insulation system components generated from the data at each end of the four row matrix and the measurements taken of the component thicknesses at each end of the cable joint sample can be directly compared. To do

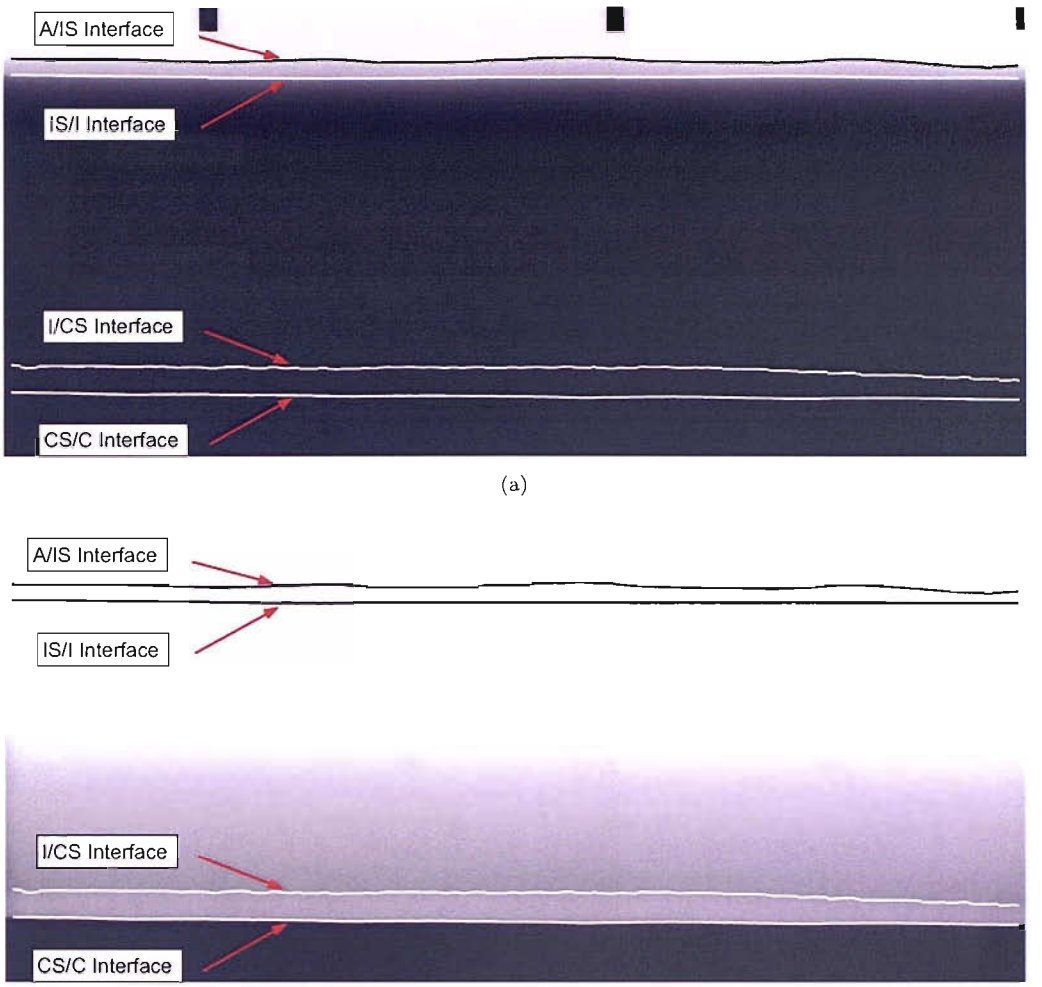

FIGURE 5.23: (a) Cable joint image, and (b) a plot of the interface lines.

this, an average was taken of the 41 data points at each end of the four row matrix. 41 data points were taken as this corresponds to 0.5 mm. An average over 0.5 mm was used to reduce the risk of an outlier skewing the data. The average thicknesses calculated are shown in the two right-hand columns of Table 5.1. Figure 5.24 compares the calculated thicknesses with the measured thicknesses. Figures 5.24(a), 5.24(b), 5.24(e), and 5.24(f) have horizontal grid lines shown on the plot. These grid lines correspond to the resolution of the eye glass. From these four figures it can be seen that the calculated and measured thicknesses of the two semiconducting shields differ less than the resolution of the eye glass. The grid lines are omitted from Figures 5.24(c) and 5.24(d) because, due to the range of thickness of the insulation, the number of grid lines would be too large, however from the raw data it can be seen that calculated and measured thickness of the insulation also differ less than the resolution of the eye glass.

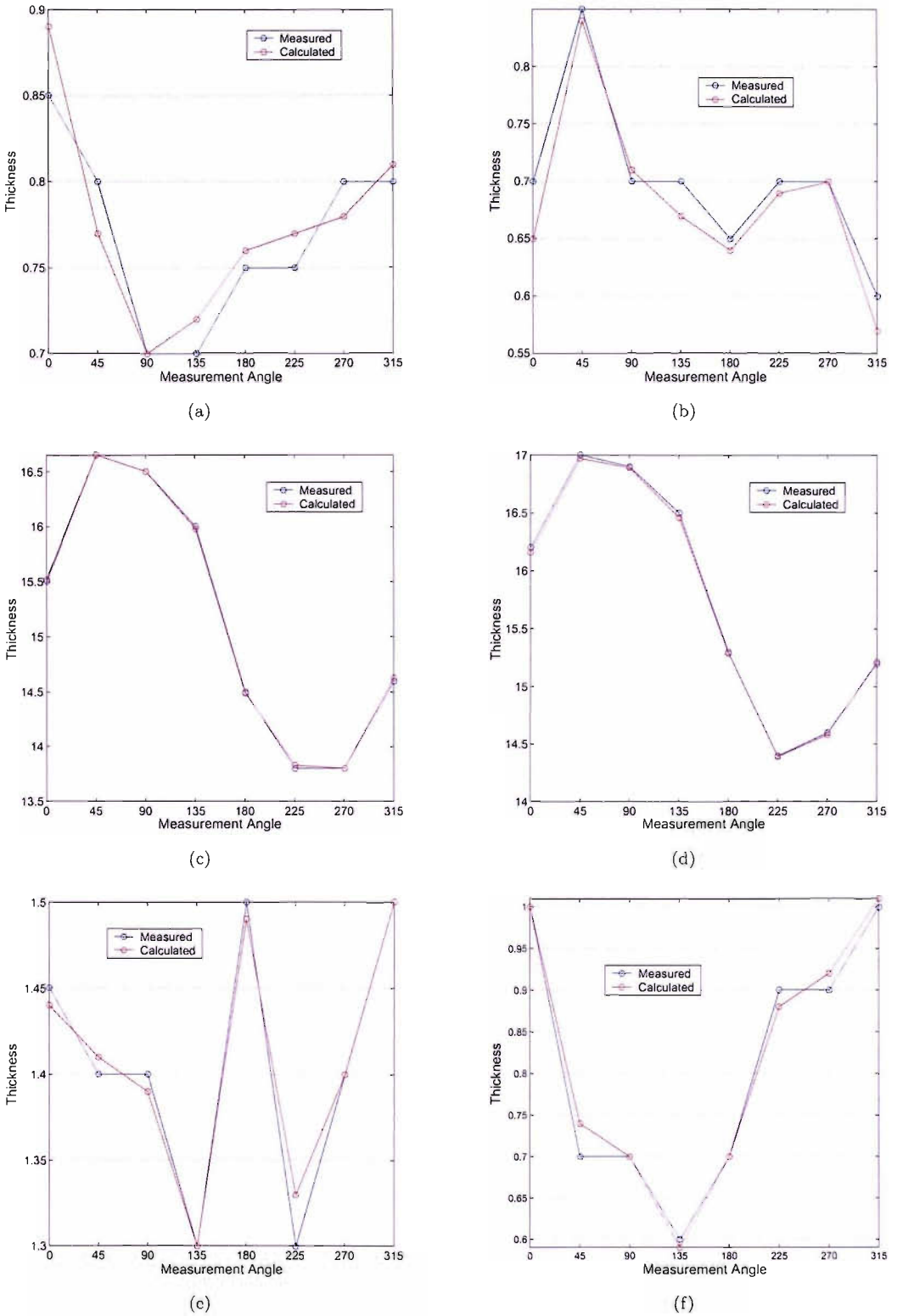

FIGURE 5.24: Comparison of calculated and measured thicknesses of the insulation system components measured at each end of the cable joint sample, (a) left hand end insulation shield, (b) right hand end insulation shield, (c) left hand end insulation, (d) right hand end insulation, (e) left hand end conductor shield, and (f) right hand end conductor shield

		Calculated Thicknesses (mm ±1 pixel width ±5 µm)					
Inspection Angle	Component	Mean	Min	Max	Standard Deviation	Left End	Right End
0	Conductor Screen	1.40	0.81	1.64	0.18	1.44	1.00
45		1.25	0.73	1.78	0.19	1.41	0.74
90		1.17	0.67	1.51	0.23	1.39	0.70
135		1.17	0.57	1.40	0.21	1.30	0.59
180		1.35	0.68	1.55	0.21	1.49	0.70
225		1.36	0.88	1.56	0.16	1.33	0.88
270		1.43	0.89	1.59	0.14	1.40	0.92
315		1.54	1.00	1.75	0.14	1.50	1.01
0	Insulation	15.65	15.43	16.20	0.22	15.52	16.16
45		16.67	16.47	16.98	0.11	16.65	16.97
90		16.59	16.39	16.92	0.15	16.50	16.89
135		16.04	15.82	16.48	0.15	15.98	16.46
180		14.75	14.55	15.31	0.17	14.49	15.29
225		13.91	13.69	14.41	0.17	13.83	14.39
270		14.00	13.75	14.6	0.19	13.80	14.58
315		14.67	14.51	15.23	0.15	14.63	15.22
0	Insulation Screen	0.83	0.49	1.04	0.11	0.83	0.65
45		0.78	0.55	0.93	0.07	0.77	0.84
90		0.75	0.56	0.89	0.07	0.70	0.71
135		0.75	0.59	0.84	0.06	0.72	0.67
180		0.77	0.60	0.93	0.07	0.76	0.64
225		0.79	0.60	0.96	0.08	0.77	0.69
270		0.79	0.56	0.92	0.07	0.78	0.70
315		0.80	0.56	0.94	0.07	0.81	0.57

TABLE 5.1: Calculated insulation component measurements of a 90 kV submarine cable joint

Figure 5.24 was generated using only the data from the ends of the cable. It is not possible, however, to compare the data from the inner slices of the cable sample in the same manner because the precise location of each cut used to make the slices is unknown. For this reason the data generated from the inner slices of the cable sample can be compared using Figure 5.25. It can be seen that all of the measurements taken from the individual slices are similar to the calculated mean value for the corresponding image angle, and none of the measurements taken are outside of one standard deviation either side of the mean value.

From the two verification methods it can be assumed that the calculated thicknesses generated using the edge detection method are accurate, and reflect the physical measurements that would be obtained if a destructive analysis of the cable joint was possible. In order to determine if standard edge detection methods could replicate this level of interface detection precision, the Canny edge detection operator was used to process the 90° full length image. From Figure 5.9, it can be seen that in order to detect the I/CS and CS/C interfaces the value of σ has to be relatively large and the threshold

		Destructive Test Measured Thicknesses (mm ±50 µm)							
Inspection		Left	Slice Number					Right	
Angle	Component	End	1	2	3	4	5	End	Mean
0		1.45	1.6	1.6	1.6	0.95	1.0	1.0	1.37
45		1.4	1.45	1.4	1.4	0.9	1.2	0.7	1.21
90		1.4	1.4	1.3	1.3	0.8	0.9	0.7	1.11
135	Conductor	1.3	1.4	1.4	1.3	0.9	1.0	0.6	1.13
180	Screen	1.5	1.5	1.4	1.4	1.15	0.9	0.7	1.27
225		1.3	1.5	1.45	1.4	1.15	1.0	0.9	1.30
270		1.4	1.5	1.55	1.6	1.25	1.0	0.9	1.38
315		1.5	1.7	1.7	1.7	1.2	1.6	1.0	1.58
0		15.5	15.6	15.4	15.5	15.85	15.75	16.2	15.71
45		16.65	16.6	16.5	16.5	16.5	16.9	17.0	16.64
90		16.5	16.4	16.5	16.5	16.75	16.7	16.9	16.62
135	Insulation	16.0	16.0	16.0	16.2	16.2	16.1	16.5	16.10
180		14.5	14.7	14.7	14.9	14.8	15.2	15.3	14.86
225		13.8	13.7	13.75	14.0	14.2	14.2	14.4	13.92
270		13.8	13.7	13.95	13.9	14.2	14.55	14.6	13.94
315		14.6	14.8	14.6	14.6	14.7	14.7	15.2	14.67
0		0.85	0.9	0.95	0.95	0.9	0.8	0.7	0.86
45		0.8	0.8	0.8	0.85	0.75	0.75	0.85	0.78
90		0.7	0.7	0.8	0.85	0.7	0.85	0.7	0.76
135	Insulation	0.7	0.7	0.8	0.8	0.8	0.9	0.7	0.77
180	Screen	0.75	0.9	0.8	0.9	0.9	0.7	0.65	0.80
225		0.75	0.7	0.75	0.8	0.8	1.0	0.7	0.80
270		0.8	0.8	0.65	0.85	0.9	0.9	0.7	0.80
315		0.8	0.95	0.7	0.9	0.85	0.8	0.6	0.80

TABLE 5.2: Insulation component measurements taken from slices of a 90 kV submarine cable joint

values set low. With this configuration of the Canny operator, all four interfaces can be found, however this also introduces large amounts of noise. To improve the noise levels within the image, the value of σ can be decreased and the threshold values increased. With these settings it is possible to produce a relatively noise free image of the A/IS and IS/I interfaces. For these reasons, the 90° full length image was processed twice. For the first iteration, σ was set to 5, and the values of the upper and lower thresholds were set to 0.025 and 0.001, respectively. Using these settings, Figure 5.26(a) was produced. This image clearly displays the I/CS and CS/C interfaces, however there is some non-detection of the A/IS interface. This non-detection was overcome by passing the Canny operator over the original full length image again, however, for this second iteration σ was set to 1.5 and the upper and lower thresholds were set to 0.08 and 0.04, respectively. This produced a relatively noise-free image of the A/IS and IS/I interfaces (Figure 5.26(b)). The dimensions of the the conductor shield, insulation and insulation shield could then be found by locating the I/CS and CS/C interfaces in Figure 5.26(a)

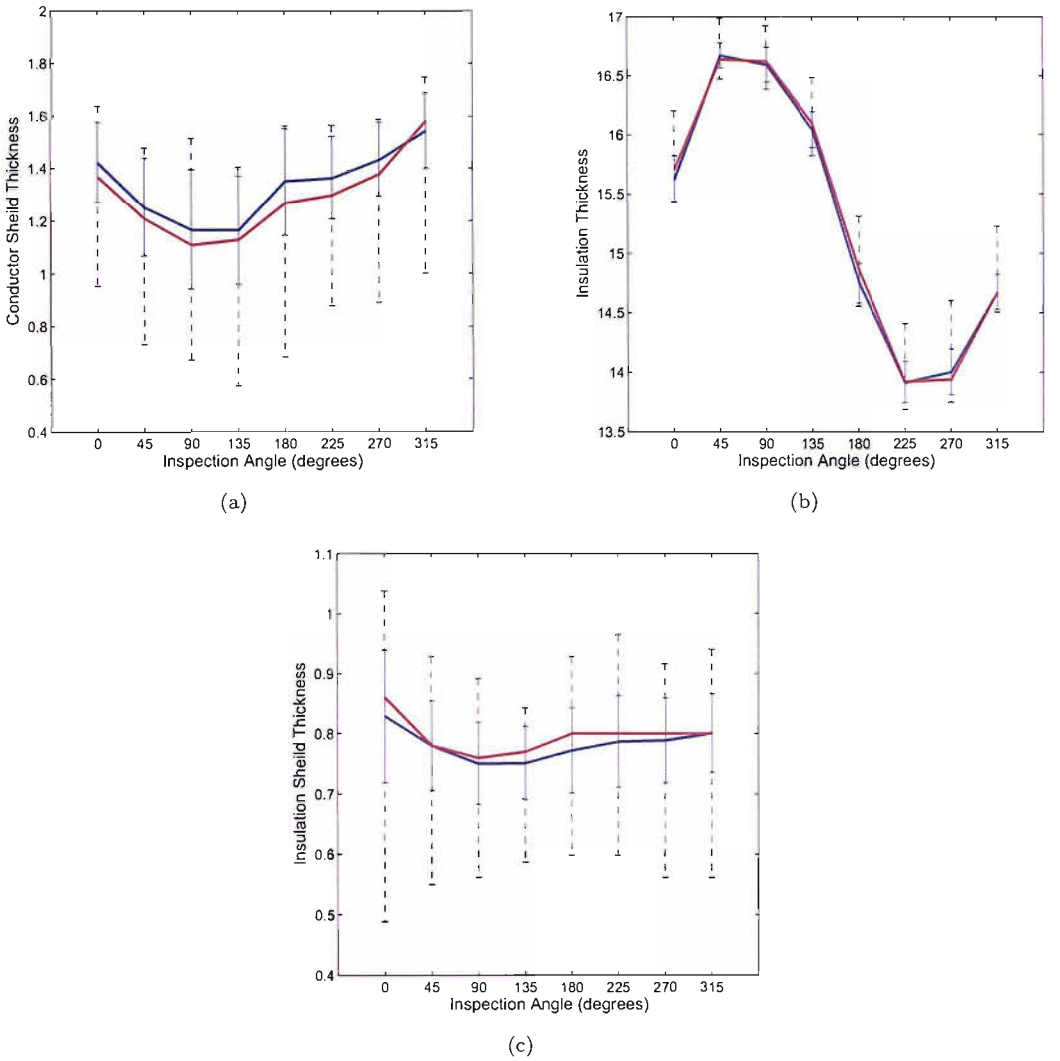

FIGURE 5.25: Calculated thicknesses (blue trace) with confidence limits (blue - 1 standard deviation, black - Min/Max) and measured slice thicknesses (red trace) (a) conductor shield, (b) insulation, and (c) insulation shield.

and the A/IS and IS/I interfaces in Figure 5.26(b). Table 5.3 compares the results obtained using this method of Canny edge detection and the results obtaining using the proposed feature extraction method. The values stated in the table have tolerances of ± 1 pixel width and then have been rounded to the nearest 10 µm. From the table it can be seen that the results generated by both methods are relatively similar; with a maximum variation of 4.1%. This confirms that the proposed system produces similar results compared with standard edge detection techniques, however, to generate the Canny interface information, six variables had to be manually tuned in order to optimise the edge detection. Once these variables had been chosen, two separate images were produced. These images then had to be inspected in order to determine the location of the

Measurement Method	Component	Calculated Thicknesses (mm)					
		Mean	Min	Max	Standard Deviation	Left End	Right End
Feature Extraction	Conductor	1.17	0.67	1.51	0.23	1.39	0.70
Canny Edge Detection	Screen	1.16	0.68	1.49	0.21	1.38	0.73
Feature Extraction	Insulation	16.59	16.39	16.92	0.15	16.50	16.89
Canny Edge Detection		16.61	6.41	16.90	0.13	16.51	16.88
Feature Extraction	Insulation	0.75	0.56	0.89	0.07	0.70	0.71
Canny Edge Detection	Screen	0.77	0.59	0.90	0.07	0.68	0.74

TABLE 5.3: Comparison of the proposed feature extraction interface detection method and interface detection using the Canny edge detection operator

interfaces. To do this, knowledge of the cable joint geometry was required so that the location of the I/CS and CS/C interfaces were not affected by the surrounding noise components within the image. This method of interface detection, therefore requires manual tuning, prior knowledge of the cable exposure geometry, and the interface location process is dependent on information from the operator. This operator interaction, however, is not required in order to determine the locations of the interfaces using the proposed feature extraction method. This makes detection of the interfaces considerably easier and removes the time costs imposed by the manual aspects of the Canny detection method. The proposed interface detection method is also free from salt and pepper noise; is not image specific and therefore can be used to inspect all cable geometries; and it can be used to accurately measure the thickness of the insulation system components. This infers that the calculated mean, minimum, and maximum component thickness data can be used to determine whether the cable joint conforms to the stated specification for the cable. Should the minimum thickness of any of the components be smaller than the specified tolerated thickness, then the cable joint should be refitted before the cable is introduced into the cable network. A refit should also be undertaken should the maximum be larger than the specified maximum.

A second advantage to this inspection method is that the image data is significantly compressed. An individual, non-montaged imaged requires 8.65 MB of storage space. This is reduced to a 4 x 2045 matrix requiring 16.36 kB. This significantly reduces the storage space required, and facilitates the production of a 3D image, as described in Chapter 7.

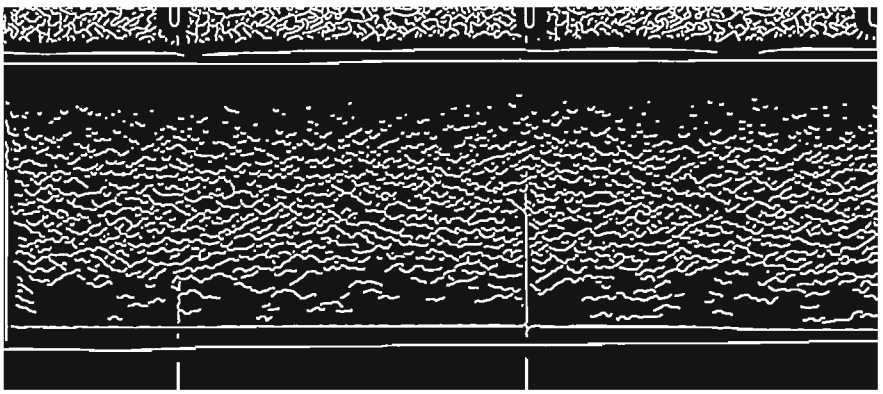

(a)

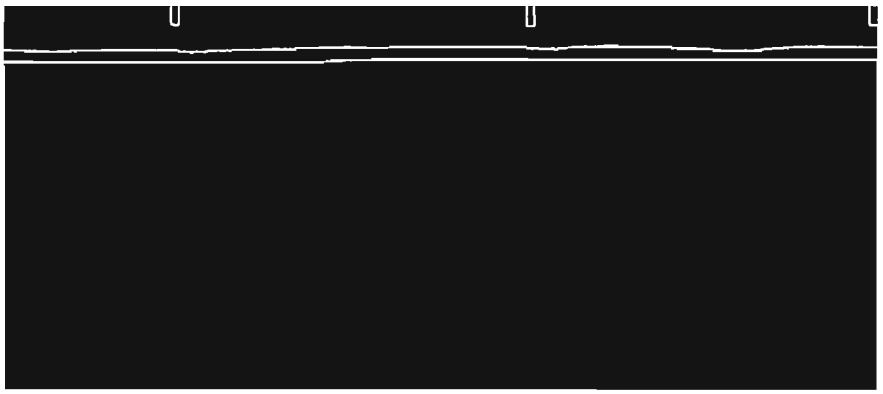

(b)

FIGURE 5.26: Canny edge detection images used to generate the component thickness calculations shown in Table 5.3.

5.4 Summary

The x-ray images can be used to perform dimensional checks on cable joints. The size of the components can be determined by measuring the distance between the interfaces. To find the interfaces, standard edge detection methods could be used, however the results of finding the interfaces in this manner is either incomplete interface detection, or complete detection images that contain considerable levels of noise. To overcome this, a set of algorithms have been developed that find the interfaces using feature extraction to locate known characteristics in the images. To do this, the images are differentiated using an averaging differentiator. This produces a new image that displays the low pass filtered gradients of the original image. The changes in gradient associated with the changes of attenuation caused at the boundary of two materials can then be found. Due to the ramp like nature of the images of cable joint insulation, the four interfaces between the air, insulation shield, insulation, conductor shield and conductor can be

found in each column of the image. This method of detection is superior to the standard edge detection techniques described because it does not suffer from the same levels of false positives that the standard techniques suffer from, but there is still complete detection of the interfaces. The size of the individual components of the cable joint is determined from the differentiated image by counting the number of pixels between each component interface and then multiplying the number counted by the size of the pixels, taking into account the magnification in the image. The dimensional checks required for the assessment of the manufacturing quality of the cable joint can then be performed digitally. This infers that the mean, minimum, maximum, and standard deviation of the thickness of each component can be produced, including the locations of the minimum and maximum thickness found. The proposed system, therefore, produces a more thorough analysis of the dimensions of the components of the insulation system, because this level of analysis would be too time consuming using the original system. The accuracy of this detection method has been assessed by imaging a sample of a cable joint, followed by the digital detection of the interfaces. The results of this inspection were compared with sample measurements from the cable joint. The results of this comparison verified that the interfaces could be found to within 100 µm. Due to the accuracy and resolution of this inspection method, it is therefore possible to use the dimensional information generated to determine if the cable joint has been manufactured to within the dimensional specifications stated by the manufacturer. A further advantage of the proposed detection method is that the resulting data is significantly reduced in volume compared to the raw image data. The obtained data can then be used to produce 3D images of the cable joint.

Chapter 6

Insulation System Defect Detection

The procedure used to join two cable lengths together is a manual process (Chapter 2, Section 2.2). It is, therefore possible that defects can be accidentally introduced into the insulation system of the cable joint. The two main types of defects that can be found in the insulation system of the cable joint are inclusions (mainly metallic or carbonised particles) or voids (gas or a vacuum within the insulation) [105]. These defects can reduce the expected working lifetime of the cable joint if they are large enough to subject the insulation system surrounding the defect to a significantly increased electrical stress. For this reason it is necessary to ensure that the insulation system of each cable joint does not contain any inclusions or voids that will have an adverse affect on the performance of the cable joint. The size and number of inclusions or voids that are considered to be detrimental to the performance of each length of parent cable either side of the cable joint are stated in Standards [10–12]. There are no standards, however, associated with hand lapped polymeric cable joint manufacture. The pass/fail criteria for joints is generally stated as no detectable inclusions or voids should be found within the insulation system of the joint. Current inspection procedure therefore requires that each joint be inspected to find any defect that is visible in the x-ray image. The size of the smallest detectable defect of the proposed system must therefore equal or better those detected using the current system for the proposed system to be a valid inspection facility.

To detect defects with the original system, the x-ray photographic plate is inspected for regions within the image that are different to the surround cable joint image. This can be achieved digitally by inspecting the pixel intensities of the CCD camera x-ray image. A defect introduced into the insulation system of a cable joint will manifest itself in the x-ray image as a group of pixels with greyscale intensities that are significantly different to the intensities of the pixels associated with the surrounding defect free insulation system. Metallic or carbonised particles are generally radiologically more dense compared with the insulating and semiconducting materials of the cable joint insulation system. This means that inclusion in the insulation system will absorb/scatter more x-ray flux compared with a defect-free section of the insulation system. As a result, less x-rays are detected by the CCD array and so the inclusion presents as a group of pixels with reduced greyscale intensities. The converse is true for a void whether it is a vacuum or gaseous defect. The volume of a void will produce a reduced attenuation pathway for the x-ray flux due to the reduce radiological density of the void, consequently it will manifest itself in the x-ray image as a group of pixels with increased greyscale intensities.

Figure 6.1(a) is a 8-bit greyscale image of a section of defect-free joint insulation. The range of pixel intensities that make up this image are shown in the histogram in Figure 6.1(b). Due to the frequency spectrum of x-rays generated to irradiate the insulation, and the nature of the interaction between these x-rays and the insulation, the histogram of the pixel intensity distribution of a defect-free section of insulation tends towards a normal distribution [105]. It can be seen from 6.1(b) that the mean of the pixel intensity distribution for this section of insulation is around 180. If a defect is introduced into the insulation, the surrounding defect-free insulation will still produce a distribution similar to Figure 6.1(b), however, a second normal distribution will also be generated that is associated with the defect. Figure 6.1(c) is a section of insulation system that is similar to Figure 6.1(a), however in the centre of this section of insulation is a metallic inclusion. As described above, the inclusion presents as a group of pixels that are darker than the surrounding defect-free insulation pixels. These pixels produce a second distribution of greyscale intensities that are centred around 110 (Figure 6.1(d)). A defect can therefore be found by inspecting regions of the cable joint image for distributions of pixel intensities that are significantly different to the intensity distributions of the surrounding defect free regions [94].

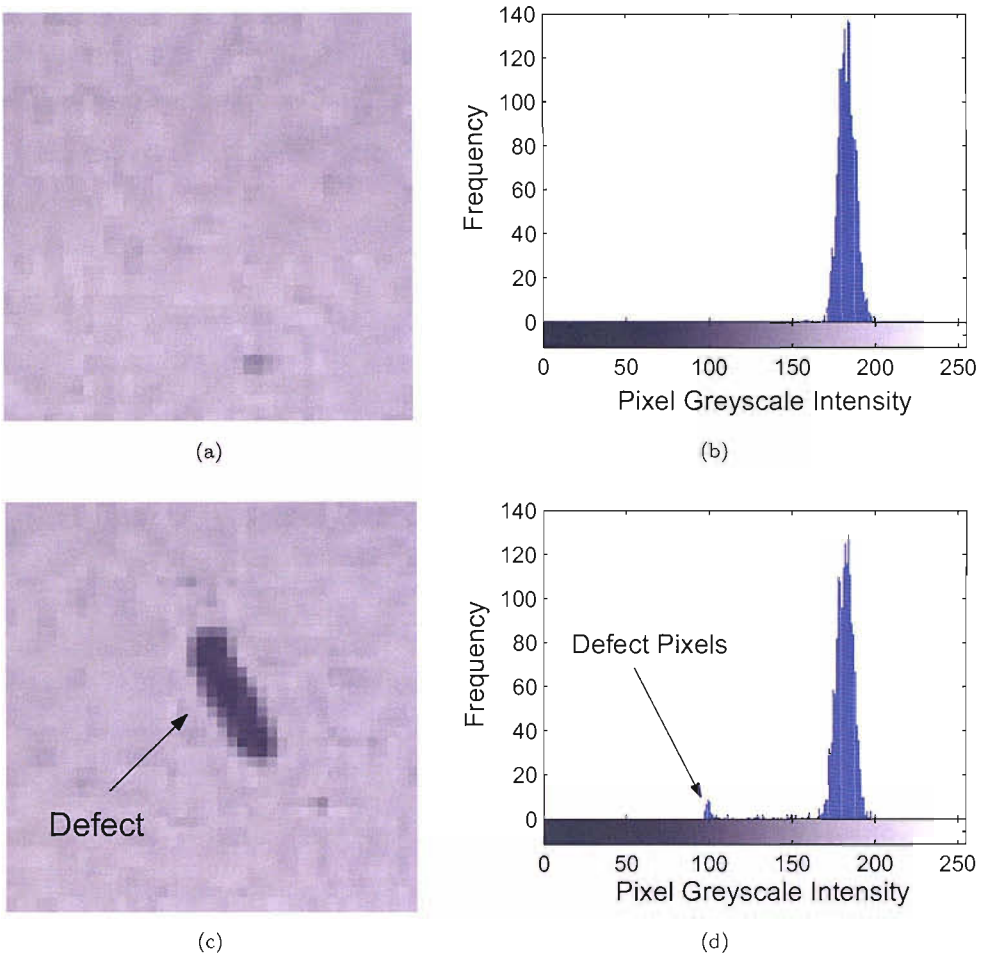

FIGURE 6.1: The manifestation of a defect within the insulation system of a cable, (a) section of defect-free insulation, (b) histogram of the pixel intensities of the defect-free insulation, (c) section of insulation containing a defect, and (d) histogram of the pixel intensities of the insulation containing a defect.

6.1 Defect Detection Procedure

The photometrically corrected x-ray images generated to find the component interfaces of the cable joint can be used to detect defects in the cable joint. The edges of the defects could be found using the edge detection methods described in Chapter 5. The size of defects, however, can be considerably smaller than the components of the insulation system, and the change in greyscale intensity can also be considerably less. The minimum resolution of the standard edge detection techniques are therefore not stringent enough to make these methods applicable to defect detection. It is possible, however, to detect a defect within the insulation system using the expected statistical differences between the pixel intensities of the defect-free regions of the insulation system and the pixel

intensities associated with the defect. For an inclusion the image has to be inspected for groups of pixel with a reduced pixel intensity, whereas for a void the groups of increased intensities have to be found. This process can be improved, however, if the image characteristics that are generated by the geometric shape of the cable joint are removed.

6.1.1 Removal of defect-free Cable Joint Insulation System Image Data

Chapter 4, Section 4.2 describes the general characteristics of a cable joint image that are generated due to the cylindrical nature of the cable. The main effect on the image captured by the CCD array caused by the shape of the cable joint is to produce a ramp like profile in the intensity mesh plot (Figure 4.3(c)). If a defect is introduced into the cable joint, then it will therefore cause local changes to the ramp shape of the mesh plot. This means that the image data relating to a defect within the cable joint is offset from zero by the ramp; with this ramp being directly attributable to the defect-free insulation system surround the defect. If this defect-free image data could be removed, the defects would no longer be offset from zero and the resultant image would only contain data relating to the defects within the cable joint.

Figure 6.2(a) shows an x-ray image of section of defect-free cable joint insulation. The ramp like shape of the cable joint image can be seen in the mesh plot (6.2(b)). As there are no defects within this section of cable joint, if all the data relating to the defect free insulation system was removed, there would be no image data remaining in the resultant image. It is possible, however, to artificially introduce defects into this image by simply reducing or increasing the pixel intensity values of regions within the image. The altered regions will therefore contain pixels with a similar distribution of intensities compared to the surrounding insulation system, however the mean of the pixel intensity distribution of the defect will be different, therefore the altered pixels will have the characteristics of either an inclusion or a void. Figure 6.2(c) shows the section of cable joint shown in Figure 6.2(a), but with five defects artificially introduced into the cable joint using the method described above. The defects introduced were five square regions measuring 40 x 40 pixels. Each defect therefore represents a square region measuring 0.48 x 0.48 mm. The size of these defects was set to be relatively large for display purposes. The change in intensity of these manufactured defects ranges

from -4000 to + 3000 greyscale levels, which is also considerably larger than the change in intensity that would be expected for an inclusion or a void. Despite the size and intensity changes of these defects, only four defects can be seen in Figure 6.2(c) due to the defect pixel intensities being offset by the underlying defect-free insulation system (Figure 6.2(d)). To remove this offset, the pixel image data associated with geometric shape of the joint in Figure 6.2(a) can simply be subtracted from Figure 6.2(c). The results of this subtraction are shown in Figure 6.2(e). In this image, the defects are no longer offset by the underlying insulation system (Figure 6.2(f)), and as a result all five defects are visible. The second benefit of removing the defect free insulation image data is that defect-free insulation can be characterised as the regions of the image with a distribution of pixels centred around zero, where as a defect will be represented by a group of pixel that are distributed around a non-zero mean. As a result, information relating to the surrounding pixel intensities is no longer required in order to detect a defect, simplifying the detection process.

It was possible to produce the defect image and mesh plot in Figures 6.2(e) and 6.2(f) by simply subtracting the Figure 6.2(a) from Figure 6.2(c) because these two figures are identical except for the artificially introduced defects. For the defects introduced during manufacture, this is not possible as a defect-free image of the cable joint will not exist. This means an artificially generated defect-free image has to be created. The main requirement of the artificially generated defect-free cable joint image is that the individual columns of the image must emulate the ramp profile of the cable joint with the defect removed.

Along the length of the cable joint this ramp profile will change subtly, however over a short distance the ramp profile will not change significantly (Figure 6.3). This means that each column of the artificially generated defect-free image can be produced using the average of the adjacent columns of the cable joint image. For a section of defect-free cable joint it would be possible to generate the artificial defect-free cable joint image using only the average of the columns either side of the column under investigation. In order to maintain the edges of the image data, this average can be calculated using the median of the adjacent columns. For the columns of the image containing a defect, using just the two columns either side of the column under investigation is not effective because a significant defect will span more than one column. This means that to produce a good quality artificially generated defect-free cable joint image, the number of columns that

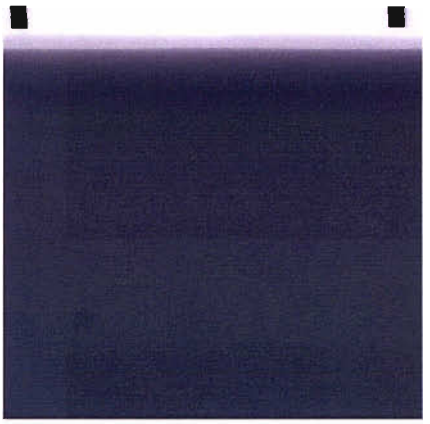

(a)

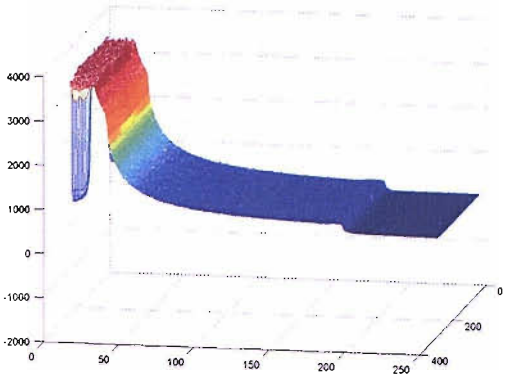

(b)

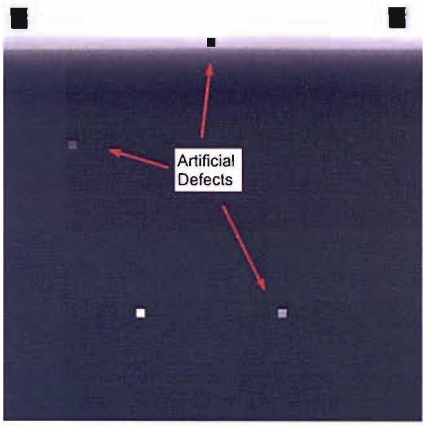

(c)

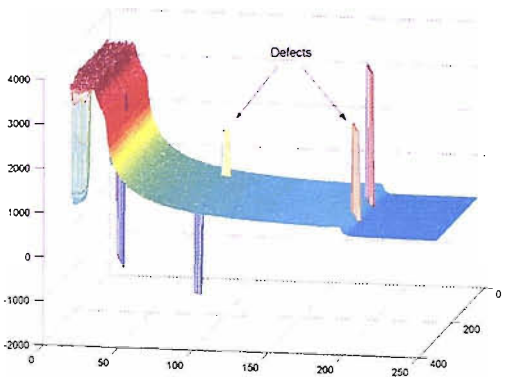

(d)

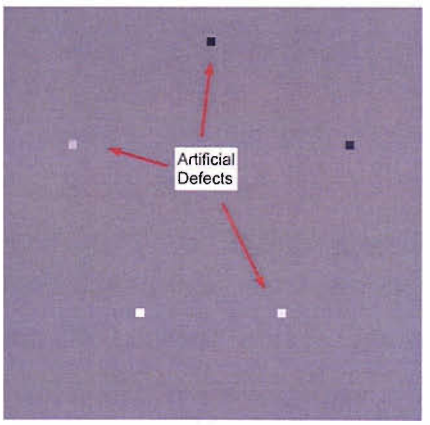

(e)

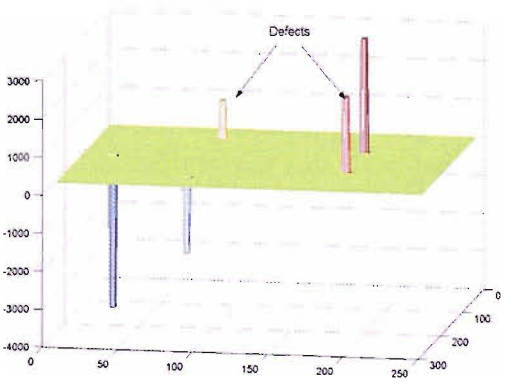

(f)

FIGURE 6.2: Removal of the defect-free insulation system signal, (a) original image, (b) mesh plot of original image, (c) image with manufactured defects, (d) mesh plot of image with manufactured defects, (e) image of defects with ramp removed, (f) mesh plot of defect with ramp removed.

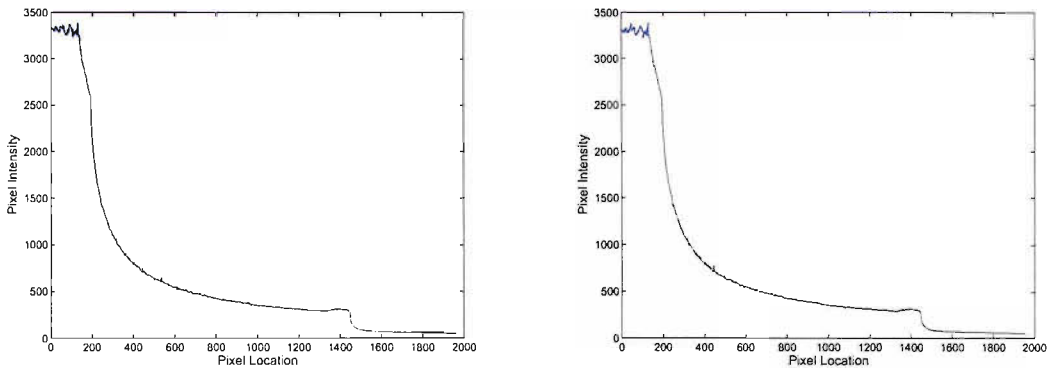

(a) (b)

FIGURE 6.3: The local consistency of the ramp profile of two adjacent columns of a cable joint image.

have to be sampled must be at least twice the number of columns that a defect would span. This means that if a defect has a diameter of 100 µm it will span at least 8 columns of the image, therefore to generate the columns of the defect-free image for the columns passing through this 100 µm defect, at least 16 columns must be averaged. This assumes that the size of the defects is known, however this is not the case. For this reason the sample size used to generate the column medians must be large enough to remove even the largest of defects. The number of columns averaged in order to generated the defect-free image was therefore set at 205 (2.5 mm), as this span of columns is considerably larger than any defect that could be introduced into the cable joint. Once the defect-free image has been generated in this manner, it can be subtracted from the original image to generate an image containing only the defects within the cable joint.

To demonstrate this process a section of cable joint had two defects introduced into the insulation system. The first defect consists of a drilled 1.5 mm hole. The hole extends from the insulation shield to the conductor. This hole was introduced to replicate an air filled void. The second defect consists of a 1 mm hole drilled to the conductor, into which a 200 µm steel wire has been inserted. This defect replicates a metallic inclusion in the insulation system. The size of these defects is considerably larger than the defects that might be found in a cable joint, however they have been used simply to demonstrate the ramp removal process. Figure 6.4(a) displays the cable joint containing these two defects, however only the top of the 200 µm wire can be seen. In Figure 6.4(b) the image has been brightened, which has made more of the steel wire visible and some of the outline of the 1.5 mm hole. A defect-free version of these images were generated

using the techniques described above (Figures 6.4(c) and 6.4(d). Both drilled holes and the wire have been removed in these defect-free images. The defect-free image was then subtracted from the original image to produce Figure 6.4(e). Due to the limitations of the printed representation of this image, a section of the hole and wire have been reproduced as separate images (Figures 6.4(f) and 6.4(g)). The brightness of each of these images has been adjusted to improve the visualisation of each defect. From Figure 6.4, it can therefore be seen it is possible to remove the defect-free insulation data from a cable joint image by generating an artificial defect-free cable joint image. This image can then be inspected to determine the level of inclusion contamination of the cable, followed by an inspection to find any voids within the insulation system.

6.1.2 Inclusion Detection

During the hand lapping of the insulation and semiconducting tapes around the cable joint conductor, it is possible that foreign particles can be introduced in between two layers of tapes. If the inclusion is conductive, it can cause the surrounding insulation to be subjected to a raised electrical stress which could reduce the working lifetime of the cable joint insulation system. The main types of inclusions that detrimental to the lifetime of the joint are metallic or carbonised particles. With the original system it is possible to detect inclusions as small as 50 μm. This means that the original system is able to detect inclusions within the cable joint that are similar in size to the smallest inclusions that are recorded during the insulation contamination examination conducted as part of the factory tests on the parent cable.

In order to detect an inclusion in the cable joint, the x-ray image has to be inspected for regions that contrast significantly with the surrounding defect-free insulation system. The contrast associated with the inclusion is caused by the interaction of the x-ray flux with the inclusion. Metallic or carbonised particles are significantly more radiologically dense compared with the surround defect-free insulation system. As a result, there is more absorption/scattering of the x-ray flux passing through the inclusion than the x-ray flux passing through the adjacent insulation system. This means that the CCD array will capture less signal and so the inclusion manifests itself as a region of darker pixels. The change in greyscale level of the pixels associated with the defect is determined by the size and type of inclusion. The larger the defect, the darker the central section of the

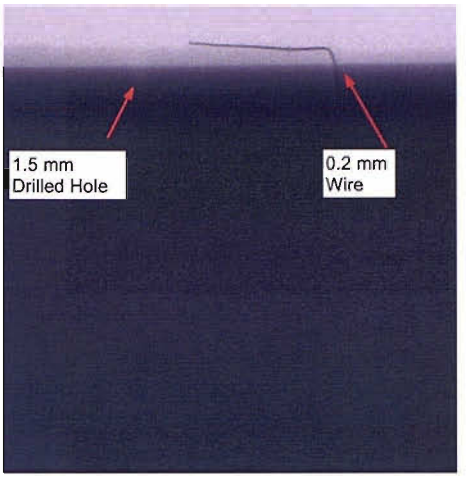

(a)

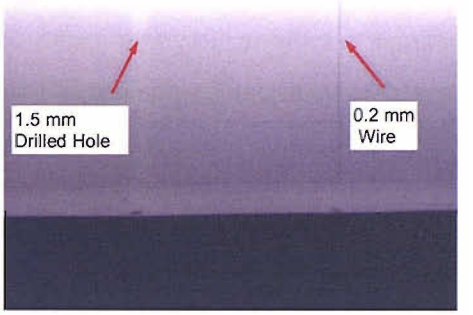

(b)

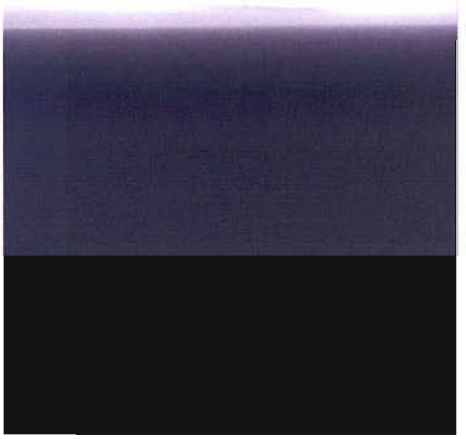

(c)

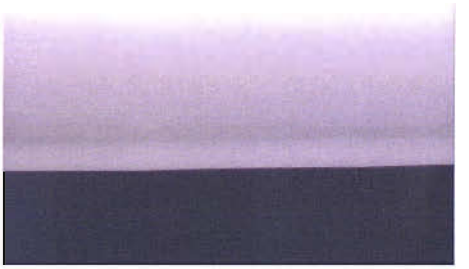

(d)

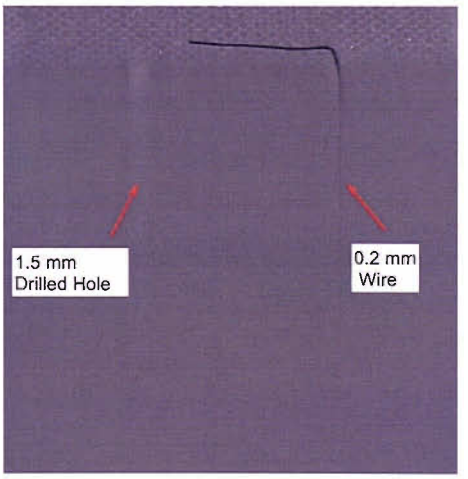

(e)

(f)

(g)

FIGURE 6.4: Removal of defect-free image data (a) defect image, (b) brightened defect image, (c) artificially produced defect-free image, (d) brightened defect-free image, (e) flattened image, (f) section of 1.5 mm drilled hole, and (g) section of 150 µm wire.

defect becomes because there is increased absorption/scattering of the x-ray flux caused by the increased thickness of the defect. The more radiologically dense the material is, the greater this absorption/scattering becomes. Metallic and carbonised particles, however, are considerably more radiologically dense compared to the materials of the insulation system, therefore, a 50 µm particle of either type will produce a significant greyscale change. This means that inclusions within the cable joint insulation system can be found by simply detecting groups of pixels that are significantly darker than the surrounding defect-free insulation.

6.1.2.1 Detection of Inclusions using Distinct Distributions

The darker pixels associated with an inclusion in the flattened cable joint image can be characterised as any pixel that has a significantly large negative value. As a result the pixels associated with the inclusion form a distribution that is distinct from the distribution of the pixels associated with the insulation. This is the situation in Figure 6.1, where a distinct distribution of inclusion pixels intensities can be seen to the left of the distribution of the insulation pixels. For a normal distribution, any pixel that is more than 3σ away from the mean of the distribution can be considered to be 99.9973% likely to not be from the original distribution [106]. If the average pixel intensity relating to the defect-free insulation system in the flattened cable joint image is determined, along with the standard deviation of the distribution of these pixels, then an inclusion can be found by locating any pixel with an intensity that is more than three standard deviations below the calculated average.

To find the average pixel intensity of the insulation the mean pixel intensity for the region surrounding each pixel has to be calculated. The mean of the distribution, $\bar{P}_{(x,y)}$, of the pixels surrounding the central pixel, $P_{(x,y)}$, is determined by:

$$\bar{P}_{(x,y)} = \frac{1}{m \times n} \times \sum_{i=0,}^{m-1} \sum_{j=0}^{n-1} P_{(x+a,y+b)} \tag{6.1}$$

where:

$$a = i - \frac{m-1}{2} \tag{6.2}$$

$$b = j - \frac{n-1}{2} \tag{6.3}$$

The size of the region used to generate the $\bar{P}_{(x,y)}$ in Equation 6.1 is defined as a rectangular region measuring m x n pixels. For the determination of the average insulation pixel intensity, the region should be square to prevent geometric distortions in the mean. The height and width should also be of an odd number so that $P_{(x,y)}$ is central to the region, therefore:

$$m = n = Z \in \mathbb{N} | Z = 2x - 1, x \in \mathbb{N} \tag{6.4}$$

From testing it was found that a 7 x 7 region was the optimum size for determining the local means of the image. This is because a smaller region would be more susceptible to outliers, however any larger and the influence of distant pixels on the mean becomes significant. Once $\bar{P}_{(x,y)}$ for each pixel has been calculated, an average pixel intensity for the insulation can be calculated using the median of every $\bar{P}_{(x,y)}$. The median of $\bar{P}_{(x,y)}$ (global median) is used rather than the mean of the $\bar{P}_{(x,y)}$ (global mean) because any $\bar{P}_{(x,y)}$ associated with the inclusion will have an effect on the global mean, however they will not alter a global median because the majority of the pixels in the image are associated with defect-free insulation.

Once the global median has been determined the standard deviation of the distribution of insulation system pixels has to be calculated. This could be achieved by using the standard deviation of the pixel intensities of the whole image, however this standard deviation would also take into account the deviation caused by the inclusion pixels. To overcome this, the standard deviation of the distribution of insulation pixel intensities can be calculated in a similar manner to the calculation of the global median. The standard deviation, $\sigma_{P(x,y)}$, of the regions surrounding each pixel can be determined using:

$$\sigma^2_{P(x,y)} = \frac{1}{(m \times n) - 1} \times \sum_{i=0,\ j=0}^{m-1\ n-1} \left(\bar{P}_{(x+a,y+b)} - P_{(x+a,y+b)}\right)^2 \tag{6.5}$$

The size of the region used to calculate $\sigma_{P(x,y)}$ was also set at 7 x 7 pixels for the same reasons stated above. Once $\sigma_{P(x,y)}$ has been calculated for each pixel, the median value can determined. With the mean and standard deviation of the distribution of pixels associated defect-free insulation calculated, any pixel with an intensity more than 3σ below the mean can be found. These pixels can then be plotted on a blank binary image to produce an image of the inclusions.

To demonstrate the implementation of this method of detecting inclusions using contrast change, Figure 6.5(a) displays a section of the 200 µm wire from Figure 6.4. The dark strip of pixels is the wire. To the right of the wire it is possible to see a region of slightly brighter pixels associated with the 1 mm hole that the wire was inserted into. The mesh plot of this image is shown in Figure 6.5(b). From this image it can be seen that the wire causes a significant channel through the mesh plot. The central region of the wire is therefore easy to find, however due to the level of noise within the image, the edges of the wire can be difficult to locate accurately. To improve this, a 3 x 3 median filter can be passed over the image. A 3 x 3 filter was used as this is the smallest operator template that can be used to effectively filter the image, as a result, only the high frequency noise is removed while any small inclusions should remain. Figures 6.5(c) and 6.5(d) show the effect of passing this filter over Figure 6.5(a). The removal of the high frequency noise content in the image makes the wire more slightly more defined. The median filtered image can then be thresholded to find the pixels that are significantly different from the average pixel intensity of the defect-free insulation surrounding the wire. Figure 6.5(e) shows the binary image of the pixels that were 3σ below the mean value of surrounding insulation pixels. From this image it can be seen that the wire has been detected. This can then be superimposed back onto the original image to show the position of the inclusion.

6.1.2.2 Inclusion Size Determination

The size of any detected inclusion can be determined by counting the number of columns and rows that the inclusion spans. The maximum number of columns/rows spanned by the inclusion will therefore provide an estimate of largest dimension of the the inclusion. The number of rows/columns that an inclusion spans can be calculated by scanning the binary inclusion image for white pixels. Any groups of white pixels can then be

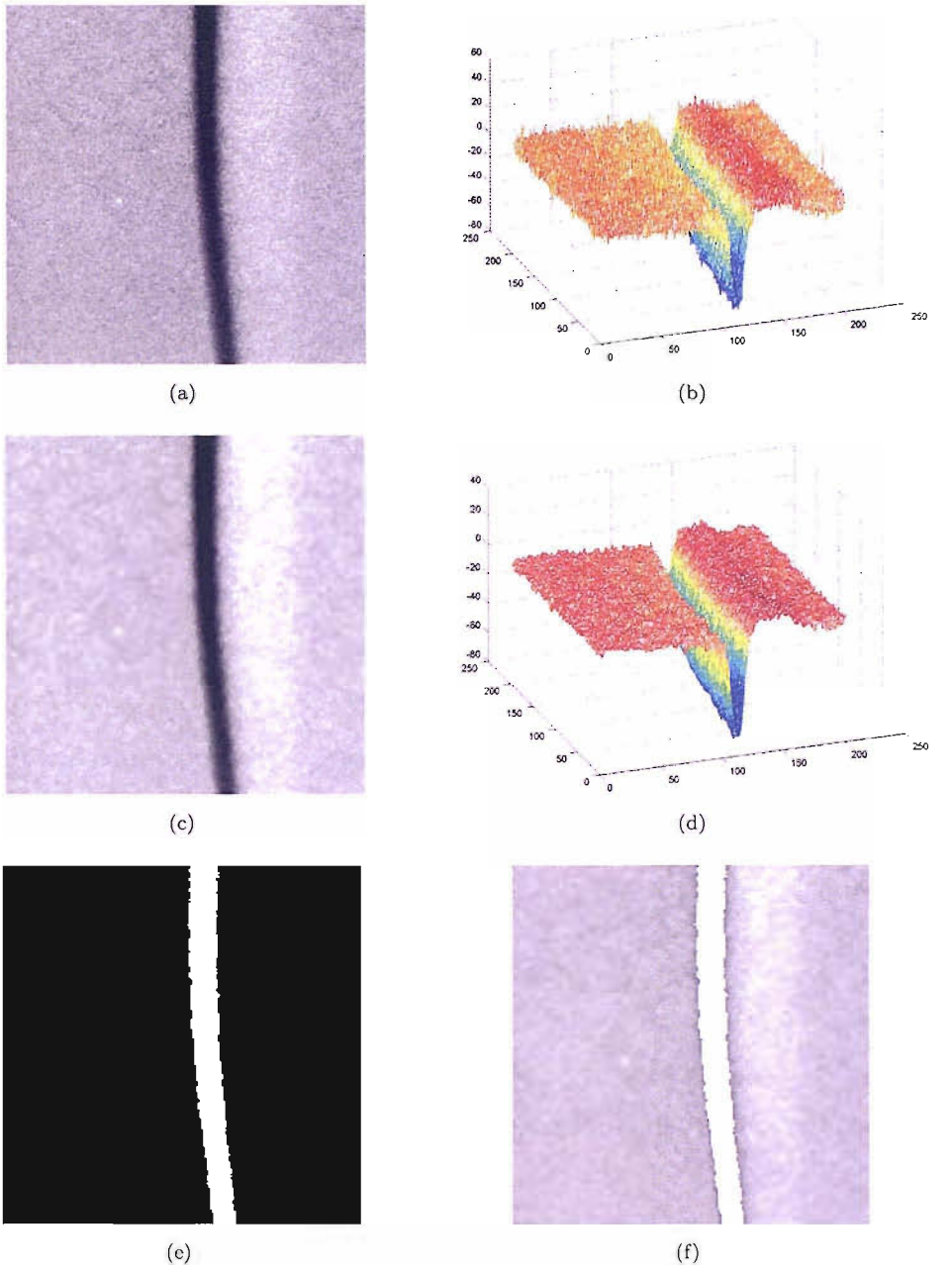

FIGURE 6.5: Detection of inclusions (a) the original image containing a 200 µm wire, (b) the mesh plot of (a), (c) the original image smoothed, (d) the mesh plot of (c), (e) the inclusion binary image, and (f) the binary inclusion image superimposed back onto the original image.

inspected to determine the maximum number of white pixels in each row and column of the image. These pixel dimensions can then be multiplied by the size of the individual pixels to determine the maximum dimensions of the inclusion.

The wire in Figure 6.5 spans the full height of the image, however, the width of the wire can be found by counting the number of white pixels per row in the image. From this the calculated wire thickness can be obtained. This can then be compared with the nominal thickness of the wire to determine the accuracy of the inclusion detection process. The average number of white pixels per row in Figure 6.5 is 16.73 pixels, with a median of 17. This means that because each pixel is 12.21 µm wide, the calculated mean size of the wire is 204 µm, and the calculated median is 208 µm. The nominal diameter of the wire was 200 µm, which equates to 16.38 pixels. This means that the diameter of the wire, using either the mean or median thickness, has been found to within one pixel width. The maximum detected width of the wire was 18 pixels and the minimum was 16, producing a detected diameter variation between 195 and 220 µm. This has been caused by the fact that because 200 µm equates to 16.38 pixels, the minimum number of pixels that that could be significantly affected by the wire is 16 and the maximum 18, with the median expected to be 17 and the mean between 16 and 17. For this reason it can be assumed that the inclusion detection system is accurate to within two pixel widths, i.e. the size of any defect detected can be confidently stated within $\pm$ 1 pixel, or in this instance $\pm$ 12.21 µm.

6.1.2.3 Application of Inclusion Detection to a Full Image

The above example used to demonstrate the detection of inclusions using distinct distributions has been applied to the 200 µm wire from Figure 6.4, however the minimum inclusion size detectable by the original system is 50 µm. To determine if the proposed system is also able to detect defects as small as 50 µm, the 200 µm wire was removed from the sample and a 50 and a 100 µm wire inserted into the drilled holes. Due to the reduced rigidity of the 50 µm wire, this was inserted into the 1.5 mm hole, whereas the 100 µm wire was inserted into the 1 mm hole. The cable joint and wires can be seen in Figures 6.6(a) and 6.6(b). In the brighter of these two images it can be seen that during the drilling of the holes, the drill bit has dragged five small pieces of copper swarf from the conductor up into the holes. There are two pieces of swarf at the

bottom of the left hand 1.5 mm hole, two at the bottom of the right hand 1 mm hole, and a single piece at the top of the left hand 1.5 mm hole. The wires and swarf are just visible in the flattened cable joint image (Figure 6.6(c)), however they are easily discerned in the the binary inclusion image (Figure 6.6(d)). The locations of both the wires and the swarf in relation to the cable joint insulation system components can be seen in Figures 6.6(e) and 6.6(f). From the binary image it is possible to determine the size of the wires and the swarf. The left hand section of Table 6.1 shows the calculated size of the two wires and the confidence limits of the wire thicknesses. From the table it is possible to see that both wires have been detected within ± 1 pixel width, and the mean thicknesses are relatively close to the nominal thickness of each wire. The three groups of swarf pieces are shown in Figure 6.7. The left hand column of images in this figure are the photometrically corrected images, and the right hand column are the binary images. The calculated sizes of the pieces of swarf are displayed in the right hand section of Table 6.1. From the table it can be seen that a cable joint would fail the inspection system had any of the four the four largest inclusions been introduced into the insulation system of the joint, however the inclusion near the surface of the cable is permitted under the insulation contamination examination protocol detailed in Chapter 2, Section 2.1.1.5. From this example it is possible to see that the proposed inspection method is capable of detecting inclusions as small as 50 µm to within ± 1 pixel. This level of detection confidence means that a cable joint can be inspected for inclusions to the same specification as the parent cable. This means that the proposed inspection method for detecting inclusions within a cable joint could be used to replace the current manual inspection method.

	50 µm Wire (µm)	100 µm Wire (µm)		Inclusion 1 Width (µm)	Inclusion 2 Width (µm)
mean	48.47	97.68	Fig. 6.7(a)	330	574
min	36.63	85.47	Fig. 6.7(c)	439	146
max	61.05	109.89	Fig. 6.7(e)	122	
std	5.98	4.37			

TABLE 6.1: The calculated dimensions of the two wires in Figure 6.6

6.1.3 Void Detection

The above inclusion detection method makes it possible to determine the inclusion contamination levels within the cable joint, however voids in the insulation still have to be

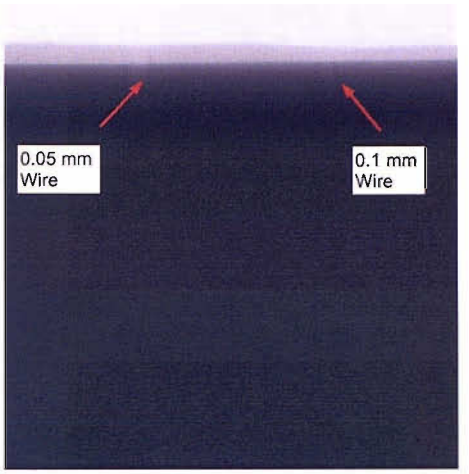

(a)

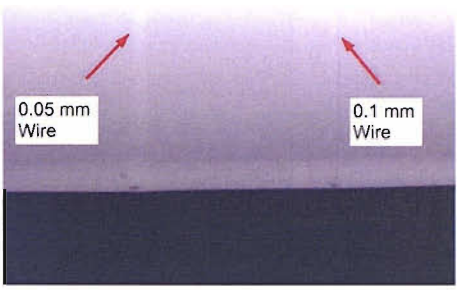

(b)

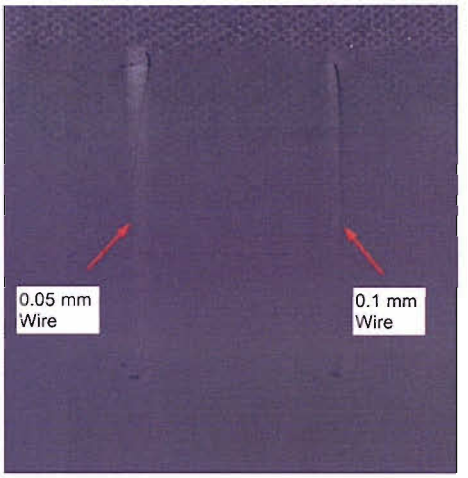

(c)

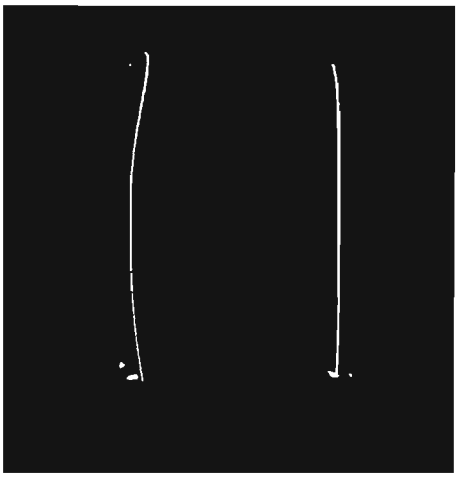

(d)

(e)

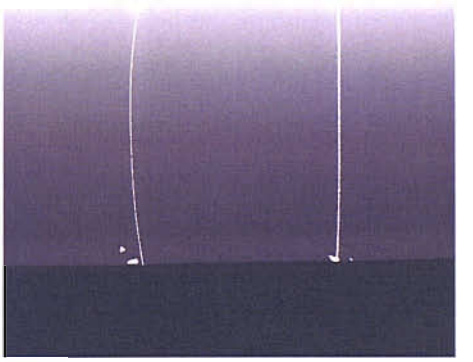

(f)

FIGURE 6.6: Full cable joint image inclusion detection (a) image with 2 inserted wires, (b) a brightened version of (a), (c) the flattened image, (d) the inclusion image, (e) the inclusion image superimposed onto (a), and (f) a brightened version of (e).

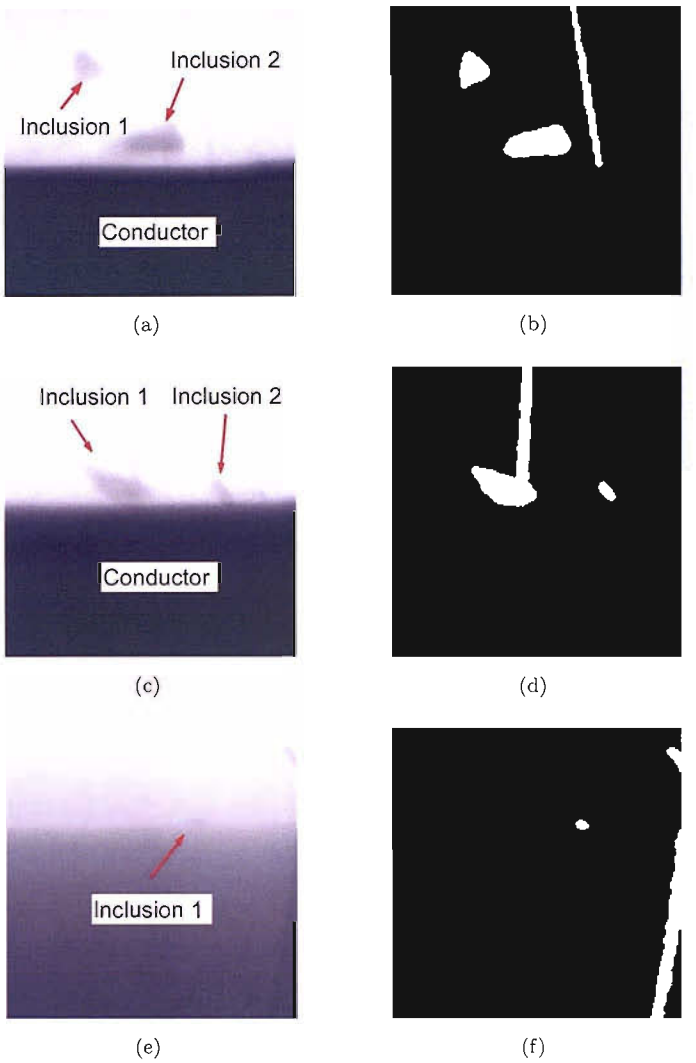

FIGURE 6.7: Swarf Detection (a) the original image of the bottom of the 1.5 mm drilled hole, (b) inclusion binary image of (a), (c) the original image of the bottom of the 1 mm drilled hole, (d) inclusion binary image of (c), (e) the original image of the top of the 1.5 mm drilled hole, and (f) inclusion binary image of (e).

found. A void in the insulation system may be caused by incomplete degassing of the cable joint after manufacture [1]. As a result a small vacuum or gaseous pocket within the insulation system is formed. The presence of such a void will therefore cause the surrounding insulation to be subjected to increased electrical stresses, which, should the void be sufficiently large, could cause the cable joint to fail. The minimum detectable void size with the original system was in the region of 200 µm. This level of resolution is deemed sufficient by the cable industry in order to ensure that the cable joint will not fail prematurely. Due to the manual nature of the system however, it is not assured that all 200 µm voids will be found, rather that it is possible to detect a void of this size,

however only voids above 400 µm will definitely be found. For this reason, the proposed system must be able to confidently detect 200 µm voids.

The detection of voids within a cable joint using x-ray images, relies on the fact that the radiological density of the vacuum or gas within a void is significantly less than radiological density of the insulation system component that the void is located within. As a result voids absorb/scatter less x-rays than the surrounding insulation system. This means that a section of cable joint containing a void will allow more x-rays to pass unhindered through it compared to a section of defect-free insulation system. A void will therefore present itself as a slightly brighter region within the cable joint image. In terms of the image ramp, a void will therefore present itself as a positive inflection, or spike. It should therefore be possible to detect voids by searching the flattened cable joint for groups of pixels that have a mean pixel intensity greater than zero. The ease in which this can be achieved is determined by the contrast change in the image between the defect free sections of cable joint and the region of the cable joint containing the defect.

The change in contrast caused by a defect is determined by the size, type, and location of the void. Figure 6.8 shows a side-on view of two voids within a cable joint. Both voids are 1 mm in diameter. For the defect closer to the outer surface of the cable joint, the void represents a 3.97% of the total of the x-rays pathway through the cable joint. If the void is a vacuum, the volume of this defect can be considered to not interact with the x-ray flux passing through it, therefore not causing any attenuation of the x-ray flux. This mean that the x-ray signal captured by the CCD array at the centre of the void should be 3.97% larger than the signal captured directly adjacent to the void. Should the void be smaller, in the region of 200 µm, the signal difference at the centre of the void reduces to 0.79%. The lower void in Figure 6.8, despite being identical in size to the void above it, represents only 2.13% of the total of the x-ray pathway through the cable joint. Had the void measured 200 µm in diameter, this would be reduced to 0.43%. This means that despite the fact that the two defects are the same size, the relative change in contrast in the cable joint image for the lower defect will only be 54% of the change in contrast of the void closer to the cable joint outer surface. The relative change in signal strength of both voids would be reduced further should the void contains a gas rather than a vacuum, because the molecules of the gas present will interact with the x-ray flux causing some attenuation. This means that a large vacuum void located near

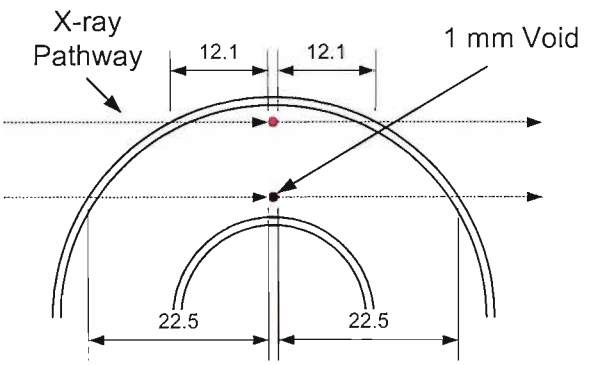

FIGURE 6.8: The attenuation pathway changes caused by voids.

the surface of the cable will therefore produce a bigger signal change at the centre of the void compared with a small gaseous void located near the conductor surface.

To detect either of these two voids, it should, therefore, be possible to inspect the flattened cable joint image for groups of pixels with a mean greater than zero, due to the increase signal captured by the CCD array. Finding the edges of a void using this method, however is not particularly accurate because voids are generally spherical, and therefore between the centre of the void and the edge of the void the signal change reduces proportionally with the reduction of void thickness that the x-rays have to pass through. The transition, in the image, between the void and the surrounding defect-free insulation is, therefore, not well defined, as a result the difference in the signal between the edge of the void and the defect-free insulation is similar to the noise level within the image. It would be possible, however, to use the change in signal intensity as a qualitative inspection method for the detection of voids.

In order to provide a quantitative void detection method, the presence of a void has to be detected and then the edges of the void also have to be discerned. To find the edges of voids, the variance of the pixel intensity distribution of the region of the image at the edge of the void can be used, by comparing it to the variance of the surrounding defect-free insulation system. The distribution of pixels for a section of defect-free insulation system in the flattened image will have a mean centred around zero, and a relatively small variance, in the region of 0.15. Due to the similarity of the attenuation of x-rays that pass through the section of cable joint containing the void, the variance of the pixels at the centre of the void should be similar to the surrounding defect-free insulation system, however, the mean of the distribution of these pixels will be slightly

raised. At the edge of the defect, however the pixels will be a combination of defect-free insulation system pixels and void pixels. This will therefore increase the variance of the distribution at that point, despite the fact that the mean of the distribution is relatively unaffected. It is therefore possible to find the edges of a void by inspecting the flattened image for regions of pixels that have a raised variance. The main problem with this method of detection is that the variance is not just raised at the very edge of the void, rather it is raised across the region between the centre of the void and the edge of the void. To find the edges of the void it is therefore necessary to find the central pixels of the regions with an increased variance that lie furthest from the void centre. To do this the centre of the void can be found by using the change in pixel intensity described above, and then the outer edge of the void can then be found by locating the raised variance pixels furthest from the centre of the void.

6.1.3.1 Locating the Centre of a void

To improve the detection of the centre of a void is necessary to improve the signal to noise ratio within the image. This can be achieved by averaging out the image noise. To average out the noise in the image, the flattened cable image can be smoothed. Normally significant smoothing of an image is not desirable because the smoothing process also causes a reduction in edge definition [31]. The centre of a void, however, can still be found with the edges smoothed. This is due to the fact that the centre of the void is not determined by the distance from the edge of the void, rather it is the point of the highest change in signal intensity. To implement this smoothing a Gaussian operator can be used. The equation of a Gaussian operator is shown in Chapter 5, Section 5.1.1. The reason for choosing a Gaussian operator to smooth the image is that the operator places more importance on pixels closer to the centre of the smoothing operator compared with pixels near the edge of the operator. This means that the Gaussian filter will smooth the image while still retaining some edge definition, offering a improved smoothing performance compared with direct averaging using the mean [85].

The amount of smoothing caused by the Gaussian operator is determined by the size and variance, σ^2, of the filter. If size or variance, of the operator are too large, then the image is over smoothed and as a result both the void and noise data will be removed from the image. Alternatively if the size or variance are too small, then the image noise

is not removed. The optimum size of the operator is determined by the size of smallest void that has to be detectable. For the original system, the smallest detectable void diameter was 200 µm. In order to smooth the image while still being able to detect 200 µm voids, the Gaussian operator should not be greater than 200 µm, which equates to 16 rows/columns. The height and width of the filter should also be an odd number of pixels to ensure that the pixel being smoothed is at the centre of the operator. Lastly the operator should be symmetrical due to the spherical nature of voids. For these reasons the size of the Gaussian operator was set at 15 x 15 pixels. The value of σ^2 determines the relationship between the distance of the pixel from the centre of the operator and influence that this pixel exerts on the smoothed pixel value. A large value of σ^2 will produce an averaging operator that tends towards direct mean averaging, however a small value of σ^2 reduces the level of smoothing. The value of σ^2 therefore has to be large enough to smooth out the noise, but not so large as to allow outlying pixels to have a significant influence on the smoothing operation. From testing the optimum value of σ^2 was set at 3.

The effect of smoothing the flattened cable joint image using a 15 x 15 pixel Gaussian smoothing operator with a σ^2 of 3 is shown in Figure 6.9. Figure 6.9(a) is a section of the 1.5 mm hole from the flattened cable joint image in Figure 6.4(e). The central brighter strip of the image is the drilled hole. This image still contains a large quantity of noise, which produces the rough texture of the mesh plot in Figure 6.9(b). Without prior knowledge of the defect it would be difficult to determine which pixels in this mesh plot relate to the drilled hole and the which are noise. After the image has been smoothed using the 15 x 15 Gaussian operator (Figure 6.9(c)), this decision process is made easier due to the reduction in noise, as demonstrated by the smoother texture of the mesh plot in Figure 6.9(d). Figure 6.9(e) displays the effect of this smoothing: the image contains considerable less noise and the centre of the drilled hole is more obvious, however the location edges have been lost.

It is possible to find the centre of this void by thresholding the smoothed image. From Figure 6.9(d) it can be seen that the transition between the defect-free insulation and the void is a gradual change. The point at which the surface of the plot changes from defect-free insulation to the void can be defined as the pixel location where the intensity of the pixel change significantly from the average intensity of the defect free insulation. The method of thresholding this image is the same as the method used to threshold

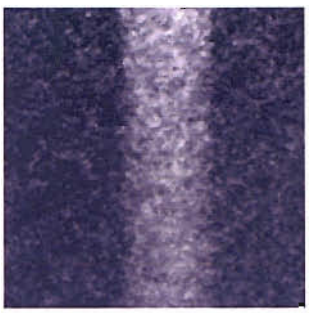

(a)

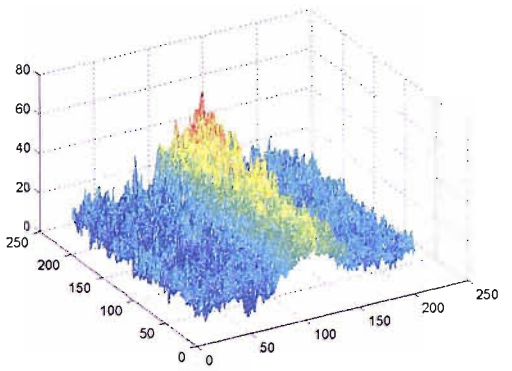

(b)

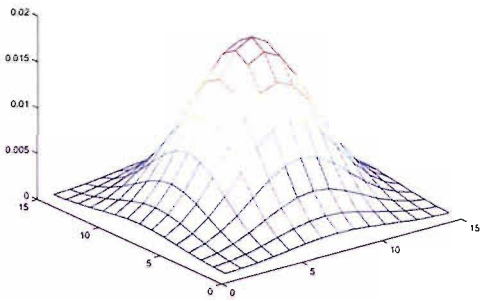

(c)

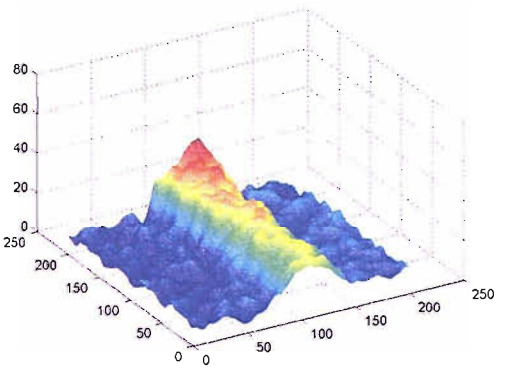

(d)

(e)

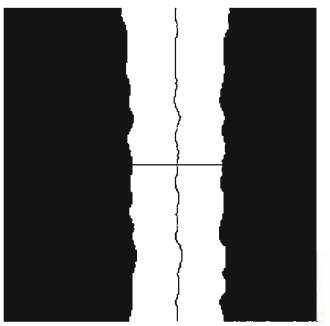

(f)

FIGURE 6.9: Detection of the centre of a void (a) the original image, (b) the unsmoothed mesh plot of (a), (c) the Gaussian operator, (d) the smoothed mesh plot, (e) the smoothed image, and (f) the thresholded image.

the inclusion image (Section 6.1.2), however the image used to generate the mean and standard deviation is the Gaussian smoothed image, and the threshold value is 3σ above the mean rather than below. Figure 6.9(f) shows the thresholded image of Figure 6.9(e). This thresholded imaged is also a binary image in which the central section of the drilled hole has been found. This thresholded image can then be used to find the centre of the void by determining the central pixel of each row and column of the void. The pixel that lies on the central row and column of the void will therefore be a good estimate of the centre of the void. The two black lines in Figure 6.9(f) mark the central pixels of each row and column of the drilled hole. The intersection of these two lies therefore defines the central point of the drilled hole passing through that section of the image. With the centre of the void determined, it is then necessary to find the edges of the void using the variance of the pixel intensities.

6.1.3.2 Detection of the Edges of a Void using Changes in the Pixel Distribution Variance

To detect the edges of a void, the variance of the distribution, $\sigma^2_{P(x,y)}$, of the region of pixels surrounding each pixel, $P_{(x,y)}$, has to be calculated. The variance of the pixels can be determined using Equation 6.5. As with inclusion detection, the size of the the region used to generate the variance for each pixel should follow Equation 6.4. The size of m and n should also be no greater than the size of the minimum void size that has to be detectable in order that the central section of the void will have a similar variance compared to the surrounding defect-free insulation system. For this reason the size of the region of the image used to find the $\sigma^2_{P(x,y)}$ was set at 15 x 15 pixels.

The effect of passing this variance operator over the image is shown in Figure 6.10. The image and mesh plot in Figures 6.10(a) and 6.10(b) have been generated using the same section of the 1.5 mm hole used in Figure 6.9. Figure 6.10(c) is the mesh plot of the of the values of the variance for the image. It can be seen that the variance of the defect-free insulation either side of the hole and the variance of the pixels in the central section of the hole are similar, and are in the region of 0.15, however at the edges of the hole the variance is considerably larger. The edges of the hole can therefore be determined by finding any variance that is significantly above the mean variance of the image. This requires that the image is thresholded. In order to perform this thresholding, a process

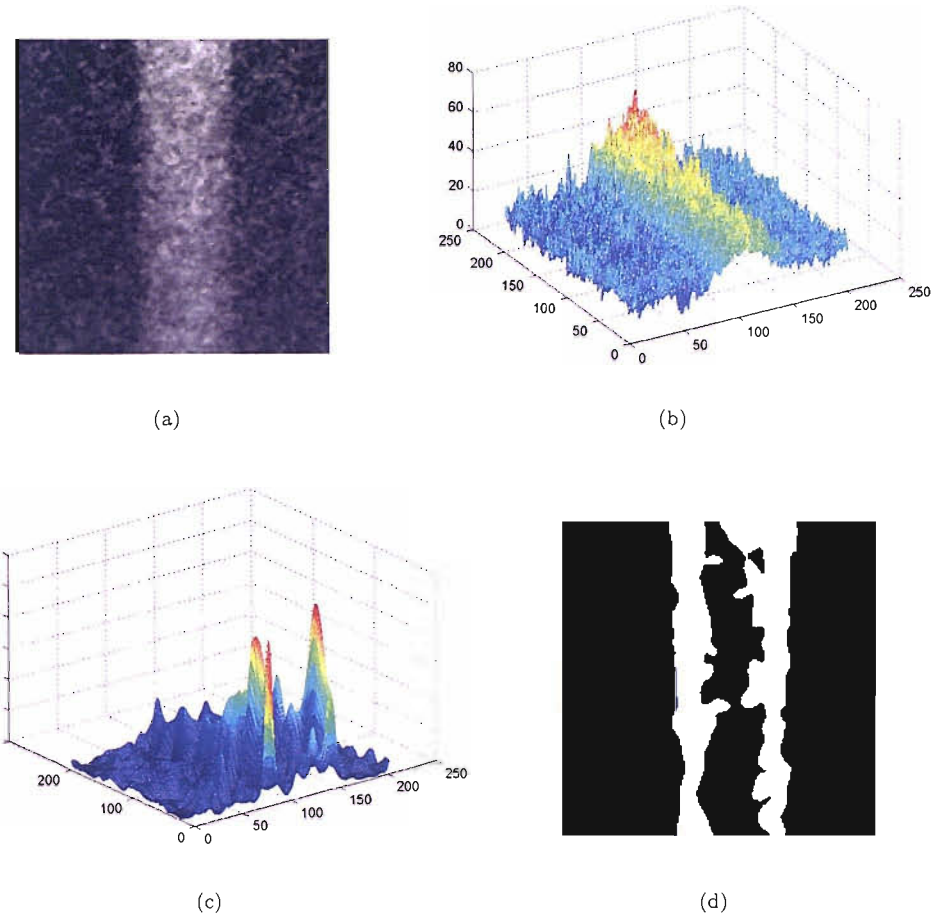

FIGURE 6.10: Void edge detection (a) the original image, (b) the mesh plot of (a), (c) the mesh plot of the variance of (b), and (d) the thresholded variance image.

similar to the process described in Section 6.1.3.1, can be used. The average value of the variance can be determined using the median value for the whole image, due to the fact that the majority of the image should be defect-free, however the standard deviation of the variance, $\sigma_{\sigma^2(x,y)}$, has to be found using Equation 6.6.

$$\sigma_{\sigma^2(x,y)} = \sqrt{\frac{1}{(m \times n) - 1} \times \sum_{i=0,}^{m-1} \sum_{j=0}^{n-1} \left(\bar{\sigma^2}_{P(x+a,y+b)} - \sigma^2_{P(x+a,y+b)} \right)} \tag{6.6}$$

Once the value of $\sigma_{\sigma^2(x,y)}$ has been found it is possible to threshold the image finding any pixel with an variance greater than the median of the variance plus $3\sigma_{\sigma^2(x,y)}$. The effect of applying this thresholding to the variance image is shown in Figure 6.10(d). The thick white lines in this image then have to be thinned to produce a line, one pixel wide, that marks the edge of the void.

6.1.3.3 Thinning the Void Line Image

The centre of the void can be found using the processes described in Section 6.1.3.1, and the transition between the centre of the void and the surrounding defect-free insulation system can be found using the processes in Section 6.1.3.2. To find the edge of the void, the transition pixels (Figure 6.11(a)) furthest away from the centre of the void (Figure 6.11(a)) have to be found. This is achieved by initially dividing the void in half vertically. Then the top and bottom pixels of each half of the void are found. The rows between the top and bottom of each half are then scanned to find the transition pixel furthest from the centre line of the void. This process is then repeated using the horizontal centre line and the top and bottom halves of the void. The pixels found using this process become the edge pixels for the void. Figure 6.11(c) shows the result of thinning Figure 6.11(a). For this void however there was no need to use the horizontal centre line to thin the transition image because the drilled hole passes through the image, and therefore there should be no horizontal edges. The edge image can then be superimposed back onto the original image in order to highlight the edges of the voids. Figure 6.11(d) shows the lines superimposed onto the flattened image.

6.1.3.4 Void Size Determination

The size of any void found using this method of void detection can be estimated by determining the maximum number of columns and rows between the void edge lines. The maximum dimension of the void can then be found by multiplying the maximum number of row/columns by the size of each pixel. The hole in Figure 6.11, like the wire in Figure 6.5, spans the whole image, as a result only the width of the hole can be used to determine the accuracy of the void detection system. The maximum number of pixels between the void edge lines was found to be 117 pixels. This equates to 1.429 mm. The size of the drill bit used to make this hole however was 1.5 mm. This infers that the maximum size of the hole detected in the image is 71 µm, or nearly six pixels, smaller than the expected size of the hole. The discrepancy between the two sizes could be due to one of two possible reasons. Firstly the insulation is constructed from EPR rubber. This could mean that the hole has closed slightly after being drilled, causing the hole to be smaller than 1.5 mm. The second explanation for the discrepancy is that the edges of the hole do not significantly reduce the attenuation of the x-rays and as a result, the

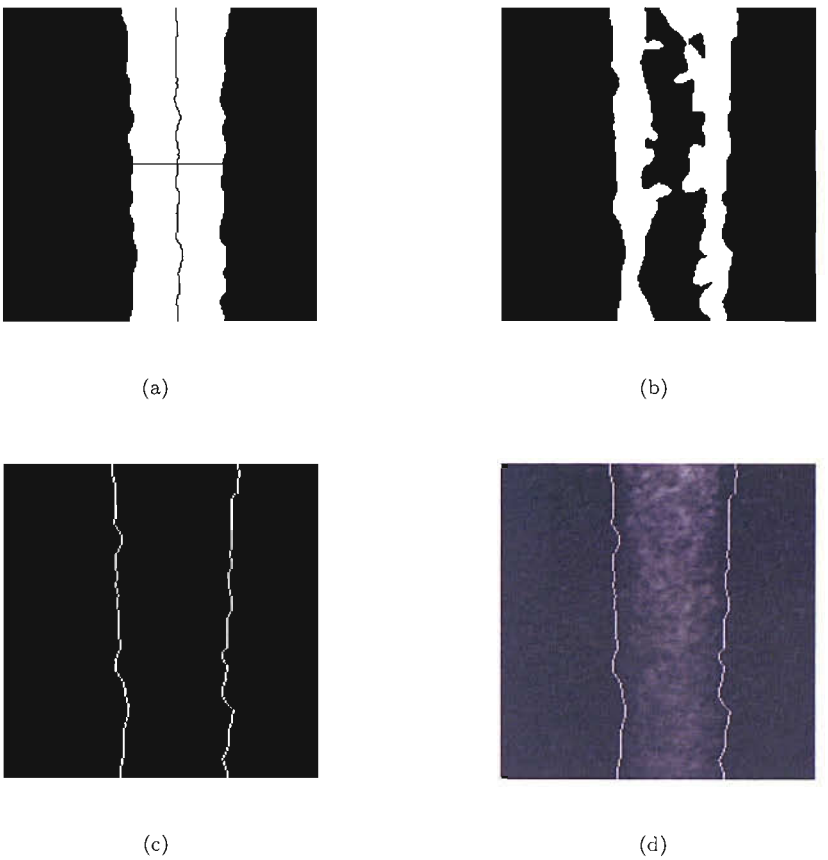

FIGURE 6.11: Edge thinning (a) the centre of the void, (b) the edge transition pixels, (c) the thinned edge image, (d) the thinned edge image superimposed back onto the original image.

actual edge of the void is not readily detected by the the inspection system. This would mean that the detected edge and the actual edge do not coincide, and as a result the size of the hole is reduced. The actual accuracy of the void detection system proposed is, therefore, unknown. To determine the accuracy of detection process, known voids that do not shrink would have to be created within the cable joint. The time scale of this project, however, has not allowed for the production and inspection of such voids, however, as a measure of void detection resolution, artificial voids can be introduced into the cable joint image digitally. These voids can then be inspected to give estimation of the accuracy and sensitivity of the system.

6.1.3.5 Void Sensitivity Testing

To artificially introduce voids of this size into a cable joint image, structures with characteristics similar to a void have to be generated and then superimposed onto the flattened cable joint image. As voids are generally spherical the artificial void has to be circular, with a gradual transition from the centre of the void to the edges of the void, and the transition between the void and the defect-free insulation should be continuous. To generate a structure with these properties, a Gaussian bell shape can be produced. The shape of this function gives a central maximum, with a smooth reduction in intensity that diminishes radially in relation to the distance from the centre. If the Gaussian function is normalised, then voids of different greyscale contrasts can be simulated by multiplying the pixel intensities of the Gaussian bell by a scalar. For the system to be comparable with the original inspection method, the size of the artificial voids should be 200 µm, or 16 pixels. Figure 6.12(a) displays a normalised 16 x 16 Gaussian bell shape with a variance of 4 that represents a void with maximum central greyscale contrast change of 20. This artificial void can then be added into a section of defect-free insulation to simulate a section of insulation containing a defect (Figures 6.12(b) and 6.12(c)). The centre of the void can then be found using the Gaussian smoothed image (Figure 6.12(d)) and the edges using the variance image (Figure 6.12(e)), in order to produce the void edge image (Figure 6.12(f)).

The sensitivity of the system can therefore be determined by producing a range of 200 µm voids with different greyscale contrasts, and then determining the minimum greyscale change required in order for a defect to be detected. To do this three sections of defect-free insulation were sampled from the insulation near the surface of the cable, the central region of the insulation, and the insulation close to the conductor surface. A voids was then introduced into each sample. The greyscale change of the void was then increased until the void detection process detected at least some of the void. The greyscale levels were then increased until size of the void detected measured 3 x 3 pixels. After this the greyscale was increased to obtain an estimate of the greyscale change required to detect the full extent of the void. The highest value per sample region for all three thresholds were then noted (Table 6.2). Figures 6.13 - 6.15 shows one example of each region used during this sensitivity test. The top images in each figure are the insulation image with the defect introduced. The lower images show the detect void.

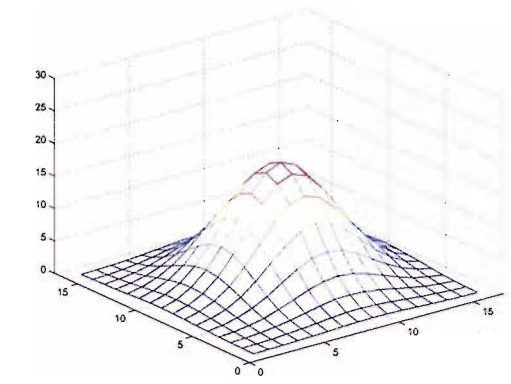

(a)

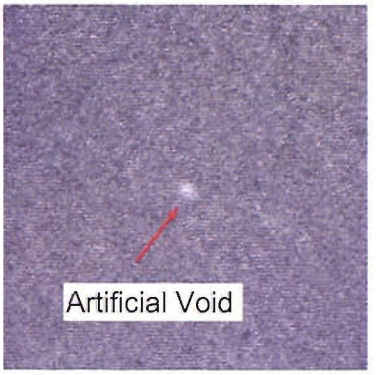

(b)

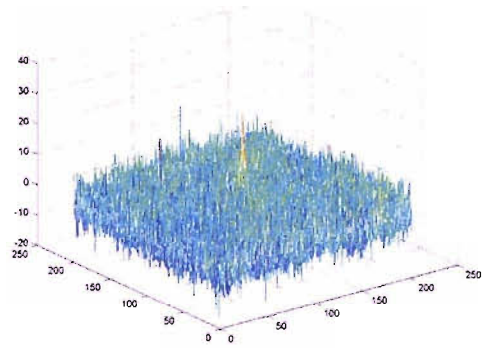

(c)

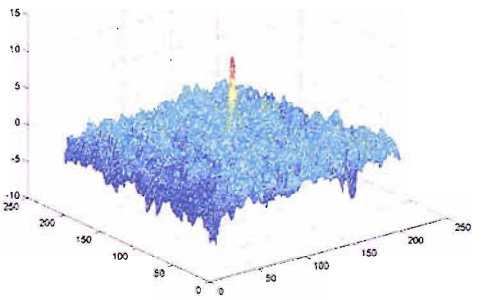

(d)

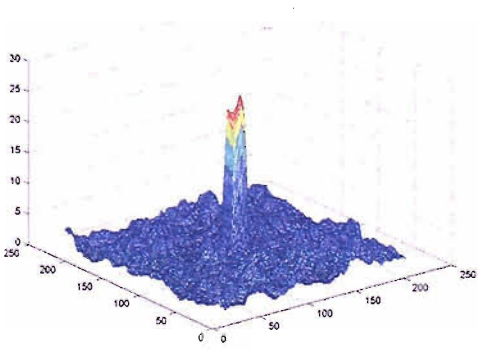

(e)

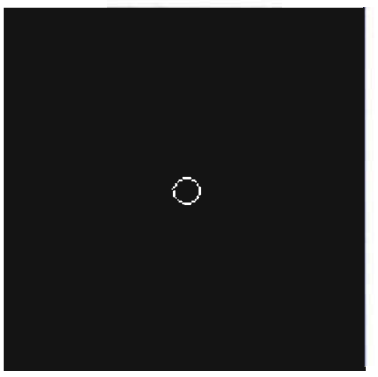

(f)

FIGURE 6.12: Artificial Void Generation and Detection (a) the Gaussian bell void, (b) the void superimposed into a section of insulation, (c) the mesh plot of (b), (d) the Gaussian smoothed void centre detection mesh plot, (e) the variance image edge detection mesh plot, and (f) binary image of the edge of the void.

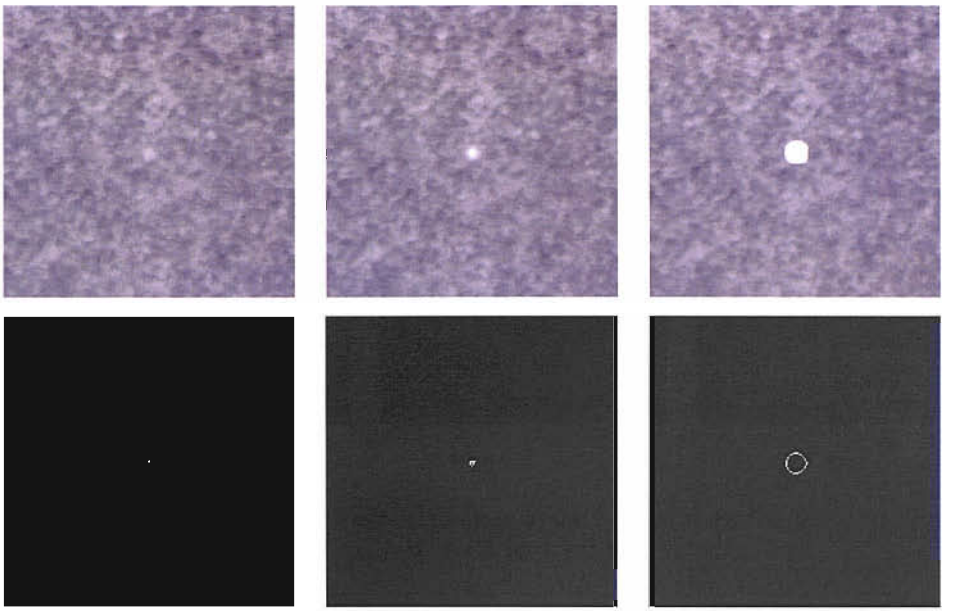

(a) (b) (c)

FIGURE 6.13: Sensitivity Test: Void close to the surface of the the cable (a) minimum detected void, (b) 3 x 3 void, (c) fully detected void.

Void Detection Threshold	Close to the Cable Surface	Central Insulation Region Region	Close to the Conductor Surface
Minimum	8	7	5
3 x 3	17	12	12
Full Extent	500	500	500

TABLE 6.2: The greyscale threshold levels required to detect a void

From Table 6.2 it can be seen that the minimum change required to for a defect to be detected varies from 5–8 greyscale scale levels. The smallest change required is found closer to the conductor surface, and the largest at the cable surface. This change in the minimum greyscale threshold could be due to the fact because the CCD array receives a smaller signal closer to the conductor compared with the cable surface, the variance of the signal received will be less, therefore the influence of the artificial void is increased. A similar trend is found for the 3 x 3. The three regions all require a very large signal for the full extent of the void to be found. The value of 500 greyscale levels is unlikely to occur in a real world void measuring 200 x 200 µm.

From these results, it can therefore be assumed that a 200 µm void will be detected if at the centre of the void the pixel intensity is at least 8 greyscale levels greater than the surrounding insulation system, however only when the greyscale change is greater

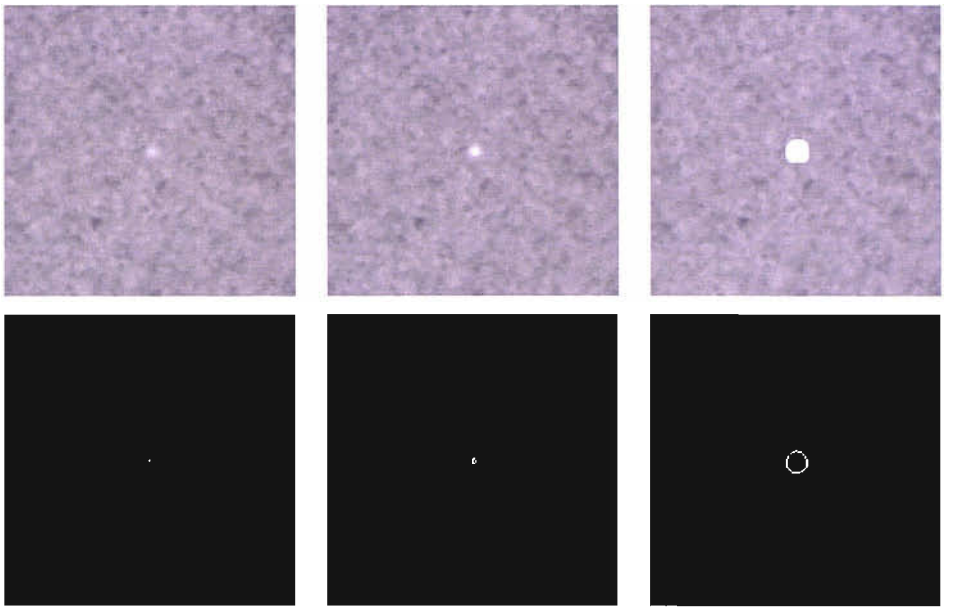

(a) (b) (c)

FIGURE 6.14: Sensitivity Test: Void in the centre of the insulation (a) minimum detected void, (b) 3 x 3 void, (c) fully detected void.

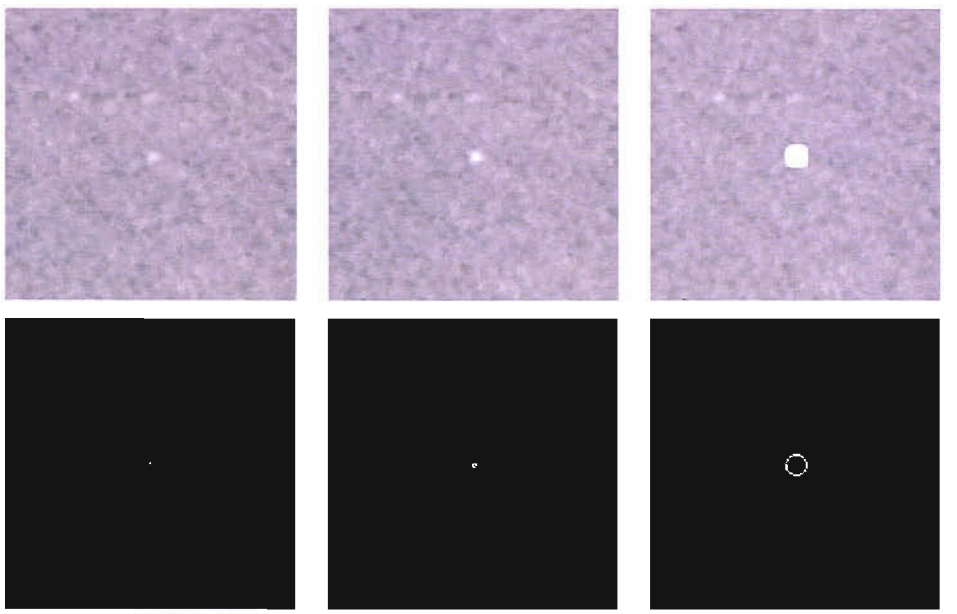

(a) (b) (c)

FIGURE 6.15: Sensitivity Test: Void close to the surface of the the conductor (a) minimum detected void, (b) 3 x 3 void, (c) fully detected void.

than 17 will the void definitely be detected. Despite the increased greyscale difference required to detect a void close to the surface of the cable, these voids will be easier to detect because a void closer to the cable surface represents a bigger reduction to the x-ray attenuation pathway compared to a similar sized void close to the conductor. This means that a void closer to the surface of the conductor will produce a greater greyscale change compared with the same void closer to the conductor. This method of void detection, however will not be able to be used to quantify the void size. For this reason, it is only possible to state that the void detection process is qualitative with a minimum resolution of 200 μm because the full extent of the void cannot be detected. This is also the case with the original system because the edges of the void will be undefined and so only the minimum size of any defect could be stated. It is also difficult to determine the actual minimum void size detectable using the original system because the actual size of any voids detected is also unknown. This infers that it should be possible to detect 200 μm voids using the proposed system as long as the greyscale change is above 17 greyscale levels. Further work is required to determine the greyscale level change of known 200 μm voids in various positions within the insulation system of a cable joint. Once this work has been undertaken, then the level of confidence of the proposed detection system could be determined. At that stage it will be possible to determine if the proposed void inspection system could be used to replace the current inspection method.

6.1.3.6 Application of Void Detection to a Full Image

The void detection method described above has been limited to a section of the 1.5 mm drilled hole in the central section of the insulation. To demonstrate the full capability of the void detection method, the processes described can be applied to a full image. Figure 6.16(a) is a section of cable with a 1 mm and 1.5 mm hole drilled from the outer surface of the cable to the outer surface of the conductor. The 1 mm hole represents the smallest void that could be introduced into the cable joint after manufacture. This image has then been flattened (Figure 6.16(c)). The edges of the voids have then be found using the methods described above (Figure 6.16(d)). These void edges have then been superimposed back onto the photometrically corrected image (Figures 6.16(e) and 6.16(f)). From this example it is possible to see that the edges of the of holes have been found within the insulation, however the edges of the portion of the holes within the

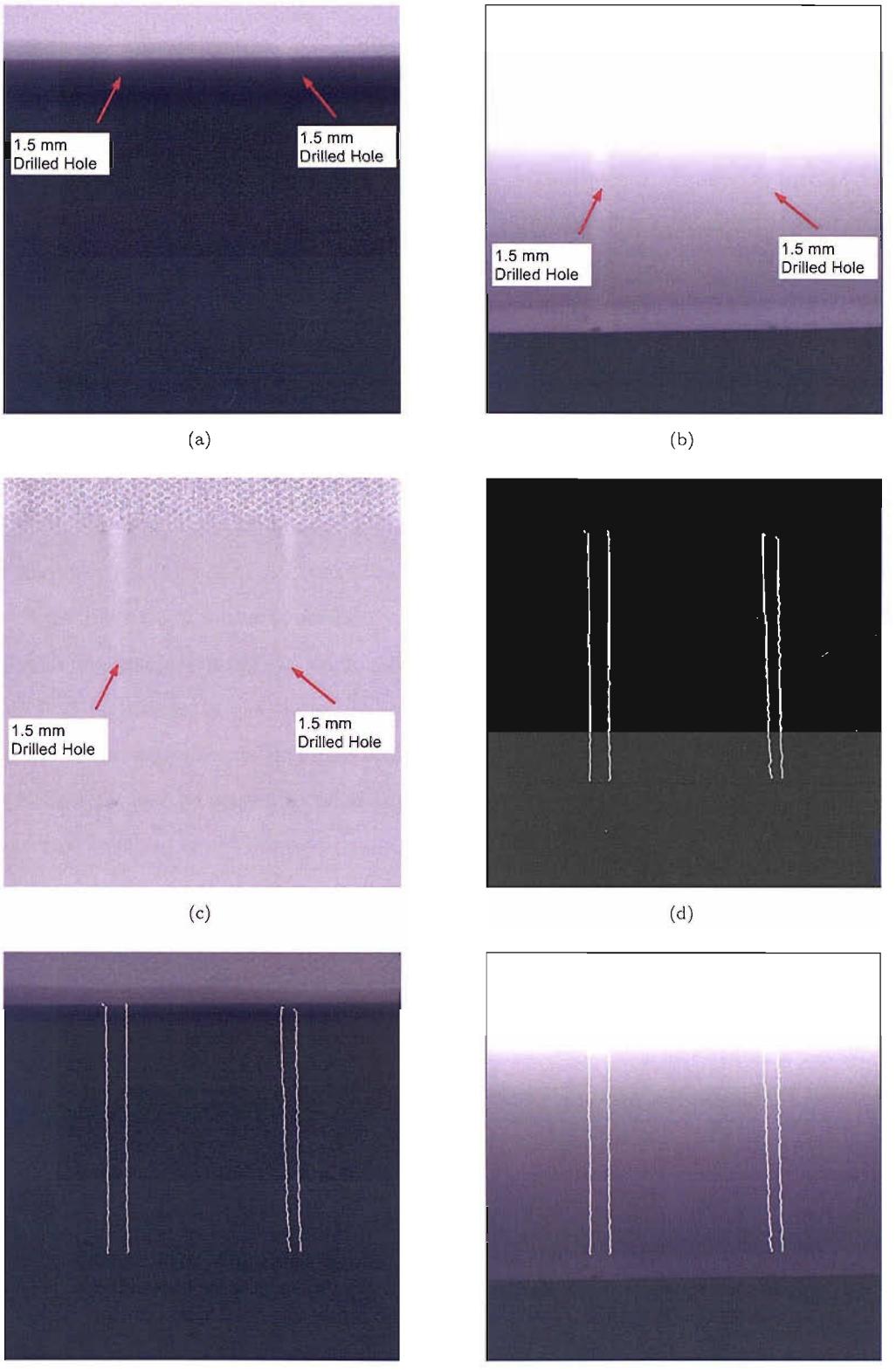

FIGURE 6.16: Full cable joint image void detection (a) image with 2 drilled holes, (b) a brightened version of (a), (c) the flattened image, (d) the void edge image, (e) the void edge image superimposed onto (a), and (f) a brightened version of (e).

conductor and insulation shields have not been detected. This is due to the fact that the semiconducting material used to manufacture these screens is significantly less dense compared with the EPR rubber of the insulation. This makes it more difficult to detect a void in these regions. The detection of voids within these shields is still a necessary requirement for cable joint inspection, however it is a subject that requires further work.

6.2 The Complete Detection Process

From Sections 6.1.2 and 6.1.3, it can be seen that inclusions and voids can be found within separate images. The inspection system, however, requires that both types of defects be found in the same image. To demonstrate this, the two wire image from Figure 6.6 has been inspected for inclusions and voids. The results of this inspection are shown in Figure 6.17. From this figure it can be seen that the both wires and the swarf have been found successfully, and the holes containing these wires have been found in the insulation region, demonstrating that the proposed system is able to detect voids and inclusions in the same image. From this image it is also possible to visualise the inclusions and defects in relation to each other. Should the resolution of the void inspection process be shown to be able to detect 200 µm voids, then the proposed defect inspection method could be used to replace the current inspection method. The benefits of the conversion to these digital inspection methods are that the voids and defects are shown clearly in the images removing the need for trained operatives. The method is fully repeatable and does not suffer from human error. These improvements, therefore, make the detection of defects within a cable joint more accurate, repeatable and reliable.

6.3 Summary

Defects can be introduced into the insulation system of a cable joint due to the manual nature of the manufacturing process. These can either be inclusions or voids, which can alter local the electric stress in the insulation system. If the defect is large enough, it can potentially reduce the working life time of the cable joint. For this reason significant defects have to be detected prior to energisation of the cable system. The presence of a defect in the insulation system of a cable joint will either decrease (inclusion) or increase (void) the pixel intensities of the groups of pixels associated with the defect due

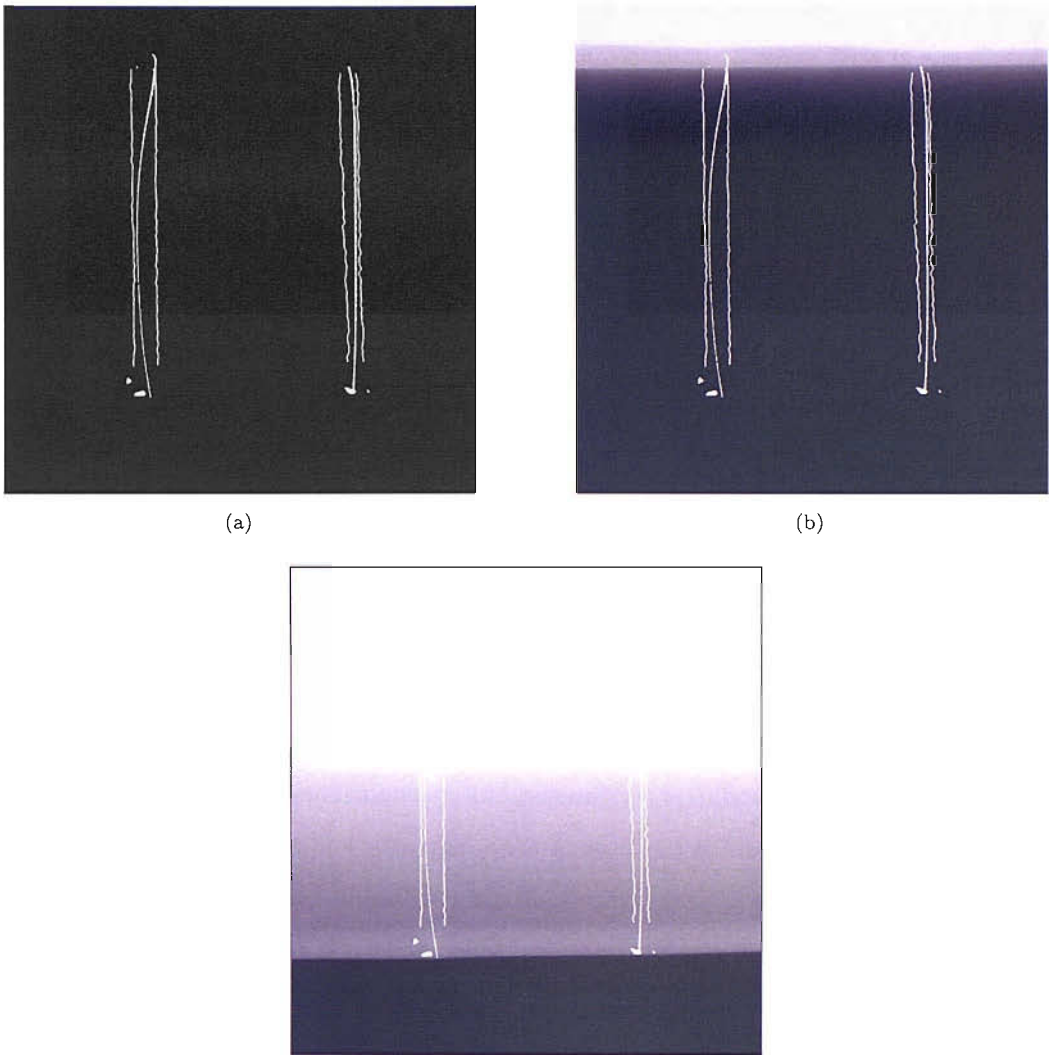

FIGURE 6.17: Full image defect detection (a) the binary defect image, (b) the original image with the binary image superimposed, and (c) brightened version of (c).

to the interaction of the defect with the x-ray flux used to image the joint. The smaller the defect, the smaller this change in intensity becomes. With the original system it is possible to detect inclusions as small as 50 µm and voids believed to be small as 200 µm. Defects of this size do not produce changes in the digital x-ray cable joint image that are significant enough to detect using standard edge detection techniques. To be able to detect such defects, the statistical relationship between the pixels associated with the defect and the pixels associated with defect-free insulation can be used. Defect-free insulation produces a pixel intensity distribution that tends towards a normal distribution. The groups of pixels associated with a defect will alter this distribution. The change in attenuation caused by an inclusion is significant enough to produce a distinct group

of pixels with a reduced pixel intensity mean. To find an inclusion, the image has to be inspected for groups of pixels that are distributed about a mean that is significantly less than the mean of the surrounding defect-free insulation. Using this method it is possible to find inclusions as small as 50 μm, anywhere within the insulation system of a cable joint. The size of the inclusion within the image can also be determined accurately to within ± one pixel width/height. The distribution of pixels caused by a void will have a mean slightly larger than the mean of the distribution of defect free insulation. For small voids, the difference between these two means is not significant enough to produce to distinct distributions, however the pixels associated with the void will alter the variance of the distribution of pixels in the region surrounding the void. For this reason only the centre of a void can be found using the change in mean pixel intensity, whereas the edges have to be found using the variance of the region containing the void. The determination of the size of void within the image, however, is less accurate compared with the size determination of an inclusion. This is due to two reasons; firstly, the edges of voids in the image, unlike inclusions, are relatively continuous with the surrounding defect-free insulation, and secondly, it is difficult to produce a void with accurately known dimensions. Further work is required to determine the resolution of the void detection method. Once this has been performed it should be able to replace the original manual defect detection procedure with a digital inspection system that has accurately known detection resolutions and that does not suffer from human error and the problems associated with the production and storage of photographic film plates.

Chapter 7

Three-Dimensional Image Production

The digital image processing techniques described in Chapters 5 and 6 can be used to perform dimensional measurements on, and determine the defect status of, the insulation system of cable joints. The results generated, using these techniques, can then be used to determine if the cable joint has been manufactured to the pre-determined specification stated by the manufacturer. To determine if the cable joint is fit for service, the mean, minimum and maximum size of the insulation components has to be checked against the stated specifications for these components. Then the number, size and geometric density of any defects found has to be checked against the specification to determine if the joint can be considered to be sufficiently defect-free. The joint can therefore be passed or failed by simply comparing the data from the inspection with the specification, reducing the level of operator skill and knowledge. The data produced from the inspection process, however, is only two-dimensional (2D). This means that any defects found can only be contextualized with defects within the same plane. To overcome this problem, a 3D virtual image of the cable joint can be generated. The defects found can then be added to this virtual cable joint to determine the 3D relationship of the defects from the 2D images. This virtual tool, therefore, combines all the data obtained from the whole inspection process, making comprehension and visualisation of the inspection much easier, once again reducing the skill levels required to inspect the cable joint. The second benefit of the virtual cable joint is that if the cable does contain too many defects or too large a defect, or if any of the components of the insulation system have

been manufactured outside of the dimensional tolerances of the specification of the cable joint, then the decision on how to refit the cable joint is made easier by being able to localise the defective areas of the joint. The virtual images of cable joints that meet the manufacturer's specification can also be used to monitor the manufacturing process to determine if the production of joints can be improved. This chapter describes the methods implemented to generate the 3D virtual cable joint.

7.1 Vertical Image Montaging

The images used to perform the dimensional and defect status checks on the insulation of the cable joint are the full length montaged images generated using the splicing techniques described in Chapter 4, Section 4.8. These images can be arranged in 3D space in order to generate the virtual cable joint. To do this, a known datum on all the images is required. The datum used has to be a feature that is common in all the images of the cable joint. From this datum, it should be possible to determine the 3D location of each plane in which the 2D images lie.

The only feature that is constant in every image is the axis of rotation of the cable joint sample between the conical tip of the polariser and the conical tip of the brass studding (Figure 4.20). Any feature, interface or defect, in a cable joint is located at a fixed distance from this centre of rotation. The pixels in each image also remain at a constant height above this axis of rotation due to the alignment process described in Chapter 4, Section 4.6. This means that the centre of rotation can be used as the datum. Using the centre of rotation of the cable joint also has the benefit that it can be used as the origin in a polar co-ordinate 3D space. With this 3D co-ordinate system, the distance from the original that a feature is located is simply the distance between the feature and the centre of rotation, and the angle between the horizontal and plane in which the feature is found, is the imaging angle. This means that if the centre of rotation is known, in relation to each image, then all the features found using the proposed inspection processes can be arranged in 3D space.

7.1.1 Locating the Centre of Rotation

In order to determine the distance between a feature in the image and the centre of rotation, the location of the centre of rotation must be found in relation to a common point in each image. Due to the manufacturing and alignment processes, the centre of rotation of the cable joint is defined by the axis passing through the rotational centres of the conical tip of the polariser and the conical tip of the brass studding. The horizontal alignment process described in Chapter 4, Section 4.6.2 also means that this axis runs parallel with the pixel rows of the CCD array. This means that if the pixel row associated with the centres of both of the conical tips can be found, then this row can be considered to be the axis through the centre of rotation of the cable joint. To find this row the polariser and brass studding tip should be imaged, however the length of the polariser tip prevents it from being imaged as it does not extend far enough to encroach on the field of view of the camera. The brass studding, however can be rotated so that it does extend into the field of view of the camera. For this reason the axis of rotation is found by imaging the brass studding.

Figure 7.1(a) displays an image of the brass studding. This image was produced using the same exposure settings as used to generate the cable joint images, however the x-ray source voltage was reduced to 50 kV to increase the contrast between the brass of the studding and the background. The edges of the studding were then found using the Canny edge detection operator. Figure 7.1(b) displays the result of finding the edges in Figure 7.1(a). The edges lines in this image have been increased to 5 pixels wide in order to improve the visualisation of the edges. From this image the top and bottom edges of the studding can be found by locating the rows containing the highest and lowest edge line pixels (Figure 7.1(c)). The axis of rotation of the studding will therefore be parallel to these two top and bottom edge lines, and bisect region between the lines (Figure 7.1(d)). Processing the brass studding image in this way obtains the row of pixels through which the axis of rotation of the cable joint passes. This means that if the axis of rotation is known, and the distance between the axis of rotation and any feature in the image can be obtained by simply calculating the arithmetic difference in pixels between the axis and the feature and then multiplying the number of pixels by the known pixel size generated using Equation 4.11.

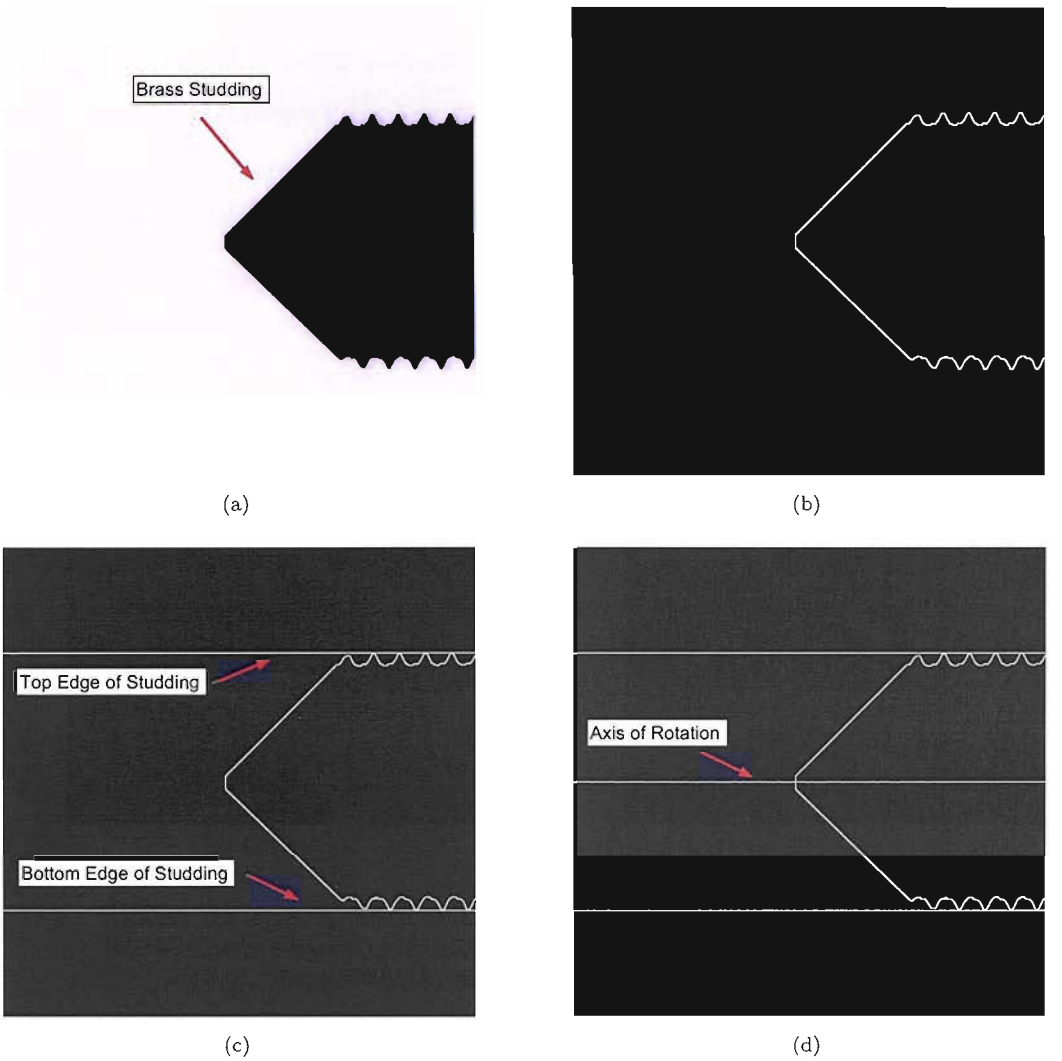

FIGURE 7.1: Locating the axis of rotation of the cable joint (a) brass studding image, (b) the Canny edge image of Figure 7.1(a), (c) locating the top and bottom edges of the studding, and (d) locating the axis of rotation.

The main problem with using this technique is that, as described in Chapter 4, Section 4.2, cable joints in the range 66 – 275 kV can have a radius greater than 27.6 mm. This means that for these cable joints it is not possible to capture one single image that displays the axis of rotation and the insulation semiconducting screen of the joint. As described in Chapter 4, Section 4.6.1, steel spacers are used to vary the height of the axis of rotation in order to image the insulation system of larger cable joint samples. The location of the axis of rotation can therefore be found by imaging the brass studding in the same way as in Figure 7.1(a), then after the spacers have been removed the brass studding can be imaged again. The pixel separation between the original row of the axis of rotation and the new row containing the axis of rotation can therefore be calculated

by the counting the number of pixels between these two rows. This process, however assumes that axis of rotation is visible in both images. For large cables, however, the camera has to be retracted back from the centre of rotation of the cable joint sample in order to provide enough clearance to insert the cable joint sample into the mount. This increases the magnification introduced into the images, and as a result reduces the field of view of the camera. This, along with the radius of the conductor, can mean that the axis of rotation of the cable joint can drop below the bottom row of the field of view of the camera when the spacers are removed. This means that to image the axis of rotation in the lower position, two images have to be vertically montaged.

In order to achieve this vertically montaged image, a known point has to be present in each image in order to provide a splice location. This process is the same the splicing process used to horizontally montage images, described in Chapter 4, Section 4.8. To do this a steel scribe (Figure 4.22) can be held in place by magnetic mount so that the tip of the scribe is visible in both images (Figure 7.2). These two images of the brass studding then have to be spliced at the row containing the tip of the scribe. To do this the edges of the images are found using the Canny edge detector, as described above (Figures 7.2(b) and 7.2(d)). The row containing the tip of the scribe in each image is then found. The edge line images are then spliced at the relevant row and combined. This produces the image in Figure 7.3. The change in height of the axis of rotation can then be found using this vertically montaged image in the same way as described above.

The change in height of the axis of rotation from Figure 7.1(d) to Figure 7.3 was caused by the removal of a 18 mm steel spacer. From the two images, the change in height of the axis of rotation was calculated to be 1475 pixels. The size of the pixel in the two images is 12.21 x 12.21μm. This means that from the images, the calculated height drop of axis of rotation is 18.01 mm. This implies that the vertical montaging of images to calculate change in the height of the centre of rotation is an accurate way to determine a datum point that can be used to locate each image in the correct plane in 3D space.

7.1.2 Combining the Images

The purpose of calculating the change in height of the centre of rotation caused when the steel spacers are removed, is to determine the location of the centre of rotation in relation to the cable joint images generated when the spacers are removed. As the original height

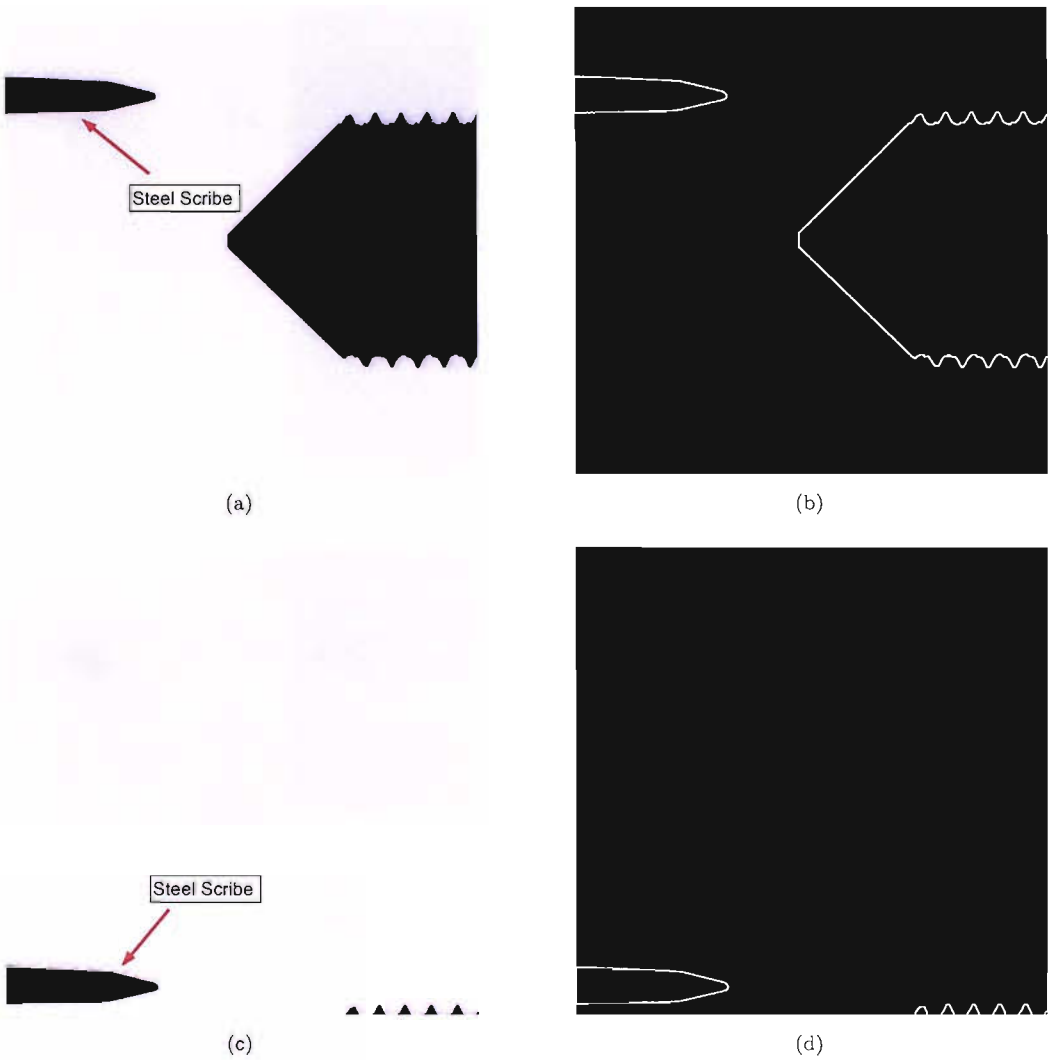

FIGURE 7.2: Vertical image montaging used to find the change in height of the centre of rotation of cable joint sample, (a) camera image of the brass studding and steel scribe, (b) the Canny edge image of Figure 7.2(a), (c) the image of the brass studding and scribe with the 18 mm spacers removed, and (d) the Canny edge image of Figure 7.2(c)

of the centre of rotation is known, its new location can be easily determined in relation to its original height. The construction of the virtual cable joint is simplified if the new height is stated in relation to the bottom row of the cable joint image because the height of the interfaces and defects are calculated using the bottom row of the image as the origin.

Once the height of the centre of rotation is known, in relation to the bottom row of the images, the distance between the centre of rotation and the interfaces or defects can be calculated. This means that because the centre of rotation is common to all the

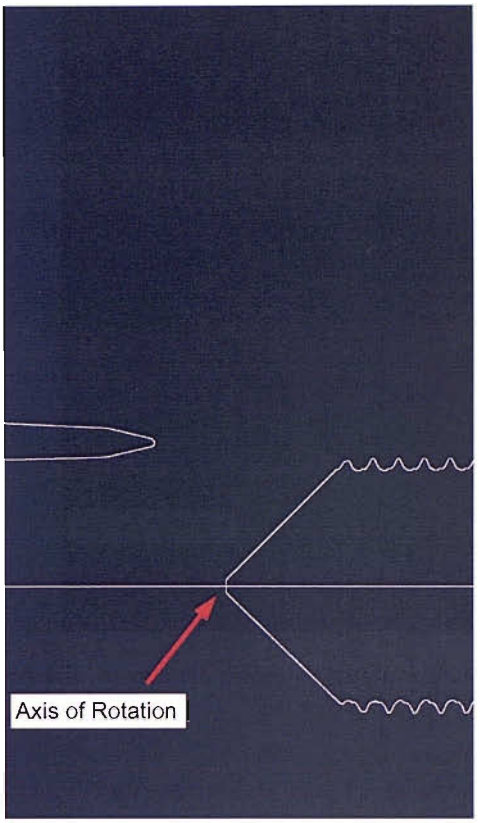

FIGURE 7.3: Vertically montaged centre of rotation image generated from Figures 7.2(b) and 7.2(d)

images, the diametrically opposed images can be montaged together, i.e. the 0° and 180° images of the insulation system can be combined into one image because they lie in the same plane as each other. This is achieved by producing a blank image space that is the same width as the original full length images generated using the techniques described in Chapter 4, Section 4.8, and that is twice the height of the distance from the centre of rotation to the top of the images. The central row of this blank image space will, therefore, be the same row in which the centre of rotation lies, and the top and bottom edges of this image will correspond the the top edges of the diametrically opposed images, i.e. the top edge of the image space will correspond to the top edge of the 0° full length image and bottom edge the 180° full length image. The 0° full length image can therefore be inserted into the top half of the image space with its top edge coinciding with the top edge of the image space. The 180° full length image, however has to be inverted so that the top and bottom edges interchange locations. The new inverted image can then be inserted so the new bottom edge (formally the top edge of the uninverted image) coincides with the bottom edge of the image space. Figure 7.4(a)

displays the image generated from the 0° and 180° images of the insulation system of the 90 kV cable joint. The centre of rotation for this image was, as stated in Section 7.1.1, 1475 pixels below the original height of the centre of rotation shown in Figure 7.1, however the centre of rotation in this image was at 980 pixels above the bottom of the image. The centre of rotation, therefore, lies at a distance 495 pixel below the bottom of the original image. This means that the image in Figure 7.4(a) has a central band 990 pixels high running across the whole image that are related to conductor, however this section of the conductor was not captured in the original images. This does not pose a significant problem because this section of the cable joint is made of copper and consequently would absorb or deflect the majority of the x-ray flux impinging on it. This band of the image in Figure 7.4(a) was therefore set to black to mimic the conductor that is visible in the original full length images.

The benefit of producing this image is that, unlike the full length images of the insulation system, the whole of the conductor can be seen. It is not possible to see the conductor in Figure 7.4(a) due to the undetectable contrast changes in the centre of the image. This image can be brightened to in order to highlight the conductor (Figure 7.4(b)). In this image is possible to see the conductor shield either side of the conductor. The conductor appears to be relatively straight and smooth, however due to the brightening process removing the outer edges of the cable it is not possible to see if the conductor is running centrally through the cable. To verify this the interface line plots can be used.

It would be possible to find the interface edges in the image in Figure 7.4, however the original interface plots can be used. The heights of the interfaces are stated in terms of their height above the bottom row of the image. These heights can therefore be adjusted so that they are the height of the interface above the centre of rotation by adding the distance in pixels that the centre of rotation is below the bottom of the image. The average height of the conductor shield in the interface line plots in Figure 5.22 is 273 pixels, this means that the height of the conductor shield above the centre of rotation is 768 pixels. The interfaces in the 0° line plot can therefore be converted in this way, however the interfaces in the 180° have to be below the centre of rotation, therefore the corrected heights have to be negative. Once the heights of the two interfaces in both interface line plots have been converted, a new interface line plot can be generated with the origin of the y-axis coinciding with the centre of rotation of the cable joint (Figure 7.5). In order to ensure that this new interface line plot correctly represents the full span

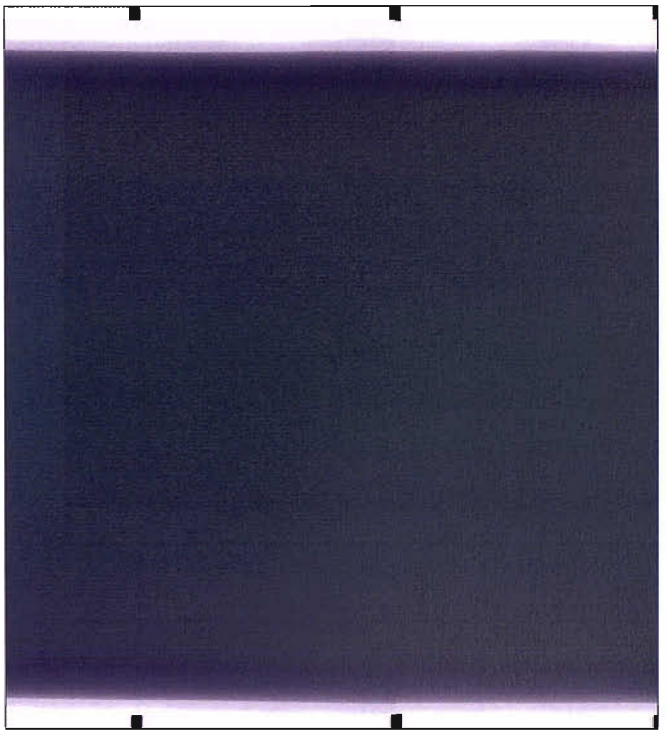

(a)

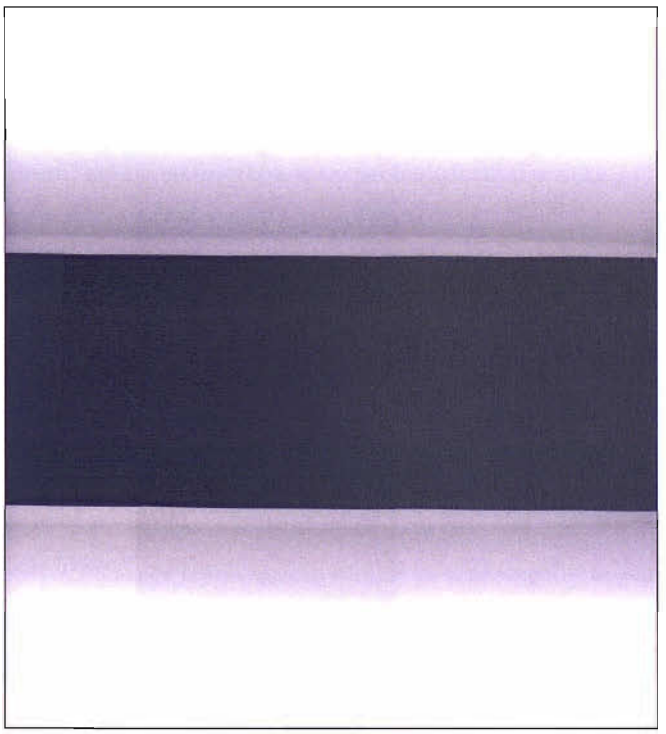

(b)

FIGURE 7.4: (a) The full cable joint image of a 90 kV cable joint generated from the 0° and 180° full length cable joint images, and (b) the brightened full cable joint image

of the cable joint, it is possible to calculate the diameter of the cable for each column of the plot. The calculated diameters can then be compared with measurements taken of the actual cable joint diameter. For the cable in Figure 7.5 the diameters measured as part of the component thickness verification in Chapter 5, Section 5.3.1 can be used. Figure 7.6 displays the calculated and measured mean diameters of the cable joint for the four image planes. From this plot it can be seen that the mean calculated and measured diameters differ less than 50μm, and this difference is likely to be caused by the different sampling rates used to generate the data, i.e. only seven samples were used to generate the measured mean, whereas the calculated mean has 4460 samples. It can be assumed, therefore that the interface lines in Figure 7.5 correctly represent the interface spacing for the full span of the cable joint, and as a result, this interface plot can be used to inspect the conductor in the cable joint. From Figure 7.5 it is possible to see that the conductor appears to be running parallel with the outer surface of the cable, however the insulation in the upper section of the image is thicker than the insulation in the lower section of the image. In order to determine the exact eccentricity of the conductor within the cable joint, all four sets of diametrically opposed interface plots must be generated. From the four plots generated it is possible to determine the eccentricity of the conductor, however the interpretation of the information in the four plots can be difficult. The plots, however, can be arranged in 3D space and thus form a skeleton of the virtual cable joint, hence easing the interpretation of the data.

7.2 The 3D Virtual Cable Joint

The four full span cable joint interface line plots can be combined together in 3D space using the axis of rotation as the datum. The central row of all four interface plots lie on the axis of the centre of rotation. The four plots can therefore be combined into one plot using the angular separation of the imaging angles as the angular separation between the four plots. The 2D image produced would therefore contain 32 lines arranged radially around and in parallel to the central axis of rotation. These 32 lines can then be used to generate a more tangible 3D virtual cable joint.

The cable joint sample is imaged at 8 distinct imaging angles, therefore each interface between two components in the cable joint is defined in the 3D virtual cable joint by 8 interface lines. Figure 7.7(a) shows the lines associated with the interface between the

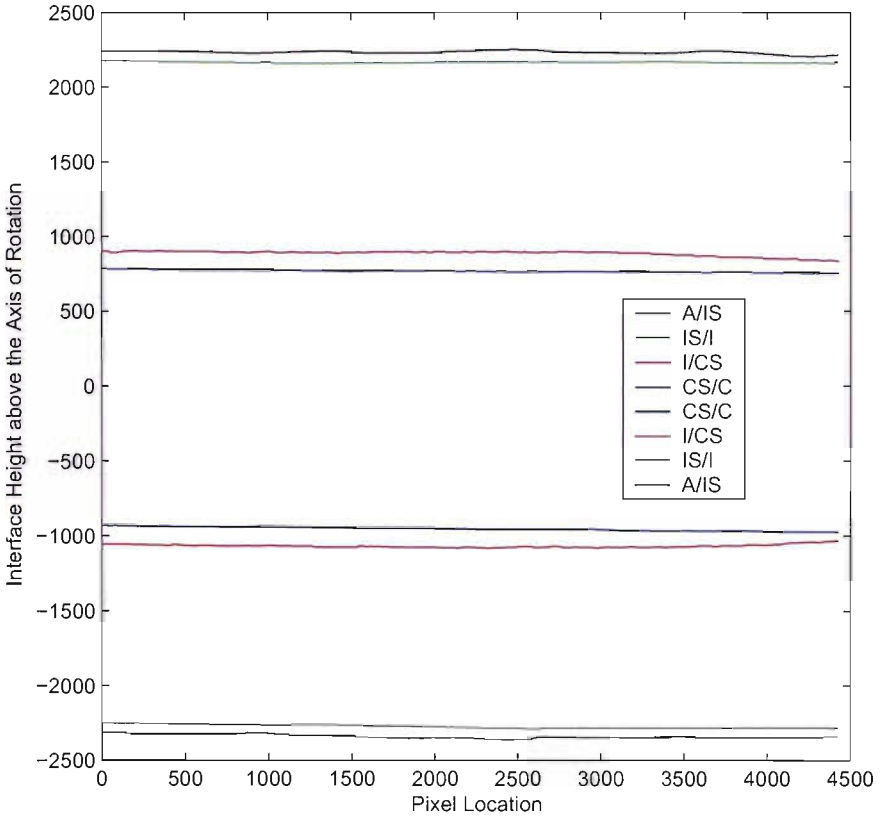

FIGURE 7.5: The interface line plot of Figure 7.4(a)

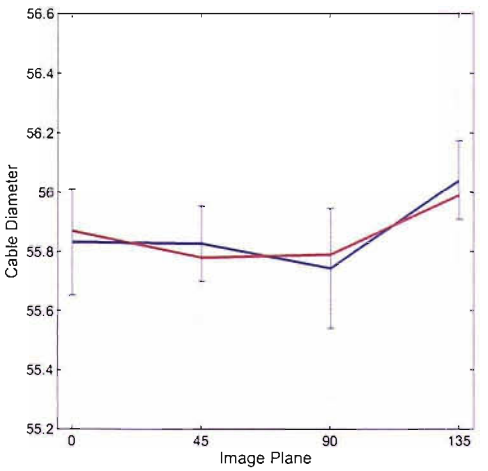

FIGURE 7.6: Mean calculated cable diameter (blue trace) with confidence limits (blue - 1 standard deviation, black - min/max) and mean measured diameter (red trace)

conductor and the conductor shield for the 90 kV cable joint. The 8 lines are arranged around the axis of rotation, which is located along the 0 axis of the x-z planes. These lines, therefore define the outer contour of the conductor. From Figure 7.7(a), this could imply that the conductor is octagonal, however it is known that the conductor has an external contour that is relatively round. This misinterpretation could have been removed by imaging the cable joint at more than 8 imaging angles, however this would increase the time required to perform the inspection process. The number of lines used to define the edge of the conductor, however, can artificially increased using linear interpolation. It can be assumed that the shape of each component will not dramatically change over at 45° angle. This means that if the conductor radius is calculated to be 10 mm at 0° and 9 mm at 45°, then at 22.5° the conductor radius can be assumed to be 9.5 mm. Using this interpolation process the number of lines used to define the shape of each component can be increased. From testing the number of lines required to generate a good representation of the shape of each component was found to be 32 lines. Figure 7.7(b) shows the effect of using linear interpolation to increase the number of lines used to defined the conductor from 8 lines to 32. From this image the cylindrical nature of the conductor is more apparent. The visualisation of the conductor can be further improved by rendering these 32 lines. Figure 7.7(c) shows the effect of rendering the conductor. The gaps between the lines in Figure 7.7(b) are filled by joining the 32 data points in each x-z plane. The colour of the lines used to join the data points has been set to mimic the copper colour of the conductor. This rendered image also has end caps added to the ends of the conductor to improve the interpretation of the shape of the conductor. The rendered virtual image can therefore be used to inspect the shape of the conductor. Figure 7.7(c) can be easily manipulated to rotate the conductor around all three axes. This allows an operator to see every surface of the conductor. To improve this inspection a light can be added that highlights the variations in the surface of the conductor (Figure 7.7(e)).

The result of combining the interface data relating to the conductor shield/conductor interface is the production of a tangible 3D image of the conductor. This process can then be repeated for the conductor shield, insulation, and insulation shield. Figure 7.8 shows the 3D images of all four components of the cable joint.

The conductor, conductor shield, insulation, and insulation shield can then all be combined into a single image to produce the 3D virtual cable joint image. Figure 7.9 displays

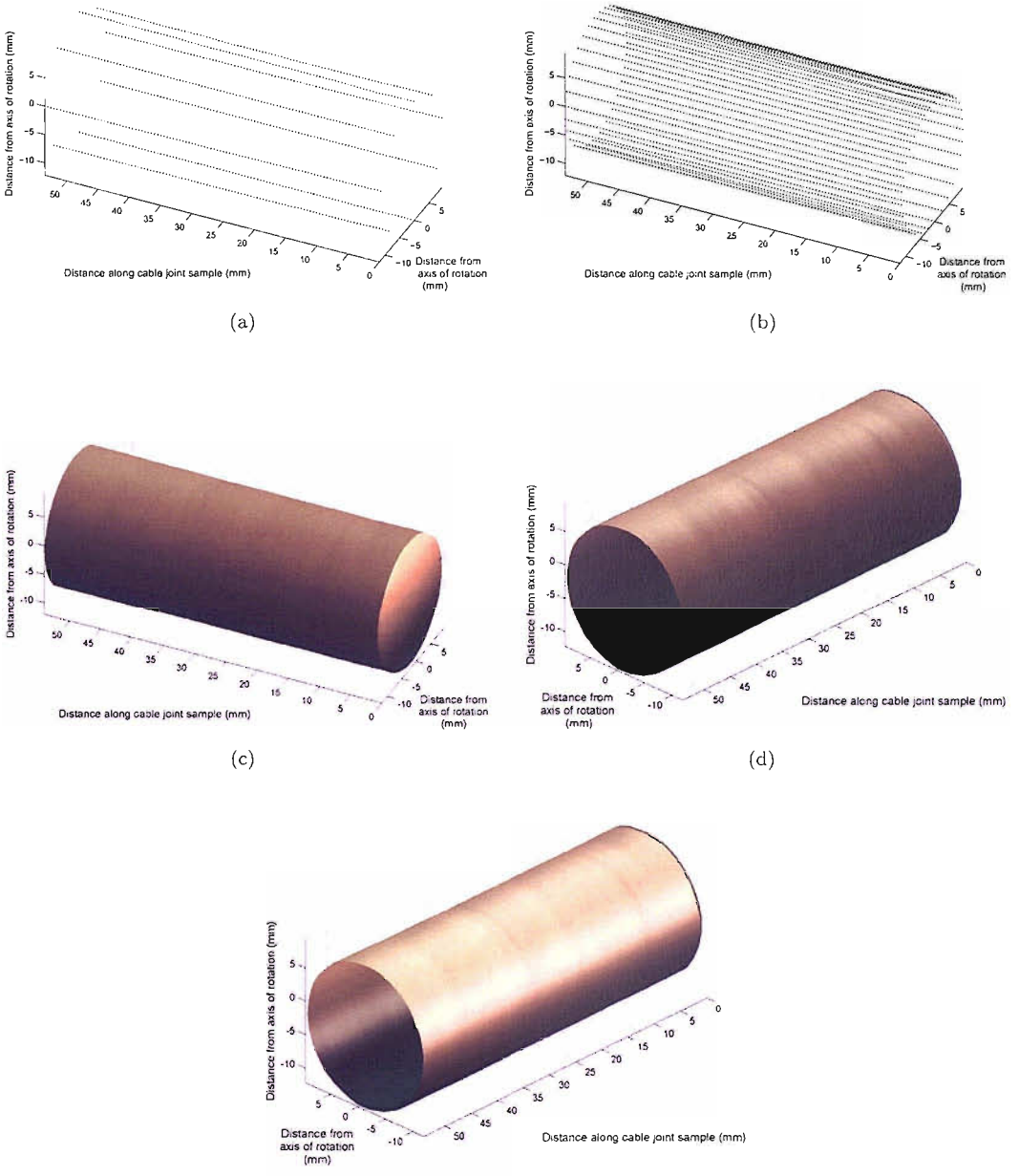

FIGURE 7.7: 3D virtual image of the conductor (a) 8 line wire plot, (b) 32 line wire plot, (c) rendered image, (d) rotated rendered image, and (e) lighting added rotated image.

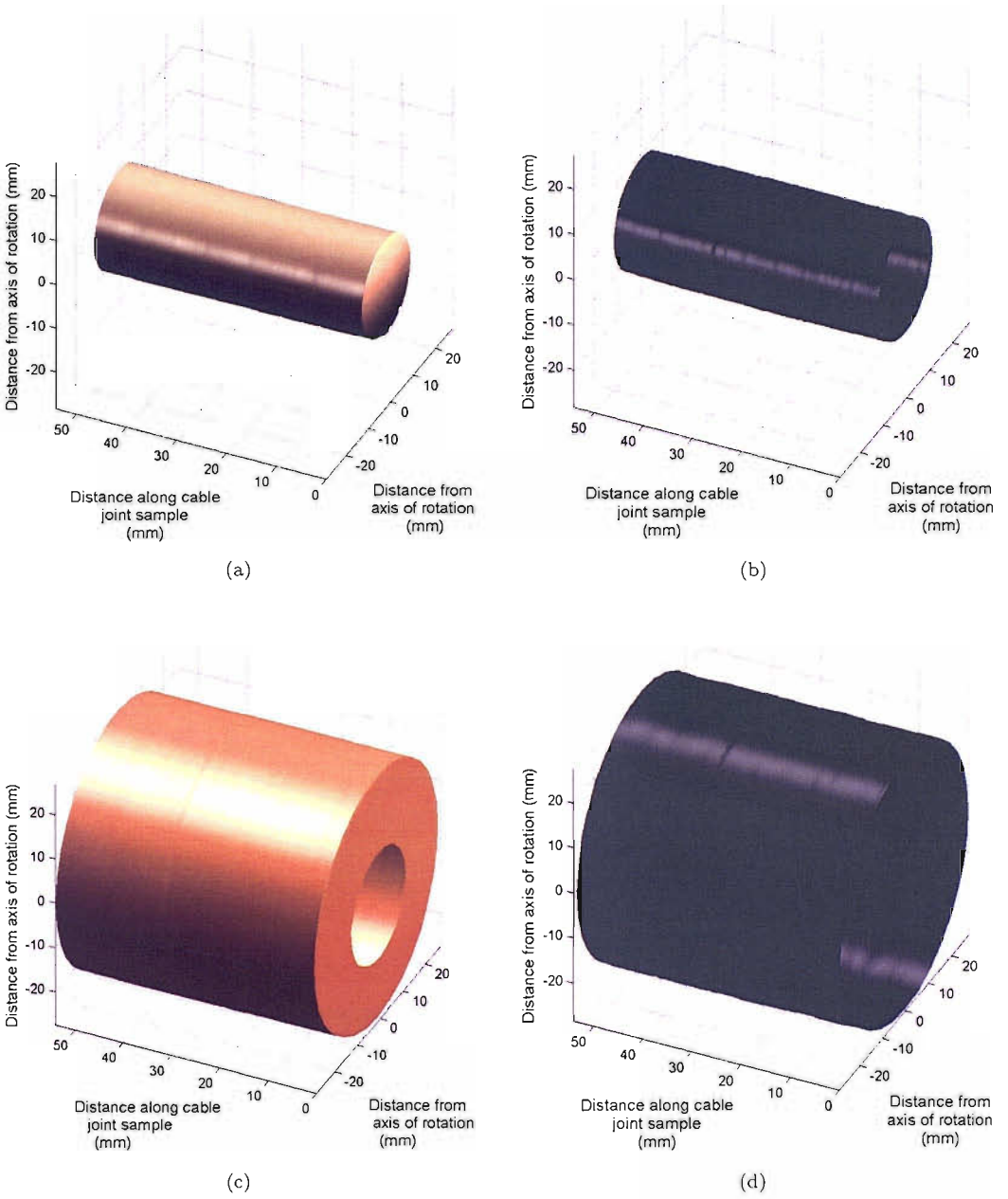

FIGURE 7.8: 3D virtual image of the (a) the conductor, (b) the conductor shield, (c) the insulation, and (d) the insulation shield.

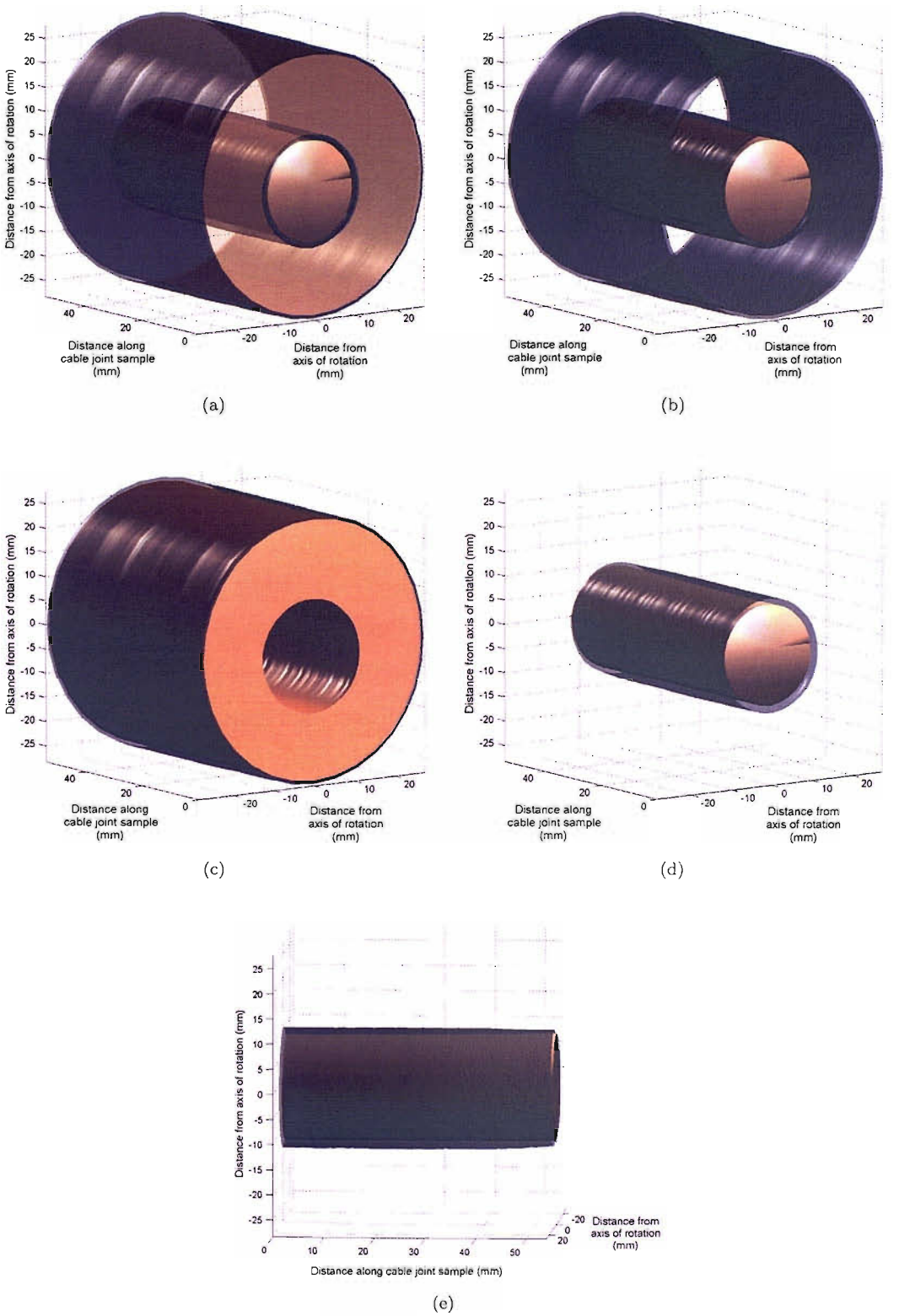

FIGURE 7.9: 3D virtual 90 kV cable joint (a) full image, (b) insulation face removed, (c) insulation and insulation shield, (d) the conductor and conductor shield, (e) the thinning of the conductor shield.

the 3D virtual cable joint image of a 55 mm section of a 90 kV cable joint. Figure 7.9(b) displays all four components in the same 3D image space. So that the details of all the components can be seen, the insulation shield, insulation and conductor shield have been made semi-transparent. With this reduction of the opaqueness of the outer three components of the cable joint, the geometric relationships between the four components of the joint can be visualised. This visualisation has been increased in Figure 7.9(b) by removing the insulation from the system. By removing the insulation the interfaces between the four components is clearer. The virtual cable joint can also be used to inspect the changes in thickness of the components, especially the semiconducting screens. Figures 7.9(c) and 7.9(d) display a semi-transparent insulation shield on opaque insulation and a semi-transparent conductor shield on an opaque conductor respectively. These images can be manipulated to view these components from a range of angles. Figure 7.9(e) displays a side on view of Figure 7.9(d). From this image it can be seen that the conductor screen tends to thin slightly towards the right-hand end of the sample. Figure 7.10 shows the two end slices of the sample. From the two photographs of the slices it can be seen that the conductor shield is thinner in Figure 7.10(b) compared to the thickness of the shield in Figure 7.10(a). The markings on the faces of these two slices are the measurement markings used to determine the thicknesses of each component (Chapter 5, Section 5.3.1).

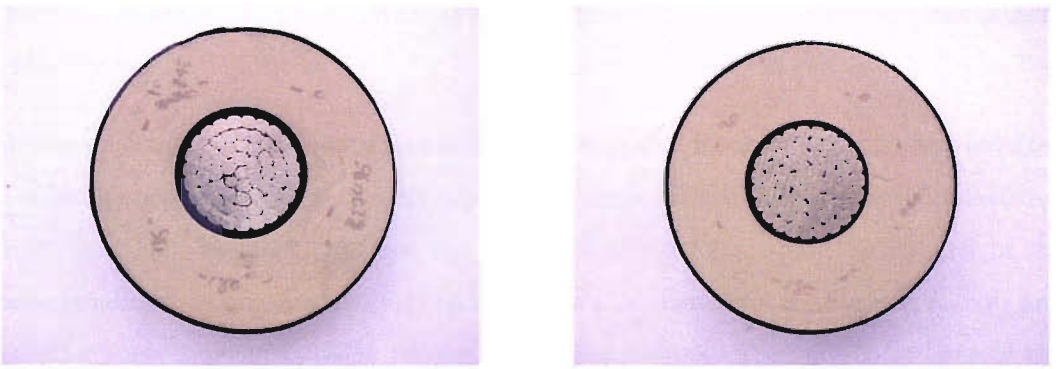

(a) (b)

FIGURE 7.10: The end slices of the 90 kV cable joint (a) the left-hand slice, and (b) the right-hand slice

7.2.1 3D Defect Plotting

The information obtained from the interface detection process described in Chapter 5, can therefore be used to generate a 3D virtual cable joint that can be used to visualise the internal structure of the cable joint. The virtual joint produced, however, does not contain details of any defects in the insulation system. The defects in the insulation found using the methods described in Chapter 6 can be added to the virtual cable joint by plotting the inclusions and edges of the voids in the plane of the virtual cable joint that corresponds to the exposure angle used to image the defects. The result of plotting the defects in this way is that the 2D slice through the defect is located in the 3D volume of the cable joint.

In order to demonstrate the 3D defect representation, a further section of 90 kV submarine cable joint was used. Into this joint were drilled a 1 mm and a 2 mm hole. The 1 mm hole extended from the outer surface of the cable to the surface of the conductor. The 2 mm hole however was only drilled 12 mm into the insulation system. This meant that the bottom of the hole was located in the central region of the insulation. The 1 mm hole was drilled into the cable joint in the 90° imaging plane of the joint, however the 2 mm hole was drilled into the cable in the 180° imaging plane. The axis separation of the two holes was set at 10 mm. Into the 1 mm hole was inserted at 200 µm wire. This wire extended from the surface of the conductor to the surface of the cable (Figure 7.11).

This arrangement of the defects meant that no horizontal image montaging was required in order to image, only 8 rotationally separated images. These defects were manufactured at 90° and 180° in order that the full extent of the defects would be imaged in the corresponding imaging angles. Figure 7.12 shows the two defects. Figures 7.12(e) and 7.12(f) display the binary edge images of the two defects. The interfaces lines of the insulation components have also been added to these image to show the relative locations of the defects. Due to incomplete void detection in the two semiconducting screen components, the holes have not been shown in these regions of the image, however the entire length of the wire can be seen.

In order to plot these defects into 3D space, the virtual cable joint has to be constructed using the interfaces from all eight images using the techniques described in Section 7.2.

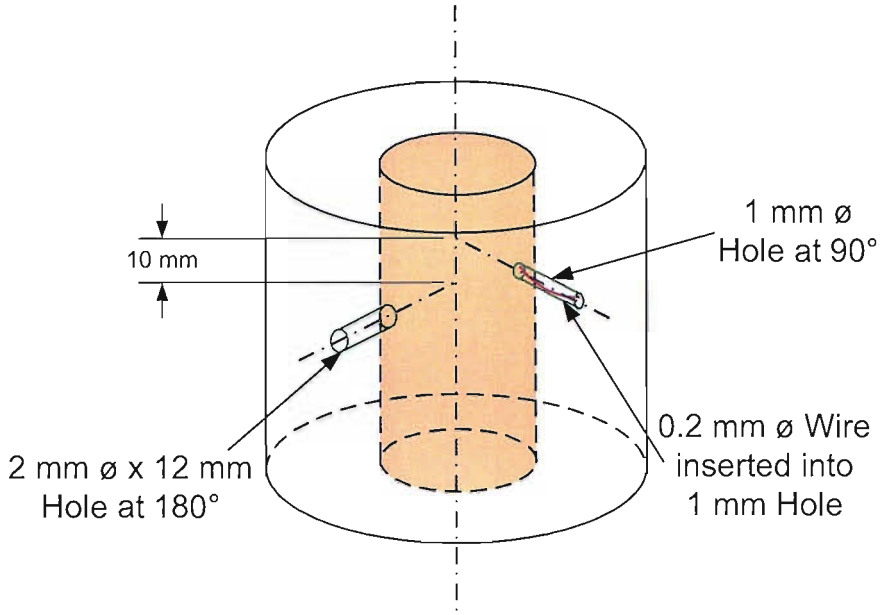

FIGURE 7.11: The defects introduced into the cable sample.

Once this image has been produced, the defects can been added. This is achieved by determining the distance of each pixel associated with a defect from the centre of rotation. This distance, along with the imaging angle, will then provide the polar coordinates of each pixel. These coordinates can then be converted to cartesian coordinates in order to plot the defects in the virtual cable joint image. In order to differentiate between an inclusion and a void, any pixel associated with an inclusion is plotted in red, whereas a void is plotted in green. Figure 7.13 shows the implementation of this defect plotting for the defects in Figure 7.12. From this image the inclusions and voids can easily be seen, plus the relative 3D locations of these defects can also be visualised. Plotting the defects into the virtual cable joint image in this manner, therefore, combines the data obtained from the proposed inspection methods.

7.3 Cable Joint Inspection Results

The proposed interface detection, defect detection, and virtual cable joint inspection algorithms can be used to generate a table of data detailing the size of the components of cable joint and any defects found in the joint, and a virtual cable joint that displays the geometrical relationship of the data in the table. Both of these products of the digital inspection process improve the ease in which data relating to the manufacturing

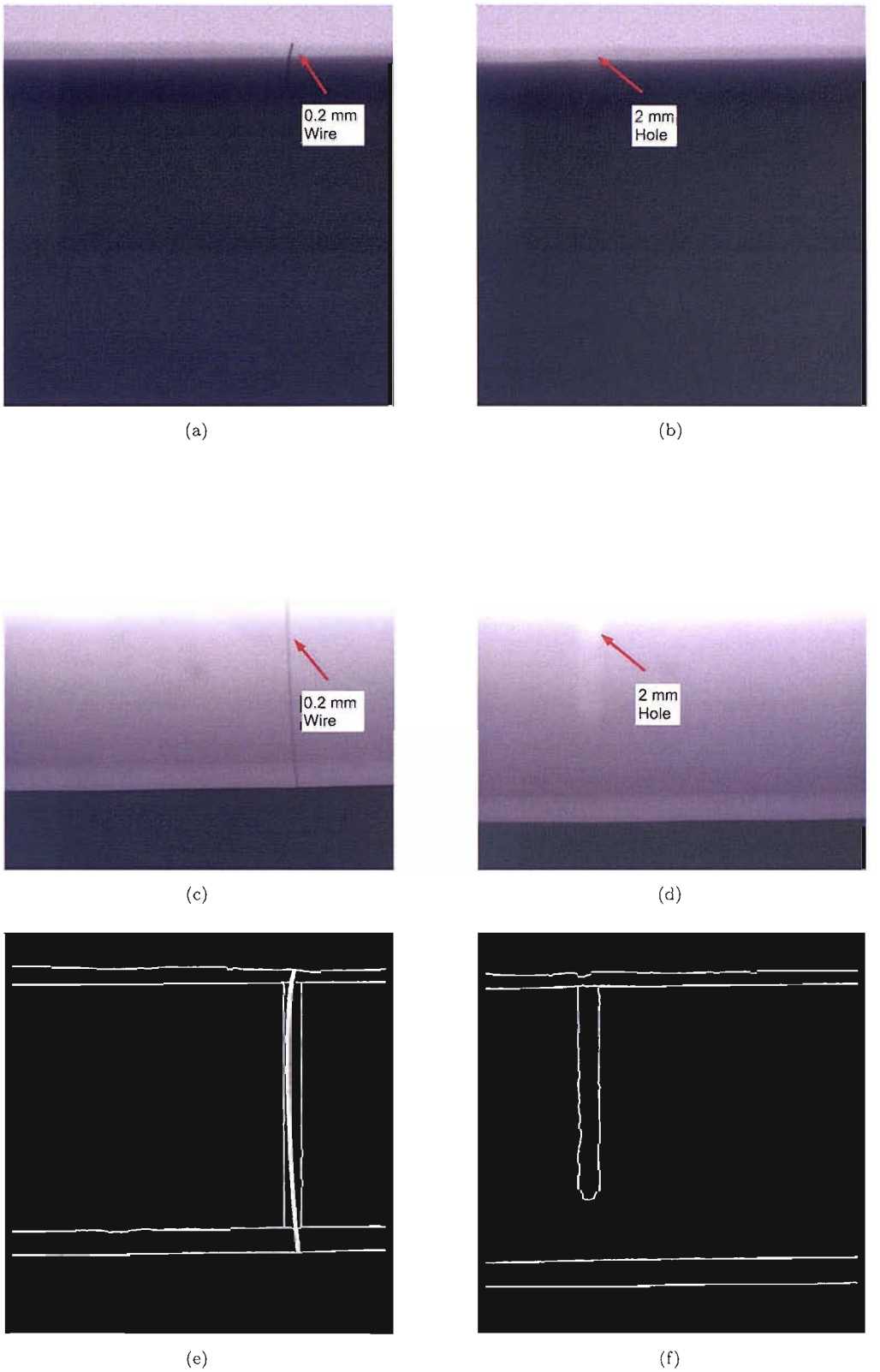

FIGURE 7.12: The x-ray images of the 2 defects (a) the 200 µm wire inserted into the 1 mm hole, (b) the 2 mm hole, (c) the brightened version of (a), (d) the brightened version of (b), (e) the binary image of the defects in (a), and (f) the binary image of the defects in (b)

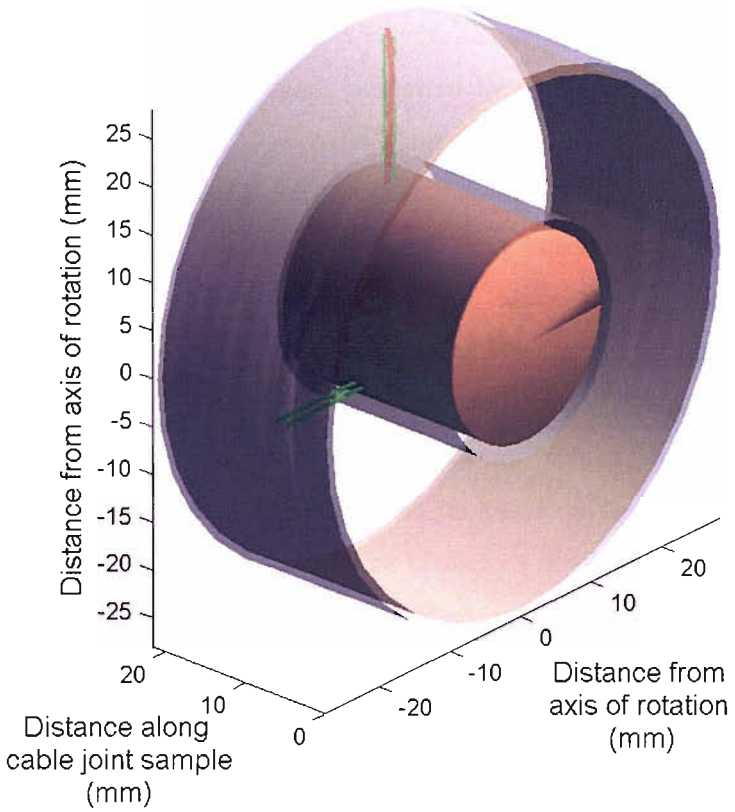

(a)

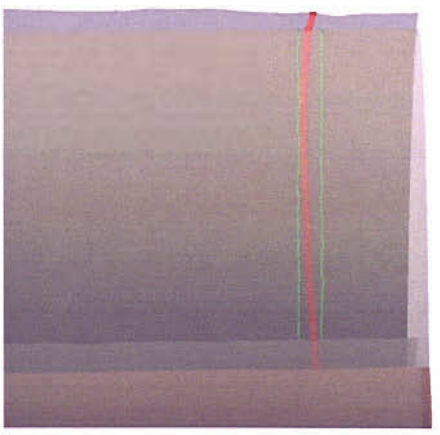

(b)

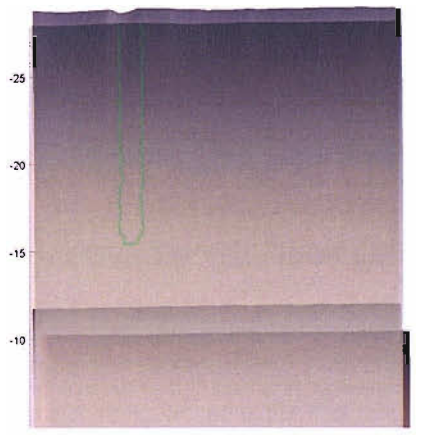

(c)

FIGURE 7.13: 3D virtual image of the (a) the conductor, (b) the conductor shield, (c) the insulation, and (d) the insulation shield.

quality of the cable joint can be obtained. Once this data has been obtained it has to be analysed in order to determine if the joint fit for service. The data from the table is primarily used in order to make this decision, the virtual cable joint can improve the visualisation of this data.

Table 7.1 and Table 7.2 display the dimensional data for the 90 kV cable joint from Figure 7.9. The mean, minimum, minimum location, maximum, maximum location, and standard deviation of each cable joint component is detailed in Table 7.1. The eccentricity and overall cable joint diameter are detailed in Table 7.2. The eccentricity is defined as the distance between the central axis of the cable joint and the central axis of the conductor. A positive eccentricity value means that the the conductor is located further away from the insulation shield for that imaging angle, whereas a negative value means the conductor is closer to the insulation shield. The location of the minimum and maximum values of the component data are included in both the tables so that the minimum or maximum dimension can be found on the virtual 3D cable joint. For example the minimum thickness of the insulation semiconducting screen is 0.49 mm. This minimum thickness is found on the 0° imaging angle 52.01 mm from the left-hand end of the cable joint sample. Figure 7.14 displays a side-on view of the virtual cable joint with the 0° insulation shielding uppermost in the image. From this figure it is possible to see that insulation shield thins dramatically in the region around 52 mm. It is therefore possible to determine the thickness of each component from Table 7.1 and then the virtual cable joint can be used to put these thickness into context with the actually cable joint.

Table 7.3 shows the defects that were found in the cable joint in Figure 7.13. The cable joint contained a 200 µm wire, a 1 mm hole, and a 2 mm hole. The size of the defects have been calculated, however only the size of the wire is absolute. The locations of the defects have been stated as the centre of the each defect. For this reason the radial location of the wire would is shown as being central to the insulation, however, the wire extends from the conductor surface to outer surface of the cable. From the table the axial spacings and angular spacing of each defect can be seen, for example the two holes appear to be spaced 9.89 mm apart, which, if manufacturing tolerances are taken into account, is comparable with the intended spacing of 10 mm.

Using these tables and the virtual cable joint, a decision can be made by comparing this

Conductor Dimensions (mm)						
Inspection Angle	Mean Value	Min Value	Min Location	Max Value	Max Location	Standard Deviation
0	21.08	20.98	11.33	21.20	49.88	0.05
45	21.05	20.93	12.33	21.18	38.78	0.07
90	21.01	20.81	6.01	21.18	52.15	0.09
135	21.06	20.96	0.01	21.21	53.82	0.06
Conductor Shield Dimensions (mm)						
Inspection Angle	Mean Value	Min Value	Min Location	Max Value	Max Location	Standard Deviation
0	1.42	0.95	54.00	1.64	29.52	0.15
45	1.25	0.73	53.71	1.48	6.81	0.19
90	1.17	0.67	49.56	1.51	6.89	0.23
135	1.17	0.57	53.87	1.40	0.01	0.21
180	1.35	0.68	53.99	1.55	10.95	0.21
225	1.36	0.88	53.74	1.56	12.54	0.16
270	1.43	0.89	53.39	1.59	25.49	0.14
315	1.54	1.00	53.82	1.75	28.60	0.14
Insulation Dimensions (mm)						
Inspection Angle	Mean Value	Min Value	Min Location	Max Value	Max Location	Standard Deviation
0	15.63	15.43	11.94	16.20	54.00	0.20
45	16.67	16.47	28.14	16.98	53.86	0.11
90	16.59	16.39	16.26	16.92	49.47	0.15
135	16.04	15.82	7.81	16.48	53.88	0.15
180	14.75	14.55	6.52	15.31	54.00	0.17
225	13.91	13.69	15.90	14.41	53.97	0.17
270	14.00	13.75	0.01	14.60	53.38	0.19
315	14.67	14.51	33.13	15.23	53.50	0.15
Insulation Shield Dimensions (mm)						
Inspection Angle	Mean Value	Min Value	Min Location	Max Value	Max Location	Standard Deviation
0	0.83	0.49	52.01	1.04	29.93	0.11
45	0.78	0.55	48.49	0.93	19.11	0.07
90	0.75	0.56	44.57	0.89	19.82	0.07
135	0.75	0.59	43.58	0.84	20.57	0.06
180	0.77	0.60	11.44	0.93	21.79	0.07
225	0.79	0.60	12.01	0.96	23.77	0.08
270	0.79	0.56	13.87	0.92	8.72	0.07
315	0.80	0.56	53.69	0.94	9.10	0.07

TABLE 7.1: Statistical analysis of the manufacturing quality of the cable joint in Figure 7.9 (Table 2 of 2). Location values are from the left-hand end of the cable joint

data in the tables with the predefined cable joint specification. This process is similar to the original inspection process, in that the decision as to whether the cable joint is fit for service is made using the data obtained from the manual inspection of the cable joint, however the digital inspection process has been improved so that the inspection system:

Conductor Eccentricity (Positive - Away from the Cable Edge) (mm)						
Inspection Angle	Mean Value	Min Value	Min Location	Max Value	Max Location	Standard Deviation
0	0.50	0.37	22.36	0.64	43.36	0.06
45	1.32	1.08	48.17	1.48	2.80	0.09
90	1.15	0.93	45.71	1.37	5.75	0.11
135.	0.47	0.35	41.90	0.59	21.10	0.06
180.	-0.50	-0.64	43.36	-0.37	22.36	0.06
225.	-1.32	-1.48	2.80	-1.08	48.17	0.09
270.	-1.15	-1.37	5.75	-0.93	45.71	0.11
315.	-0.47	-0.59	21.10	-0.35	41.90	0.06
Cable Outer Diameter (mm)						
Inspection Angle	Mean Value	Min Value	Min Location	Max Value	Max Location	Standard Deviation
0	55.83	55.47	10.50	56.29	29.93	0.18
45	55.83	55.57	48.61	56.09	22.66	0.13
90	55.74	55.30	12.94	56.08	37.83	0.20
135.	56.04	55.71	53.69	56.34	26.07	0.13

TABLE 7.2: Statistical analysis of the manufacturing quality of the cable joint in Figure 7.9 (Table 2 of 2). Location values are from the left-hand end of the cable joint

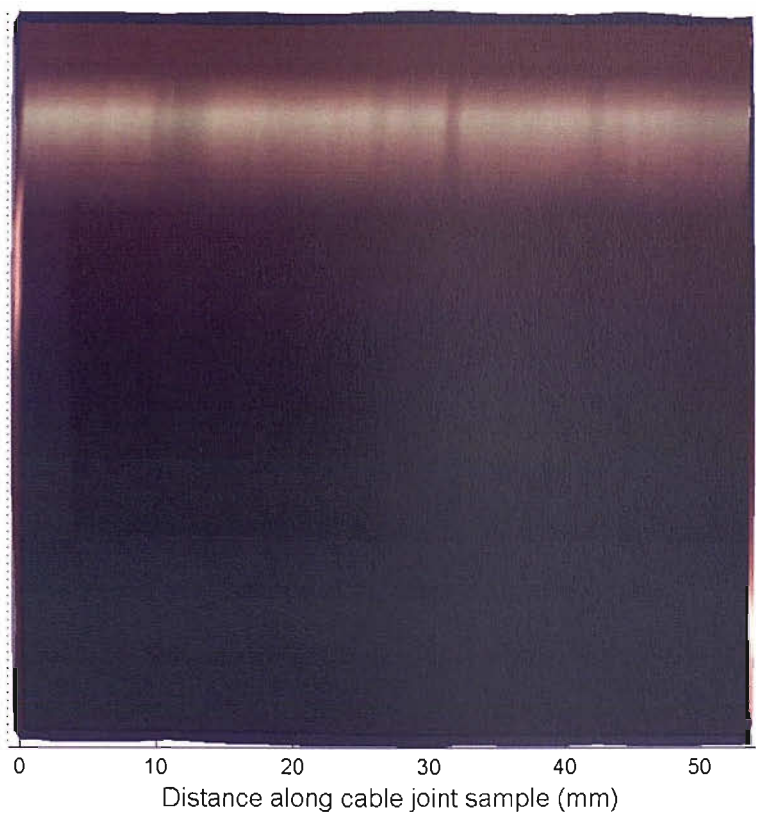

FIGURE 7.14: Side on view of the virtual cable joint insulation shield and insulation.

	Size (mm)	Axial Location (mm)	Radial Location (mm)	Angular Location (°)
Wire (200 µm)	0.195	17.03	19.60	90
Hole (1 mm)	0.941	17.32	19.89	90
Hole (2 mm)	1.905	7.12	20.62	180

TABLE 7.3: Size and location of the defects found in the the cable joint in Figure 7.13. Location values are from the left-hand end of the cable joint

- does not suffer from operator error,
- is repeatable,
- requires significantly less operator knowledge and technical skill in order to be accurately performed,
- can be used to sample the dimensions of the components of the cable joint with a sample spacing as small as 11.75 µm,
- can produce in-depth statistical analysis of the sizes of the cable joint components,
- can be used to show the size and geometric density of any defects introduced into the cable joint,
- can be used to generate a tangible 3D image of the cable joint in order to visualise the results of the inspection, and
- can be stored electronically for easy distribution future reference.

These improvements therefore make inspection of cable joints more, accurate, reliable, and detailed. As a result, the manufacturers of cables will be able to improve the level of quality assurance that they can provide relating to the production of cables by providing their customers with an in depth analysis of the internal structure of each cable joint.

7.4 Summary

Inspecting the full length cable joint images using the proposed interface and defect detection image processing algorithms, produces 2D images of the internal structure of the cable joint. The data in these images can be combined into a single 3D image due to the known geometric relationships between the images. To be able to combine the

2D images into one single 3D image, a known datum, present on every image, must be defined. The centre of rotation of the cable joint can be used as this datum. The centre of rotation, however, can lie outside of the field of view of the cable joint image. This problem is overcome by vertically montaging two images together. Once the centre of rotation is found, the diametrically opposed full length cable joint images can be combined to produce four full length, full span images. The interface locations in these images can then be plotted in 3D space, using the centre of rotation of the cable joint as the origin. These interface lines can then be rendered to produce images of the individual components of the cable joint. The individual components can then be combined into a single 3D virtual cable joint. Into this image can be added any defect found to show the relative locations of the defects. This virtual cable joint, in combination with the raw data from the interface and defect inspection process can then be used to determine if the cable is fit for service. This process is similar to the original inspection process, however the proposed digital inspection is more accurate, reliable and detailed; requires a reduced operator skill base; and provides the cable manufacturer with a valuable quality assurance tool.

Chapter 8

Conclusions

The manufacturers of high voltage cables need to be able to provide a level of quality assurance relating to the function and manufacture of the insulation systems of their cables. The standard factory tests are designed primarily for the assessment of the individual cable lengths. To complete these tests, sample slices of the cable are required, namely for dimensional checks and sample tests. These tests cannot, therefore, be used in order to ascertain the manufacturing quality of the cable joint.

Ultrasound and radiography provide viable methods of inspecting the insulation system of cable joints. Of these two methods, radiography provides greater penetration power and a finer spatial resolution. The Tony Davies High Voltage Laboratory at the University of Southampton currently has an inspection facility that uses x-rays to image cable joints. There are however, problems associated with the production and inspection of the photographic film used in this system, that can be overcome by converting the imaging and inspection of the cable joint to a digital system. To complete this conversion the photographic plate was replaced by a CCD array coupled to a scintillating screen. A CCD x-ray camera was chosen because it provided the best spatial resolution, image quality, contrast and field of view. To improve the quality of the images captured, the current analogue controlled macrofocus x-ray source was replaced with a digitally controlled microfocus source that was used in a pseudo-radial configuration in order to improve the quality of the images captured by the CCD array.

The images captured by the CCD array can be enhanced and inspected using digital imaging processing techniques. To improve the signal to noise ratio in the x-ray images,

and to improve the detection of features within the image, photometric correction techniques were used. The optimum exposure settings required to generate these images of the cable joint were found by establishing which exposures utilised the full greyscale range of the camera without saturation. Using three test objects, it was found that the quality of the images generated by the CCD camera were significantly better than the quality of the images obtained using film based methods. The disadvantage of using the CCD array to capture the images is that the field of view of the CCD array is considerably smaller than that of the photographic film. To overcome this, the individual images of cable joints were montaged together, thus making it possible to image large sections of cable joints. To completely image the insulation system, the cable joint has to be imaged at different imaging angles. It was found that the optimum separation between imaging angles was 45°. The size of the features within these images, however, could not be determined without establishing the magnification introduced into the image by the pseudo-radial configuration of the x-ray source. With the magnification known, the montaged images from the eight imaging angles can be inspected to determine the size of the components of the insulation system and to estimate the size of any defects in the insulation system of the cable joint.

The size of the individual components of the insulation system can be determined by measuring the distance between the component interfaces. To find the interfaces, standard edge detection methods could be used, however these methods suffer either from incomplete interface detection, or complete detection with considerable levels of false positives. A new method of detection has been proposed that finds the interfaces using feature extraction. This is achieved by first differentiating the montaged images using an averaging differentiator. The interfaces can then be found by locating changes in the profile of the differentiated image caused by the boundaries of the insulation system materials. These interfaces can be found in each column of the image due to the exposure configuration of the cable joint. This means that because only the four interface locations between the air, insulation screen, insulation, conductor screen and conductor are searched for in each column, the image produced displays complete interface detection with no false positives. The size of the individual components of the cable joint can be determined by calculating the pixel separation between each component interface and then multiplying this value by the size of the pixels. This enables dimensional checks to

be performed along the length of the cable joint at pixel width sampling distances, producing a more thorough analysis of the dimensions of the components of the insulation system. To determine the accuracy of this process, a cable joint sample was imaged and inspected. The measurements generated were then compared with sample measurements taken during a destructive test of the cable joint sample. The results of this comparison verified that the interfaces could be found to within 100 µm. It is therefore possible to use this method of NDT inspection to determine whether the cable joint has been manufactured to within the dimensional specifications stated by the manufacturer.

Defects in the cable joint can be detected by locating regions of pixels that have intensities that are significantly different to defect-free insulation. To enhance this detection, an artificially generated defect-free image can be subtracted from the cable joint image to produce an image containing only the defects within the cable joint. In this image, an inclusion will present itself as a region of pixels with reduced intensities with a defined edge. These pixels can be found by locating any pixel intensity that is more than three times the standard deviation of the distribution of defect-free insulation pixels intensities below the mean intensity of the distribution of defect-free insulation. The location of any pixel found can then be plotted onto a binary inclusion image. The resolution of this inspection method makes it possible to detect accurately, to within ± 1 pixel width, inclusions as small as 50 µm, which means that the inclusion status of the cable joint can be determined to within the same specification as the parent cable. A void will present itself in the image as a region of pixels with increased intensities, however due to the nature of the void, the edges are not as well defined and the difference in intensities between a void and defect-free insulation is small. It is therefore not possible to locate voids by simply detecting pixels with a raised intensity, however the defects can be found by using the variance of the pixel distributions within the image. The variance of the distribution of pixels of defect-free insulation and at the centre of a void will be relatively similar. Across the transition from the centre of the void to the defect-free insulation, the variance will increase. This raised variance can then be used to find the edges of the void. The main problem with this method is that the whole transition region is detected. To determine the edge of the void it is therefore necessary to thin this region away from the centre of the void. The centre of the void can be found by smoothing the cable joint image with a Gaussian operator in order to highlight the slight increase in pixel intensity near the centre of the void. The void edges found can then be

plotted onto a binary void image. The accuracy of this method of void detection cannot be determined due to the fact that the size of artificially manufactured voids cannot be stated, however, from the sensitivity testing of this method of void detection, a 200 µm void will be found within the insulation system if there is at least a 17 greyscale level change between the centre of the void and the surrounding defect-free insulation. Using this method will not produce absolute void sizing, for this reason detection of voids is semi-quantitative, however as long as a 200 µm defect can be detected, then this method of void detection can be used to pass or fail the cable joint.

It is possible to convert the eight sets of binary interface, inclusion, and void images into a virtual 3D cable joint. The 3D virtual cable joint can then be used to determine the size and eccentricity of the central conductor and to contextualize the 2D data from the eight imaging angles. A skeleton of the 3D image can be generated using the interface lines from the eight imaging angles, which can then be rendered to produce a tangible 3D object that displays the relative size of the insulation system components. Any defects found can then be added into this image. The 3D virtual cable joint, therefore, combines the data obtained from the inspection of the cable joint into one single image. This image can also be manipulated, which allows an operator to view the internal structures of the cable joint and any defects found.

The initial results obtained from the proposed inspection system indicate that it is possible to convert the existing inspection method to a digital system. The advantage of this conversion is that the digital processes are more accurate, reliable and detailed; requires a reduced operator skill base and is not subjected to human error; does not suffer from the problems associated with the production, inspection, storage and distribution of photographic film; and provides the cable manufacturer with a powerful quality assurance tool.

8.1 Future Work

The proposed algorithms have been developed in order to digitally inspect the x-ray images of cable joints. This inspection can be used to obtain the dimensions of the components of the insulation system; the presence of inclusions at any location within the insulation system, and voids within the insulation. The voids used to demonstrate

this process were drilled holes within cable samples and digitally introduced voids. To confirm that these voids exhibit the properties of voids within a cable joint, known voids within test objects should be produced. Figure 8.1(a) displays a rod of resin which was manufactured such that air bubbles were allowed to remain within the sample. Figure 8.1(b) displays a region of the rod containing two bubbles from the resin rod. This image was generated using a transmission microscope. Due to the cylindrical nature of the resin rod, some distortion of the bubbles has occurred due to the lens effect of the rod. This has elongated the bubbles, however the width of the bubbles should not have been affected. Included in this image are two known circles. The numbers next to these circles are the diameters of the circles in millimetres. For this reason it can be assumed that diameter of Bubble 1 is 800 µm and the diameter of Bubble 2 approximately 500 µm. In order to demonstrate that voids of this nature can be detected, this sample was imaged using the original inspection facility. The original inspection facility was used to image the voids because the low penetration power required to image the resin cannot be produced by the new microfocus source. The photographic plate was then inspected and the size of the voids was determined to be 500 µm and 800 µm. A section of the x-ray film plate produced was then digitized using the 35 mm negative scanner described in Chapter 4, Section 4.5. It can be seen from Figure 8.1(c) that these two bubbles have produce two lighter regions within the x-ray image. From this void analysis, it therefore possible to state that voids can be detected using x-ray technology. Further work should, therefore, concentrate on the production of voids of known sizes in cable joints and the detection of these. This work should also include the detection of voids within the conductor and insulation shields, and develop the dimensional analysis of voids so that the absolute sizes of voids can be obtained, along with determination of the minimum detectable void dimensions.

The x-ray images of a cable joint are a 2D shadow graph. A defect within one of these images will not necessarily lie in the vertical plane that passes through the axis of rotation of the cable joint. The defects introduced into the cable joint sample in Section 7.2.1 were introduced at 90° and 180° so that they did lie in the vertical plane during the 90° and 180° imaging angles allowing the defect to be introduced into the virtual cable joint in the correct plane. A defect in the cable joint, however, could be found on any plane within the image. To determine the angular location of the radial plane through the cable joint that contains the defect, and the radial position of the defect within this

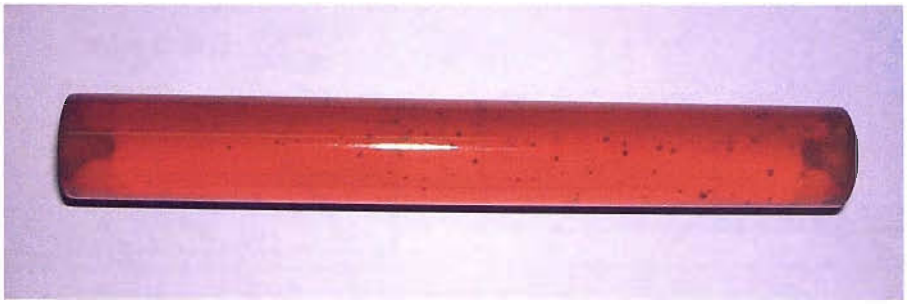

(a)

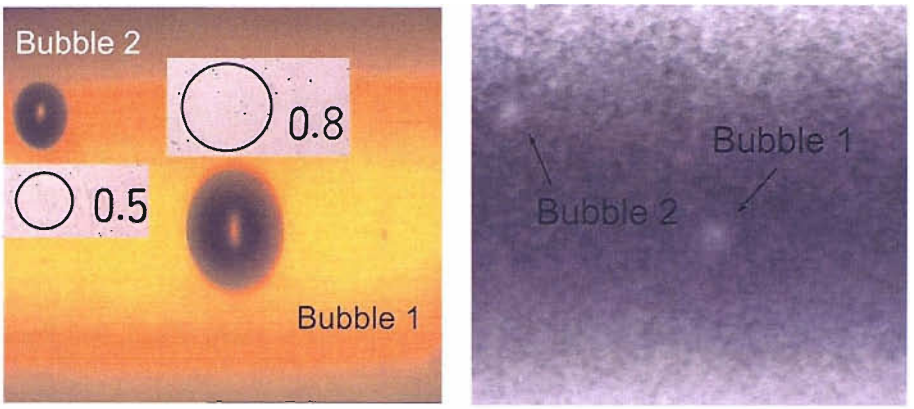

(b) (c)

FIGURE 8.1: Known voids manufactured in a resin rod, (a) the resin rod, (b) microscope image of two voids, and (c) scanned photographic x-ray image of two voids in (b).

plane, more than one image is required. Figure 8.2 displays three representation of the side-on views of the cable joint from Figure 7.12 during the imaging process. It can be seen from this figure, that despite a wire defect being insert into the cable joint in the 90° imaging angle, the defect is also present in the 45° and 135° imaging angles.

If the actual location of the defect had not been known prior to the investigation, the location of the defect can be found by using trigonometric relationships of the pixels associated with the defect present in all three images. This could be achieved by searching adjacent imaging angle defect images column by column for defects. If a two or more images contained a defect within the same column then it is likely that these two defects are the same defect imaged from different angles. The location of the defect could then be found by projecting the horizontal planes that the defect lies on in each image, on one single image, and where these planes meet, the defect should lie. Figure 8.3 demonstrates this process. The defect found in Figure 8.3(a) appears to be located close to the surface of the conductor. The actual location however could be anywhere along the red line. The defects in Figures 8.3(b) and 8.3(c) both appear to be relatively central to

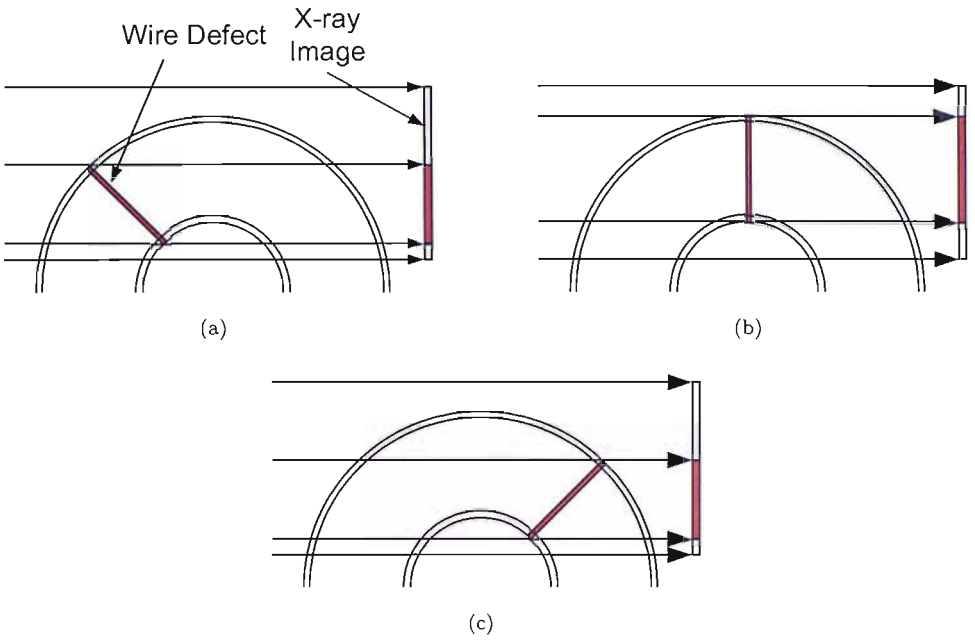

FIGURE 8.2: The presence of the wire defect from Figure 7.13 in neighbouring imaging angles, (a) 45°, (b) 90°, and (c) 135°.

the insulation, however their locations could be anywhere along the green and blue lines respectively. In all three images the centre of the defect lies on the same column. For this reason it is likely that the defect in all three images is the same defect viewed from three different angles. The axial location of this defect is known as it is the same in all three images. The radial location however has has to be found using the red, green and blue projections. Figure 8.3(d) displays where these three projection intersect. It is this point that determines the radial location of the defect. This method of defect location can also be used to ensure that any noise in the image is not plotted as a defect because to locate the defect it is necessary to have at least two images of the defect, and it is unlikely that two identical regions of noise will be found in the correct locations on two or more images.

During the manufacture of a cable joint it is possible that joint insulation system tapes do not bond completely with the central conductor or the insulation of the parent cables either side of the joint, known as delaminations and disbonds respectively. These incomplete bonds can produce voids between the tapes and the conductor/parent cable which can reduce the working lifetime of the cable joint. Further work on the proposed inspection system should also address these defects.

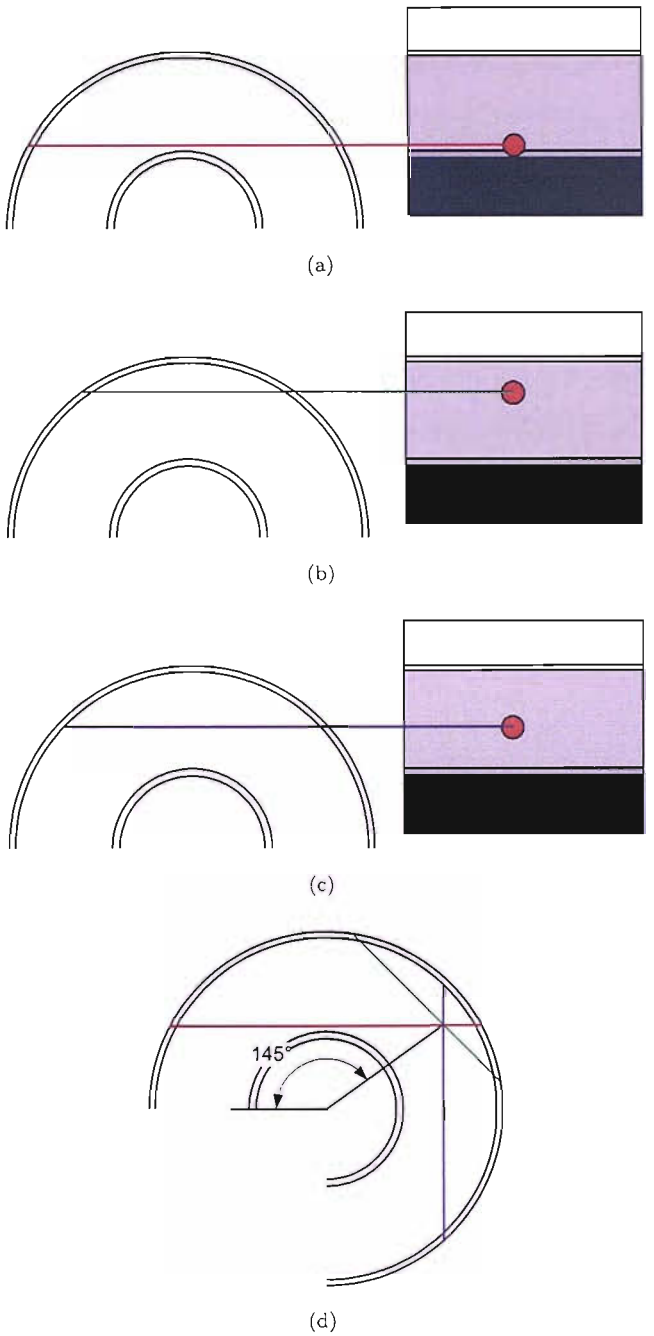

FIGURE 8.3: Determination of the angle of the plane containing a defect (a) 0°, (b) 45°, (c) 90°, and (d) the projected angular planes.

The new irradiation chamber has been designed in order to prove that it is feasible to convert from the current conventional photographic x-ray image capture and manual inspection method, to a digital image capture and inspection system. For this reason the irradiation chamber was designed to irradiate cable joint samples. Consequently, it would not be possible to use the new irradiation chamber in its current configuration to inspect cable joints prior to installation into a new cable network, because it would not be possible to load the cable into the chamber. This means that before the new system can be used in a field situation, it would therefore be necessary to modify the irradiation chamber such that it would be able to take a cable joint. Following this, the cable joint sample mount would have to be replaced with a mount that could index a full cable joint past the x-ray source and camera. Once these two modifications have been made it should be possible to use the digital system to inspect a full cable joint.

Appendix A

Factory Test Methods

A.1 Electrical Resistance Measurements of the Conductor

To test the d.c. resistance of the conductor, the complete cable length has to be stored in a controlled temperature environment for at least 12 hours and then the resistance of the conductor measured. Alternatively a sample of conductor can be conditioned for one hour in a temperature-controlled bath before the resistance is measured. The d.c. resistance can then be corrected to a temperature of 20°C and a length of one kilometer using the temperature correction factors detailed in Table A.1. The conductor is then deemed fit for service if this corrected resistance value does not exceed the maximum valued specified in accordance with the appropriate manufacturing standard. Table A.2 details shows the maximum permitted resistance per kilometer as stated in [14].

Temperatures below 20 °C		Temperatures above 20 °C	
Temperature of conductor at time of measurement (°C)	Correction Factor	Temperature of conductor at time of measurement (°C)	Correction Factor
5	1.064	21	0.996
6	1.059	22	0.992
7	1.055	23	0.988
8	1.050	24	0.984
9	1.046	25	0.980
10	1.042	26	0.977
11	1.037	27	0.973
12	1.033	28	0.969
13	1.029	29	0.965
14	1.025	30	0.962
15	1.020	31	0.958
16	1.016	32	0.954
17	1.012	33	0.951
18	1.008	34	0.947
19	1.004	35	0.943

TABLE A.1: Temperature correction factors for d.c. conductor resistance to correct the measured resistance at room temperature to 20 °C

A.2 Partial Discharge Testing

To determine if the cable's insulation system contains any significant defects the cable is energized and tested at 1.75 rated voltage, U_0, for 10 seconds and then slowly reduced to 1.5 U_0. For the insulation to be deemed defect free, the magnitude of charged detected at 1.5 U_0 should not exceed 10 pC for cables rated at voltages between 30 kV – 150 kV [11].

A.3 Dimensional Checks

The measurements have to be taken at least 16 hours after the extrusion, vulcanization, or cross-linking of the insulation or sheathing materials, at ambient temperature, in accordance with the British Standard BS EN 60811-1-1:1995. The average value of the insulation has to be equal to or greater than the specified nominal thickness and the minimum at any point should not be less then 90% of the nominal thickness, plus 0.1 mm. The average thickness of the semiconducting sheaths should not be less than the specified nominal thickness and the minimum thickness at any point should not be less than 60% of the specified nominal thickness. The minimum thickness of the metallic sheath should not be less than 95% of the nominal thickness, plus 0.1 mm for lead and

Nominal cross-sectional area (mm^2)	Maximum Resistance of conductor at 20 °C (Ω)		
	Annealed Copper Conductor		Aluminium Conductor
	Plain Wires	Metal-Coated wires	
0.5	36.0	36.7	–
0.75	24.5	24.8	–
1	18.1	18.2	–
1.5	21.1	12.2	–
2.5	7.41	7.56	–
4	4.61	4.70	7.41
6	3.08	3.11	4.61
10	1.83	1.84	3.08
16	1.15	1.16	1.91
25	0.727	0.734	1.20
35	0.542	0.529	0.868
50	0.387	0.391	0.641
70	0.268	0.270	0.443
95	0.193	0.195	0.320
120	0.153	0.154	0.253
150	0.124	0.126	0.206
185	0.0991	0.100	0.164
240	0.0754	0.0762	0.125
300	0.0601	0.0607	0.100
400	0.0470	0.0475	0.0778
500	0.0366	0.0369	0.0605
630	0.0283	0.0286	0.0469
800	0.0221	0.0244	0.0367
960	0.0189	0.0189	0.0313
1000	0.0176	0.0177	0.0291
1200	0.0151	0.0151	0.0247
1600	0.0113	0.0113	0.0186
2000	0.0090	0.0090	0.0149

TABLE A.2: Temperature correction factors for d.c. conductor resistance to correct the measured resistance at room temperature to 20 °C. To obtain the maximum resistance of hard-drawn copper conductors, the values for annealed copper conductors should be divided by 0.97

alloy sheaths and no less than 85% plus 0.1 mm for aluminium sheaths. The minimum thickness of the oversheath should also be no less than 85% of the specified nominal thickness, plus 0.1 mm [11].

A.4 Resistivity tests on the semiconducting screens

To monitor these resistive properties, unaged and aged samples of the inner and outer semiconducting screens are tested. The cable is aged by heating the cable sample in an air oven at 10°C above the maximum conductor temperature of the cable in normal

operation for seven durations of 24 hours. The semiconducting screen is then deemed fit for service if both the aged and unaged screens do not exceed 500 Ω/m [11].

A.5 Hot set test for XLPE insulation

This test involves cutting pieces of insulation from the inner, middle and outer part of the sample's insulation. The thicknesses of the test pieces have to be no less than 0.8 mm and no greater than 2.0 mm. The samples are then heated in an oven to 200°C with a 20 N/cm^2 load hanging from the lower surface of the sample. The sample is then kept under these heat and load conditions for 15 minutes. For sufficient cross-linking to have taken place the sample must not elongate more than 175% while under the heat and mechanical stress, and the maximum permanent elongation after cooling should be no more than 15% [11].

A.6 Shrinkage test for XLPE insulation

This test involves taking a 300 mm length of insulation from the sample. The central 200 mm of the sample is marked out with two vertical lines and then the sample supported at each end in an oven set at 130°C for 6 hours. This is used to age the cable. During the test period the sample should not shrink by more than 6% in order for the cable sample to pass this test [11].

A.7 Cross-linking by product concentration

To measure the change in weight and therefore the amount of cross-linking, 20 mg cubes of insulation can be heated to a temperature of 175°C for 30 minutes. If sufficient cross-linking has occurred the total mass should not reduce by more than 1.6%; the average rate of change of mass should be less than 0.18%min^{-1} over the first five minutes of the test; and between 15 minutes and 30 minutes the rate of change of the sample should be less than 0.015%min^{-1}.

A.8 Measurement of capacitance

The capacitance is measured between the conductor and the metallic sheath. For a cable to comply with the manufacturer's specification, the measured value should not exceed the specified value by more than 8%.

Appendix B

Scintillating Screen and CCD Array Comparison Chart

Feature	Marconi (CCD42-40)	Photonic Scince (Sony ICX285AL)	Hamamatsu (C4880-50)	Hamamatsu ORCA-ER	Hamamatsu ORCA-HR
Pixel Size (µ)	13.5	6.45	13.0	6.45	5.9
Pixel Format	2048 x 2048	1392 x 1040	1024 x 1024	1280 x 1024	4000 x 2624
Array Area (mm)	27.6 x 27.6	8.98 x 6.71	13.3 x 13.3	8.67 x 6.45	23.6 x 15.5
Taper	01:01	1.61:1	01:01	1.6:1	2.0:1
Image Pixel Size (µm)	13.5	10.36	13.0	10.0	11.8
Image Area (mm)	27.6 x 27.6	14.4 x 10.8	13.3 x 13.3	13.4 x 10.0	47.2 x 31.0
Readout Method	Full Frame	Interline scan	Full Frame	Interline scan	Interline scan
Quantum Efficiency (@550 nm)	92%	65%	80%	70%	50%
Full Well Capacity	100 000	n/a	80 000	18 000	13 300
Readout Noise (e rms)	3	n/a	4	8	13
Dynamic Range	33 333:1	n/a	20 000:1	2 250:1	1 000:1
Digitisation	12 bit	12 bit	16 bit	12 bit	12 bit

TABLE B.1: Specifications of the currently available scintillating screen and CCD array x-ray cameras

Appendix C

New Inspection Facility Designs

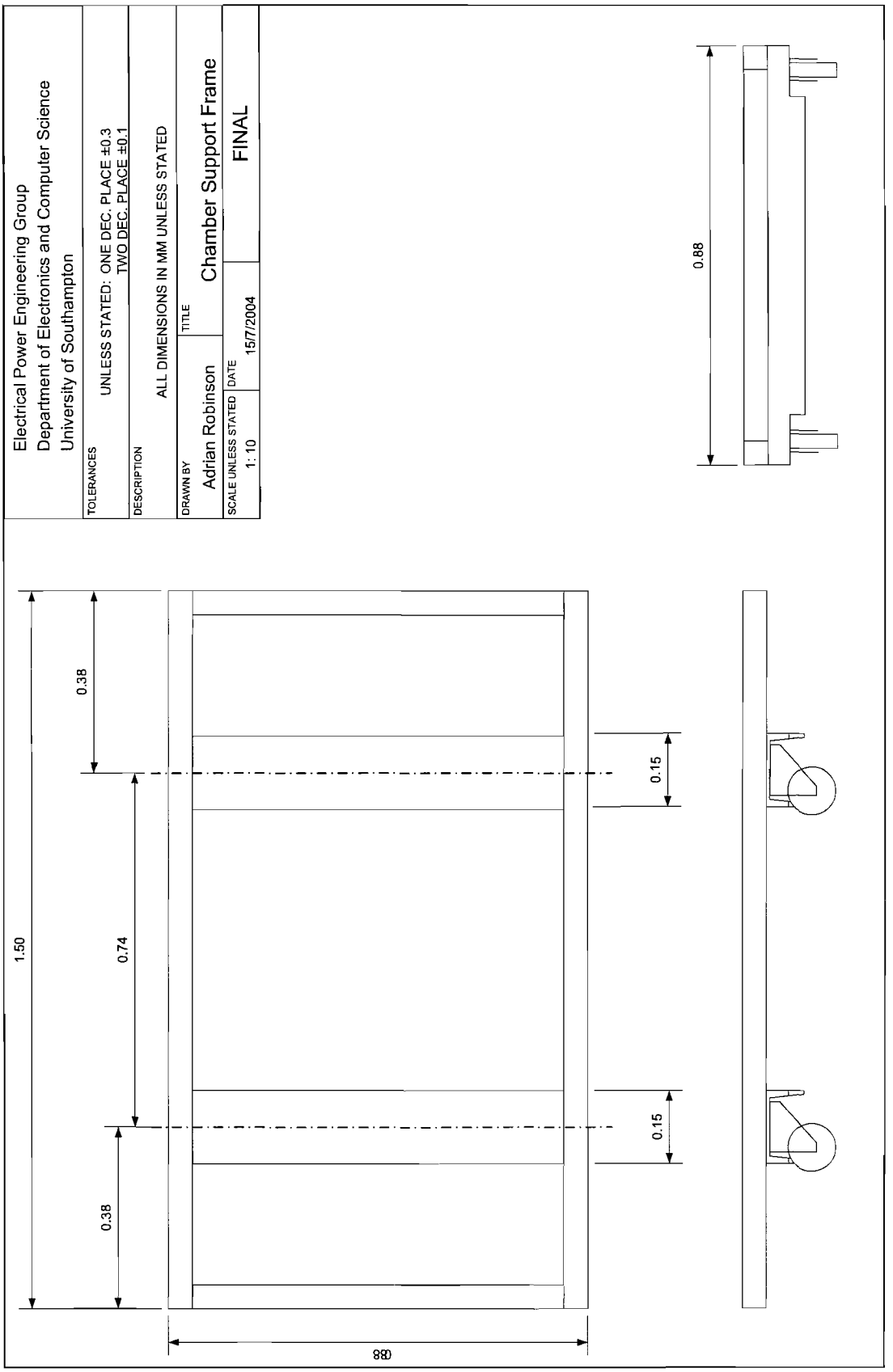

FIGURE C.1: The irradiation chamber support frame.

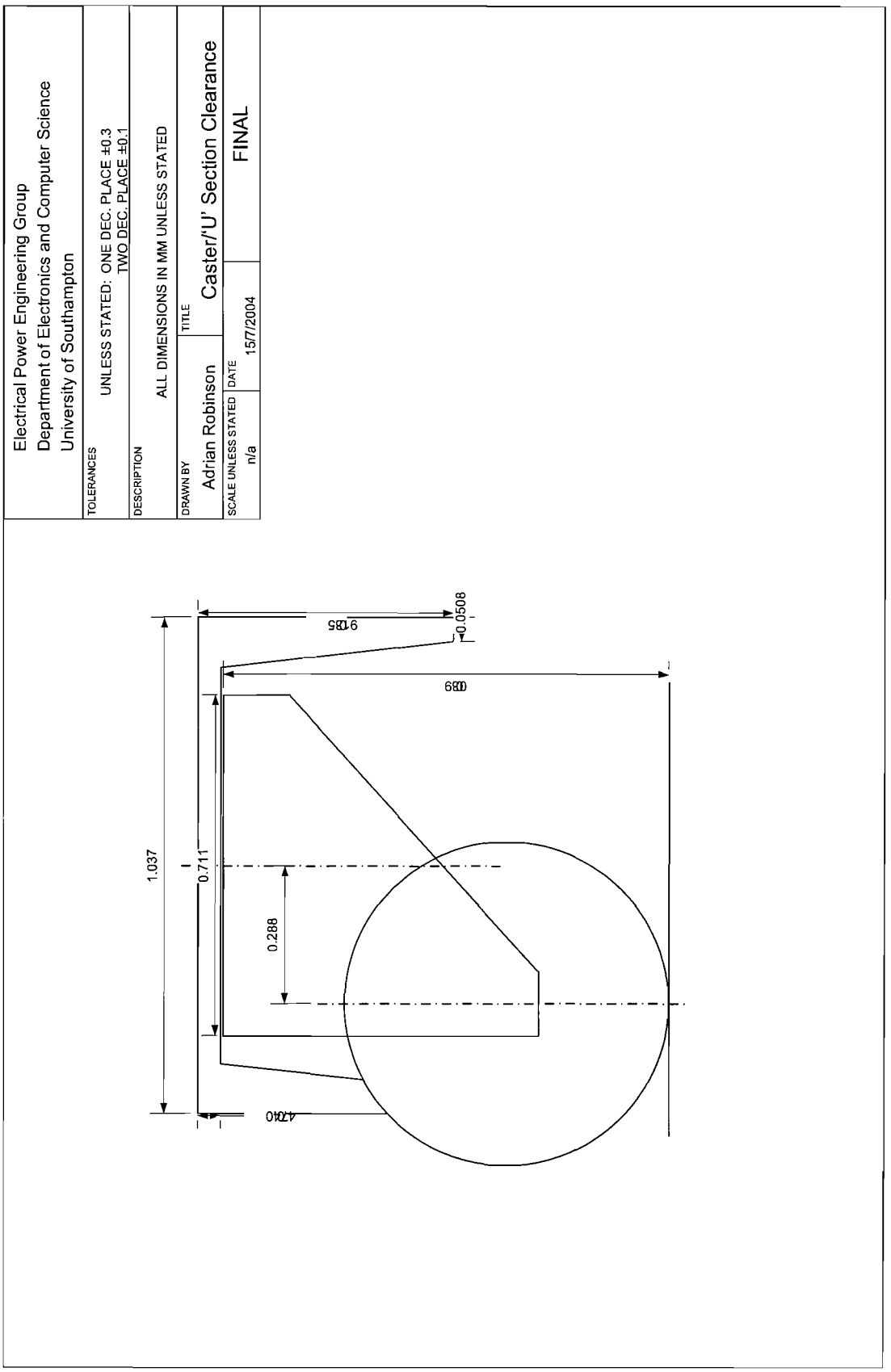

FIGURE C.2: The modification to the 'U' of the support frame required to allow free movement of the casters.

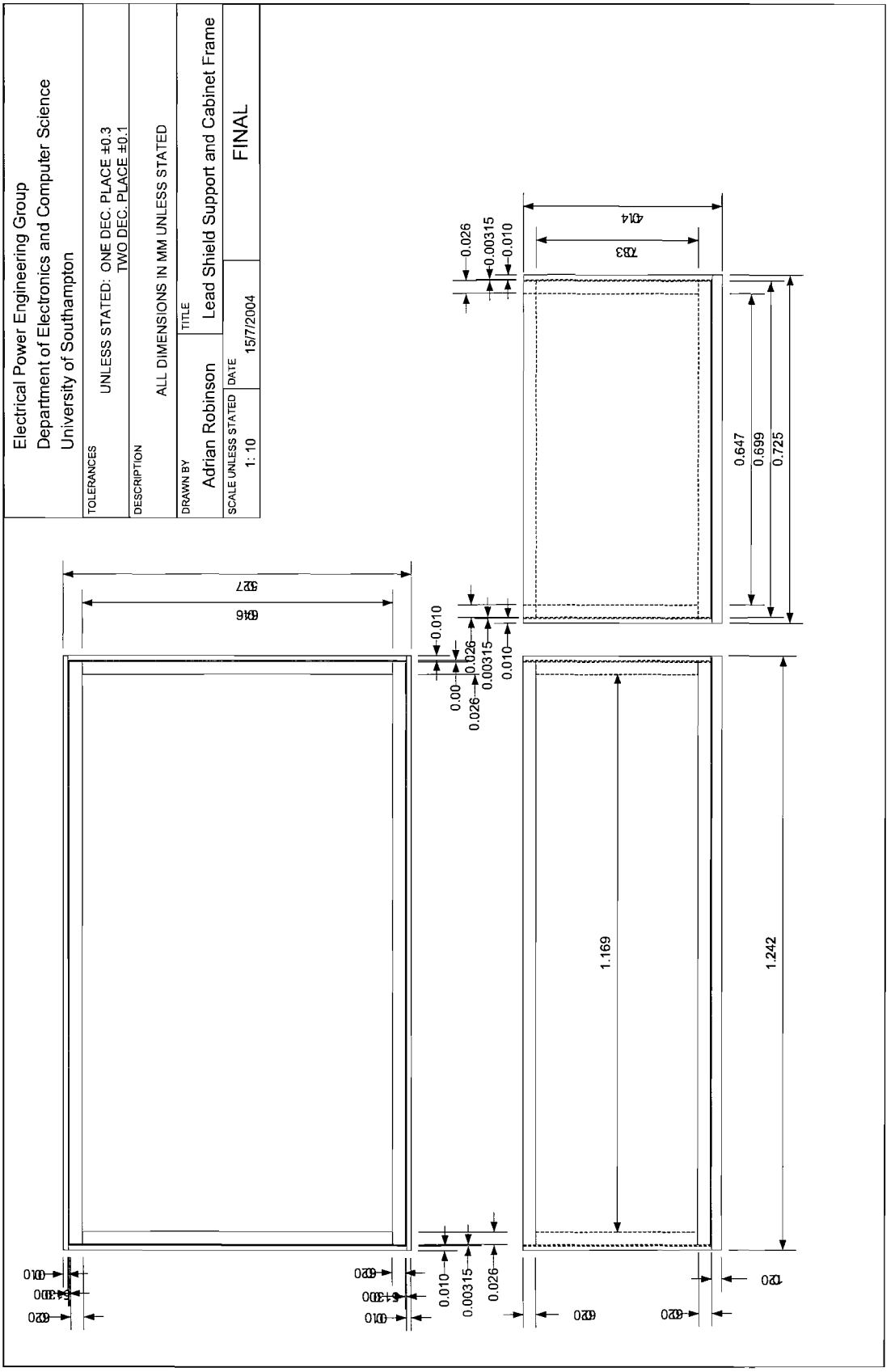

FIGURE C.3: The box frame used to support the lead shielding.

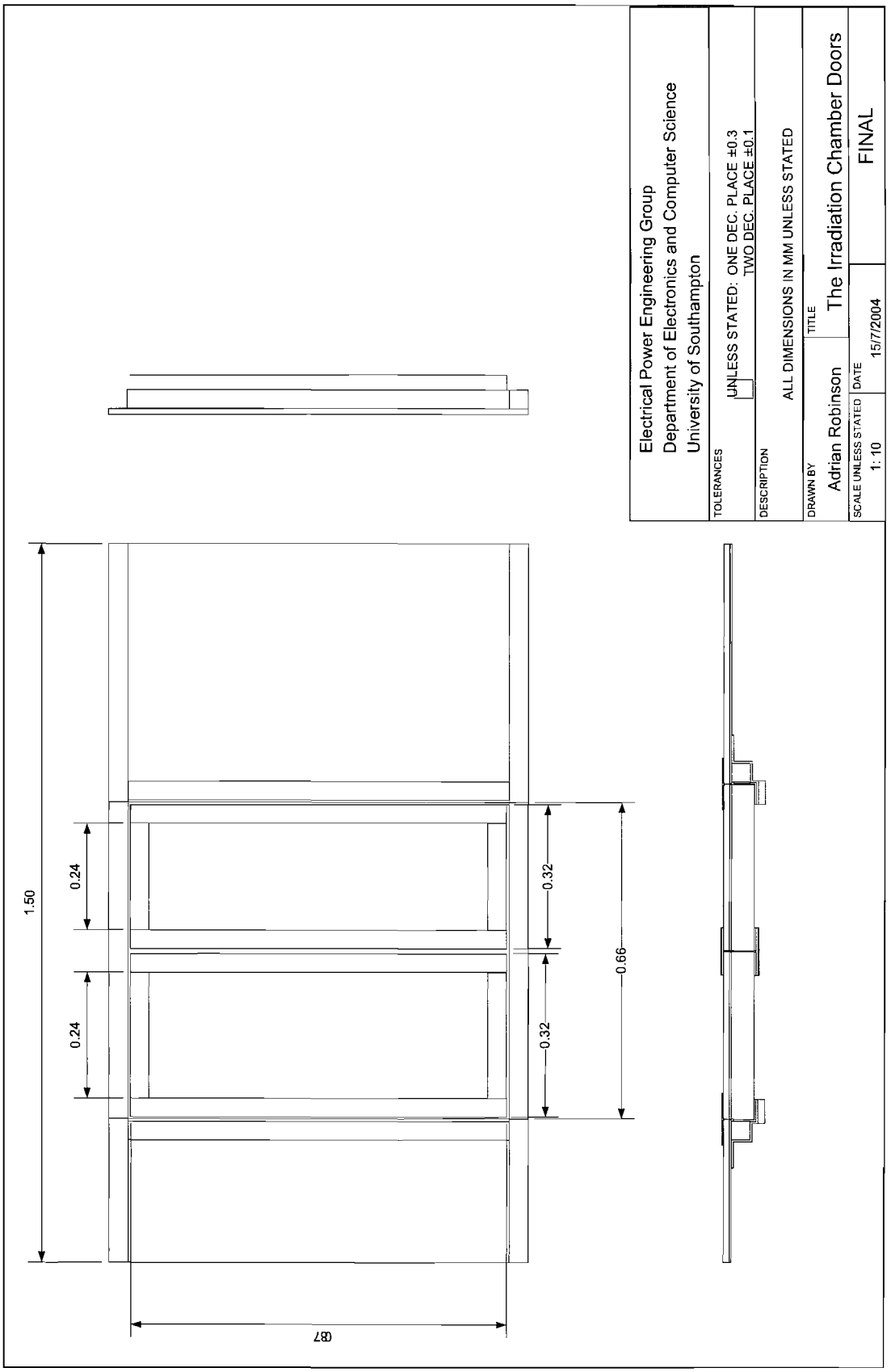

FIGURE C.4: The top of the cabinet and cabinet doors.

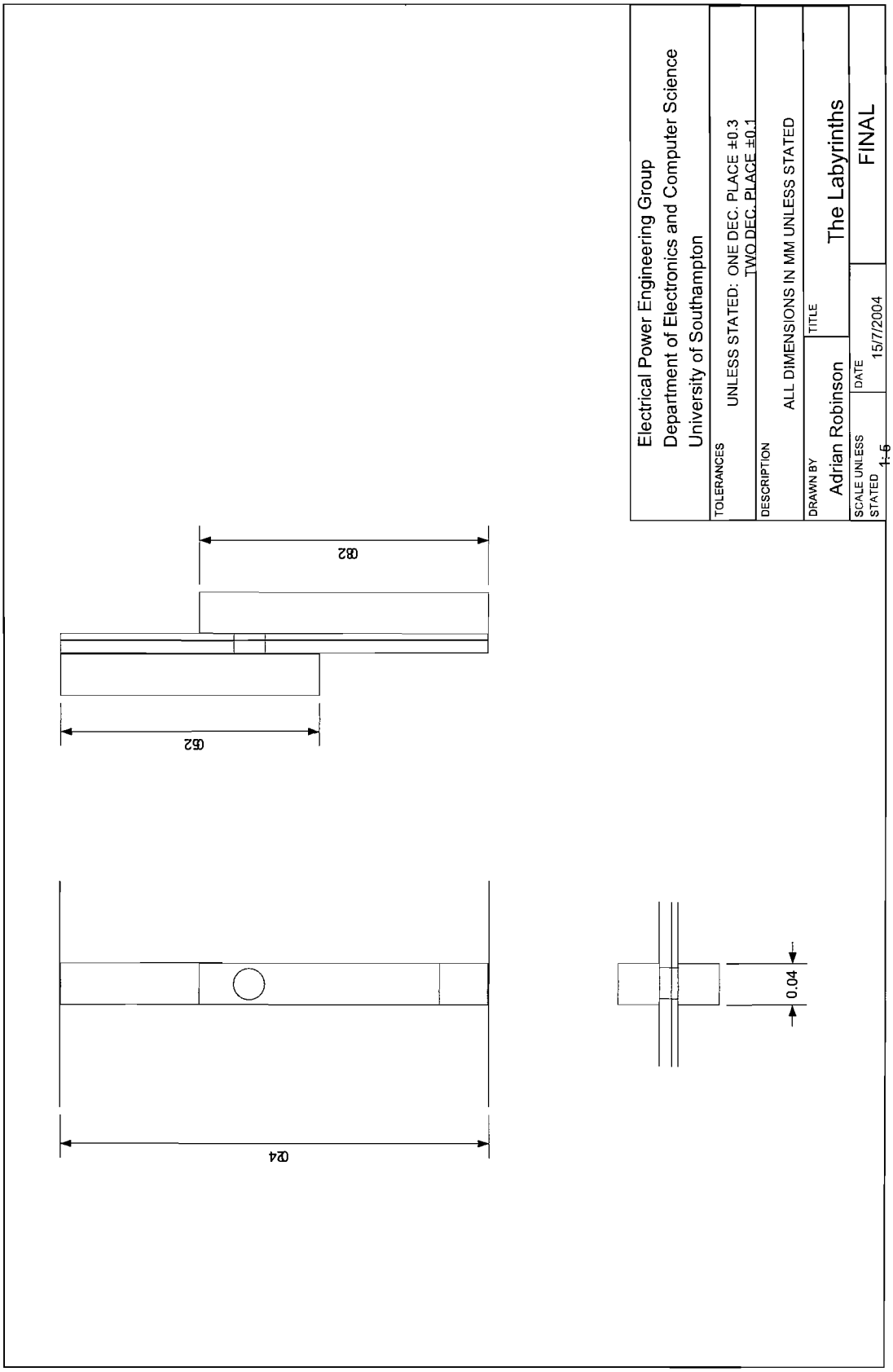

FIGURE C.5: The services labyrinth.

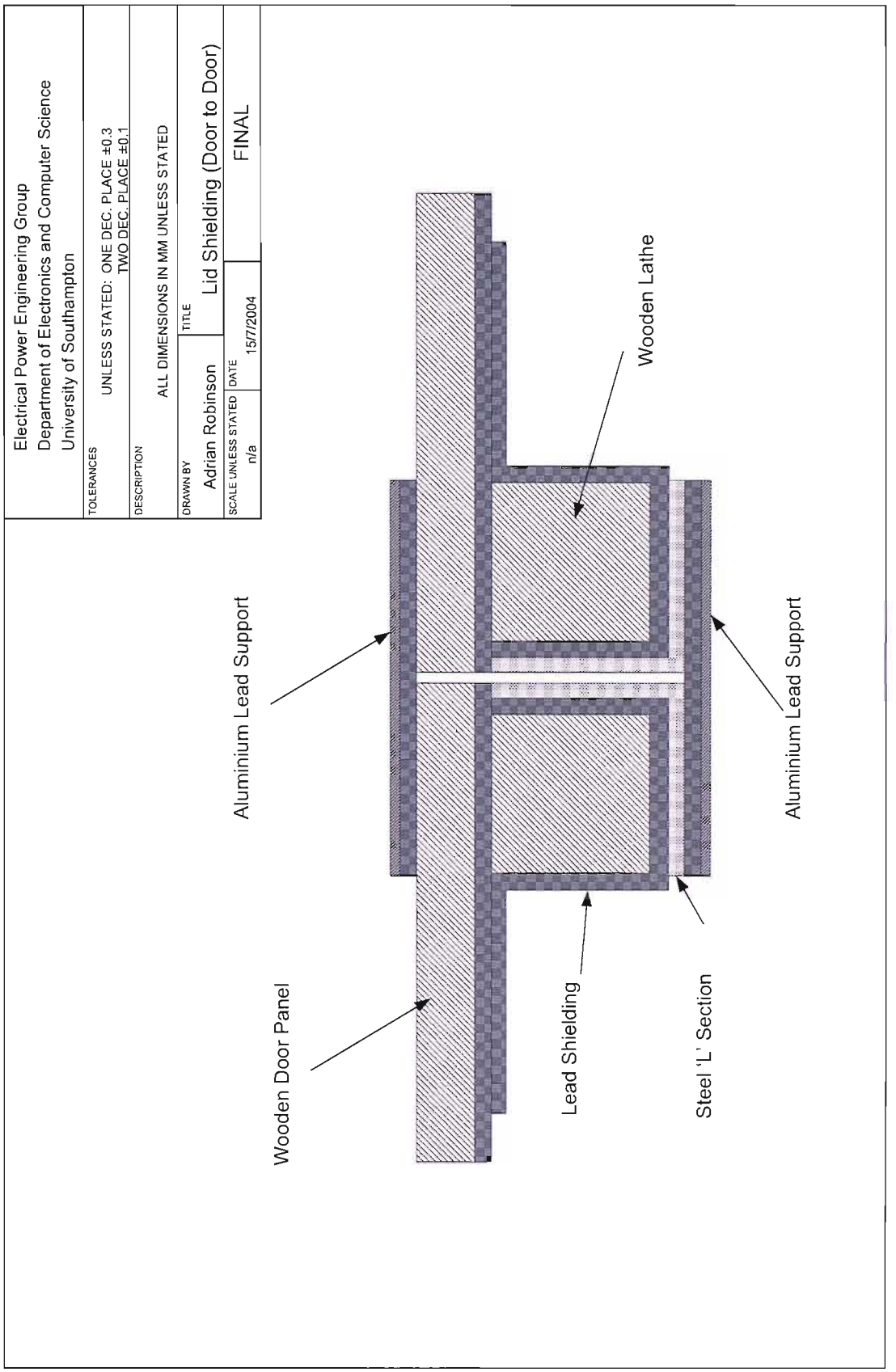

FIGURE C.6: Lead shielding around door to door interface.

FIGURE C.7: Lead shielding around door hinge edge.

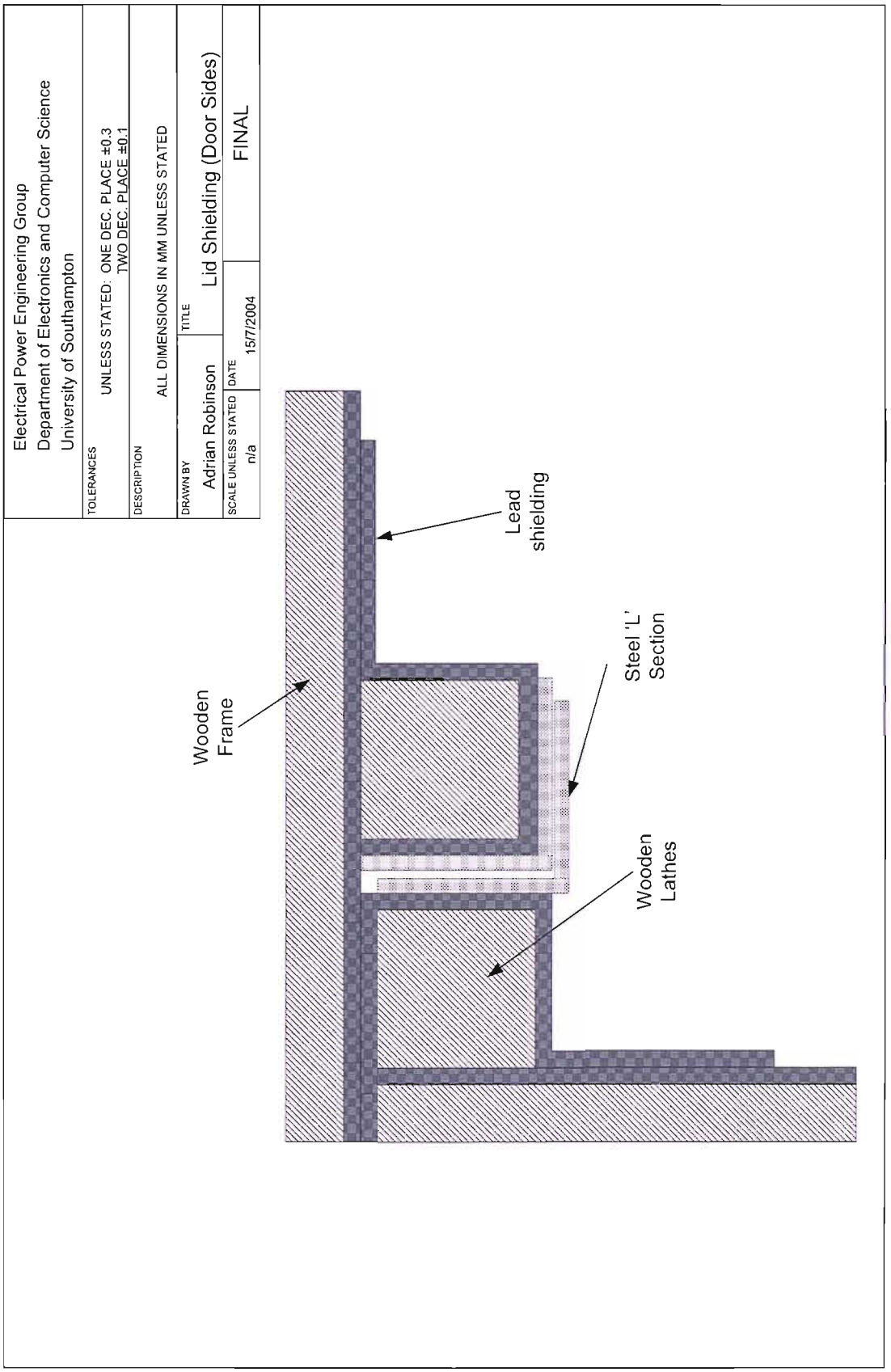

FIGURE C.8: Lead shielding around door side edges.

FIGURE C.9: The microswitch mounts.

Electrical Power Engineering Group
Department of Electronics and Computer Science
University of Southampton

TOLERANCES	UNLESS STATED: ONE DEC. PLACE ±0.3 TWO DEC. PLACE ±0.1
DESCRIPTION	ALL DIMENSIONS IN MM UNLESS STATED
DRAWN BY: Adrian Robinson	TITLE: Microswitch Configuration
SCALE UNLESS STATED: 1: 10	DATE: 15/7/2004
	FINAL

FIGURE C.10: The microswitch configuration.

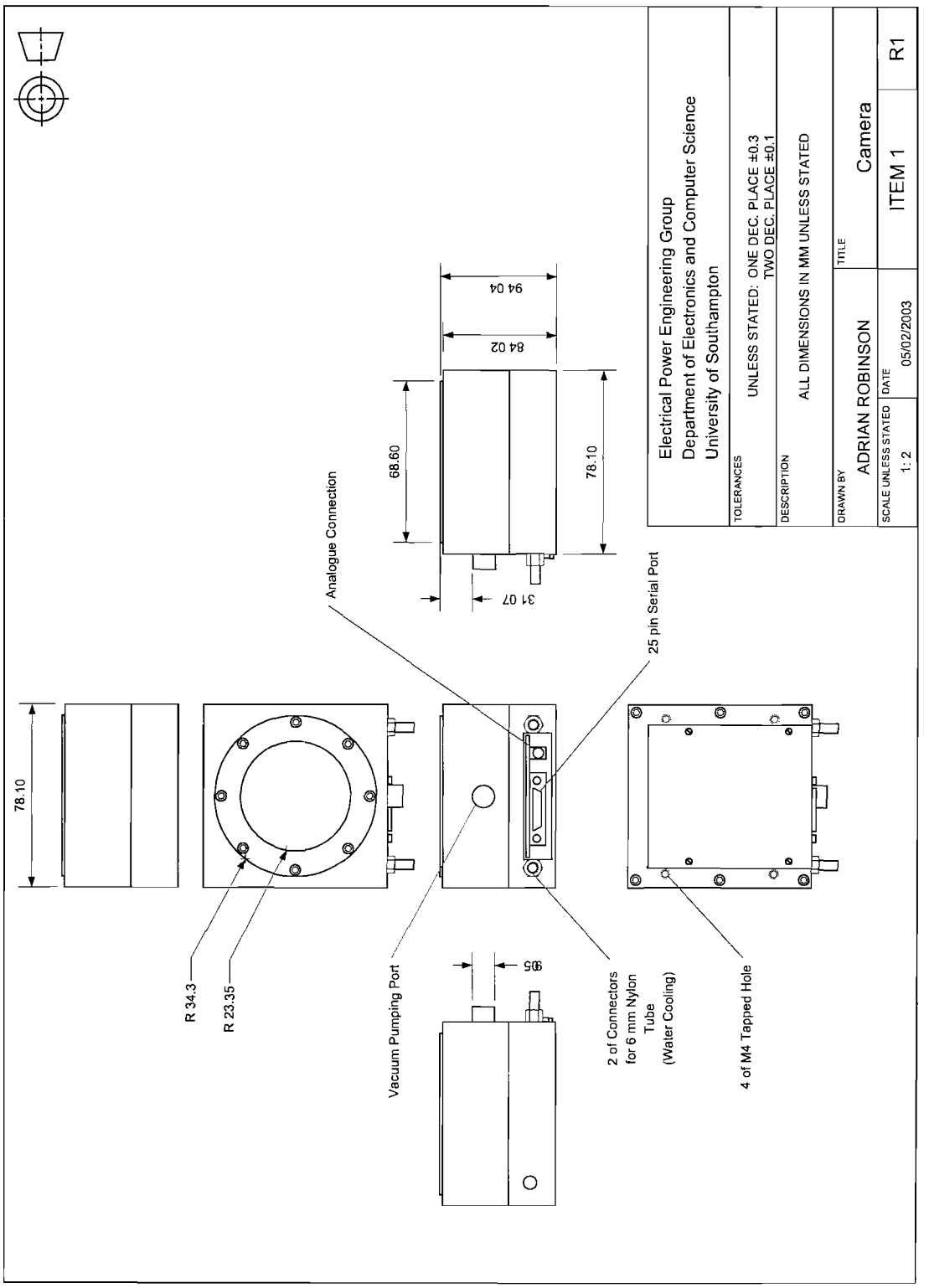

FIGURE C.11: The X-CAM x-ray CCD camera.

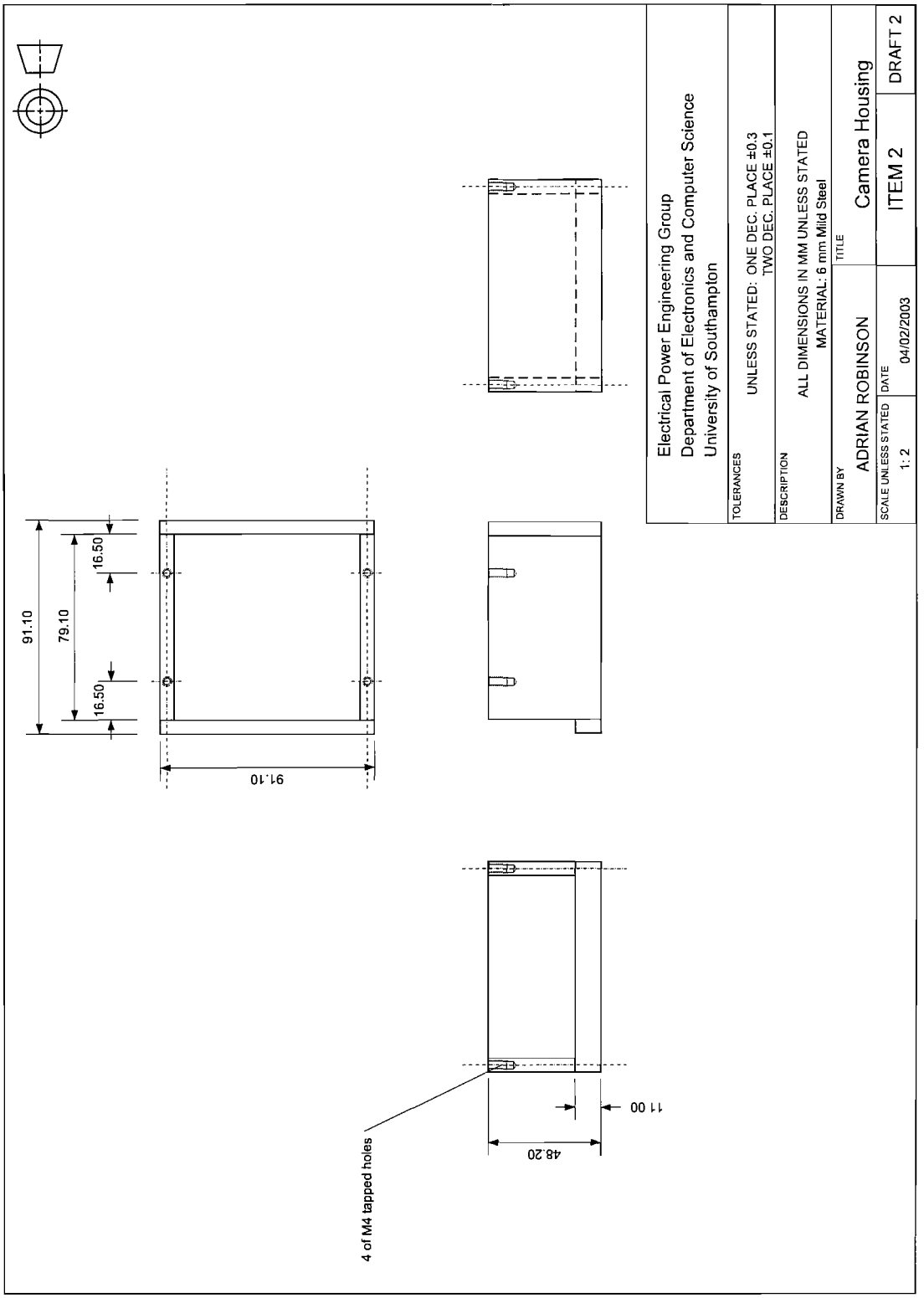

FIGURE C.12: The intermediate irradiation chamber camera housing.

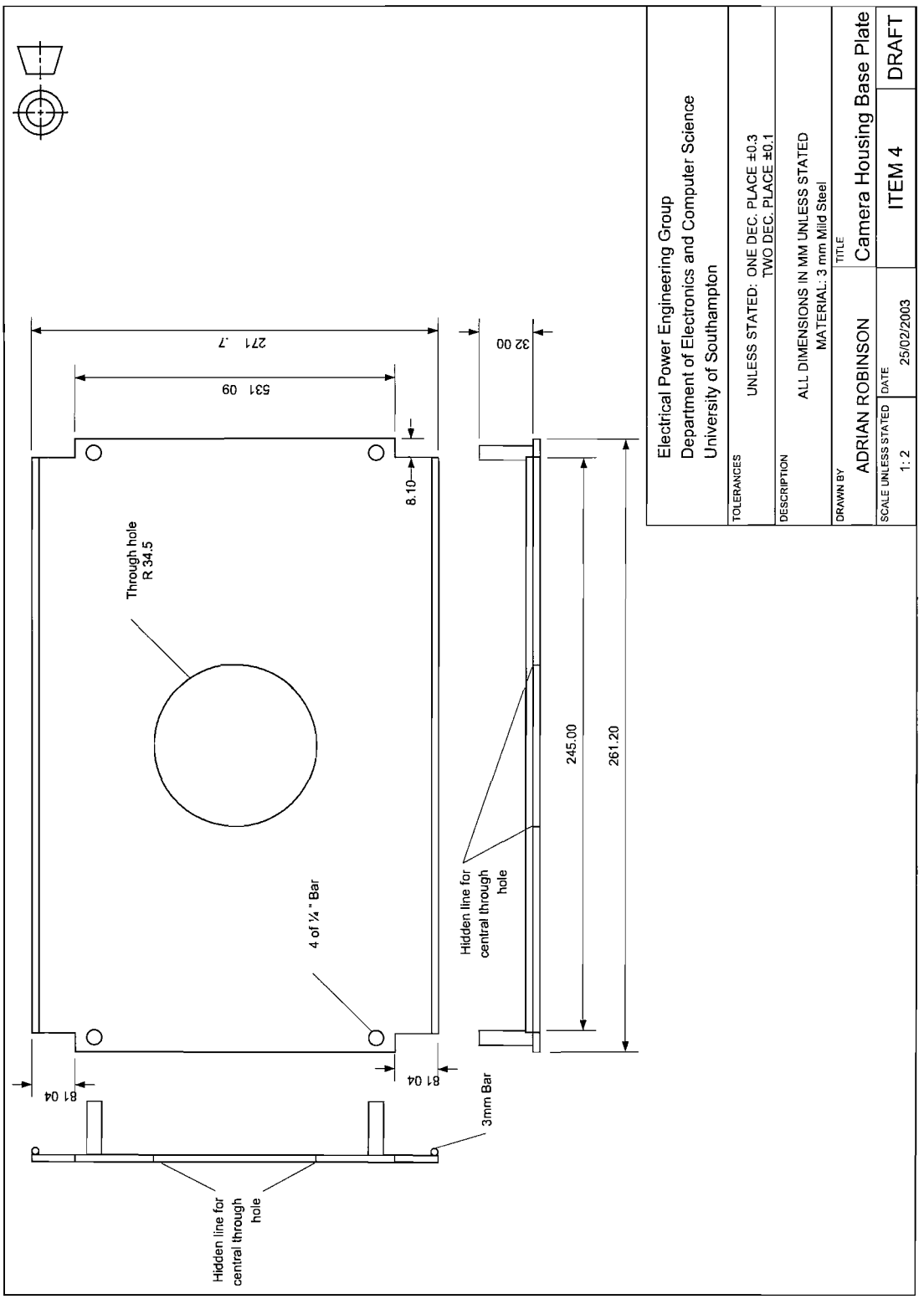

FIGURE C.13: The intermediate irradiation chamber camera housing baseplate.

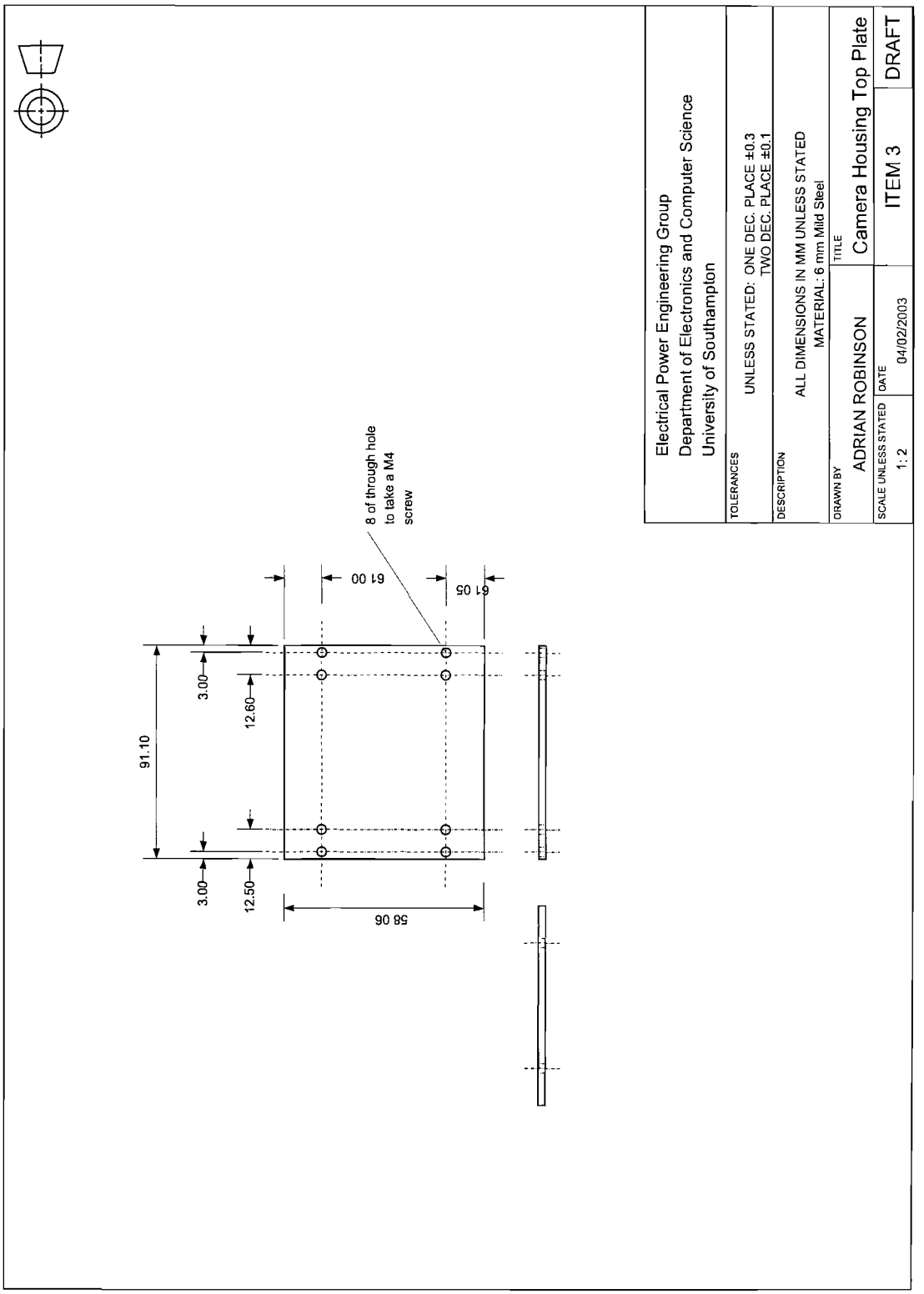

FIGURE C.14: The intermediate irradiation chamber camera housing top plate.

Appendix D

Irradiation Chamber Safety Control and Warning Systems

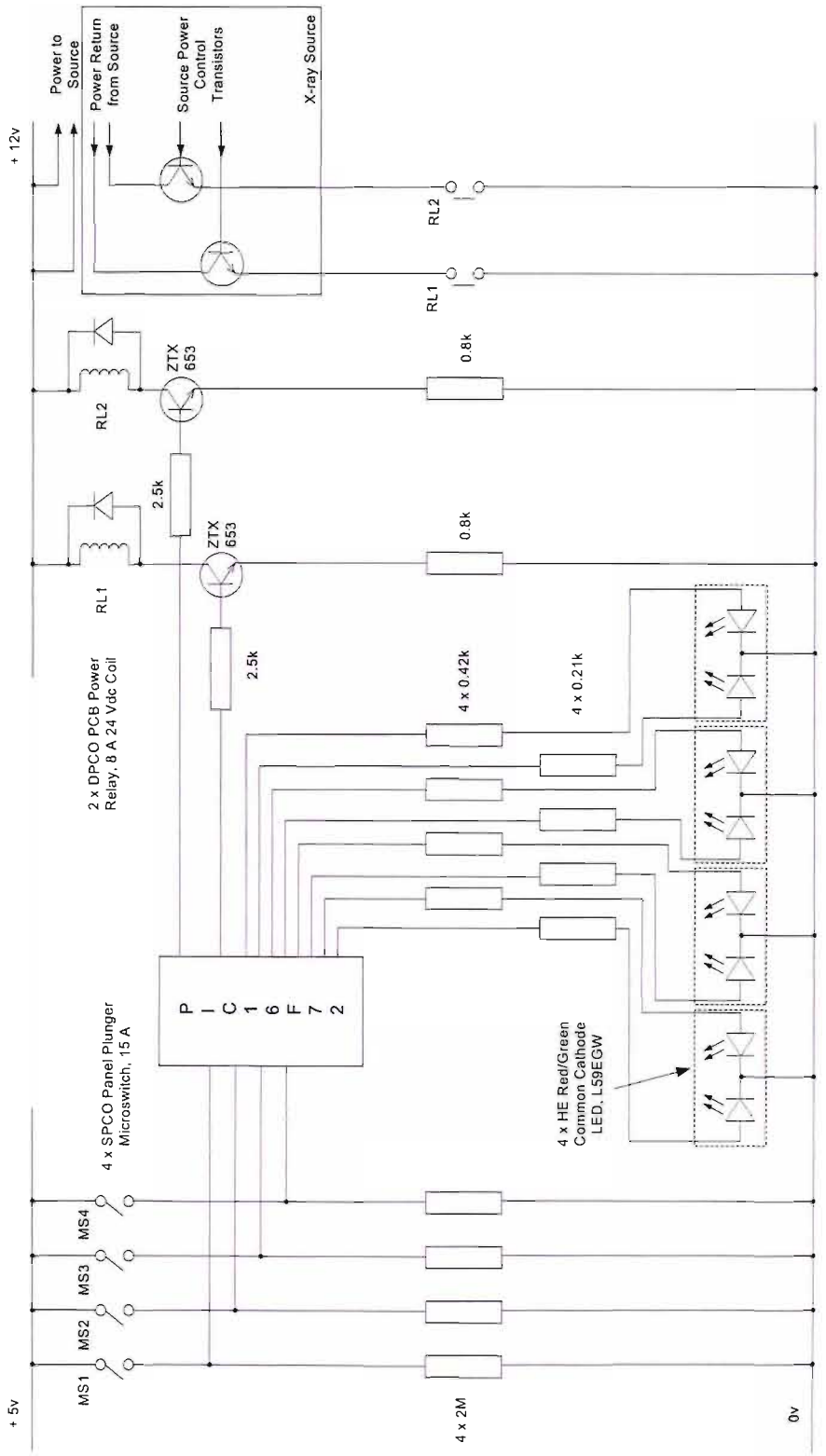

FIGURE D.1: The circuit diagram of the x-ray source power and safe working conditions management.

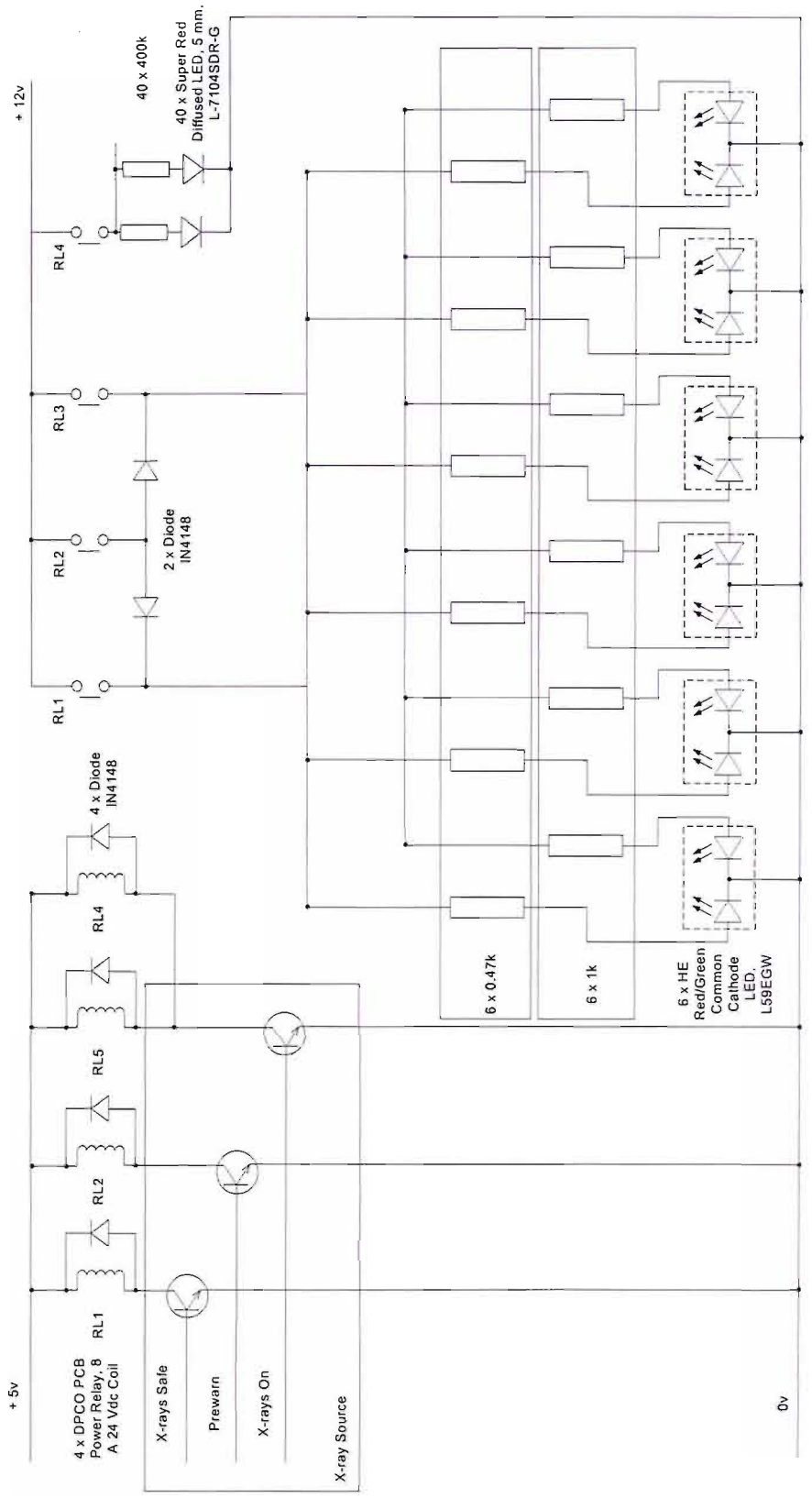

FIGURE D.2: The circuit diagram of the x-ray source warning lamps.

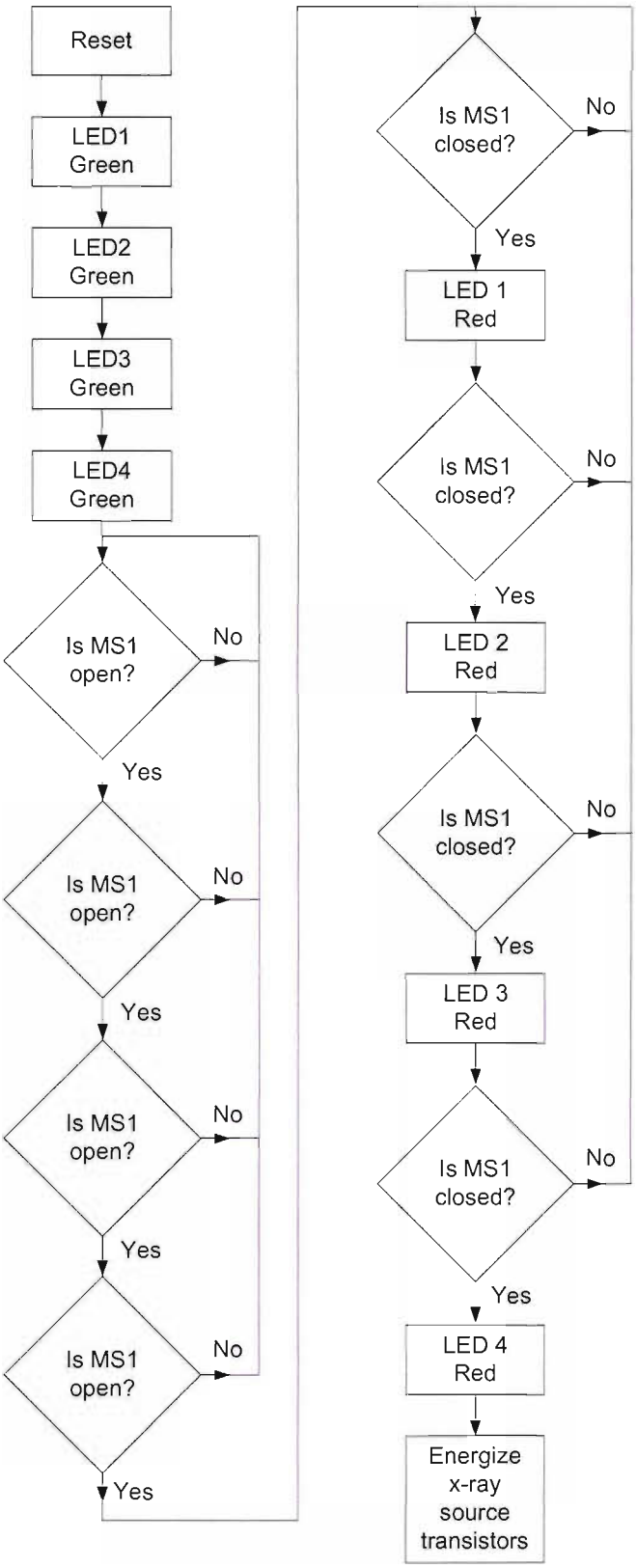

FIGURE D.3: The flow chart of the safety control of the new irradiation chamber.

Appendix E

Program Flow Charts

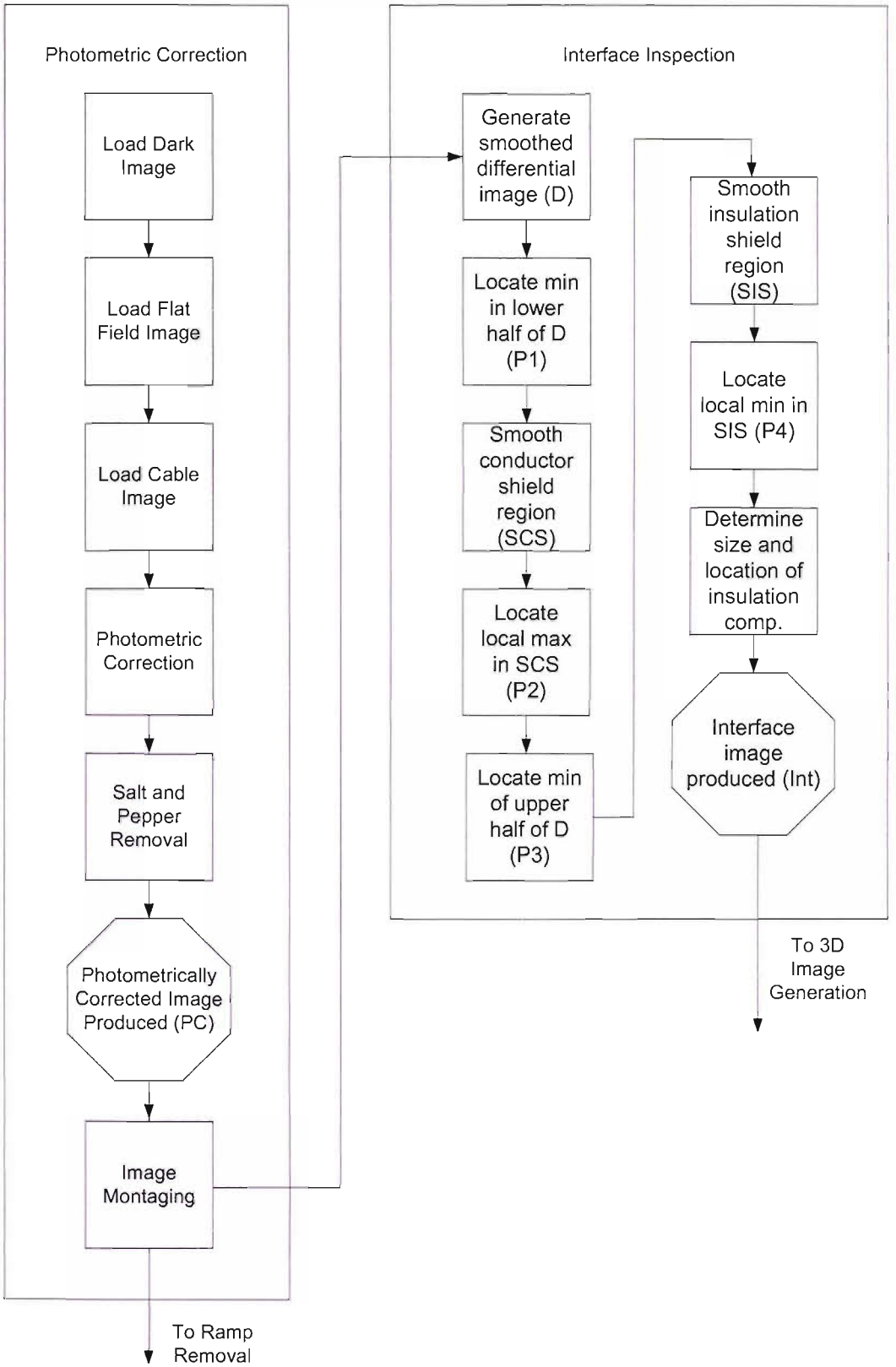

FIGURE E.1: Photometric correction and interface inspection

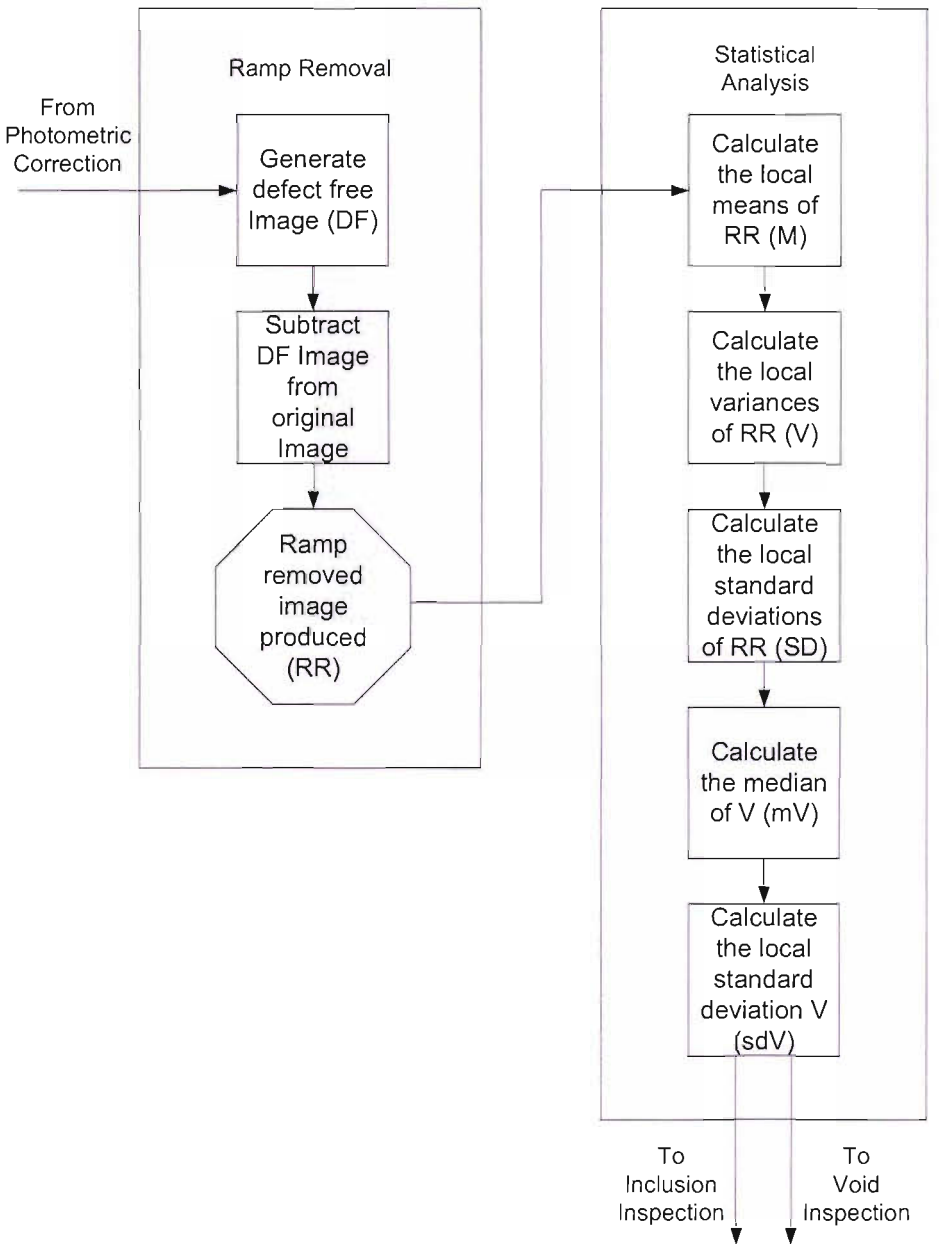

FIGURE E.2: Non defect image data removal and statistical image analysis

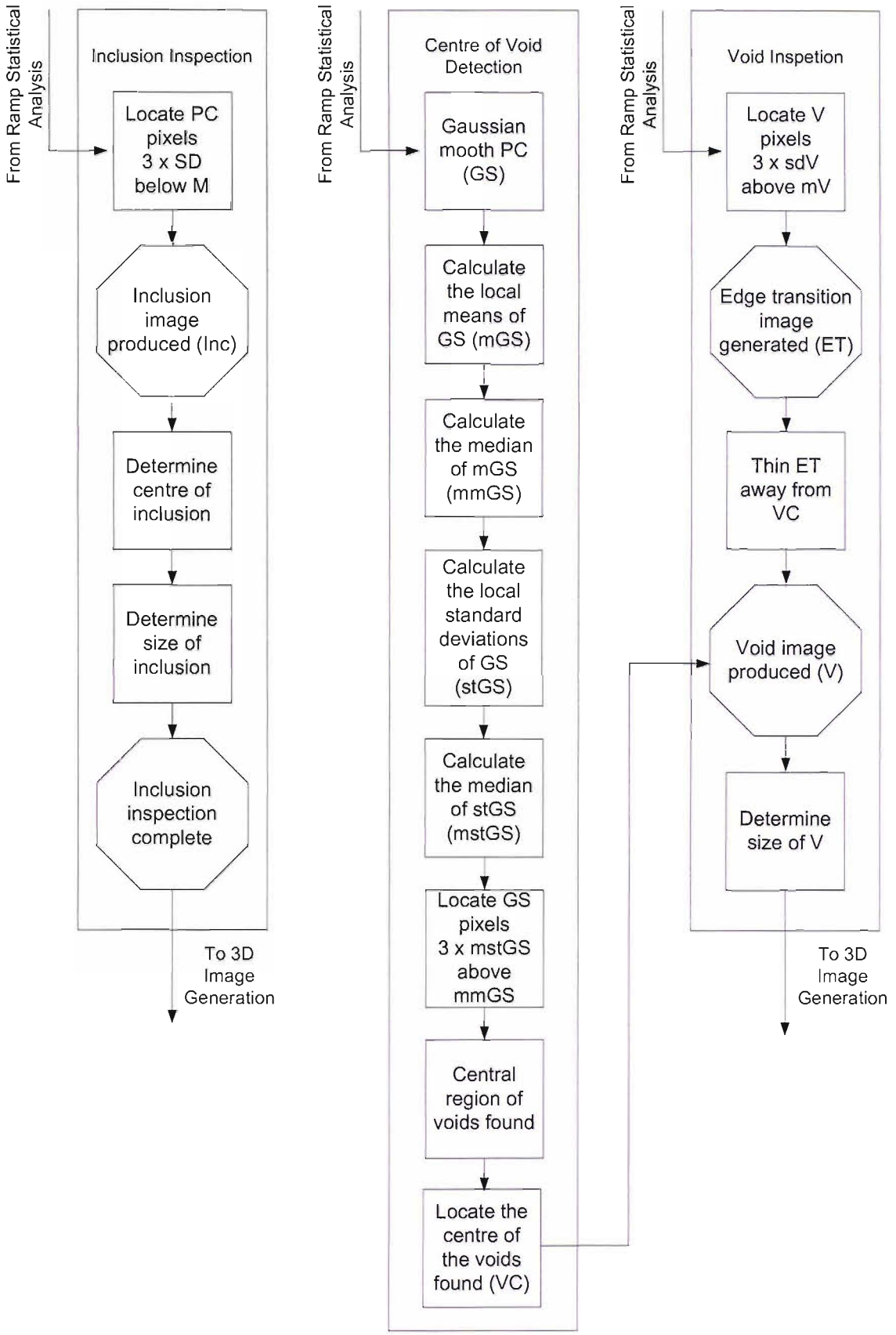

FIGURE E.3: Inclusion and void detection

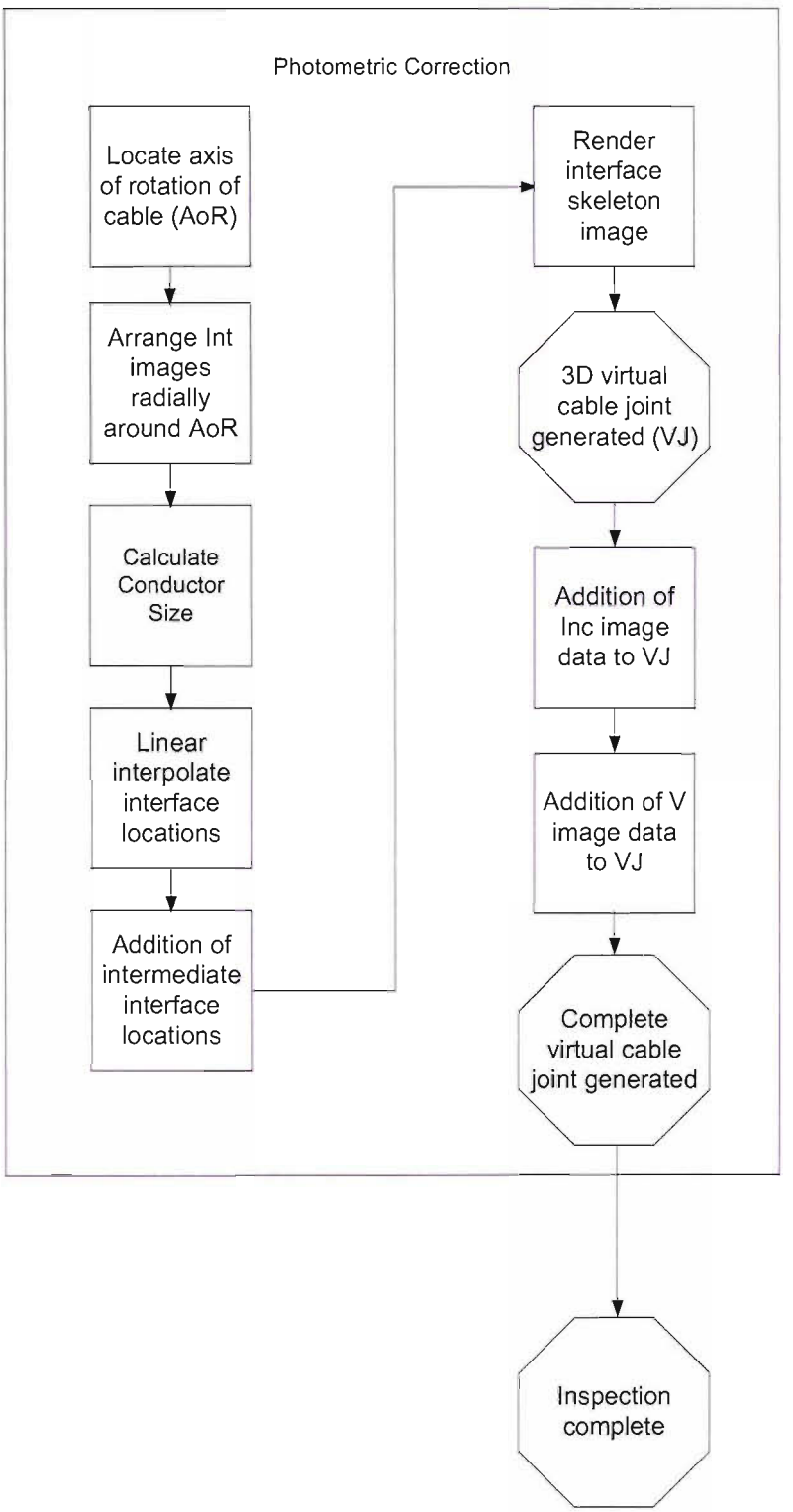

FIGURE E.4: Virtual 3D cable joint generation

Appendix F

New Inspection Facility Assessment of Risk Form

Assessment of Risk

School of Electronics and Computer Science

Description of work activity: Inspection of cable joint insulation systems using x-rays

Area: The Tony Davis High Voltage Lab		Assessed By:				Expiry / Review:
Building:	20	Name:	Paul Lewin			Date:
Room:	Main Hall	Signed:		Date:		

Hazard	Those Exposed	Existing Controls to Risk	Further Action Required[1]
X-rays	Operator	The x-ray source is housed in a lead-lined irradiation chamber. The x-rays are confined to the irradiation chamber by the lead shielding. To prevent the x-ray source being energised with one of the chamber doors open, microswitches are strategically positioned so that the power to the x-ray source is isolated if either door is opened. The services to and from the x-ray source and CCD camera pass through a lead-lined labyrinth, maintaining the shielding integrity. There is an "X-RAYS" on sign that is illuminated when the source is energised to alert the operator that the source is energised. There is also a pre-warning bank of LED's to alert the operator that the source is about to be energised. The operator must regularly check the integrity of the lead shielding while the x-ray source is energised using a Geiger counter.	None
Electric Shock	Operator	All equipment is either double insulated or earthed. All equipment is regularly safety tested.	None
Heavy Apparatus	Operator	The irradiation chamber is heavy and can be difficult to move. Care must be taken to avoid injury when attempting to move the cabinet. The hinged cabinet doors are also heavy. Care should be taken when opening and closing these doors.	None
Trip Hazards	Operator	The irradiation chamber is connected to the control PC, a water chilling unit, a vacuum pump, and the CCD array control hardware. The trip hazard caused by these connections has been reduced by ensuring they do not impinge on any walk ways.	None
Lead Poisoning	Operator	The internal surfaces of the irradiation chamber are lead lined. Should the operator need to touch these areas, either gloves should be worn or the operator's hands should be thoroughly washed afterwards.	None

[1] ***n.b. work cannot proceed until above actions are complete***

I agree to abide by the precautions set out above	**Name:**	
	Signed:	**Staff/Student No:**
	Date:	Copy sent to the School Safety Advisor

FIGURE F.1: Assessment of Risk Form.

Bibliography

[1] G. F. Moore. *Electrical Cables Handbook.* Blackwell Science Ltd, 3 edition, 1997.

[2] K. Suzuki, S. Saito, and S. Yoshida. Power cable insulation. *IEEE Transactions on Electrical Insuation*, 21(6):945–52, December 1986.

[3] A. Farkas and U. Nilsson. Development of insulating materials for improved cable performance. *Power Technology International*, pages 277–8,230, 1989.

[4] J. L. Parpal, R. Awad, M. Choquette, J. Becker, L. Hiivala, S. Chatterjee, T. Kojima, R. D. Rosevear, and O. Morelli. Successful testing of 345-kv xlpe cables and premolded joints at ireq. *IEEE Transactions on Power Delivery*, 12(2):547–50, April 1997.

[5] A. Ross. High voltage polymeric insulated cables. *Power Engineering Journal*, 1 (1):51–8, Jan 1987.

[6] A. J. Cantor, P. K. Cheo, M. C. Foster, and L. A. Newman. Application of submillimeter wave laser to high voltage cable inspection. *IEEE Journal of Quantum Electronics*, 17:447–89, 1981.

[7] Y. F. F. Ho. *Space Charge Measurements of XLPE - A Comparison of AC and DC Stressing.* PhD thesis, Department of Electronics and Computer Science, University of Southampton, 2001.

[8] W. G. Lawson, M. Rechowicz, and S. J. Rigby. Developing crosslinked polyethylene cables for high voltage power transmission. *Electronics and Power. Journal of the Institute of Electrical Engineers*, 24(2):116–20, Feb 1978.

[9] J. C. Chan, E. T. Cometa, M. D. Hartley, and L. J. Hiivala. Field failure analysis of medium voltage xlpe - insulated power cables. In *Conference Record of the 1990*

IEEE International Symposium of Electrical Insulation, pages 277–80, Toronto, Canada, June 1990. IEEE.

[10] International Electrotechnical Comission Standard IEC 60502-4. Power cables with extruded insulation and their accessories for rated voltages from 1 kv (um = 1,2 kv) up to 30 kv (um = 36 kv) - part 4: Test requirements on accessories for cables with rated voltages from 6 kv (um = 7,2 kv) up to 30 kv (um = 36 kv), February 2005.

[11] International Electrotechnical Comission Standard IEC 60840. Power cables with extruded insulation and their accessories for rated voltages above 30 kv (um = 36 kv) up to 150 kv (um = 170 kv) - test methods and requirements, April 2004.

[12] International Electrotechnical Comission Standard IEC 62067. Power cables with extruded insulation and their accessories for rated voltages above 150 kv (um = 170 kv) up to 500 kv (um = 550 kv) - test methods and requirements, October 2001.

[13] S. Hiyama and Y. Fujiwara. Testing methods for power cable insulation. *IEEE Transactions on Electrical Insulation*, 21(6):1051–6, Dec 1986.

[14] International Electrotechnical Comission Standard IEC 60228. Conductors of insulated cables, November 2004.

[15] M. S. Mashikian, R. Bansal, and R. B. Northrop. Locaiton and characterization of partial discharge sites in shielded power cables. *IEEE Transactions on Power Delivery*, 5(2):833–9, 1990.

[16] W. L. Weels and J. P. Steiner. Instrumentation for the detection and location of incipient faults on power cables. *IEEE Transactions on Power Apparatus and Systems*, 101:2328–35, 1982.

[17] S. A. Boggs. Partial discharge: Overview and signal generation. *IEEE Electrical Insulation Magazine*, 6:33–9, 1990.

[18] R. T. Harrold. Acoustical technology applications in electrical insulation and dielectrics. *IEEE Transactions on Electrical Insulation*, 20(1):3–19, 1985.

[19] D. W. Auckland, A. J. McGrail, C. D. Smith, B. R. Varlow, J. Zhao, and D. Zhu. Application of ultrasound to the inspection of insulation. *IEE Proceeding - Science, Measurement, and Technology*, 143(3):177–81, 1990.

[20] A. McGrail, A. Risino, D. W. Auckland, and B. R. Varlow. Use of a medical ultrasonic scanner for the inspection of high voltage insulation. *IEE Electrical Insulation Magazine*, 9(6):5–10, November/December 1993.

[21] D. W. Auckland, B. R. Varlow, and C. Maloney. Ultrasonic detection of insulation degradation. *IEE Proceeding - Science, Measurement, and Technology*, 137(6): 356–60, 1990.

[22] J. Pope. *Medical Physics: Imaging.* Heinemann, 1998.

[23] D. W. Auckland, C. D. Smith, and B. R. Varlow. Application of ultrasound to the ndt of solid insulation. *IEE Proceeding - Science, Measurement, and Technology*, 141:20–4, 1994.

[24] P. Blumler and G. Salge. Nuclear magnetic resonance imaging of morphological changes during electrical treeing in polyethlyene due to partial discharges. In *IEEE International Conference on Conduction and Breakdown in Solid Dielectrics*, pages 168–72, Vasteras, Sweden, June 1998.

[25] C. Cornelissen and A. Schnettler. Non-destructive diagnostic facilities for cable systems. In *IEEE International Symposium on Electrical Insulation*, pages 557–60, Boston, MA USA, April 2002.

[26] C. Cornelissen, Weismath, A. Schnettler, and Blumich. Ultrasound and nuclear magnetic resonance for non-destructive diagnostics of cable systems. In *IEEE International Conference on Properties and Applications of Dielectric Materials*, pages 557–60, Nagoya, June 2002.

[27] C. Nicholls. Introduction to nmr methods for ndt. In *IEE Colloquim on NMR/MRI used in NDT*, pages 1–3, London, UK, February 1994.

[28] J. Blitz, W. G. King, and D. G. Rogers. *Electrical, Magnetic, and Visual Methods of Testing Materials.* Butterworths, London, 1969.

[29] R.R. Peeters, P. Kornprobst, M. Nikolova, S. Sunaert, T. Vieville, G. Malandain, R. Deriche, O. Faugeras, M. Ng, and P. Van Heckel. The use of super-resolution

techniques to reduce slice thickness in functional mri. *International Journal of Imaging Systems and Technology*, 14(3):131–8, 2004.

[30] P. Glover and P. Mansfield. Limits to magnetic resonance microscopy. *Reports on Progress in Physics*, 65(10):1489–511, October 2002.

[31] E. R. Davies. *Machine Vision: Therory, Algorythms, Practicalities.* Accademic Press, 1990.

[32] J. D. Farina, R. A. Rubino, and P. K Cheo. Industrial far-infrared lasers for inspection and quality control. In *5th IEEE/OSA Conference on Lasers and Electro-Optics*, pages 282–4, Baltimore, MD, USA, 1985.

[33] P. K. Cheo. Far-infrared laser scanner for high voltage cable inspection. *Infrared and Millimeter Waves - Electromagnetic Waves in Matter*, 12(2):279–314, 1984.

[34] Far-infrared cable inspection laser. *Electrical Power Research Institute*, EL-7455: 72, 1991.

[35] P. K. Cheo, J. R. Dunphy, M. C. Foster, R. W. Gagnon, L. G. Puffer Jr., and B. B. Silverman. A far-infrared laser scanner for high-voltage cable inspection. Technical report, Electric Power Research Institute, Oct 1982.

[36] Members of the Industrial Radiology Group of the Institute of Physics. *Handbook of Industrial Radiology.* Edward Arnold & Co, London, 1944.

[37] E. P. Bertin. *Principles and Practice of X-Ray Spectrometric Analysis.* Plenum Press, 1979.

[38] J. G. Brown. *X-rays and Their Applications.* Iliffe Books Ltd, 1966.

[39] R. H. Herz. *The Photographic Action of Ionizing Radiations.* Wiley-Interscience, New York, 1969.

[40] W. J. Meredith and J. B. Massey. *Fundamental Physics of Radiology.* Wright, Bristol, 2 edition, 1972.

[41] R. E. Jacobson. Photographic processes-1890 to the present day. *Journal of Photographic Science*, 39(2):70–6, 1991.

[42] Health and Safety Excutive. Approved code of practice and guidance: Ionsing radiations regulations 1999.

[43] P. Hewitt. Occupational health problems in processing of x-ray photographic films. *Annals of Occupational Hygiene*, 37(3):287–95, 1993.

[44] P. Gerstenberger. Microfocus x-ray equipment. *Materials Testing*, 26(10):344–8, 1984.

[45] E. Nabel. Comparison of microfocus x-ray units. *British Journal of Non-Destructive Testing*, 28(3):133–8, 1986.

[46] R. V. Ely. An x-ray radiographic technique for resolving fine structures. In *Proceedings of the conference on dielectric materials, measurements, and applications*, pages 20–24, Lancaster, UK, July 1970. IEE.

[47] M. J. Yaffe and J. A. Rowlands. X-ray detectors for digital radiography. *Physics in Medicine and Biology*, 42(1):1–39, 1997.

[48] J. A. Rowlands. Current advances and future trends in x-ray digital detectors. *IEEE Instruments and Measurement Magazine*, 1(26-8), 1998.

[49] R. Orava. New detectors for radiology. *Physica Medica*, 15:295–300, 1999.

[50] J. Bell. A direct digital image capture system: The future of digital x-ray. *Medical Imaging Technology*, 17:105–9, 1999.

[51] H. C. Davidson, D. J. Johnston, M. E. Christian, and H. R Harnsberger. Comparision of radiographic image quality from four digitization devices as viewed on computer screens. *Journal of Digital Imaging*, 14(1):24–9, 2001.

[52] D. Wysnewski and R. Wysnewski. Computed radiography. In *NDE of Aging Aircraft, Airports, Aerospace Hardware and Materials*, 1995.

[53] T. S. Jones. Evaluation of digital x-ray radiological imagin systems for us air force applications. *Materials Evaluation*, pages 971–5, August 2001.

[54] J. Wilson and J. Hawkes. *Optioelectronics An Introduction.* Prentice Hall Europe, London, 1998.

[55] W. Yi, W. Jingjin, W. Kuilu, L. Guozhi, Z. Guofu, Z. Yuanlin, and D. Hongliang. Portable pulsed electronic digital imager. *NDT & E International*, 32:215–8, 1999.

[56] G. Giakos. A novel sensor for x-ray imaging applications. *IEEE Transactions on Instrumentation and Measurement*, 49:300–6, 2000.

[57] S. Suryanarayanan, A. Karellas, and S. Vedantham. Theoretical analysis of hybrid flat-panel detector arrays for digital x-ray flouroscopy: General system architecture, and noise processes. *IEEE Sensors Journal*, 1:168–74, 2001.

[58] E. Palecki D. Lee, L. Cheung and L. Jeromin. A discussion on resolution and dynamic range of se-tft direct digital radiographic detector. In *Annual Meeting on the Physics of Medical Imaging*, Newport Beach, CA, 1996.

[59] P. Soltani, D. Wysnewski, and K. Swartz. Amorphous selenium direct radiography for industrial imaging. In *Computerized Tomography for Industrial Applications and Image Processing in Radiology*, Berlin, Germany, 1999.

[60] T. Jones, H. Berger, and G. Cevallos. Electronic, digital x-ray imaging systems. In *ASNT Fall Conference and Quality Testing Show*, Pittsburgh, Pennsylvania, 1997.

[61] A. Davis, R. Hills, M. Sheats, and T. Claytor. High-energy x-ray and neutron modeling and digital imaging for nondestructive testing applications. *SPIE*, 4142: 108–18, 2000.

[62] B. Ramsey, D. Sharma, R. Austin, V. Gostilo, V. Ivanov, A. Loupilov, A. Sokolov, and H. Sipila. Preliminary performance of cdznte imaging detector prototypes. *Nuclear Instruments and Methods in Physics Research, Section A*, 458:55–61, 2001.

[63] F. Sauli. Gas detectors: Recent developments and future perspectives. *Nuclear Instruments and Methods in Physics Research, Section A*, 419:189–201, 1998.

[64] M. Li, M. Dixit, and P. Johns. Photon counting digital radiogrphy using high-pressure xenon filled detectors. *Nuclear Instruments and Methods in Physics Research, Section A*, 471:215–221, 2001.

[65] G. Giakos and S. Chowdhury. Multimedia imaging detectors operating on gas-solid-state ionization principles. *IEEE Transactions on Instrumentation and Measurement*, 47:1248–54, 1998.

[66] B. D. Ramsey. The microstrip proportional counter. *Proceedings of the International Society of Optical Engineers*, 1743:96–193, 1992.

[67] A. H. Walenta and H. J. Besch. Gas-filled detectors in medical and industrial imaging. *Proceedings of the International Society of Optical Engineers*, 2278:2–15, 1994.

[68] M. S. Dixit, J. C. Armitage, J. Dubeau, D. G. Gobbi, P. C. Johns, D. Karlen, and F. G. Oakham. Development of gas microstrip detectors for digital x-ray imaging and radiation dosimetry. *IEEE Transactions on Instrumentation and Measurement*, 47(3):809–13, June 1998.

[69] F. Brant. Guarantee casting quality with automatic x-ray inspection. *Modern Casting*, pages 39–41, October 1999.

[70] D. Zweig. Concurrent growth. *Printed Circuit Fabrication*, 19:40–4, 1996.

[71] M. P. Tornai, C. N. Archer, A. G. Weisenberger, R. Wojcik, V. Popov, S. Majewski, C. E. Keppel, C. S. Levin, V. Timpnis, and V. V. Nagagkar. Investigation of microcolumnar scintillators on an optical fiber coupled compact imaging system. *IEEE Transactions on Nuclear Science*, 48(3):637–44, June 2001.

[72] D. Lehmann and J. Gustafson. Realtime x-ray inspection: microfocus radioscopy; what it is and how it differs from conventional x-ray techniques. In *NEPCON West*, volume 3, pages 1307–12, Norwalk, CT, 1998.

[73] K. Kaufmann. Nondestructive testing using microfocus x-rays. *Lasers and Optronics*, 18(7):25–6, 1999.

[74] Agfa-Gevaert. Radiographic systems: Structurix film systems, September 2000.

[75] J. H. MacDonald, K. Wells, A. J. Reader, and R. J. Ott. A ccd-based tissue imaging system. *Nuclear Instruments and Methods in Physics Research, Section A*, 392:220–6, 1997.

[76] J. H. MacDonald, K. Wells, and R. J. Ott. Preliminary results from a novel ccd-based imaging system for biomedical applications. In *IEEE Symposium on Nuclear Science and Medical Imaging*, pages 1741–5, San Francisco, USA, 1995.

[77] E. J. Bowen. Electron energy transfer processes. In *The International Symposium of Energy Transfer in Radiation Processes*, Cardiff, UK, 1965.

[78] W. H. Tait. *Radiation Detection.* Butterworths, London, 1980.

[79] Hamamatsu Photonics K. K. X-ray imaging, 2001.

[80] Marconi Applied Technologies. Ccd sensors technical note: Glossary of terms, January 2001.

[81] G. A. Hay. X-ray imaging. *Journal of Physics E: Scientific Instruments*, 11:377–86, 1978.

[82] C. W. E. Eijk. Inorganic-scintillator development. *Nuclear Instruments and Methods in Phsycis Research A*, 460:1–14, 2001.

[83] Marconi Applied Technologies. Technical notes on the mft of ccd sensors, November 2001.

[84] A. R. Cowen. Digital x-ray imaging. *Measurement, Science and Technology*, 2: 691–707, 1991.

[85] M. Nixon and A. Aguado. *Feature Extraction and Image Processing.* Newnes, Oxford, 2002.

[86] A. Ortiz and G. Oliver. Radiometric calibration of ccd sensors: Dark current and fixed pattern noise estimation. In *International Conference on Robotics and Automation*, pages 4730–5, New Orleans, LA, April 2004.

[87] T. Tsukamoto, T. Satoh, A. Miyamoto, Y. Sugimoto, and T. Tauchi. Properties of a ccd sensor for vertex detector application. *Nuclear Instruments and Methods in Physics Research, Section A: Accelerators, Spectrometers, Detectors and Associated Equipment*, 383(1):256–9, December 1996.

[88] P. Martinez and A. Klotz. *A Practical Guide to CCD Astronomy.* Cambridge University Press, Cambridge, UK, 1998.

[89] S. L. Barma, M. W. Tate, S. M. Gruner, and E. F. Eikenberry. Calibration procedures for charge-coupled device x-ray detectors. *Review of Scientific Instruments*, 70(7):2927–34, July 1999.

[90] S. Vedantham. *Design and Characterization of a High-Resolution Cadiovascular Imager.* PhD thesis, Worcester Polytechnic Institute, 2002.

[91] X. Jiang, S. Qi, W. Wang, and W. Wang. Flat field correction method for image taken by a fiber optic taper coupled ccd camera. *High Power Laser and Particle Beams*, 16(11):1361–4, November 2004.

[92] R. J. Wonnacott and T. H. Wonnacott. *Introductory Statistics*. John Wiley & Sons, 1985.

[93] J. H. Hubbell and S. M. Seltzer. X-ray mass attenuation coefficients. http://physics.nist.gov/PhysRefData/XrayMassCoef, July 2004.

[94] A. P. Robinson, P.L. Lewin, S. J. Sutton, and S. G. Swingler. Automated high voltage cable inspection using x-ray images. In *International Conference on Solid Dielectrics*, volume 2, pages 687–90. IEEE, July 2004.

[95] R. E. Turner, O. L. Landen, D. K. Bradley, A. S. Alvarez, P. M. Bell, R. Costa, J. D. Moody, and D. Lee. Comparision of charge coupled device vs film readouts for gated micro-channel plate cameras. *Review of scientific instruments*, 72(1): 706–8, January 2001.

[96] J. Canny. A computational approach to edge detection. *IEEE Transactions on Pattern Analysis and Machine Intelligence*, PAMI-8(6):679–98, 1986.

[97] A. Watt. *The Computer Image*. Addison-Wesley, 1998.

[98] J. R. Parker. *Algorithms for image processing and computer vision*. Wiley, 1997.

[99] B. McCane. Edge detection. http://www.cs.otago.ac.nz/research/vision/Research/... ...TeachingVision/EdgeDetectionNotes.pdf, Feb 2001.

[100] S. R. Gunn. On the discrete representation of the laplacian of gaussian. *Pattern Recognition*, 32:1463–1472, 1999.

[101] S. R. Gunn. Edge detection error in the discrete laplacian of gaussian. In *IEEE International Conference on Image Processing*, pages 515–519, Chicago, USA, 1998.

[102] A. P. Robinson, P.L. Lewin, S. J. Sutton, and S. G. Swingler. Inspection of high voltage cables using x-ray techniques. In *International Symposium on Electrical Insulation*, pages 372–5. IEEE, Sept 2004.

[103] Y.H.Lee and S.A.Kassam. Generalized median filtering and related nonlinear filtering techniques. *IEEE Transactions on Acoustics, Speech and Signal Processing*, 33(3):672–683, Feb 1985.

[104] H. G. Senel, R. A. Peters II, and Benoit Dawant. Topographical median filters. *IEEE Transactions on Image Processing*, 10(12):1–16, 2001.

[105] A. P. Robinson, P.L. Lewin, S. J. Sutton, and S. G. Swingler. X-ray image processing for high voltage cable inspection. *IEE Proceeding of Science, Measurement and Technology*, 152(4):187–195, July 2005.

[106] G. Currell. *Essential mathematics and statistics for science.* Wiley, Chichester, 2005.